Observation and modeling of pollution events in Chile

Rémy Lapere

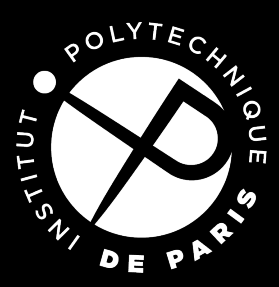

NNT : 2021IPPAX057

Thèse de Doctorat

Observation et modélisation des événements de pollution au Chili

Thèse de doctorat de l'Institut Polytechnique de Paris
Préparée à l'École Polytechnique, Laboratoire de Météorologie Dynamique
École doctorale n°626 : Ecole Doctorale de l'Institut Polytechnique de Paris
Spécialité : Mécanique des fluides et des solides, acoustique

Thèse présentée et soutenue à Palaiseau, le 30 Septembre 2021, par

Rémy Lapere

Composition du jury :

Philippe Drobinski Directeur de Recherche CNRS Laboratoire de Météorologie Dynamique	Président du Jury
Claire Granier Directrice de Recherche CNRS Laboratoire d'Aérologie	Rapporteure
Gilles Forêt Maître de Conférence UPEC Laboratoire Inter-Universitaire des Systèmes Atmosphériques	Rapporteur
Laura Gallardo Profesora Universidad de Chile	Examinatrice
Fabien Solmon Physicien adjoint CNAP Observatoire Midi-Pyrénées	Examinateur
Laurent Menut Directeur de Recherche CNRS Laboratoire de Météorologie Dynamique	Directeur
Sylvain Mailler Ingénieur des ponts, des eaux et des forêts Laboratoire de Météorologie Dynamique	Co-Directeur
Jean-Christophe Raut Maître de Conférence SU Laboratoire ATmosphéres, Milieux et Observations Spatiales	Invité
Florian Couvidat Ingénieur Institut National de l'Environnement Industriel et des Risques	Invité

Remerciements

Remercier, de l'ancien français *mercier* signifiant *exprimer la gratitude*. Gratitude, formation régressive depuis *ingratitude*, provenant du latin *ingratus*, ingrat. Dans les lignes qui suivent, je vais donc à nouveau (re) exprimer ma non-ingratitude (mercier) aux personnes ayant de près ou d'un peu plus loin (voire beaucoup plus loin, le Chili c'est pas à côté) fait partie des maillons de la chaîne téléologique aboutissant à l'élaboration de l'humble manuscrit que vous, lectrice/lecteur, avez entre les mains (ou plus vraisemblablement l'écran).

À tout seigneur tout honneur. Merci à Laurent et Sylvain de m'avoir donné ma chance en me supervisant en stage, puis d'avoir suffisamment bien supporté l'expérience pour envisager de la renouveler pour trois ans (et même encore un peu plus). Vous avez su me laisser beaucoup de latitude (ce qui est pratique au vu de la géographie du Chili, me laisser beaucoup de longitude ne m'aurait pas servi à grand chose), tout en préservant de la bande passante pour toujours répondre présents et m'orienter dans la quête de résultats parfois chimériques (voilà il fallait le faire c'est fait). Votre capacité à adopter une fréquence de nudging optimale laisserait Hans von Storch pantois. Je vous remercie également d'avoir pris le temps de m'expliquer les subtilités du cœur du réacteur de CHIMERE par le Menut, le tout sans jamais marteler les choses au Mailler.

Nicolás, muchisimas gracias por nuestra colaboración prolífica y encantadora que guió mi tesis. !A pesar de vivir en un barrio de quicos, no eres un weon! Ojalá trabajemos juntos de nuevo durante los años que vienen.

Je souhaite par ailleurs adresser de chaleureux remerciements aux membres de mon jury et comité de thèse qui m'ont fait l'honneur de prêter attention à mes travaux et leur nom à la page de garde de mon manuscrit. Leur expertise alliée à leur enthousiasme ont permis de fructueux échanges lors des comités intermédiaires et de la soutenance finale, ouvrant de nouvelles perspectives intéressantes pour de futurs travaux dans le prolongement des résultats présentés dans ce manuscrit. Mention particulière pour Philippe qui "*ne comprend rien à la chimie*" (*sic*) mais qui a tout même accepté d'être président de mon jury à deux reprises, et qui m'a par ailleurs confié des responsabilités d'enseignement passionnantes.

Alexis, je ne sais pas dans quelle mesure je dois te remercier. Tu m'as fréquemment soumis à la tantetion de ne pas travailler et atantet à l'avancée de mon projet de thèse par ta volonté de me convertir au "re-wilding" en piégeant le bureau avec des bouts de bois mort (mais bien sûr), d'aiguiser mon goût pour les musiques douteuses (voire franchement douteuses), ou encore de me démontrer la proposition de Tantet sur la réduction des opérateurs de transfert non-linéaires (que j'ai parfaitement comprise, cela va sans dire). Et non, je n'oublierai pas d'arroser les plantes.

A la liste des fauteurs de trouble il faut que j'ajoute Mathieu, Antoine et Joan. Entre les discussions venues d'un autre monde autour d'un déjeuner ou d'un café, et les matchs de basket de haute volée, on ne s'ennuie pas avec vous. J'aimerais aussi mentionner ici les différentes générations de doctorants, post-docs et chercheurs avec qui j'ai eu l'occasion d'interagir au LMD et qui m'ont permis d'en savoir un peu plus sur une large sélection de thématiques de recherche.

Inévitablement, ma famille au sens large (maman, papa, Clem, Chloé, Antoine, Max, JB, Marie...) a accompagné et facilité la poursuite de cette reconversion inattendue. Plus généralement, et pour ne pas basculer dans un inventaire à la Prévert, je vais simplement profiter de ces quelques lignes pour remercier pêle-mêle les personnes dont le prénom commence par une lettre contenue dans l'ensemble $\mathcal{E}$ défini ci-après, et qui se reconnaîtront: $\mathcal{E} = \{ABCDEFGHIJKLMNOPQRSTUVWXYZ\}$. Une pensée également pour Tozeur Belmanière et Frivoly T, ainsi que la rousse et la noire, qui m'ont proposé, à leur façon, moultes distractions bienvenues durant mes heures de télétravail normandes.

Une civilisation sans la science, ce serait aussi absurde qu'un poisson sans bicyclette.

Pierre Desproges, *Vivons heureux en attendant la mort (1983)*

Résumé de la thèse

Le Chili est fréquemment confronté à d'importants pics de pollution atmosphérique, notamment dans sa région centrale qui comprend la capitale, Santiago, et ses 7 millions d'habitants. Cette pollution est principalement d'origine anthropique (trafic automobile, chauffage au bois, industries) mais revêt également une composante naturelle en lien avec les feux de biomasse et les émissions de poussières désertiques. Les concentrations de surface observées sont délétères aussi bien concernant la matière particulaire (les aérosols) que les espèces gazeuses (l'ozone en particulier), ce qui représente un poids sanitaire, économique et environnemental pour le pays. Ce problème est à la fois chronique, avec des concentrations au-delà des seuils recommandés par l'OMS la majeure partie de l'année, mais aussi aigu, avec des pics de pollution pouvant ponctuellement atteindre des niveaux comparables à ceux observés dans les mégapoles indiennes ou chinoises.

Les caractéristiques géographiques atypiques et complexes de cette fine bande de terre bordée par l'océan Pacifique à l'Ouest et la Cordillère des Andes à l'Est, le désert d'Atacama au Nord et les champs de glace de Patagonie au Sud, en font un lieu particulièrement propice à l'accumulation des polluants atmosphériques, et où les dynamiques d'advection comportent des particularités propres aux environnements montagneux. Du fait de cette complexité et de cette spécificité, la pollution de l'air au Chili, notamment du point de vue de la modélisation, est relativement peu étudiée au regard des enjeux attenants pourtant cruciaux en termes de santé publique et d'environnement. En particulier, la proximité du bassin de Santiago, générant des flux d'émission de polluants considérables, avec les glaciers Andins distants de quelques dizaines de kilomètres seulement, fait craindre une accélération de la fonte de ces derniers via le dépôt de matière particulaire opaque. Bien que ce phénomène soit encore mal quantifié, les conséquences associées pourraient être d'importance pour les écosystèmes et les ressources en eau de la région. Du point de vue sanitaire, des événements extrêmes de pollution se produisent régulièrement ces dernières années, induisant des hospitalisations massives pour problèmes respiratoires, malgré des politiques de plus en plus contraignantes sur les émissions. L'origine de ces épisodes exceptionnels n'est, malgré leur impact, néanmoins pas toujours identifiée.

L'objectif général de cette thèse est alors de mieux caractériser la pollution atmosphérique au Chili, de ses sources à ses impacts, en passant par la dynamique sous-jacente. En particulier, les questions de recherche abordées dans cette thèse concernent (i) **l'ampleur du flux de transport régional de polluants au Chili central en été et en hiver et les dynamiques associés**, (ii) **la caractérisation des sources et impacts des épisodes extrêmes de pollution enregistrés ces dernières années en hiver comme en été**, (iii) **le trajet des émissions urbaines de carbone suie jusqu'à leur dépôt sur les glaciers Andins**.

Dans cette optique, les analyses s'appuieront principalement sur les données de mesure opérationnelles des réseaux locaux de suivi de la météorologie et de la qualité de l'air, combinées à des campagnes de mesures ponctuelles réalisées par nos collègues de l'Université du Chili, les mesures satellitaires proposant à la fois des données agrégées (MODIS, IASI) ou avec un raffinement sur la verticale (CALIOP), les réanalyses climatologiques (ERA5) permettant de lier la dynamique de grande échelle et les phénomènes locaux, ainsi que la modélisation déterministe régionale de chimie-transport avec le modèle WRF-CHIMERE développé dans l'équipe.

Cette dernière composante de modélisation de la qualité de l'air est innovante dans le cas du Chili. Avant cette thèse, très peu d'études abordaient les problèmes de qualité de l'air du Chili au travers de simulations de chimie-transport. L'un des atouts majeurs de cette modélisation, exploité dans ce travail, est de pouvoir réaliser des scénarios modulant les émissions afin d'isoler et évaluer la contribution de certaines sources à la composition atmosphérique observée. L'utilisation de traceurs passifs permet également la mise en lumière des trajectoires relatives aux processus de transport des polluants. La modélisation se concentre principalement sur les aérosols, en particulier les particules fines et le carbone suie, mais aborde également la chimie de l'ozone et ses précurseurs. La difficulté de cette approche par la simulation réside dans la topographie complexe de la région qui requiert une haute résolution spatiale, alliée à la forte saisonnalité des émissions de polluants, et à des

dynamiques de transport induisant une forte non-localité du phénomène de pollution atmosphérique.

Les conclusions principales de cette thèse concernent (i) l'identification de la source des événements extrêmes de particules fines à Santiago en hiver, attribués aux barbecues massifs organisés lors des matchs de football de l'équipe nationale, (ii) l'estimation des impacts sur la qualité de l'air et des rétro-actions météorologiques liés aux polluants émis massivement lors des incendies exceptionnel de 2017, (iii) la caractérisation du transport saisonnier à l'échelle du Chili central, (iv) la mise en évidence de la formation d'une bulle d'ozone persistante au-dessus de Santiago en été en lien avec la dynamique montagne-vallée, (v) la qualification et quantification des exports de carbone suie d'origine anthropique vers les glaciers de la Cordillère des Andes.

Summary of the thesis

Chile regularly faces concerning atmospheric pollution peaks, particularly so in its central region which comprises Santiago, the capital city, home to 7 million inhabitants. This bad air quality in the country is mainly of anthropogenic origin (road traffic, residential heating with wood burning, industry) but also entails a natural component related to forest fire emissions and mineral dust from arid deserts. Noxious surface concentrations are observed both in terms of particulate matter (aerosols) and gaseous species (especially ozone), which imply a significant burden on public health, the economy and the environment for the second geopolitical power of South America. Foul air is observed all year long (chronic exposure) with concentrations of criteria pollutants well above the recommend WHO standards for the majority of the year. Sporadically, peak events of particulate matter and haze are also observed (acute exposure) that compare with levels recorded in Chinese and Indian megacities.

The atypical and complex geographical features of the narrow strip of land that is Chile, trapped between the Pacific Ocean in the west and the Andes Cordillera in the east, and bounded by the Atacama desert in the north and the Patagonian ice fields in the south, make for conditions particularly favorable to the accumulation of atmospheric pollutants, with underlying advection dynamics specific to mountainous environments. Due to such a complex, idiosyncratic situation, air pollution in Chile is not as extensively studied as could be expected given the critical stakes involved in terms of public health and environmental protection. This is especially true regarding atmospheric composition modeling, which is challenging in this region of the world and thus seldom attempted despite its potential.

In environmental terms, one of the major threats is connected to the location of the Santiago basin close to the foothills of the Andes Cordillera. Glaciers of the mountain range are only a few kilometers away from the capital city, and thus within reach of its strong emissions of pollutants. In particular, export and deposition of urban light-absorbing particulate matter onto said glaciers threatens to increase their melting rate. Although this phenomenon is still not very well quantified, the associated consequences are paramount for ecosystems and water resources in the region. From a public heath perspective, extreme events of air pollution were still recorded in the recent years, despite the implementation of ever more stringent policies on emissions, leading to massive fluxes of hospital admissions for respiratory issues. The source of these peak events is still not very well identified.

In this context, the objective of this PhD work is to better characterize air pollution in Chile, from its sources to its impacts through the underlying atmospheric dynamics. More specifically, the research questions addressed in this thesis are related to (i) **the magnitude and dynamics of transport of pollution at the scale of central Chile in summertime and wintertime**, (ii) **the characterization of the sources and impacts of recently recorded extreme events of bad air quality**, (iii) **the pathways of urban black carbon from its emission to its deposition onto glaciers of the Andes**.

To do so, the analyses rely on data from automated local networks of meteorology and air quality monitoring, combined with sporadic measurement campaigns conducted by our colleagues at the University of Chile, satellite data from MODIS, IASI and CALIOP providing aggregated total column data and information of the vertical, climatological reanalyses such as ERA5 to relate synoptic-scale circulation to local phenomena, and regional chemistry-transport modeling with WRF-CHIMERE, which is developed in the team.

The latter air quality modeling approach is relatively when it comes to Chile. Before this PhD work there were little studies addressing air pollution in this region through the use of chemistry-transport modeling. One of its main advantage, on which this work builds, is the ability to run scenarios modulating emissions in order to isolate and assess the effect and contribution of given sources to observed atmospheric composition. Passive tracers in the model also offer the possibility to highlight the pathways and transport processes of pollutants. Our modeling approach focuses mainly on aerosols, especially fine particles and black carbon, but also investigate

the chemistry of ozone and its precursors. The complexity of such a modeling methodology lies in the complex, steep topography of the area that requires high spatial resolution, combined with the pronounced seasonality of pollutants emissions, and transport dynamics inducing a strong non-locality of atmospheric pollution.

The main outcomes of this thesis are related to (i) the identification of the source of wintertime extreme fine particles events in Santiago, that were found to be connected massive barbecue cooking by its inhabitants during soccer games of the national team, (ii) the estimation of the impacts on air quality and the meteorological feedback of the pollutants emissions during the historic 2017 mega-fires in southcentral Chile, (iii) the characterization of seasonal transport of pollutants in central Chile, (iv) the discovery of the formation of a persistent ozone bubble above Santiago in summertime in connection with mountain-valley circulation dynamics, (v) the quantification and qualification of anthropogenic black carbon export from urban areas to glaciers of the Andes Cordillera.

Resumen de la tesis

Chile se enfrenta regularmente a picos de contaminación atmosférica preocupantes, especialmente en su zona central, donde Santiago la capital está ubicada, y donde viven 7 millones personas. La mala calidad del aire en el país es principalmente de origen antropogénico (tráfico, calefacción residencial con leña, industria) pero también conlleva un componente natural relacionado con las emisiones de los incendios forestales y el polvo mineral de los desiertos áridos. Se observan concentraciones superficiales nocivas tanto de partículas (aerosoles) como de especies gaseosas (especialmente el ozono), que implica una carga importante para la salud pública, la economía y el medio ambiente. El aire viciado se observa durante todo el año (exposición crónica) con concentraciones de contaminantes criterio muy por encima de las normas recomendadas por la OMS durante la mayor parte del año. Esporádicamente, también se observan picos de partículas y esmog (exposición aguda) que se comparan con los niveles registrados en las megaciudades chinas e indias.

Las características geográficas atípicas y complejas de la estrecha franja de tierra que es Chile, atrapada entre el Océano Pacífico al oeste y la Cordillera de los Andes al este, y limitada por el desierto de Atacama al norte y los campos de hielo patagónicos al sur, hacen que se den unas condiciones especialmente favorables para la acumulación de contaminantes atmosféricos, con una dinámica de advección subyacente propia de los entornos montañosos. Debido a esta situación tan compleja e específica, todavía falta mucho para entender la contaminación atmosférica en Chile, considerando la magnitud de las consecuencias en términos de salud pública, de economía y de impacto medioambiental. Esto es especialmente cierto en cuento a la modelización de la composición atmosférica, que es un reto sobre el territorio Chileno y, por tanto, poca veces se intenta a pesar de su potencial.

Desde el punto de vista medioambiental, una de las principales amenazas está relacionada con la ubicación de la cuenca de Santiago cerca de los contrafuertes de la Cordillera de los Andes. Los glaciares de la cordillera están a pocos kilómetros de la capital y, por tanto, al alcance de sus fuertes emisiones de contaminantes. En particular, la exportación y deposición de partículas urbanas opacas sobre estos glaciares amenaza con aumentar su ritmo de deshielo. Aunque este fenómeno aún no está muy bien cuantificado, las consecuencias asociadas son primordiales para los ecosistemas y los recursos hídricos de la región. En terminos de salud pública, en los últimos años se han seguido registrando episodios extremos de contaminación atmosférica, a pesar de la aplicación de políticas cada vez más estrictas sobre las emisiones, lo que ha provocado flujos masivos de ingresos hospitalarios por problemas respiratorios. El origen de estos picos todavía no está muy bien identificado.

En este contexto, el objetivo de esta tesis de doctorado es caracterizar mejor la contaminación del aire en Chile, desde sus fuentes hasta sus impactos a través de la dinámica atmosférica subyacente. Más específicamente, las preguntas de investigación que se abordan en esta tesis están relacionadas con (i) **la magnitud y dinámica del transporte de la contaminación a escala de Chile central en verano e invierno**, (ii) **la caracterización de las fuentes e impactos de los episodios extremos de mala calidad del aire registrados recientemente**, (iii) **las vías del carbono negro urbano desde su emisión hasta su deposición en los glaciares de los Andes**.

Los análisis se basan en datos de redes locales automatizadas de meteorología y monitoreo de la calidad del aire, combinados con campañas de medición esporádicas realizadas por nuestros colegas de la Universidad de Chile, datos satelitales de MODIS, IASI y CALIOP que ofrecen datos agregados de columna total tan como información sobre la vertical, reanálisis climatológicos como ERA5 para relacionar la circulación a escala sinóptica con los fenómenos locales, y la modelización regional de química-transporte con WRF-CHIMERE que esta desarrollado en el equipo.

Este último enfoque de modelización de calidad del aire es relativamente nuevo en Chile. Antes de este trabajo de doctorado había pocos estudios que abordaran la contaminación del aire en esta región mediante el uso de la modelización de química-transporte. Una de sus principales ventajas, en la que se basa este trabajo, es

la capacidad de ejecutar escenarios que modulan las emisiones para aislar y evaluar el efecto y la contribución de fuentes particulares a la composición atmosférica observada. Los trazadores pasivos en el modelo también ofrecen la posibilidad de poner de relieve las vías y los procesos de transporte de los contaminantes. Nuestro enfoque de modelización se centra principalmente en el material particulado y el carbono negro, pero también investiga la química del ozono y sus precursores. La dificultad de esta metodología de modelización radica en la compleja y abrupta topografía de la zona, que necesita una alta resolución espacial, combinada con la pronunciada estacionalidad de las emisiones de contaminantes, y la dinámica de transporte que induce una fuerte no-localidad de la contaminación atmosférica.

Los resultados principales de esta tesis se relacionan con (i) la identificación de la fuente de eventos invernales extremos de partículas finas en Santiago, que se encontraron conectados a la cocción masiva de asados por sus habitantes durante los partidos de fútbol de la selección nacional, (ii) la estimación de los impactos en la calidad del aire y de la retroacción meteorológica de las emisiones de contaminantes durante los mega incendios históricos de 2017 en el centro-sur de Chile, (iii) la caracterización del transporte estacional de contaminantes en la zona central de Chile, (iv) el descubrimiento de la formación de una burbuja de ozono persistente encima Santiago en verano en relación con la dinámica de circulación montaña-valle, (v) la cuantificación y calificación de la exportación de carbono negro antropogénico desde las zonas urbanas hasta los glaciares de la Cordillera de los Andes.

Contents

1 | General Introduction

1.1 About air pollution

Seinfeld and Pandis [2006] define air pollution as a situation in which anthropogenic activities result in high above normal atmospheric concentrations of substances, producing a measurable effect on humans, animals, vegetation or materials. Although the substances might be either noxious or benign, undesirable effects are usually implied. An extended definition includes natural events or sources, which can also lead to harmful levels of compounds in the atmosphere (e.g. volcanic eruptions, vegetation, biomass burning...). Pollutants can be classified according to their chemical composition, their phase state (gas or aerosol), their nature (primary or secondary) and the layer of the atmosphere in which they are found (tropospheric or stratospheric). Primary pollutants are directly emitted as such into the atmosphere (e.g. sulfur dioxide, nitrogen oxides, black carbon...), as opposed to secondary pollutants that have no direct source and result from the combination of primary compounds (precursors) and chemical reactions in the atmosphere (e.g. ozone, secondary aerosols...). Although pollutants can be present in several components of ecosystems (atmosphere, water, plants, animals...), the focus of this work is made on those found in the air. Let us then first define and characterize the sub-universe inside of which our investigations are conducted.

1.1.1 The Earth's atmosphere

The atmosphere (from Ancient Greek ἀτμός (*atmos*), 'vapor', and σφαῖρα (*sphaira*), 'sphere') is the layer of gases that surrounds a planet, in our case the Earth. Most of its mass (99%) is found in the two layers closer to the ground: the troposphere and the stratosphere, which are separated by the tropopause (Figure 1.1a). Although long-lived pollutants can reach the stratosphere, the present work, like the majority of air quality oriented topics, focuses on the layer where human beings and ecosystems live and thus can be directly affected by pollutants, namely the troposphere.

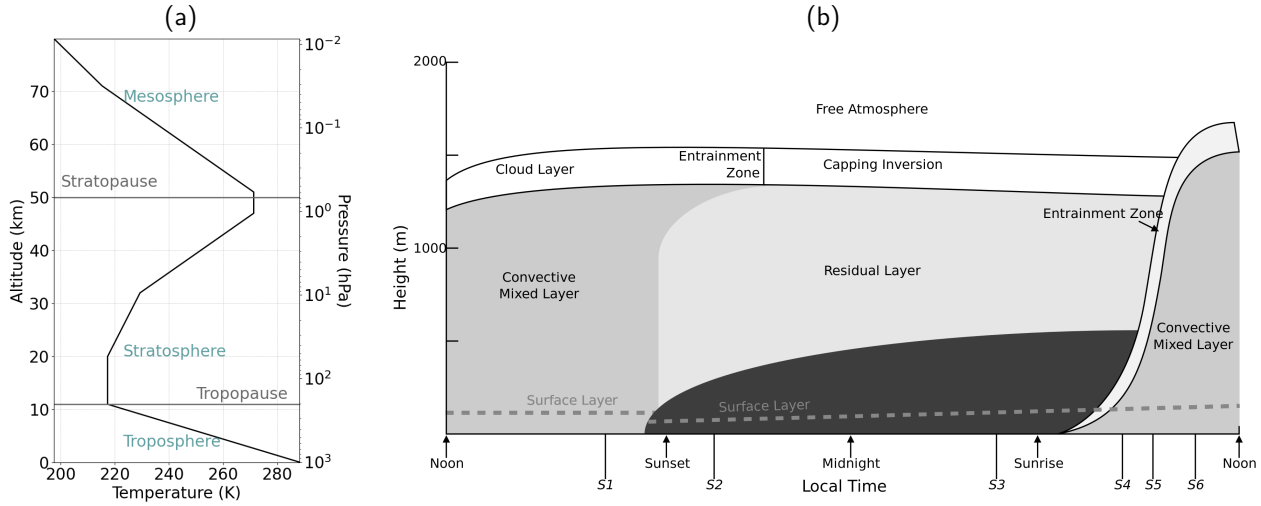

Figure 1.1: (a) US standard atmosphere vertical profile of temperature [COESA, 1976]. (b) Planetary boundary layer typical structure over a diurnal cycle in high pressure regions over land. Adapted from Stull [1988]

The troposphere is the lowest layer of Earth's atmosphere, where local meteorological phenomena combine with large scale synoptic circulation to form the weather. Its depth varies with latitude and season (around 18 km in the tropics down to 6 km in the poles during winter). It contains approximately 99% of the total mass of water vapor and aerosols, and about 80% of the total mass of the atmosphere. Its gas composition is as follows: 78% nitrogen (N_2), 21% oxygen (O_2), 0.0093% argon (Ar) and some other noble gases that make a total 99.9% of the dry mass of the troposphere. The remaining 0.1% is composed of trace gases such as carbon dioxide (CO_2), methane (CH_4), and the pollutants relevant to this work, i.e. for example, ozone (O_3), nitrogen oxides (NO_x), volatile organic compounds (VOCs), sulfur dioxide (SO_2), carbon monoxide (CO) [Allen, 1976]. In addition to dry gases, aerosols are present in the atmosphere, as well as water vapor.

The troposphere can be further separated into two distinct regions. The layer closer to the ground where the motion of air masses is influenced by surface friction and heating from the ground, is the Planetary Boundary

Layer (PBL). The PBL is governed by turbulent motion and fast vertical mixing. Depending on the season, time of the day and land profile, the height of the PBL may vary from a few hundred meters to several kilometers (Figure 1.1b). This height is a major driver of the concentration of pollutants humans are confronted with. Indeed, when the mixing layer is shallow, most pollutants cannot reach the layers aloft and remain trapped within the PBL. As a result, for the same quantity of emitted pollutants, a PBL twice as high directly leads to halved concentrations. The layer between the PBL and the tropopause is the Free Troposphere (FT), where the influence of the surface is lesser, and stronger quasi-geostrophic winds dominate. For convective PBL days, pollutants might be able to reach the FT, and be transported far from their emission site.

Atmospheric inversions (or thermal inversions) occur when the temperature of air layers close to the ground is lower than the layers higher up. These conditions create an extremely stable and shallow PBL that is favorable to the accumulation and stagnation of pollutants. This phenomenon occurs mostly in cold winter days and can create a shallow layer of highly contaminated air trapped in steep orographic configurations such as valleys or basins [e.g. Gramsch et al., 2014]. The convective or stable character of the PBL is related to the Brunt-Väisälä frequency ($N^2 = \frac{g}{\theta}\frac{\partial\theta}{\partial z}$, with g the acceleration of gravity and θ the potential temperature). The correct representation of the PBL is key for atmospheric composition modeling purposes as it governs both the dilution factor and advection trajectories of emitted pollutants.

Let us now introduce and give an overview of the main relevant pollutant species and processes we will come across throughout our upcoming atmospheric chemistry journey inside the Chilean troposphere.

1.1.2 Chemistry of the troposphere

This section describes the chemical species and processes that are relevant for the present work. The theory introduced here is based on Seinfeld and Pandis [2006].

1.1.2.1 Generalities

Generally speaking, the time evolution of the concentration of an atmospheric compound within a parcel of air is controlled by its sources and sinks. For the simple case of a first-order sink this can be expressed as in Equation (1.1), where N_X is the concentration of species X, S_X is the emission flux of compound X per unit time, and τ is the lifetime of X.

$$\frac{\mathrm{d}N_X(t)}{\mathrm{d}t} = S_X(t) - \frac{N_X(t)}{\tau} \tag{1.1}$$

The lifetime of a species corresponds to the time elapsed, for a representative molecule of the substance, between its introduction into the atmosphere and its removal. Removal processes include dry deposition (due to gravity and turbulent mixing) and wet deposition (scavenging by rainfall or dissolution in cloud droplets) on the Earth's surface, or consumption by chemical reactions (e.g. photolysis, oxidation ...). The lifetime of a pollutant defines its ability to spread within or across air layers. Typically, given the motion of air masses, species with a lifetime shorter than 1 week are unlikely to reach the stratosphere or another continent, while a lifetime of several months gives the possibility of being transported all across the globe or/and out of the troposphere. Table 1.1 summarizes typical atmospheric lifetimes of relevant compounds.

Species	Lifetime	Reference
Black carbon	up to 5 days	Lund et al. [2018]
NO_X	1 to 10 hours	Laughner and Cohen [2019]
CO	1 to 4 months	Seinfeld and Pandis [2006]
VOCs	hours to days	Monod et al. [2001]
SO_2	hours to days	Lee et al. [2011]

Table 1.1: Typical lifetimes of a selection of atmospheric pollutants.

1.1.2.2 Gaseous pollutants

Plethora of trace gases are found in the atmosphere, most of them being harmless. The focus here is set on the main problematic ones in environmental terms, that are relevant for the present work. Their main features are briefly summarized hereafter.

Ozone - O_3
Stratospheric ozone is essential to life on Earth, through its UV shielding effect. Tropospheric O_3 however is noxious, in addition to being a greenhouse gas. It is a secondary gaseous species formed by the reaction of its precursors such as NO_x and VOCs in the presence of specific wavelengths of light [Seinfeld and Pandis, 2006]. Since it is governed by solar radiation and temperature, tropospheric O_3 pollution is thus mainly observed in summertime and features a marked diurnal profile. Its photo-chemical cycle is complex (see Section 1.1.2.3) and almost justifies by itself the need for atmospheric chemistry modeling. Given the dependence of O_3 formation on the ratio between NO_x and VOCs, suburban areas downwind of large cities with extensive vegetation usually feature a more favorable environment for the production of O_3 and thus suffer greater contamination than urban areas [e.g. Menut et al., 2000]. O_3 is noxious for human health, causing respiratory disorders such as asthma [Lippmann, 1991]. Furthermore, its deposition on plant leaves affects their photosynthesis and evaporation ability, thereby damaging crop yields [Hill and Littlefield, 1969].

Nitrogen oxides - NO_x
Nitrogen oxides, NO_x=(NO+NO_2), are produced mostly at high temperatures, such as the ones found in combustion processes (car exhausts, industrial factories...) or lightnings. Around 65% of NO_x emissions come from fossil fuel combustion involved in human activities, and 14% from biomass burning whether from natural or anthropogenic origin [Ehhalt et al., 2001]. The remaining sources include bacterial processes in soils and lightnings [Ehhalt et al., 2001]. NO_x can react with a wide variety of compounds depending on atmospheric composition and sunlight conditions, forming noxious gases or particles [Seinfeld and Pandis, 2006]. In particular, it is involved in the formation of ozone photo-chemical smog, and plays a role in the acidification of clouds and thus rainfall through the formation of NH_3 [e.g. Qin and Huang, 2001]. In addition to being a precursor for other harmful pollutants, NO_x itself is noxious for human being when inhaled (irritation of the respiratory system) and is thus defined as a criteria pollutant by the WHO and subject to standard guidelines [WHO, 2003, 2006].

Sulfur dioxide - SO_2
Sulfur dioxide is primarily emitted by the burning of sulphur-containing fuels for industrial processes (60%) and shipping (6%), but also by natural sources such as biomass burning (2%), volcanic eruptions (8%) and water bodies through dimethyl sulfide (24%) [Lee et al., 2011]. When further oxidized in aqueous phase within cloud droplets, it forms sulfuric acid (H_2SO_4) leading to the infamous acid rains [e.g. Jacob, 1999, Qin and Huang, 2001]. Acid rains have adverse effects on forests, soils and freshwater ecosystems, and contribute to the corrosion of materials hence decreasing the lifetime of infrastructures [Singh and Agrawal, 2008]. SO_2 is also toxic for human beings if breathed or ingested, with respiratory symptoms, so that WHO air quality standards are defined for that criteria species [WHO, 2006].

Carbon monoxide - CO
Carbon monoxide originates from the incomplete combustion of carbon-containing compounds. Its main sources include biomass burning (30%), combustion for residential (stoves, heating) and transport (engine vehicles) purposes (12%), and oxidation from biogenic sources (hydrocarbons and methane - 57%) [Holloway et al., 2000]. In large quantities, this compound is deadly for species relying on hemoglobin as an oxygen carrier in connection with cardiovascular impairments [WHO, 1999]. CO also has a major influence on the tropospheric ozone cycle (see Section 1.1.2.3).

Volatile organic compounds - VOCs
Volatile organic compounds are organic molecules that have a vapor pressure of 10 Pa or more at ordinary room temperature (20°C) [European Union, 1999]. They include a large spectrum of species, that can be from anthropogenic (e.g. formaldehyde that evaporates from paint) or biogenic (e.g. terpenes emitted by plant leaves) origin [Koppmann, 2007]. Their main sink is oxidation by the hydroxyl radical (OH) which has a strong impact on the ozone cycle and makes the gases less volatile, leading to the formation of organic aerosols. Harmful VOCs usually do not have acute effects at usual atmospheric concentrations, but have compounding long-term health effects, particularly in indoor environments [Bernstein et al., 2008].

1.1.2.3 The tropospheric ozone cycle

Photons with a wavelength below 424 nm are able to separate an oxygen atom from NO_2 through photolysis reaction (R 1.1). This reaction is immediately followed by (R 1.2) that combines the highly reactive oxygen atom liberated with O_2 which is present in large quantities in the atmosphere, to form O_3. M is a third body needed to absorb the excess energy from the excited molecule. NO_2 photolysis is the only significant net source of ozone

in the troposphere.

$$NO_2 \xrightarrow{h\nu} NO + O \tag{R 1.1}$$

$$O + O_2 + M \longrightarrow O_3 + M \tag{R 1.2}$$

Once formed, O_3 reacts with NO, if present, to form NO_2 and O_2 (R 1.3). Eventually, NO_2 is consumed and formed so quickly in this cycle that reactions (R 1.1) through (R 1.3) will reach a steady-state. At that point, the concentration of O_3 is given by Equation (1.2) referred to as the photostationary state relation [Leighton, 1961].

$$NO + O_3 \longrightarrow NO_2 + O_2 \tag{R 1.3}$$

$$[O_3] = \frac{j_{NO_2}[NO_2]}{k_{R1.3}[NO]} \tag{1.2}$$

with j_{NO_2} and $k_{R1.3}$ the NO_2 photolysis rate and reaction constant of (R 1.3), respectively.

Most NO_x emitted by anthropogenic activities are in the form of NO (between 70% and 90% for recent car exhausts for instance [e.g. Carslaw et al., 2019]), and a typical value for $j_{NO_2}/k_{R1.3}$ is 10 ppb. Thus, for realistic NO_2 concentrations, the photostationary state relation (1.2) yields very low ozone mixing ratios compared to measurements. Several oxidation chains are actually at play in parallel to the (R 1.1)-(R 1.3) cycle, that form NO_2 without depleting O_3, hence feeding the ozone cycle and increasing the net formation of O_3. Such oxidation chains are triggered by the presence of the hydroxyl radical (OH) that consumes species like CO - net global reaction (R 1.4) - CH_4 - net global reaction (R 1.5) - and several non-methane VOCs, in NO_x-rich environments.

$$CO + 2\,O_2 \xrightarrow{h\nu} CO_2 + O_3 \tag{R 1.4}$$

$$CH_4 + 10\,O_2 \xrightarrow{h\nu} CO_2 + H_2O + 2\,OH + 5\,O_3 \tag{R 1.5}$$

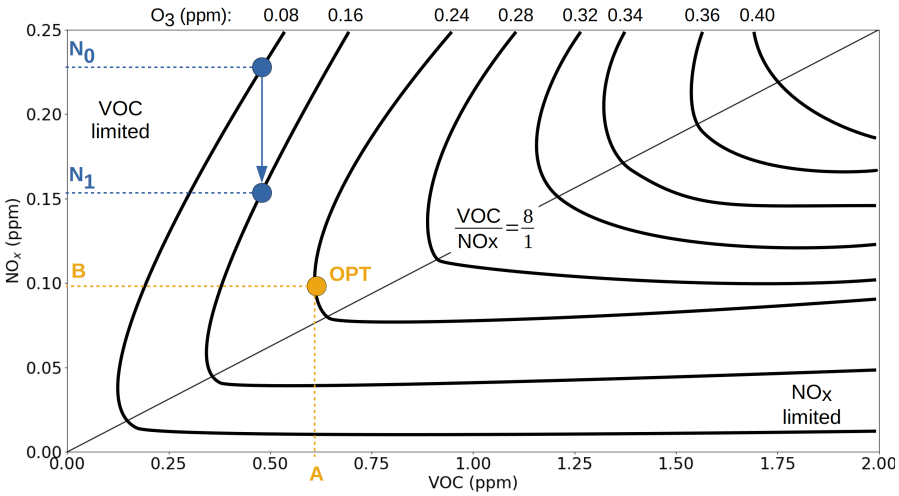

Figure 1.2: Example schematic of O_3 isopleth (Ekma diagram), inspired from National Research Council [1991]. Countours indicate O_3 production levels as a function of VOC and NO_x concentrations.

O_3 production is conditioned by the presence of sunlight, and greatly depends on temperature and the chemical state of the atmosphere [Seinfeld and Pandis, 2006]. First, during nighttime the photolysis of NO_2 cannot occur, by definition, thus preventing the start of cycle (R 1.1)-(R 1.3). At the same time, excess O_3 is consumed by reactions such as (R 1.3). As a result, a marked diurnal cycle is usually observed for surface O_3 mixing ratio, with a peak in the afternoon due to the presence of sunlight and accumulation of the day, and a minimum at night due to the activity of O_3 sinking reactions only. Second, temperature influences the rates of the chemical reactions involved in the ozone cycle, as well as the production of VOCs by vegetation. In both cases, higher temperatures are more favorable for O_3 production. Third, there is a competition between VOCs

and NO_x for the OH radical, which is the key reactive species in the formation of O_3 as the trigger of CO, CH4 and VOCs oxidations. The relationship between O_3 production and VOC/NO_x ratio is complex and described in so-called ozone isopleth diagrams [e.g. Dodge, 1977].

Figure 1.2 illustrates the non-linearity of O_3 production: for a given concentration A of VOC, there is an optimum production of O_3, OPT, associated with a specific NO_x concentration B. Departing from B, either by increasing or decreasing NO_x results in a decreased O_3 production. A direct consequence is that for environments where NO_x is in large excess such as urban centers that combine massive traffic emissions and comparatively lower VOC emissions (sparse to no vegetation), decreasing NO_x can locally increase O_3 levels. This is illustrated in Figure 1.2: transition from situation N_0 to situation N_1 (decrease of NO_x by 30% in a VOC-limited atmosphere, VOC remaining constant) doubles the production of O_3. This is typically the effect that a traffic-oriented emission policy would have on urban O_3 concentrations [e.g. Munir et al., 2012]. The ridge line VOC/NO_x=8 delimits the regimes where NO_x (VOC, respectively) is in excess and O_3 production is limited by too low VOC (NO_x, respectively) therefore corresponding to VOC-limited (NO_x-limited, respectively) atmospheric composition typical of urban (rural, respectively) environments.

1.1.2.4 Aerosols

The Intergovernmental Panel on Climate Change (IPCC) defines aerosols as 'a collection of airborne solid or liquid particles, with a typical size between 0.01 and 10 µm, that reside in the atmosphere for at least several hours' [IPCC, 2007]. Aerosols may be of either natural or anthropogenic origin. Primary aerosols are directly emitted into the atmosphere in aerosol form, as opposed to secondary aerosols that are formed in the atmosphere through oxidation of gases such as SO_2, VOCs, NH_3 and condensation processes (see Section 1.1.2.5). They are removed from the atmosphere through dry (due to gravity, turbulence) or wet (scavenging by rain or in-cloud droplets) deposition. Aerosols (or particulate matter - PM) are categorized based on their composition and size, since the processes affecting them greatly depend on these two parameters. $PM_{2.5}$ gather particles with an aerodynamic diameter smaller than 2.5 µm, called fine particles. PM_{10} gather particles with an aerodynamic diameter smaller than 10 µm. These two categories are usually the most monitored for air quality purposes and are often subject to standard levels to comply with by countries or cities [e.g. McClellan, 2002]. Aerosols with a diameter between 2.5 and 10 µm constitute the coarse particles (Figure 1.3).

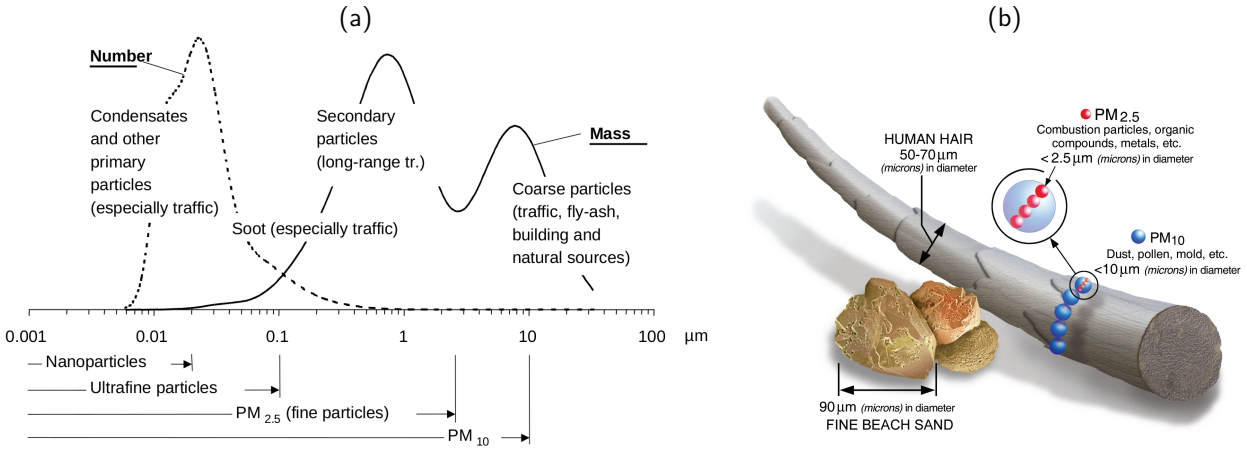

Figure 1.3: (a) Typical number and mass distribution of aerosols by aerodynamic diameter [Nielsen et al., 2008]. (b) Size comparison for PM particles. Schematic from the US Environmental Protection Agency.

Examples of naturally emitted primary aerosols include marine sea-salt due to the bursting of bubbles at the sea surface that are then pulled off and injected into the atmosphere under strong winds, mineral dust that is injected in the air by wind friction on arid soils such as deserts, ashes emitted by volcanic eruptions, and a selection of compounds released during biomass burning events. Secondary organic aerosols, which constitute a large part of secondary aerosols [Shiraiwa et al., 2017], are inherent to the presence of vegetation and oxidation of VOCs.

Anthropogenic emissions mainly originate from combustion (mostly $PM_{2.5}$ from engines and heating), and mechanical processes (coarse mode particles from soil exploitation in agriculture, public work, mining) [Penner

et al., 2001]. Such aerosols are referred to as primary particulate matter (PPM). PM from combustion are either black carbon (BC), fine mode light-absorbing aerosols, or organic carbon (OC) which encompasses any kind of organic matter in particulate phase. Particles from mechanical processes have diverse forms as they depend on the type of soil that is exploited. Human activities also participate in the formation of secondary particles through the release of VOCs for instance [Piccot et al., 1992]. Present-day estimates of annual emission fluxes of a selection of key primary aerosols are gathered in Table 1.2.

Species	Source	Emission flux ($Tg\,yr^{-1}$)	References
Black Carbon	Anthropogenic	7.2	Klimont et al. [2017]
	Biomass Burning	3.5	Ito and Penner [2005]
Organic Carbon	Anthropogenic	13	Klimont et al. [2017]
	Biomass Burning	25	Bond et al. [2004]
Sea salt	Marine	3,600	Weng et al. [2020]
Mineral dust	Desert	3,500 to 6,000	Klose et al. [2021]

Table 1.2: Present-day estimates of global annual emission fluxes of primary aerosols.

1.1.2.5 Secondary aerosols

The atmosphere acts as a chemical reactor where thermodynamics, physics and chemistry interact, leading to the creation of particulate matter from gaseous precursors. The formation of such so-called secondary aerosols follows a three-step process (Figure 1.4):

1. Nucleation: precursor gases are released into the atmosphere and condensate to become clusters of solid/liquid particles (*ultrafine mode* - size in the range of 10^{-3} to $10^{-2}\,\mu m$)
2. Condensation: additional matter from the gas phase condensates onto existing aerosols to grow fine particles (*accumulation mode* 10^{-2} to $1\,\mu m$)
3. Coagulation: existing particles collide and merge to form even bigger aerosols (*coarse mode*)

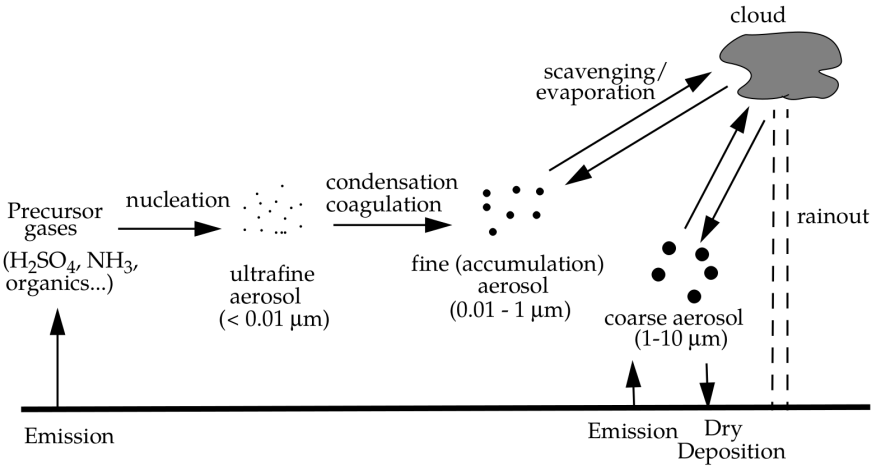

Figure 1.4: Production, growth, and removal of atmospheric aerosols [Jacob, 1999]

Generally speaking, secondary aerosols formed through gases condensation tend not to grow larger than the accumulation mode [Jacob, 1999]. Removal by sedimentation is thus unlikely given their small size and weight. The main process for the termination of their life cycle is scavenging within cloud droplets, with the subsequent rainfall bringing them onto the ground (Figure 1.4).

Secondary organic aerosols (SOA) are formed through homogeneous nucleation from the oxidation of VOCs, that are emitted by vegetation for a large part. Secondary inorganic aerosols mainly include nitrate (NO_3^-), sulfate (SO_4^{2-}) and ammonia (NH_4^+). Altogether, secondary aerosols account for 52% of all fine mode continental aerosols [Jacob, 1999].

1.1.3 The impacts of atmospheric pollution

Over the last decades, air quality has become a major concern worldwide, especially in urban areas where growing population and industrial development generate increasing atmospheric pollutants emissions and exposure. Most countries have designed laws and regulations over the last decades (such as the ban on lead-containing fuels, reduction of coal burning, norms for cleaner engines, alternating traffic ...) in order to tackle this issue through the reduction of emissions, with various degrees of success. Air pollution has numerous, intertwined impacts on many aspects of the human world. The following sections aim to briefly introduce them.

1.1.3.1 On health

The 4-day London smog of December 1952 caused around 4,000 deaths. It is the first ever studied and possibly the deadliest known event of air pollution [Wilkins, 1954]. Massive coal and fossil fuel burning associated with atmospheric stagnation and fog led to concentrations of particulate matter (or smoke) as high as 1600 $\mu g/m^3$ and SO_2 mixing ratios up to 700 ppb (Figure 1.5a) with locally up to ten times usual concentrations. The consequence was a sharp increase in death rates up to 900 deaths per day mainly related to cardiac and respiratory pathologies, with an effect on hospital admissions and deaths still visible several days after the termination of the event. Although it was already partially known at the time, this event was a great evidence of the acute effect of air pollution on human health. But air pollution has both acute and chronic effects on human health, affecting different systems and organs depending on the nature and size of the pollutant (Figure 1.6). They range from minor respiratory irritation to chronic respiratory and heart diseases or lung cancer. Short-term and long-term exposures can be related to premature mortality and reduced life expectancy [Kampa and Castanas, 2007]. In particular long-term analysis of cohorts show that chronic exposure to $PM_{2.5}$ contributes to cardiovascular morbidity and mortality [Pope and Dockery, 2006] (Figure 1.5b).

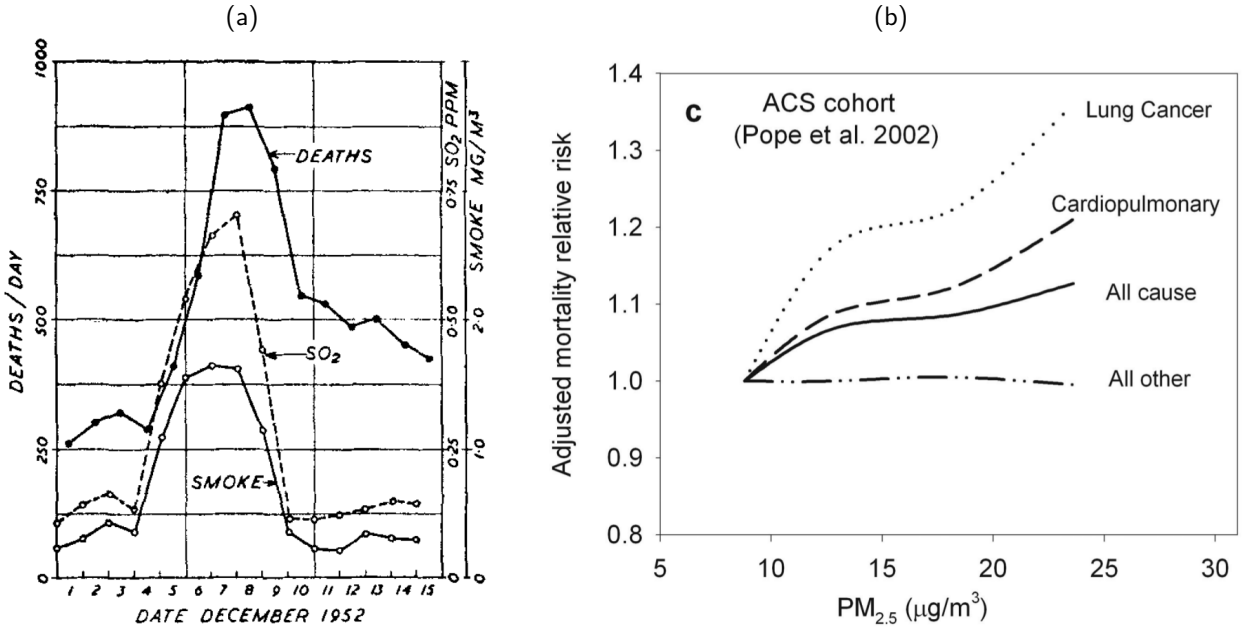

Figure 1.5: Evidences of the acute and chronic effects of $PM_{2.5}$ on health. (a) London 1952 smog daily concentrations and mortality [Wilkins, 1954]. (b) Concentration-response relationships of long-term exposure to $PM_{2.5}$ [Pope and Dockery, 2006].

The most deleterious effects of air pollutants come from their inhalation, with various deposition properties and effects on the respiratory system depending on their aerodynamic diameter [Cao et al., 2013]. Fine particles may alter or obstruct the respiratory route at the lung level, leading to necrosis of pulmonary alveoli followed by lung cancer and/or decline in the blood quality. Even finer particles can also directly penetrate into the blood stream (translocation), and modify the properties of blood cells, leading to cardiovascular impairments such as atherothrombosis [Robertson and Miller, 2018]. The detailed effects of ozone are less well known although they also correlate with increased respiratory issues such as asthma [Lippmann, 1991]. Despite the difficulty

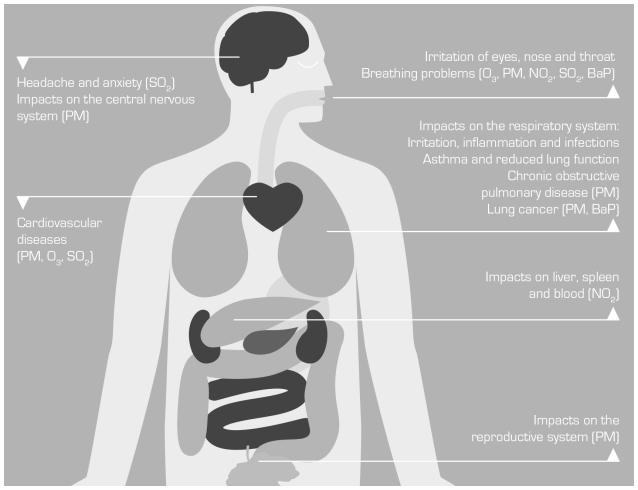

Figure 1.6: Some effects of air pollution on health. Schematic from the European Environment Agency.

to precisely quantify the effects of atmospheric pollution on human health, a 2018 report by the World Health Organization (WHO) estimates that around 7 million people die every year from exposure to fine particles in polluted air [WHO, 2018]. Air pollution can be considered one of the deadliest factors to human beings, causing around 12% of global deaths each year [WHO, 2009]. In addition, a recent body of studies report a high correlation between bad air quality and increased mental health problems in the U.S. [Khan et al., 2019], the U.K. [Roberts et al., 2019] or China [Tao et al., 2019], suggesting atmospheric pollution might favor psychiatric disorders as well.

1.1.3.2 On climate

According to the fifth assessment report of the Intergovernmental Panel on Climate Change [IPCC, 2013], the total net radiative forcing due to atmospheric pollutants is not clearly positive nor negative, and varies a lot depending on the species considered (Figure 1.7). Lots of uncertainties surround the estimation of the climate impact of pollutants. For instance, due to their diversity, the net effect of aerosols is still not established.

Aerosols and their precursors may influence climate in several ways: directly through scattering (sulfates, nitrates) and absorption (black carbon, dust) of radiation, and indirectly by acting as cloud condensation nuclei or modifying the optical properties and lifetime of clouds [Penner et al., 2001]. For instance, sulfate and nitrate aerosols scatter the incoming solar radiation, so that the fraction reaching the ground is more diffuse, inducing a cooling of the atmosphere. The aerosol-cloud interaction also provides a net negative radiative forcing as it involves a greater reflection of solar radiation by clouds, which are formed in larger amounts when the load of aerosols increases [Boucher et al., 2013]. Light-absorbing aerosols such as black carbon on the other hand lead to a strong positive radiative forcing, in particular because of their deposition on snow and ice surfaces. The effect of particulate matter deposition (black carbon and dust) on snowpacks has been found to contribute significantly to snow and ice accelerated melting through the alteration of their ability to reflect light (albedo) [Hadley and Kirchstetter, 2012, Hodson, 2014]. The Earth's albedo is then lower, more solar radiation is absorbed and re-emitted in the form of infrared radiation, which in turn warms the atmosphere. The black carbon forcing efficacy on snow is estimated to be more than three times greater than the greenhouse effect by CO_2 [Flanner et al., 2007].

Tropospheric O_3 also has a dual role in its quality of both pollutant and strong greenhouse gas, although its short atmospheric lifetime does not imply effects on the long term. Short-lived gases involved in the production (consumption) of other greenhouse gases (CO, VOCs, NO_x) also play a role as they have a net positive (negative) radiative forcing [IPCC, 2013].

1.1.3.3 On the environment

When deposited on vegetation, ozone enters the plant through its stomata, diminishes the photosynthesis ability of its host, and reduces transpiration leading to its decay [Hill and Littlefield, 1969]. Losses in crop yields and agricultural production then follow. Acid rain is also a threat to vegetation because of its corroding power [Cape, 1993]. The effect of aerosol deposition on plant leaves is not well understood as it may on the one hand provide a nutrient source enhancing growth, but may also limit the amount of solar radiation reaching the plant for

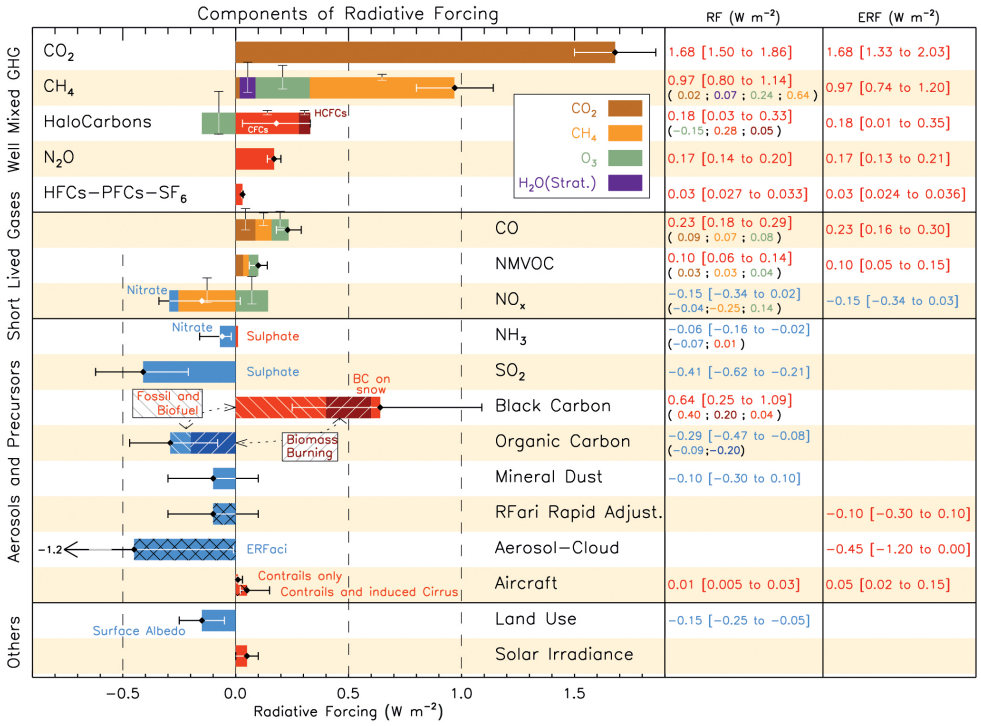

Figure 1.7: Radiative forcing by emitted components from 1750 to 2011 [IPCC, 2013]

photosynthesis thus compromising its proper operation on the other hand. For instance, the effect of black carbon deposition on vegetation is still debated - partly fertilizing when deposited on the ground [Shrestha et al., 2010], partly detrimental when deposited on the leaves [Anda and Illes, 2012]. Either way, given the large amounts found in the atmosphere, black carbon likely has a controlling effect on plants.

Water environments are also threatened by air pollution. First, deposition of light-absorbing particles on ice or snow accelerates its melting. As the melting occurs faster during the dry season, the water reservoirs constituted by glaciers might be rapidly exhausted leading to an even drier end of summer, compromising the survival of plants and animals populations and the sustainability of water supply for humans [Hock et al., 2019]. Second, sulfur- and nitrogen-containing aerosols can perturb the chemical equilibrium of waters and cause acidification and eutrophication, thus threatening aquatic species, animals and vegetation, which are sensitive to water contents and pH, such as coral reefs or phytoplankton. Sulfuric acid for instance might locally and sporadically contribute to the decrease of ocean water pH and alter its alkalinity and inorganic carbon storage, with consequences on the ocean's viability for native plants and animal species [Doney et al., 2007].

1.1.3.4 On the economy

The economic burden of atmospheric pollution is substantial as a consequence of all the aforementioned effects of pollution. Indeed, noxious impacts on human health mean more expenses for the health care system [Yang and Zhang, 2018] and less worker productivity [Hanna and Oliva, 2015], damages to ecosystems limit the services they render which need to be compensated for [Cudlín et al., 2013], buildings deterioration by gaseous pollutants forces more frequent renovations [Singh and Agrawal, 2008], agricultural losses and effects of climate change (partly related to air pollution) on food supply, population migration or weather extreme events also imply financial losses and expenses [Arent et al., 2014]. Shutdown of factories and traffic during peak events of pollution in industrial regions can also represent losses of revenue. Worldwide, the total welfare losses from air pollution are estimated to represent USD 5.112 trillion in 2013 [The World Bank and Institute for Health Metrics and Evaluation, 2016] i.e. around 7% of the global GDP that year. These numbers only encompass the costs stemming from premature mortality caused by exposure to ambient PM, indoor air pollution and ambient ozone. In Europe only, as of 2010, the overall annual economic cost of health impacts and mortality from air pollution stood at USD 1.575 trillion [WHO and OECD, 2015]. The damages of air pollution greatly vary among regions

of the world and household incomes. Asian economies, among which mostly middle income emerging countries, suffer the most in this respect, whereas Latin America, the Middle East and North Africa are comparatively less affected by atmospheric pollution in economic terms [The World Bank and Institute for Health Metrics and Evaluation, 2016] (Figure 1.8).

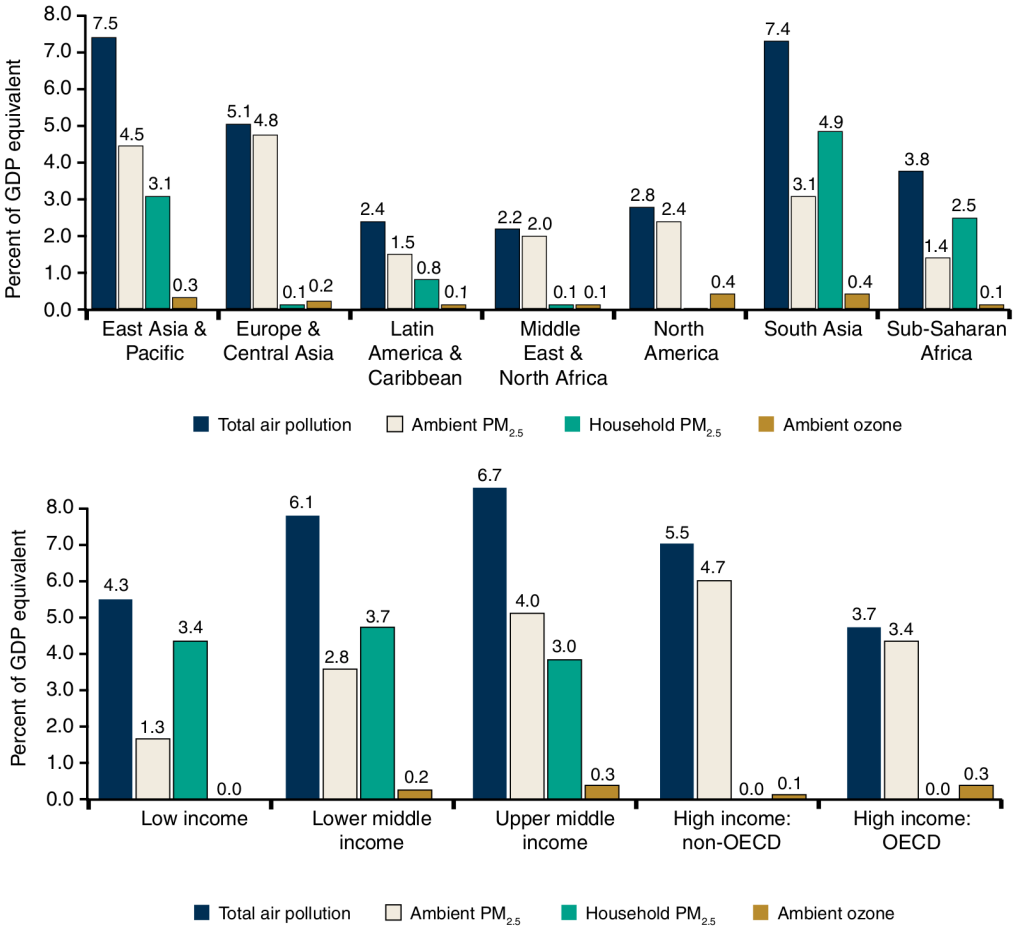

Figure 1.8: Welfare losses due to air pollution by region and income group [The World Bank and Institute for Health Metrics and Evaluation, 2016]

1.1.4 Trends in air quality

Historically, air pollution was recognized a threat to human health for the first time in Ancient Greece, *circa* 400 BC, in connection with cooking and heating emissions in cities [Fowler et al., 2020]. In the modern era, Europe and North America were the main emissions centers and regions of the world most affected by bad air quality in relation with their blooming industrialization and urbanization, up until the late 20th century. Research on air quality and atmospheric pollution mitigation therefore first started to gain importance in these continents. It is commonly acknowledged that modern-day air quality research started with the London smog episode of 1952 and the publication of Wilkins [1954]. As policies and standards were being implemented, especially on SO_2 and NO_x, air quality in Western countries began to improve. While most Western countries were able to conduct successful atmospheric decontamination plans, leading to significant improvements in air quality, some developing and emerging countries have seen their air quality issues worsen in parallel, starting in the late 20th century. This is especially the case in East and South Asia that overtook the global budget of pollutants emissions since the early 21st century [Fowler et al., 2020]. The offshoring of industrial production, particularly in Africa and Asia, transferred the associated emissions of pollutants, in addition to making urban areas grow, hence increasing exposure (Figure 1.9). For example, the age-adjusted death rate from lung cancer was multiplied by 2.6 between 1973-1975 and 2004-2005 in China [Chen et al., 2013]. Combined with India,

these two countries together represent more than 50% of global premature deaths and years of life lost due to bad air quality in the recent years [Brauer et al., 2016]. As a result, research in air quality is nowadays mainly focused on Asian countries such as China and India [Han et al., 2021], which combine the largest emissions worldwide, but also the largest populations hence yielding unprecedented exposure. Still, even in the most developed countries, air quality standards are not systematically met, and supranational/federal institutions (e.g. European Commission, US Environmental Protection Agency) often fine state authorities for crossing the target thresholds they implement on criteria pollutants [Breeze Technologies, 2021].

Pollutants of concern have evolved in the recent decades. Chlorofluorocarbons (CFCs), lead, sulfur oxides, are mostly a problem from the past as a series of regulations eventually led to a major diminution in their emissions. In parallel, emerging concern surrounding other pollutants arise such as persistent organic pollutants (POPs) or nano-particulate matter [Enyoh et al., 2021]. At the moment however, most policies related to air quality focus on controlling the levels of O_3, NO_2 and PM (2.5 and 10).

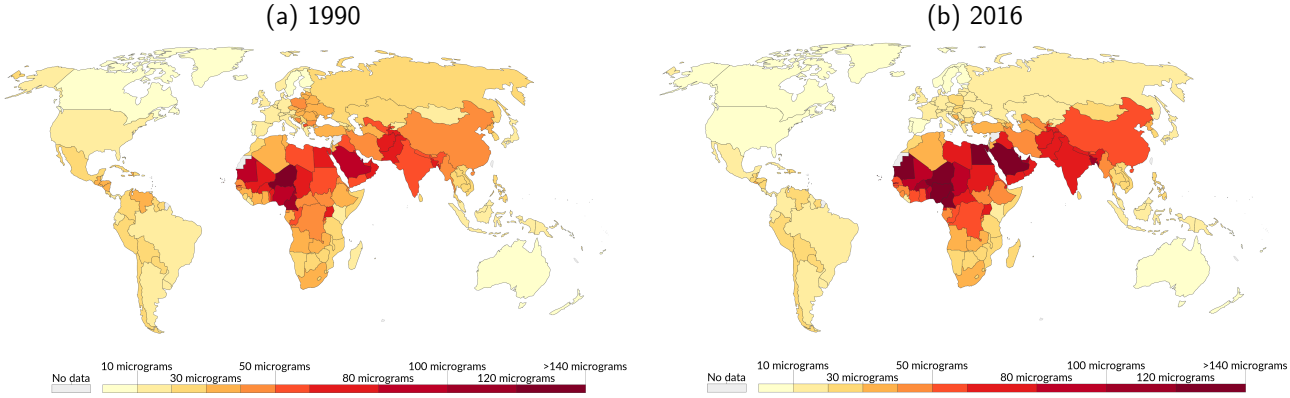

Figure 1.9: Population-weighted mean annual $PM_{2.5}$ exposure ($\mu g/m^3$) worldwide in (a) 1990 and (b) 2016 [Our World in Data, 2017]

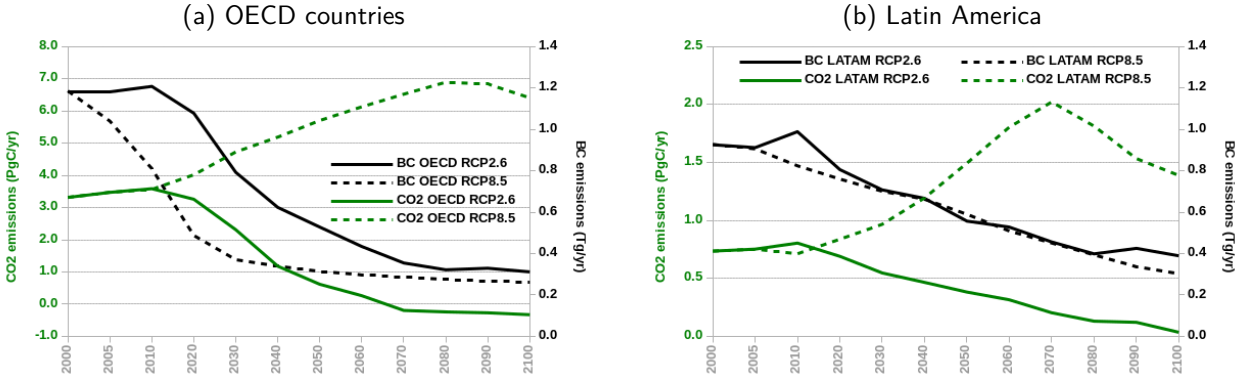

Figure 1.10: RCP2.6 (solid line) and RCP8.5 (dashed line) emission scenario for CO_2 (green) and black carbon (black) in (a) OECD and (b) Latin American countries. Based on data from IPCC [2009]

The future of air quality at the global and local scales is by far uncertain. Thereafter, possibles trajectories are discussed based on the Representative concentration pathways (RCP) built by the IPCC. It is likely that the evolution of emissions of greenhouse gases (GHG) and atmospheric pollutants lie between RCP2.6 (more optimistic scenario [van Vuuren et al., 2011]) and RCP8.5 (more conservative [Riahi et al., 2011]). RCP2.6 is the most stringent scenario. This path needs plummeting energy demand, stabilizing world population, and cleaner energy sources in order to reach a negative GHG emission balance before 2100. Such a pathway does not focus on air quality policies, since the effort is mainly put on GHG emissions. The associated air pollution scenario is mainly a co-product of the GHG scenario, without dedicated actions considered. RCP8.5 on the other hand, leads to high GHG emissions and radiative forcing at the 2100 horizon since no specific climate mitigation target is implemented in this case. Co-benefits on air quality from GHG mitigation policies seen in

RCP2.6 are thus not present, but the methodology for this scenario embeds a dedicated pathway regarding air quality policies implementation. In particular, places of the world with high exposure to pollution (i.e. highly populated and polluted areas) are assumed to take actions in order to mitigate air pollution issues in the future. The expenses saved by the absence of GHG strategy are put into air pollution mitigation instead. This is visible in Figure 1.10a for OECD countries: RCP2.6 scenario features dramatic reductions in CO_2 emissions and black carbon emissions diminish in the same way, as a co-benefit. In scenario RCP8.5 however, CO_2 emissions keep on increasing, but black carbon emissions are drastically cut. For Latin America the trends are generally the same, with less BC emissions in RCP8.5 compared to RCP2.6, although not as clear as for OECD (Figure 1.10b). In the IPCC perspective, it seems that despite the co-benefits of climate change and air pollution mitigation, there is still a trade-off between rapidly coping with climate change, and fighting air pollution in the short term, as both efforts still have some orthogonality. It is worth noting that in both scenarios, the emission levels in 2100 are similar, despite a different pathway. However, in terms of total deaths linked to air pollution, these two trajectories might lead to completely different scenarios, depending on demographic dynamics and cures evolution.

Rationale for focusing on Chile

Generally speaking, the rationale for air quality research is related to assessing and mitigating impacts on human health, hence the greater focus on China and India recently. However, climate feedback and environmental impacts of air pollution are more scarcely studied, although paramount as well. In the more recent years these topics gained importance though, in particular in the perspective of better constraining the climate feedback of aerosols.

In this context, Chile is a comparatively less studied area despite concerning air pollution levels leading to major health impacts, but affecting a smaller population. In addition, the presence of the Andes mountain range along the country implies that urban pollutants could reach its glaciers, including the highest ones. The associated consequences include an additional climate feedback on top of global warming, and a threat on freshwater supply sustainability in the region. This latter topic however, is still a rather novel research topic.

The momentum and studied areas in air quality research often come from global and local political orientations. The choice to focus on Chile in this PhD originates from the combination of a growing interest and concern regarding the poor air quality of the country, and a collaboration opportunity connected to common projects between the University of Chile and LMD.

1.2 Observation of atmospheric composition

The technologies and techniques for sounding the atmosphere and measuring its composition are continuously improved, offering an ever-refined view. Various tools and approaches exist, with different levels of complexity, providing a large panel of measurements. In the following sections, the focus is primarily made on the techniques and networks that allowed to conduct the present study, although other methods/products would be encountered in a more thorough inventory of atmospheric composition sensing. As a result, most of what is discussed hereafter primarily concerns Chile and the area of Santiago, its capital city.

1.2.1 Visual effects

Although it does not provide quantifiable, detailed scientific information, the first striking feature of a pollution peak event is its visual signature: the so-called 'smog'. The light-absorbing properties of this mixture of particulate matter and ozone lead to a dramatically reduced visibility when such pollutants are accumulated [e.g. Farber et al., 1994], as can be seen in Santiago in Figure 1.11. Generally speaking, for highly urbanized areas, visibility (except in case of natural fog) is a good indicator of the air quality [e.g. Diederen et al., 1967]. Depending on the compounds involved in the formation of the smog, its color can range from brownish (urban photochemical smog) to whitish (sulfate induced smog) to blueish (biogenic smog) to yellowish (dust).

(a) Polluted air in Santiago during a smog event. Picture @BBC

(b) Clean air in Santiago after rainfall. Picture @JulioGoffardMolina/Flickr

Figure 1.11: Effect of pollution smog on visibility

This qualitative, visible effect, can be further quantified using Aerosol Optical Depth (AOD). This variable measures, for a given wavelength, the extinction of the associated light beam by the pollutants present in the atmospheric column through scattering and absorption. AOD gives an indication of the load of particles in the atmosphere, and by comparing AOD at different wavelengths, the size distribution of said particles can be obtained.

1.2.2 Local air quality networks

Networks of ground-based, automated, continuously measuring devices, are the easiest way of assessing and forecasting air quality in urban areas. Such networks have thus been blooming all around the world for decades now, and allow for the evaluation of pollution mitigation strategies. They usually provide measurements of criteria pollutants surface concentrations such as O_3 and PM, co-located with meteorological information (temperature, relative humidity and wind at the surface, typically), at a high temporal frequency (typically every hour).

In Chile, concerns surrounding air quality have existed for quite some years, so that the network of continuous monitoring of air quality in cities is relatively wide. In Chile, the Ministry of Environment (MMA for spanish *Ministerio de Medio Ambiente*) centralizes data of 199 automated air quality monitoring stations throughout Chile, of which 83 measure $PM_{2.5}$, 153 measure PM_{10} and 60 measure O_3. This network, called *Sistema de Información Nacional de Calidad del Aire* (SINCA) [Ministerio del Medio Ambiente, 2018] is an invaluable source of information for ground level concentrations of pollutants and meteorology, and is used as the official reference for the assessment of air quality with respect to the national standards. The data is provided with an hourly frequency, dating back to before 2000 for the oldest stations. The spatial distribution of the network for the Metropolitan Area of Santiago is shown in Figure 1.12.

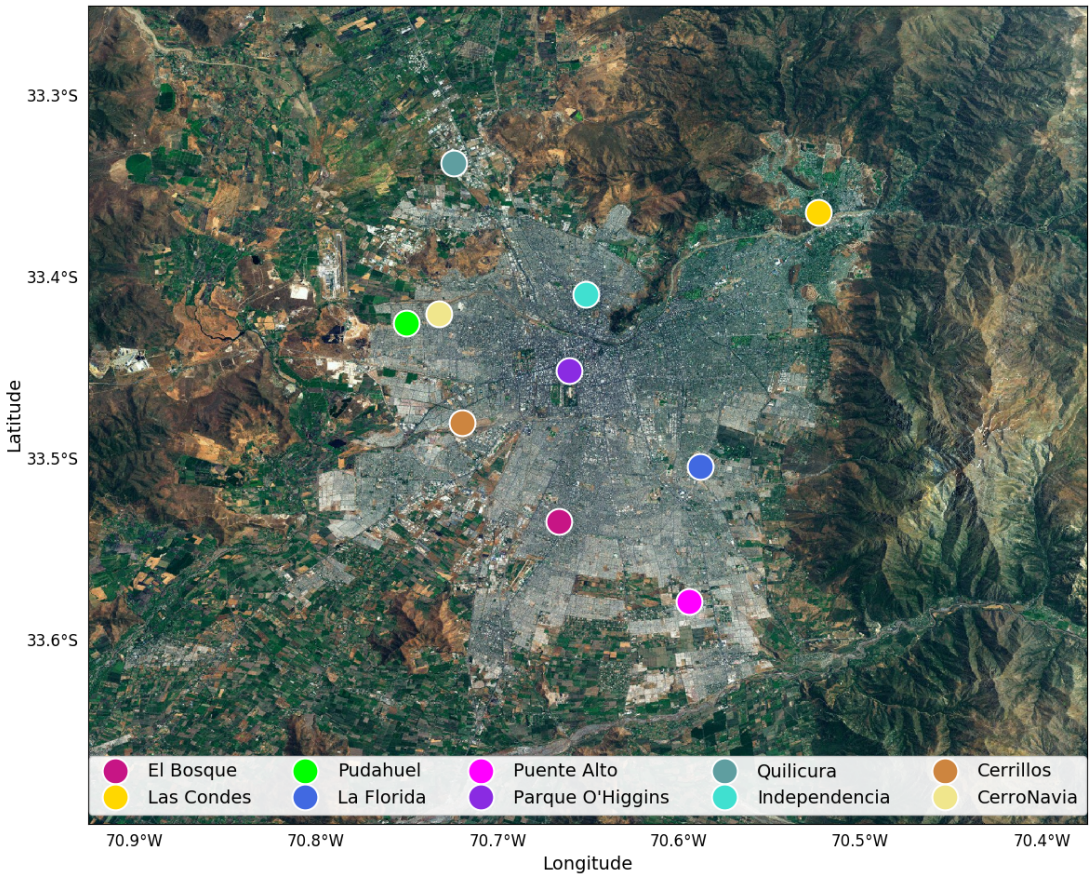

Figure 1.12: Automated air quality monitoring network in Santiago

Hereafter, a brief description of common measurement principles for the main pollutants of interest is provided. A more comprehensive picture and details on the underlying theory can be found, for example, in Liberti [1975].

PM sensors

Within the SINCA network, two measurement methods are mainly used to quantify particulate matter. The most common one is beta-attenuation based devices, which apply both for $PM_{2.5}$ and PM_{10} monitoring. The operating principle relies on the Beer-Lambert law expressed in the form of Equation (1.3).

$$C = \frac{1}{\alpha L} \ln(\frac{\Phi}{\Phi_0}) \tag{1.3}$$

where C is the PM concentration, α is the absorption coefficient measured under standard reference conditions, L is the length of the path between the emitter and receiver, Φ is the intensity of the luminance with the 'dirty' filter, and Φ_0 is the same intensity measured for the reference 'clean' filter.

A filter collecting ambient particles is placed between a constant emitter of beta particles (C^{14} element for instance) and a detector that counts beta rays (scintillation detector for instance). The difference between the attenuation recorded with a pristine filter and the filter containing particles then leads to the concentration of PM using Equation (1.3). The precision obtained with this technology is usually around a few $\mu g/m^3$.

Some sites use gravimetry-based devices instead, mostly for PM_{10} measurements. Gravimetry consists in weighting the amount of matter deposited on a beforehand tared filter, using a high precision scale. For a given amount of time, the filter is placed in the atmospheric environment of interest, and the particles deposit on the filter. The weigh difference between the initial clean filter and the dirty filter yields the weigh of PM, which enables to compute the associated atmospheric concentration. A deeper analysis of the filter can also provide information on the size distribution and chemical composition of the particles.

Ozone sensors

The main method for the measurement of ozone concentrations is UV photometry. The absorption spectrum of ozone shows that its maximum of absorption is in the ultraviolet light, close to the wavelength of the main emission ray of mercury-vapor lamps. Again, the Beer-Lambert law is involved with the same philosophy as for PM, substituting filters by air volumes, and using a mercury-vapor lamp instead of a beta particles emitter. Then, the absorption under reference and measured conditions are compared in order to retrieve the amount of ozone. The uncertainty on the measurement with this technique is generally very good, below 1 ppb.

NO_x sensors

Several methods can be used to measure nitrogen oxides such as IR, UV or mass spectrometry, chromatography... But the most common one for the Chilean network is chemiluminescence with ozone. Indeed, in the presence of O_3, NO is consumed to form NO_2 in a excited state through reaction (R 1.6). Infrared light emission ($h\nu$) then results from the decay of NO_2 to lower energy states. The amount of measured infrared light is then correlated to the amount of NO initially present. NO or NO_x can both be measured with this apparatus, with a precision greater than 1 ppb.

$$NO + O_3 \longrightarrow NO_2 + O_2 + h\nu \tag{R 1.6}$$

Measurement techniques for CO or SO_2 use the same kind of light absorption/emission properties, with different wavelengths.

1.2.3 Dedicated measurement campaigns

In addition to the automated networks, specific measurement campaigns are conducted in the region of Santiago, in order to study particular phenomena or complete existing data sets. These field campaigns usually measure ground level time series of pollutants with the same kind of instruments as the SINCA network, but also involve vertical profile measurements of concentrations, which represent a valuable complement of information [e.g. Seguel et al., 2013, Cordova et al., 2016, Gramsch et al., 2020, Huneeus et al., 2021]. To do so, tethered balloons to which meteorological probes and atmospheric composition devices are attached, are good allies. Campaigns combining the previous measurement techniques in addition to lidar/radar measurements and meteorological planes flights, such as the MILAGRO campaign in Mexico city [Molina et al., 2010] provide exceptionally rich and detailed 4-dimensional information on air quality. Although no such examples are available for Chile, such comprehensive campaigns would represent an invaluable source of information.

Citizen science is another emerging ally for air quality monitoring purposes. As sensors are getting smaller, they can now easily fit on a car, bike or in a pocket. Although examples in Chile are still lacking, this method allowing anyone to contribute just by carrying a sensor along, provides massive amounts of data with increased spatial coverage and are thus trending worldwide [e.g. Languille et al., 2020, De Craemer et al., 2020, West et al., 2020].

In addition to their atmospheric concentrations, measuring deposition rates of pollutants is also of interest, given the potential associated environmental impacts mentioned in Section 1.1.3. For example, campaigns in the Andean glaciers near Santiago revealed the content of the snowpack in black carbon, through the retrieval and melting of samples of fresh and old snow and ice [Rowe et al., 2019]. Devices are also sporadically installed in the Atacama desert to measure dust deposition fluxes and their chemical composition and size distribution [e.g. Li et al., 2019].

1.2.4 Worldwide coverage products

AERONET

The AERONET (Aerosol Robotic Network - [Holben et al., 2001] - `https://aeronet.gsfc.nasa.gov/`) gathers a group of research institutes and universities, and is administered by NASA (National Aeronautics and Space Administration). Measurement stations use photometers to derive AOD at several wavelength. Many properties of the aerosols can also be derived from these measurements, such as their size distribution, Angström exponent or single-sattering albedo (these terms will be further defined later on as needed), thus giving a good view of the total vertical column of aerosols at the site. In Chile, 13 AERONET stations are operated, one of which is in

Santiago. However, data is rather scarce, and the main limitation of photometry is that it requires sunlight, thereby preventing recordings nighttime pollution peaks in wintertime, which is when they mostly occur.

Satellite products

Several satellites orbiting the Earth carry remote sensing instruments able to provide information on atmospheric composition for gases and aerosols. Hereafter are briefly introduced the ones that were relevant for my work, many more being also of interest for atmospheric composition sensing purposes.

The Moderate-Resolution Imaging Spectroradiometer (MODIS) is an imaging sensor retrieving data in 36 spectral bands covering wavelengths between 0.4 µm and 14.4 µm. It was launched by NASA onboard the Terra and Aqua satellites in 1999 and 2002, respectively [Justice et al., 2002]. Depending on the wavelength band, its spatial resolution is between 250 m and 1 km. Terra and Aqua together cover the entire Earth every 1 to 2 days. The AOD product from MODIS is interesting for air quality applications as it provides a daily picture of the load of aerosols in the atmosphere through measurements of AOD at 550 nm, with a spatial resolution of 10 km at nadir and a 2300 km swath.

The Infrared Atmospheric Sounding Interferometer (IASI) is a Fourier transform spectrometer coupled with an integrated imaging system [Clerbaux et al., 2009]. This instrument, designed by the French national center for space studies (CNES) is onboard three satellites of the Meteorological Operational satellite (MetOp) series, launched in 2006 (MetOp-A), 2012 (MetOp-B) and 2018 (MetOp-C). Its spectral range in the infrared (3 bands at wavelengths between 8-16 µm, 5-8 µm and 3-5 µm, respectively) allows the acquisition of data regarding the main greenhouse gases present in the Earth's atmosphere, with a pixel diameter of 12 km and a 2200 km swath. MetOp satellites fly over every location of the Earth twice a day, providing a morning and evening picture every day. For my air quality study purposes, I will utilize the CO total column and O_3 tropospheric column products provided by these instruments.

The Cloud-Aerosol Lidar with Orthogonal Polarization (CALIOP) instrument is a lidar-based active sensor onboard the Cloud-Aerosol Lidar and Infrared Pathfinder Satellite Observations (CALIPSO) satellite, a joint NASA-CNES project, part of the Earth Observing System program [Winker et al., 2009]. It was launched into orbit in 2006 and is designed to provide high-resolution vertical profiles of aerosols and clouds. The CALIOP products provide more discrete data on the horizontal compared to the previously mentioned sensors, with a field of view of only 100 m and 14.55 orbits per day, separated by 24.7° longitude. As a result, for a given day, the Earth coverage is sparse so that events of air pollution lasting less than a day, with a local footprint are likely not recorded by CALIOP. For larger scale and longer lasting atmospheric events however, CALIOP provides invaluably detailed data.

A known limitation to active satellite measurements over a large part of South America is related to the South American Magnetic Anomaly (SAMA). This phenomenon is described in Appendix, although in the framework of the studies conducted in this thesis, it did not constitute a particular hurdle in obtaining data for the periods and regions I was interested in.

1.3 Modeling atmospheric composition

Numerical models of the atmosphere can be divided into two classes, generally speaking. Models based on a physical and chemical deterministic representation of atmospheric processes (the type that will be used in this work), and models based on statistical data analysis. Given the ever-increasing amount of data available through the development of atmospheric measurement networks worldwide, and the growing interest of the mathematics community in statistical modeling (machine learning, neural networks...), more and more work in atmospheric sciences is oriented towards statistical models. As is the case for air quality that can rely on expanding monitoring networks in most large cities. Such statistical approaches are usually valuable when it comes to forecasting concentrations of pollutants for the next few hours in a given region, based on current measurements, past observations and correlations. However, due to their reliance on past observations, and since they are not based on explicit causal relationships, these models are not proven to be reliable for longer term studies, such as assessing the impacts of emission control policies for instance.

Given the scope of the present work, deterministic models are thus more suited. Deterministic numerical simulation of atmospheric composition (or chemistry-transport modeling - CTM) is mostly used for three purposes:

- Understanding in greater detail the chemical and physical processes at stake in the observed atmospheric composition (transport and mixing, turbulence, gas and aerosol chemistry, anthropogenic, biogenic and natural emissions, dry and wet deposition, feedback of air pollution on meteorology...)
- Assessing the impacts on air quality of scenarios of emission control policies or climate change (sensitivity of pollutants concentrations to primary emissions and/or changes in climate)
- Forecasting short-term atmospheric composition for air quality monitoring and population exposure prevention purposes (operational forecast by regional air quality networks and national/international institutes)

1.3.1 Chemistry-transport modeling

A chemistry-transport model (CTM) is composed of several modules that articulate to simulate atmospheric composition (see Figure 1.13 for a generic overview). The final output is a 3D field of concentrations of selected compounds, and their time evolution. Generally speaking, the time evolution of the concentration of a species i can be described by the mass balance equation (1.4). The aim of a CTM is to solve this equation, under given atmospheric circulation conditions and emissions of primary pollutants.

$$\frac{\partial c_i}{\partial t} = -\underbrace{\nabla \cdot (\mathbf{V} c_i)}_{\substack{\text{Wind} \\ \text{advection}}} + \underbrace{\nabla \cdot (\mathbf{K} \nabla c_i)}_{\substack{\text{Turbulent} \\ \text{diffusion}}} + \underbrace{\chi(c_i, c_j, .., T, ..)}_{\substack{\text{Chemical and} \\ \text{physical processes}}} - \underbrace{P_i}_{\text{Sinks}} + \underbrace{S_i}_{\text{Sources}} \tag{1.4}$$

where c_i is the concentration of species i, $\mathbf{V}$ is the horizontal wind speed vector, $\mathbf{K}$ is the vertical wind speed vector, χ gathers all the chemical processes (formation, transformation...) linked to species i and interacting species, T is the temperature, P_i and S_i are sinks and sources processes, respectively. Although not noted for the sake of clearness, all terms are time-dependent.

1.3.1.1 Eulerian vs Lagrangian

There are mainly two categories of CTMs, that differ by the reference frame employed (Figure 1.14). Eulerian (or box, or grid-based) models use a spatially fixed reference frame, divided into 3D boxes (grid cells) within which physical and chemical transformations are computed. Transport and diffusion processes transfer species from one box to another. Each box is assumed to be quickly and well mixed, so that one value for a given quantity is representative of the whole grid cell. Examples of well-known Eulerian CTMs are provided in Section 1.3.2. On the opposite side of the spectrum, Lagrangian (or puff, or trajectory-based) models use a reference frame following the movements of individual air parcels from their initial position (source) to their final position (receptor). Transformation processes take place within the air parcel, and mass exchanges other than advection, such as turbulent diffusion, expand the size of the parcel or move compounds from one parcel to another. Examples of Lagrangian CTMs include FLEXPART [Stohl et al., 2005], CLaMS [McKenna et al., 2002]... Lagrangian models have a great ability to simulate advection faithfully whereas Eulerian models introduce numerical diffusion. In turn, Eulerian approaches are more simple and less computationally costly. The CTM used in this work,

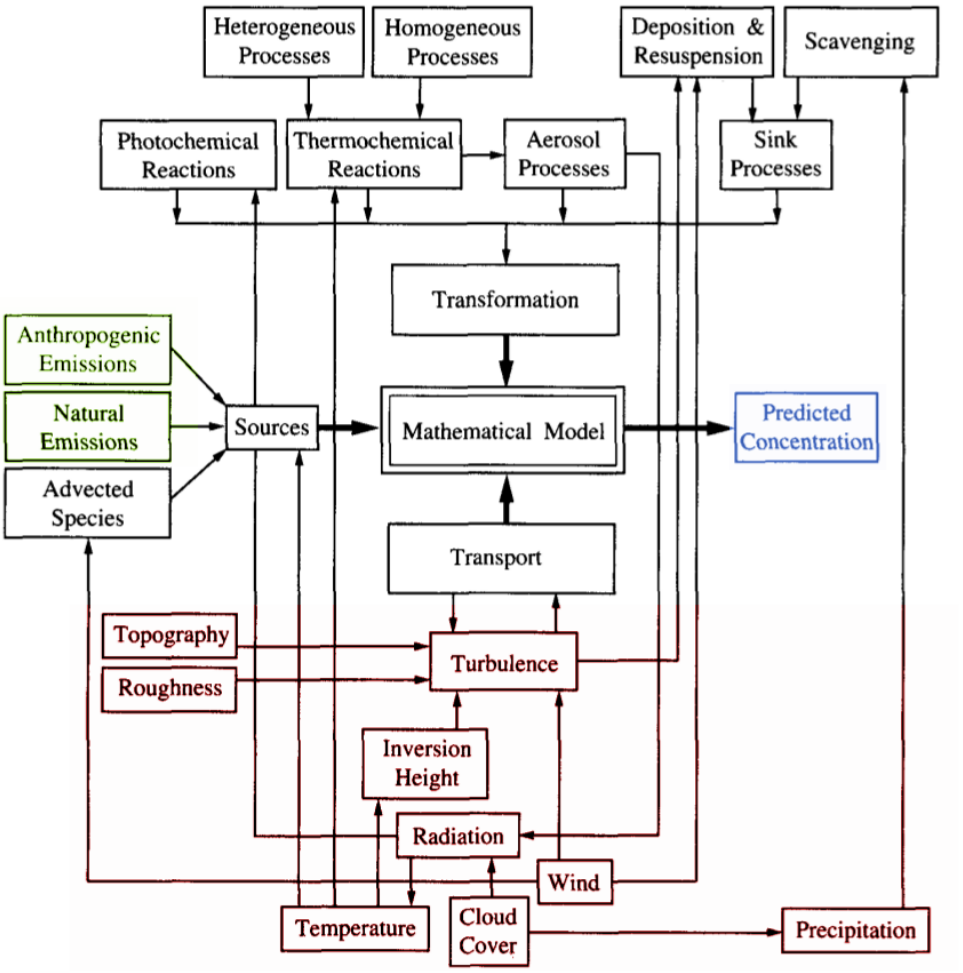

Figure 1.13: Main elements of an atmospheric chemistry-transport model, adapted from Seinfeld and Pandis [2006]. Red boxes are provided by a numerical weather model, green boxes by external modules dedicated to the computation of primary emission fluxes (see Section 1.3.1.4), and black boxes are calculated within the CTM.

CHIMERE, presented in detail in Section 1.3.2, is part of the Eulerian models landscape. From now on, modeling considerations are presented within the framework of the Eulerian approach.

1.3.1.2 Space discretization

As depicted in Figure 1.14a, the spatial domain of computation is divided into 3D boxes (latitude, longitude, altitude) in a finite-element modeling fashion. The inside of a single box is considered homogeneous in terms of atmospheric parameters, dynamics, and chemical composition. The volume of a box determines the spatial resolution of the model. The choice of the spatial resolution highly depends on the goal and area of the simulation. The study of coarse phenomena at a continent level does not require a high resolution. Conversely, a study at the scale of a city or an area with steep orography forces to go to high resolutions in order to properly simulate the processes at play (for instance, wind funneling in mountainous valleys for the transport of pollutants). Furthermore, spatial resolution is also constrained by stability considerations and computer processing time (see Section 1.3.1.3).

1.3.1.3 Time discretization

The mass balance equation (1.4) cannot be solved explicitly in its continuous form and has to be discretized in time, with a step by step resolution. The equations involved in chemistry-transport constitute a stiff system, i.e. involving a wide variety of time scales in the physical and chemical processes (e.g. from very fast chemical

(a) Eulerian approach

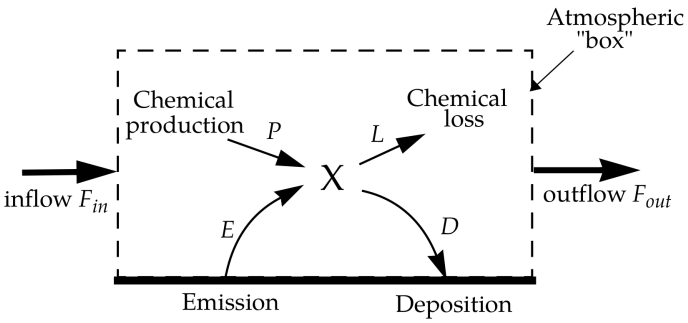

Processes computed within a grid cell for the Eulerian approach [Jacob, 1999]

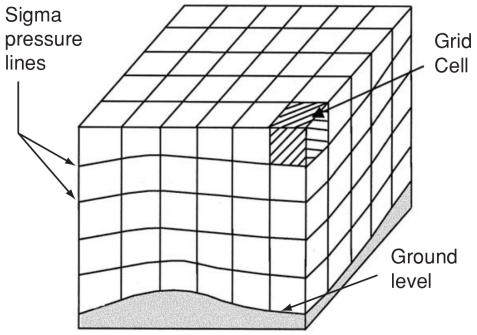

3D-gridding of space for the Eulerian approach [NARSTO, 2004]

(b) Lagrangian approach

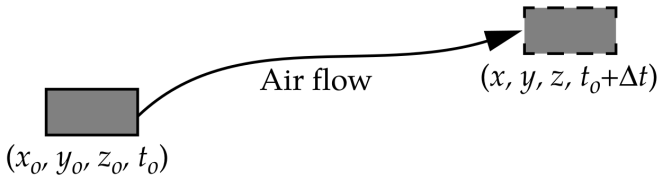

Philosophy of the Lagrangian approach [Jacob, 1999]

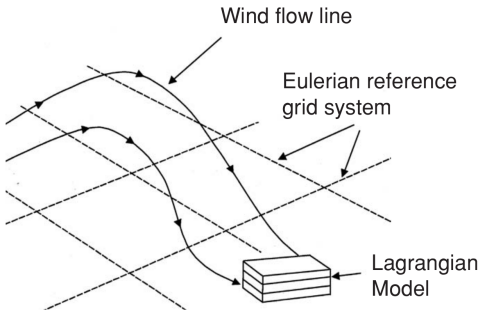

Stream lines in a Lagrangian approach [NARSTO, 2004]

Figure 1.14: Eulerian versus Lagrangian approach.

kinetics at the millisecond to gravitational sedimentation in a few days). Numerical methods such as the Gauss-Seidel algorithm permit to solve separately the equations of a system with different time frequencies, in particular physical and chemical processes. There are commonly two ways to perform time-integration for chemistry-transport (Figure 1.15). Either group all chemical processes into a single production and loss term at each chemical time step ('prod-loss budget' approach), or integrate the processes one after the other ('operator splitting'), which allows to use a different time step for each process if necessary.

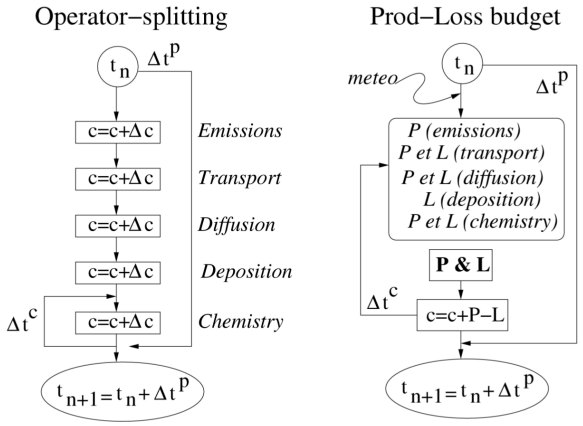

Figure 1.15: Operator splitting versus prod-loss budget. From the CHIMERE documentation.

Time discretization can be either explicit (forward), i.e. the relationship to go from time n to time $n+1$ is direct, or implicit (backward), i.e. a linear system must be solved to obtain time n based on time $n-1$. While explicit schemes are simpler, implicit approaches are more stable. Stability, i.e. whether the solution of the scheme converges (low dissipation) or explodes to infinity (high dissipation), is expressed with the

Courant-Friedrichs-Lewy (CFL) condition - Equation (1.5). The maximum Courant number C_{max} depends on the method used and is generally higher for implicit schemes, hence the better stability of the latter approach for a given configuration. The CFL constraint usually determines the maximum authorized time step for a given choice of space grid, and vice-versa if the time step is prescribed. If C becomes greater than C_{max}, the model becomes unstable and the numerical solution goes to infinity. As a result, high-resolution simulations (for urban areas, steep environments...) require a short computation time step in order to comply with the CFL condition, even more so in windy areas such as mountains, since the wind speed u is involved in the computation of C. This is why increasing the resolution of a simulation usually implies longer computer processing times too. Increasing the resolution by a factor N increases the computational cost by N^3.

$$C = \frac{u\Delta t}{\Delta x} \leq C_{max} \tag{1.5}$$

where u is the magnitude of the velocity (wind speed in the case of an atmospheric advection scheme), Δt is the discretization time step (or time resolution) and Δx is the grid cell size (or spatial resolution). This constraint is valid for the three spatial dimensions (latitude, longitude, altitude) of the simulation.

1.3.1.4 External forcings

As depicted in Figure 1.13, a CTM needs to be provided with some exogenous input data in order to run chemistry and transport computations. These so-called external forcing data include emissions inventory, meteorological fields and initial and boundary conditions.

Meteorological fields
Meteorology is key in many ways when it comes to atmospheric chemistry. Solar radiation, cloud cover, rainfall, wind, humidity, temperature, pressure... are decisive factors regarding the production and fate of pollutants. They dictate reaction rates of chemical processes, constrain advection and deposition of pollutants, and directly affect the concentration of pollutants through the depth of the mixing layer. This entanglement is also two-ways, with compounds such as light-absorbing particulate matter that have a feedback on meteorology.

Meteorological fields are provided by Regional Climate Models (RCM), which consist in a downscaling of global weather analysis or reanalysis from General Circulation Models (GCM) towards a finer resolution corresponding to the grid of the CTM simulation, using physical and dynamical parameterizations of the atmosphere.

Some CTMs include the feedback loop of pollution and interact with the numerical weather model. Such 'on-line' approaches are further described in Section 1.3.2.8. Passive models that only receive meteorological fields without feedback are called 'off-line'. Both approaches will be used in my work.

Emission fluxes
Emissions of primary pollutants and precursors, both from human activities and natural sources are the major driver of atmospheric composition. Patterns and rates of emissions are dramatically variable with times and places (more emissions in some districts, peaks due to traffic commuting each day, wood burning in wintertime which is absent in summertime...) and are consequently relatively hard to estimate. For that purpose, emissions inventories are built. Historically, they are usually static in time and designed based on national annual totals of emissions, on which are applied space (population, road, industry densities...) and time (diurnal cycles, seasons...) proxies. Examples of commonly used emissions inventories of gaseous pollutants and aerosols include European Monitoring and Evaluation Programme (EMEP) [Tørseth et al., 2012], Copernicus Atmosphere Monitoring Service (CAMS) [Granier et al., 2019], Emissions Database for Global Atmospheric Research - Hemispheric Transport of Air Pollution (EDGAR-HTAP) [Janssens-Maenhout et al., 2015].... Even with such relatively coarse approaches, observed concentrations of pollutants can usually be quite well reproduced by CTMs based on such inventories. In the last few years though, effort has been put locally on building more consistent and faithful inventories usually at the national level, at higher spatial resolutions, that are likely to improve the performance of CTMs.

Boundary and initial conditions
Regional CTMs like CHIMERE do not include the entire planet Earth in the simulation domain but focus on a specific region instead. As a result, conditions must be given at the boundaries of the domain. This atmospheric state outside of the domain is usually extracted from coarser simulations already ran and made available from global climate and chemistry-transport models. In order to avoid deviation from the large-scale atmospheric circulation provided by the GCM, spectral nudging is applied for the relaxation of the RCM fields towards the

global circulation. Spectral nudging consists in driving the RCM on a selection of spatial scales, bringing the simulation back to the global boundary conditions [e.g. von Storch et al., 2000].

In addition, at the start of a simulation period, a state of the atmosphere must be provided to the model, that is realistic and consistent with the start date. These initial conditions are usually extracted from the same data sources as for boundary conditions, i.e. GCM fields. However, the mismatch between the low resolution data from the GCM and the comparatively higher resolution of the RCM introduces physical inconsistencies. They are resolved by running the RCM during a certain amount of time (usually the order of a few weeks), prior to the study period. This so-called 'spin-up' period is then discarded as it is considered unreliable.

1.3.1.5 Simulation evaluation

In order to assess whether a simulation behaves as expected, both in terms of meteorology and atmospheric composition, comparisons between the model's outputs and observations are in order. Given the fair amount of monitoring stations and measurement campaigns in Chile, validation in the scope of the present work will mostly depend on measurements taken from the surface (either at ground level or vertical profiles). Satellite imagery is also used here for the study of larger-scale phenomena.

Although the discussion regarding the best way to perform the evaluation of a model output is still vivid among the atmospheric sciences community, with new approaches regularly suggested [e.g. Menut et al., 2017], a collection of statistics are most commonly used in the literature for the comparison between model and observation, that usually allow to account for the ability of a simulation to reproduce the mean levels and variability of observed variables [e.g. Mailler et al., 2013]. These statistics, introduced thereafter, are usually checked out both for surface time series and a selection of vertical profiles, depending on the applications and data availability.

Bias: the mean bias (MB) is the average difference between two data sets (Equation (1.6)). This measure allows to estimate whether the model mostly over-estimates (positive bias) or under-estimates (negative bias) a given quantity, on average. The limitation of this indicator is that positive biases might be compensating negative biases on the whole if they have the same magnitude (e.g. +1 bias at night and -1 bias during the day would lead to a null bias). A null bias is thus not synonymous with good performance.

$$\mathrm{MB} = \sum_{i}^{n} (\mathrm{Model}_i - \mathrm{Observation}_i) \tag{1.6}$$

Mean squared error: the mean squared error (MSE) or the root mean squared error (RMSE) represents the second moment of the error, incorporating both the variance of the estimator and its bias, as depicted in Equation (1.7). It is thus a complementary measure to the mean bias and allows to cope with its aforementioned limitation as the absolute values of two opposite biases will be added and not compensated. It is defined as the mean of the squared differences between model and observation.

$$\mathrm{RMSE} = \sqrt{\mathrm{MSE}} = \sqrt{\frac{1}{n}\sum_{i}^{n} (\mathrm{Model}_i - \mathrm{Observation}_i)^2} \tag{1.7}$$

Correlation: Pearson's correlation coefficient (r) is the covariance of the two data sets considered (model and observation) divided by the product of their standard deviations σ (Equation (1.8)). In other words, if two data sets are correlated, then a linear equation describes their relationship. It allows to measure the extent to which simulation and observation vary the same way, with the same trends, either temporally or spatially. In particular, this is useful to assess whether the diurnal cycles are well reproduced. The values of r range from -1 (anti-correlation) to +1 (correlation) with a value of 0 indicating that the two data sets behave entirely independently. Taken alone however, this indicator does not provide information on the quality of the levels produced by the model since even a perfect correlation of 1 does not say anything about the bias.

$$r = \frac{\mathrm{cov}(\mathrm{Model},\mathrm{Observation})}{\sigma_{\mathrm{Model}}\sigma_{\mathrm{Observation}}} \tag{1.8}$$

1.3.2 CHIMERE

Throughout this PhD work, the 2017 (off-line) and 2021a (on-line fully coupled) versions of the regional chemistry-transport model CHIMERE are used. As opposed to global CTMs, CHIMERE does not provide a full picture of the Earth but rather focuses on given regions of the world, from the hemispheric scale down to urban basins. Other well-known regional CTMs include WRF-Chem [Grell et al., 2005] by the US National Oceanic and Atmospheric Administration (NOAA), GEOS-Chem [Bey et al., 2001] by Harvard University and Dalhousie University, CMAQ [Byun and Schere, 2006] by the US Environmental Protection Agency (EPA), EURAD [Haas et al., 1995] by the university of Cologne (FRIUUK), CAMx [Ramboll, 2021] developed by Ramboll in the US, LOTOS-EUROS [TNO, 2021] by TNO in the Netherlands... CHIMERE [Mailler et al., 2017, Menut et al., 2021] is the state-of-the-art regional chemistry-transport model developed in the InTro team at Laboratoire de Météorologie Dynamique (LMD), in collaboration with Institut National de l'Environnement Industriel et des Risques (INERIS) and Laboratoire Interuniversitaire des Systèmes Atmosphériques (LISA). CHIMERE is distributed under the GNU General Public License, and available at `http://www.lmd.polytechnique.fr/chimere/`. In addition to its worldwide use for research purposes, CHIMERE is also one of the 7 CTMs used for daily European forecasts of air quality by the Monitoring Atmospheric Composition and Climate (MACC) EU project [Copernicus, 2018]. CHIMERE is one of the two models used for air quality forecast in France, the other one being MOCAGE, a semi-lagrangian model developed by CNRM/Météo France [Teyssèdre et al., 2007]. CHIMERE is an Eulerian 3-dimensional chemistry-transport model. It is primarily designed for producing daily forecasts of ozone, aerosols and other pollutants, as well as playing long-term simulations for emission control scenarios. Hereafter, a selection of components of CHIMERE are briefly described.

1.3.2.1 Forcings

Using the input data described thereafter, CHIMERE calculates the atmospheric concentrations of several gas-phase and aerosol species over a wide range of possible domain scales, from local to continental (typically 1 km to a few degrees in grid resolution), with an hourly frequency.

WRF
Throughout this work, the meteorological forcing is generated using the Weather Research and Forecasting (WRF) model [Skamarock et al., 2008]. WRF is a RCM, initially designed as a numerical weather prediction system simulating atmospheric conditions. Its uses range from research studies to operational forecasting, with a wide variety of scales. The model is developed and maintained by the US National Oceanic and Atmospheric Administration in collaboration with weather agencies all over the world. In my case, this model is used to dynamically downscale global weather analyses from the NCEP FNL data sets, with a 1° by 1° spatial resolution and 6-hour temporal resolution, from the Global Forecast System (GFS) [NCEP, 2000].

Emissions
Except when more detailed inventories are available for the simulation domain, global or regional emission inventories such as HTAP [Janssens-Maenhout et al., 2015] are input into CHIMERE. However, their raw format is not suited for such purposes. An anthropogenic surface emission pre-processor called emiSURF is used for their conversion [Menut et al., 2013]. Based on a top-down approach, emiSURF calculates hourly emission fluxes on the horizontal and vertical CHIMERE grid for the period of the simulation, following three main steps:

1. Pre-processing of annual/monthly databases: the original files are cropped to the simulation domain and generated for each species/month required.
2. Horizontal downscaling: the monthly fluxes are downscaled to match the CHIMERE spatial grid, either through a basic interpolation or using more refined proxies if need be.
3. Downscaling on the vertical and time dimensions, and chemistry speciation: chemical species are refined (e.g. the NO_x inventory is split down into NO and NO_2 using typical emission ratios), the raw 2D fluxes are projected on the vertical based on proxies depending on the sector of emission, and monthly fluxes are transformed into hourly values using seasonal, weekly and diurnal factors.

Biogenic emissions are estimated using the MEGAN model [Guenther et al., 2006] that provides global maps of emission factors and leaf area index (LAI), which are then projected onto the CHIMERE grid. Emission rates are then computed using dedicated parameterizations.

Fire emissions are partially external to CHIMERE, with daily emission total fluxes commonly extracted from two different channels, namely APIFLAME [Turquety et al., 2014] or the Copernicus Atmosphere Monitoring

Service Global Fire Assimilation System [Copernicus Atmosphere Monitoring Service, 2016]. However, the diurnal cycle and injection height being meteorology-dependent, these emission parameters are computed inside CHIMERE. More detail on the treatment of fires in CHIMERE simulations is provided in Section 4.2.

Mineral dust emissions are parameterized into CHIMERE, based on external mapped data such as roughness length and land-use, and meteorological parameters such as soil moisture and surface wind speeds. Similarly, sea-salt emissions are parameterized in CHIMERE based on the 10 m wind speed over the oceans.

The resuspension process is considered as an additional emission source in the model. It is significant for particulate matter and may induce a large increase of the emission flux in case of dry soils, for locations where traffic and industries initially produce particles. Resuspension processes are not well understood and empirically represented in CHIMERE based on a function of the soil water content, friction velocity, and a constant designed to close the mass budget.

Boundary and initial conditions of atmospheric composition
In the studies presented in this thesis, boundary and initial concentrations of atmospheric concentrations of gases and aerosols at the global scale are taken from the LMDz-INCA global model of climate and chemistry transport [Folberth et al., 2006]. More detail on that is provided in each section.

1.3.2.2 Time integration

For chemical processes, both the prod-loss budget and splitting approaches are available options. The numerical solution is based on the application of a Gauss-Seidel iteration scheme to the two-step implicit backward differentiation [Verwer, 1994], as described by the implicit nonlinear system in Equation (1.9). Outputs are provided at a hourly frequency, although calculations between two consecutive time steps are performed at much higher frequency.

$$c^{n+1} = \left(\mathbb{I} + \frac{2}{3}\Delta t L(c^{n+1})\right)^{-1}\left(\frac{4}{3}c^{n} - \frac{1}{3}c^{n-1} + \frac{2}{3}\Delta t P(c^{n+1})\right) \tag{1.9}$$

where c^n is the vector of concentrations at time n, Δt is the chemical time step and P and L are production and loss vector functions.

1.3.2.3 Mesh

Horizontal mesh
For the horizontal discretization of space, CHIMERE uses a staggered Arakawa C grid [Arakawa and Lamb, 1977] (Figure 1.16a). This mesh allows to compute quantities separately, either at the grid cell center, or at the center of its interfaces.

Occasionally, some regions of the study area need a higher resolution focus (finer study of the processes, steep orography forcing higher horizontal resolution...). In order to prevent a high jump in resolution from the global boundary conditions into this focused high resolution area, different domains/sub-domains and grid resolutions are used, in a 'nested' fashion, i.e. a coarse resolution large domain comprising one or more higher resolution zones. Several examples of nested domains arise throughout this work.

Vertical mesh
In order to have refined layers near the surface for urban and regional studies, and at the same time allow for the use of CHIMERE for larger scale simulations, vertical levels are distributed from the surface to 800 hPa with a layer thickness increasing exponentially, whereas from 800 hPa to the model top layers thicknesses are evenly distributed. The pressure levels are then linearly scaled to ensure that they do not cross each other, and that their relative thickness remains the same even above high topography (Figure 1.16b).

1.3.2.4 Gas-phase chemistry

Three gas-phase chemistry mechanisms are available in CHIMERE:

- The complete MELCHIOR scheme comprising 87 species and 300 reactions [Lattuati, 1997]
- A reduced version of the MELCHIOR scheme with 50 species and 120 reactions, that saves computing time [Menut et al., 2013]
- The SAPRC-07-A mechanism with 85 species and 275 reactions [Carter, 2010]

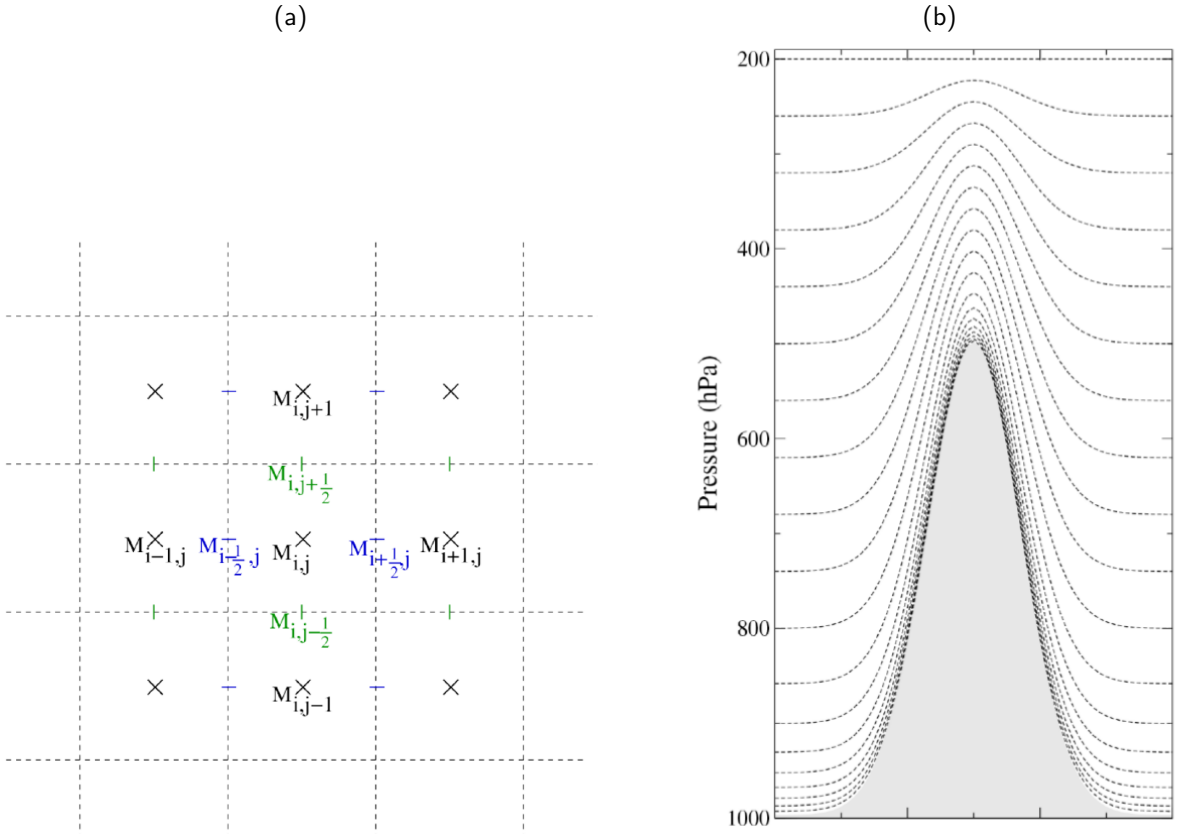

Figure 1.16: (a) Centered (black) and staggered (blue and green) grid points in the Arakawa C-grid used in the CHIMERE horizontal mesh [Mailler et al., 2017]. (b) Vertical levels adjustment to topography in the CHIMERE mesh [Mailler et al., 2017].

The choice of the mechanism depends on the purpose of the simulation. For instance a study over Galicia showed that if daily maxima of ozone and PM are targeted, SAPRC performs better [Brands et al., 2019]. On the contrary, if maxima and minima are both of importance, full MELCHIOR seems to be more suited. Given the scope of my different studies, I am mostly interested either in short-lived events of a few hours, or averaged levels over several weeks. Since acute precision on chemistry is not required and daily minima/maxima are not the targeted outputs, I thus selected the reduced MELCHIOR scheme in order to reduce computing time, which is already slowed down by the topographic configuration of the region. This scheme is also the one usually used for forecast purposes with CHIMERE, which enables comparisons between my analysis results and possible forecasts.

1.3.2.5 Aerosols chemistry

CHIMERE accounts for 6 families of chemically-active aerosols: anthropogenic primary particulate matter (PPM - including black carbon, organic carbon, industrial dust), secondary organic aerosols (SOA - biogenic and anthropogenic), sulfates, nitrates, ammonium (primary and secondary), and water. Each modeled aerosol is characterized by its composition and aerodynamical diameter. The three main chemical processes represented are:

- Nucleation (creation from precursors): this process is favored by cold and wet meteorological conditions. The newly nucleated ultrafine particles are added to the smallest bin of the species formed.
- Coagulation (collision and merger of particles): for a given component in a given size section, the evolution of its mass concentration due to coagulation depends on the combination of the mass concentrations in the other size sections and a set of coefficients related to particle characteristics and meteorological drivers. For ultrafine aerosols coagulation is essentially driven by Brownian motion, while sedimentation is the most efficient process for coarse particles.

- Absorption (gas-phase condensation onto a particle): the bulk equilibrium approach is used, with a separation between small, fast condensing bins which form a bulk particle, and bigger diameters for which thermodynamic computations (based on the module ISORROPIA) are performed in order to determine the partitioning between gas phase and particle phase concentrations at equilibrium.

1.3.2.6 Transport

The resolution of transport in CHIMERE is split between zonal, meridional and vertical directions. Each transport equation is solved separately and the derived transported concentration is the sum of the three. For direction i, the transport equation solved has the form of (1.10).

$$\Delta^{(i)}c = -\Big(\frac{F^i_{n+\frac{1}{2}}(t) - F^i_{n-\frac{1}{2}}(t)}{\Delta x}\Big)\Delta t \tag{1.10}$$

where $\Delta^{(i)}c$ is the variation of c due to transport in direction i, Δt is the physical time step, Δx is the spatial resolution, and F are the fluxes at the interfaces (blue and green points in Figure 1.16a).

Horizontal transport
Three schemes are available in CHIMERE for horizontal transport:

- Upwind scheme [Godunov, 1959] A simple first-order upwind scheme with a low computational cost but not very accurate and very diffusive. The mass flux at the interface between two cells is assumed to be the product of the wind at the interface by the tracer concentration in the upwind cell.
- Van-Leer scheme [Van Leer, 1977]: Low computational cost and good accuracy for transport of high concentrations in plumes. This scheme is recognized in meteorology for its good numerical accuracy and smaller diffusion than the upwind scheme, although it is more time-consuming.
- Third-order Parabolic Piecewise Method scheme [Collela and Woodward, 1984]: High computational cost but more accurate for long-lived species, diffusive but less than the Van-Leer scheme.

The simulations presented in this manuscript rely on the Van Leer scheme. Among the three options, this choice is a trade-off between accuracy and computational cost.

Vertical transport
Vertical transport is assumed to balance horizontal mass divergence. The vertical mass flux of dry air is calculated column-wise for each cell interface in the vertical direction, from model bottom to model top. For vertical transport, only upwind and Van-Leer schemes were available at the time of this work, but a third option was developed since, based on a Després and Lagoutière [1999] scheme [Mailler et al., 2021]. Similar to the horizontal scheme and for the same reasons, the Van-Leer option is selected for the simulations performed in this work.

1.3.2.7 Deposition

Dry deposition
Dry deposition is a vertical process that acts as a sink of gases and aerosols that fall to the ground due to gravity. Generally speaking, for a dry deposition velocity v_d the decrease of concentration c can be expressed following Equation (1.11). The approach adopted in CHIMERE is through a resistance analogy. Three different resistances govern deposition: aerodynamical resistance (r_a), surface resistance (r_s), and canopy resistance (r_c). The latter is relevant for gases only. The expression of the deposition velocity in CHIMERE is based on these resistances (r_c is complex to estimate in relation with the absorption of gases by the vegetation), and the settling velocity for aerosols, which represents the effect of gravity on particles. Wesely [1989] and Zhang et al. [2001] are two available approaches in CHIMERE. Although I am currently performing sensitivity tests and implementing an updated scheme based on Emerson et al. [2020], Zhang et al. [2001] was chosen in the framework of the studies presented in this manuscript, which are more aerosol-oriented. When relevant, more detail on deposition modeling is provided in this manuscript.

$$\Delta c = \frac{\partial}{\partial z}(v_d c) \tag{1.11}$$

Wet scavenging

In-cloud and below cloud scavenging are parameterized for gases and particles. For in-cloud scavenging of gases, dissolution (from gaseous to liquid phase) and dissipation (reverse transformation) are competing and reach an equilibrium defined by the associated reaction constants computed in CHIMERE. For in-cloud aerosol scavenging, deposition of particles is assumed to be proportional to the amount of water lost by precipitation. Scavenging by precipitation for gases and particles below clouds depends on the droplets properties such as their size, density and velocity.

1.3.2.8 On-line coupling

Trace elements, in particular aerosols, have an effect on meteorological conditions through the so-called direct and indirect feedback, briefly discussed in Section 1.1.3.2. As a result, it is paramount to include these effects in simulations in order to accurately reproduce the state of the atmosphere and evaluate emission scenarios impacts in a comprehensive manner. This coupling was not included in CTMs until quite recently, partly due to the underlying increased complexity and computing time implied by the two-way communication between the numerical weather model and the CTM, compared to the off-line approach where the flow chart is simpler (Figure 1.17). Nevertheless, this increased sophistication broadens the analysis possibilities with CHIMERE [Briant et al., 2017, Tuccella et al., 2019], and will be utilized in this work when useful.

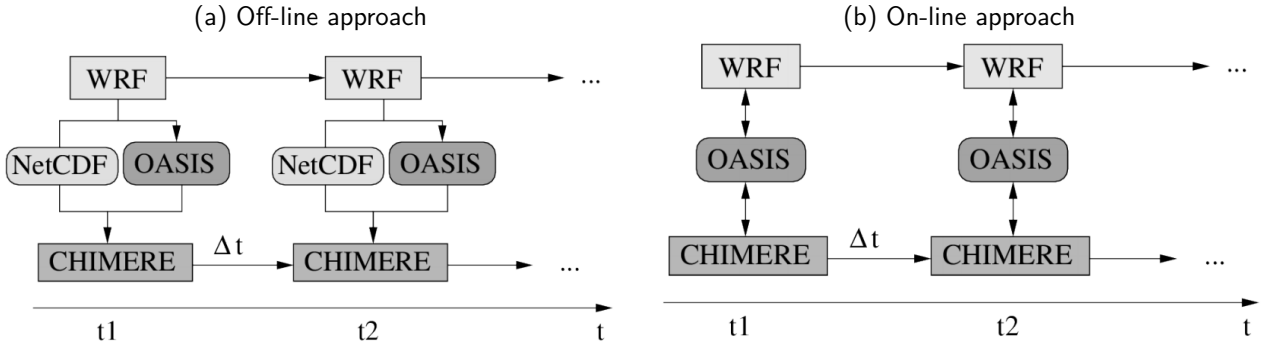

Figure 1.17: Schematic of off-line and on-line approaches in CHIMERE. Figures from the CHIMERE user guide `https://www.lmd.polytechnique.fr/chimere/docs/CHIMEREdoc_v2020r1.pdf`.

2 | Chile: general introduction, geophysical context and research questions

2.1 Brief historical background

Chile is believed to have been inhabited by human populations since at least 18,500 years ago in its southern part [Dillehay et al., 2015]. The Hispanic settlers arrived in the current Chilean territory during the 16th century, under the impulse of Pedro de Valdivia, the 'conqueror of Chile'. At that time, several distinct local communities lived in the coast and the Andes mountain range, all along the country. The Spanish power rapidly took control over the local people, whose policies rapidly led to notorious environmental changes in the country [Alaniz et al., 2019].

Spain reigned over most of the territory until the independence of Chile in 1818. Several geographical conflicts with the neighboring nations (Peru, Bolivia and Argentina) made the borders of Chile move during the 19th century and stabilize at the dawn of the 20th century to its current span. After a tumultuous early 20th century characterized by political, social and economic crises burst one after the other, the foundations of the Chilean industry were laid in the middle of the last century.

Chile remained an average economy in South America up until the end of the troubled Pinochet era (1973-1990) but started to take off in the 1990's following the opening of the market to foreign exchange, and is currently the first economy of the continent in terms of GDP per capita [OECD, 2019]. Business services and industry, of which mining is an key actor, are the two leading economic sectors of the country's economy.

Chile is a founding member of the United Nations (UN), and since 2010 a member of the Organization for Economic Co-operation and Development (OECD). As of today, the Republic of Chile is among South America's most stable economies, and the most developed country in terms of Human Development Index [United Nations Development Programme, 2020], although it is the 2nd most socially unequal country in the OECD [OECD, 2021].

As a result of this development trajectory, emissions of pollutants have been rising in the country for the last three decades, in connection with the large urban areas that spread along industrial centers. Among the specific features of the Chilean economy, its strong mining industry is responsible for massive pollutants emissions. Consequently, when air pollution in Chile started to become a relevant research question, many of the first studies analyzed the effect of copper smelters emissions on urban air quality [e.g. Gallardo et al., 2002, Hedberg et al., 2005, Moreno et al., 2010].

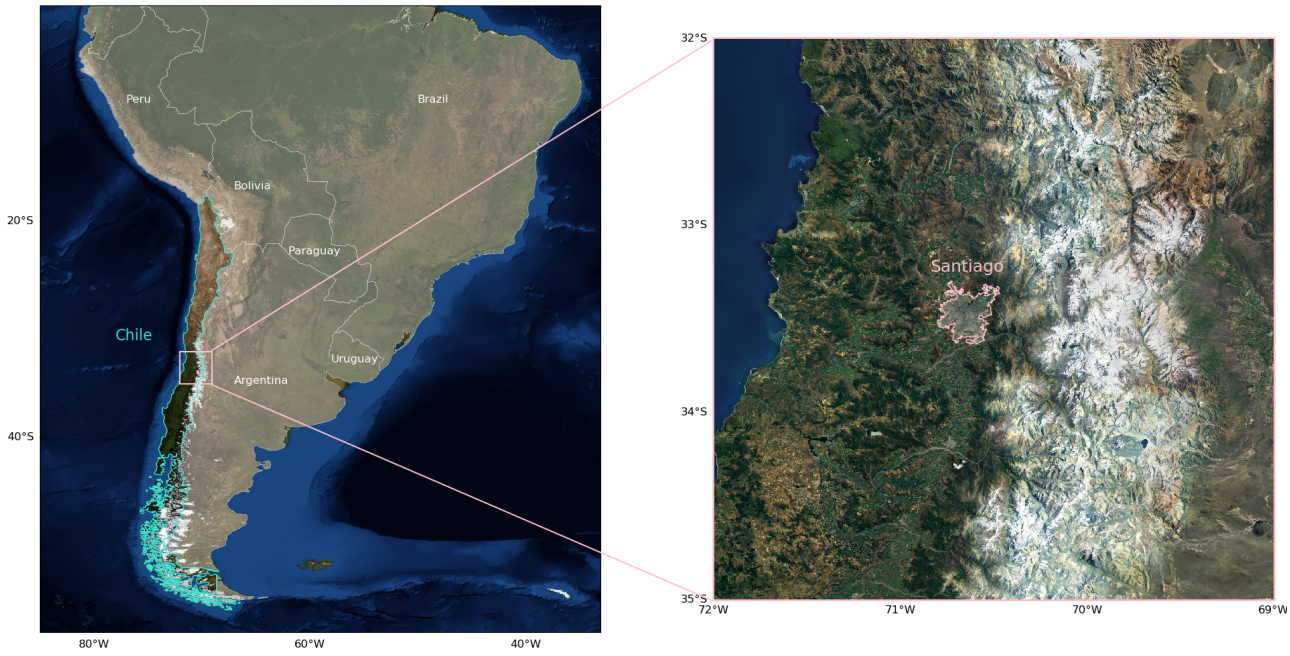

Figure 2.1: Chile in South America and zoom on central Chile and Santiago. Map background layer: Imagery World 2D, ©2009 ESRI

2.2 Geography

The territory of Chile is a narrow strip of land, framed by the Pacific ocean to the west and the Andes mountain range to the east, stretching over 4300 km from north to south but merely 350 km large at its widest point (Figure 2.1b). It is bordered by Peru and Bolivia in the north and northeast, along the Atacama desert. Argentina on the other side of the Andes follows along Chile down to the Drake Passage in the far south below Cape Horn. Some islands in the Pacific ocean are part of the country as well, such as Easter Island. Chile also claims property on the Chilean Antarctic Territory, which is still not fully acknowledged by the international community. Despite its elongated shape, the total surface area of Chile is large (756,000 km^2, 37^{th} largest in the world, comparable to Turkey). Santiago, the capital city of Chile (33.5°S, 70.5°W, 570 m a.s.l.) is situated in the central region of the country. The city is located in a confined geographical basin surrounded by the Andes in the east, a coastal range in the west, and transverse mountain chains in the south and north (Figure 2.1b).

2.3 Demography and Economy

Chile is home to 17.5 million inhabitants as of 2017, of which 40% are concentrated in the metropolitan region, where the capital city, Santiago, is located [INE, 2018] (Figure 2.2a). The growth of population in Chile is currently slowing down and is expected to peak around 2050, when a maximum population of 21 million inhabitants is reached (Figure 2.2b). In other words, the climax in terms of risks of population exposure to air pollution is expected to be around 2050 if appropriate policies are not implemented. The current high rate of urbanization in Chile makes the previous point even more critical, since the sprawl is not expected to stop in the coming years [Gallardo et al., 2018].

The Gross Domestic Product (GDP) has been increasing steadily since the 1990's, even though the growth rate is expected to slow down in the next decades to reach around 1.5% in the 2050's (Figure 2.2b). Chile is still in its economic development phase, and since development and pollution issues are often intertwined [e.g. Akimoto, 2003, Granier et al., 2011], close attention must be paid to environmental policies in the next few years.

The Human Development Index (HDI) of Chile has increased since the 1990's, catching up on the rest of OECD countries in the recent years, and well above the average for Latin America (Figure 2.2c). HDI takes into account the GDP per capita, life expectancy and education. Based on this criterion, Chile is the most developed country in Latin America (ranked 43^{rd} worldwide) just before Argentina (46^{th}) as of 2019 [United Nations Development Programme, 2020]. As a result, political games and lobbying put aside, one could expect that designing stringent policies on air quality is possibly an achievable target in this country: people being well educated, they might understand the need for such policies and support them, and Chile being rich enough could raise the money needed to enforce these actions. Politics are obviously not so simple, but the potential for a cleaner air in the country exists.

2.4 Climate

Given its elongated shape (northernmost territory at 17.5°S, southernmost at 56°S) and the presence of the Pacific ocean and the Andes, Chile comprises a wide variety of climates along the country (Figure 2.3). Each of these climates and associated regions are briefly described thereafter.

In the north

The Atacama desert covers the northernmost 1,000 km of Chile, trapped between the Peru-Chile trench in the west, and the Andes mountain range in the east. This subtropical desert is the driest non-polar desert on Earth, where some places do not receive precipitation for decades. The hyper-aridity of Atacama results from the combination of four phenomena, described in Houston and Hartley [2003]. First, the subtropical semi-permanent South Pacific High and the Hadley circulation consistently bring subsident dry air over the area thus preventing convection and the development of clouds and precipitation (zonal effect). Second, the cold Humboldt oceanic current that borders Peru and Chile cools off the air above the ocean leading to a persistent inversion which minimizes the possibility of convection and clouds formation (oceanic effect). Third, Atacama is on the Leeward side of the Andes with respect to the southeast trade winds prevailing at this latitude, and is thus subject to the blocking of moist air masses on the other side of the mountain range (rainshadow effect). Finally, this area is

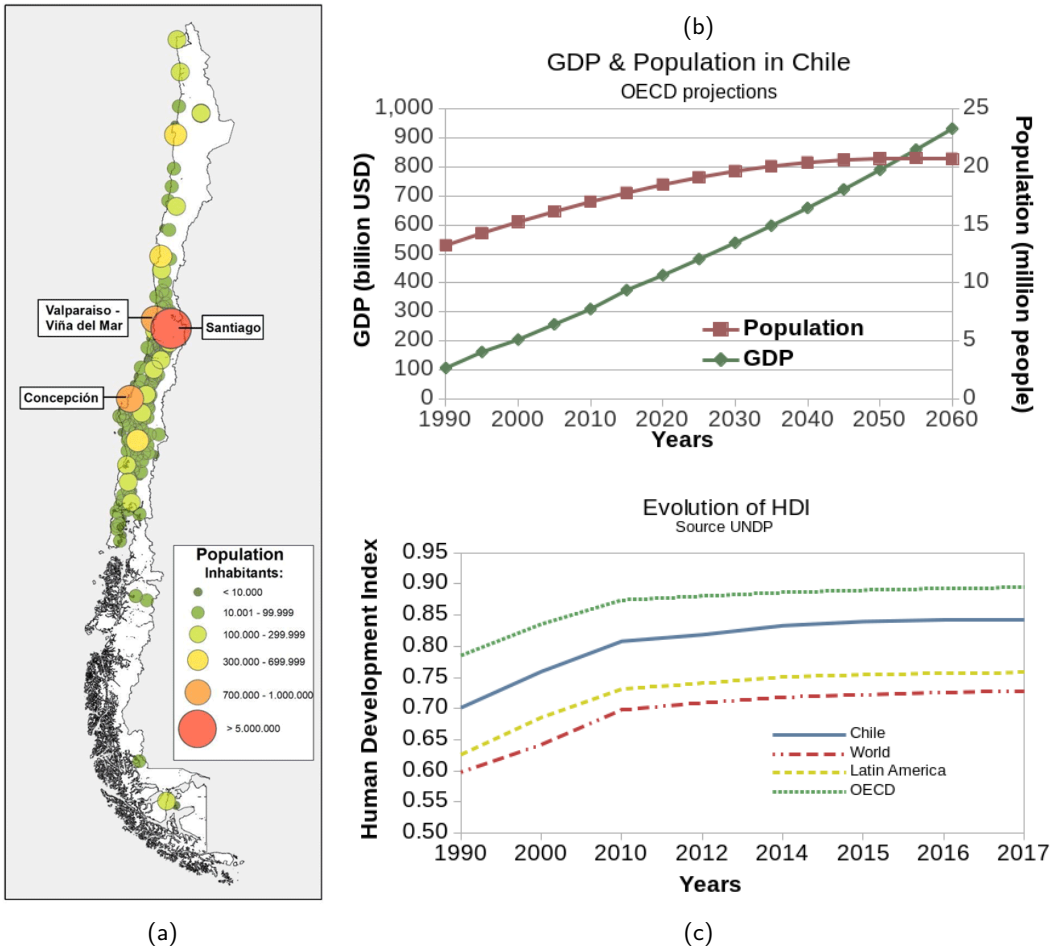

Figure 2.2: (a) Spatial distribution of population in cities of continental Chile with more than 5,000 inhabitants in 2012 [Gallardo et al., 2018]. (b) Past and future evolution of GDP (data from OECD [2019]) and population (data from United Nations [2017]) in Chile. (c) Historical evolution of the Human Development Index for Chile, Latin America, OECD and World (data from United Nations Development Programme [2018]).

far away from the Amazonian-Atlantic moisture source (continentality effect). The region is mostly composed of stony terrain, salt lakes, sand, and lava. As a result of this dry climate and barren soil, dust storms can be observed although it is not a common phenomenon [e.g. Reyers et al., 2019]. Another weather component typical of this region is the so-called *Camanchaca*: marine stratocumulus cloud banks formed over the Pacific coast move inland, creating a thick fog that does not precipitate. This is an important source of moisture for the region and local inhabitants extract irrigation and drinking water from the *Camanchaca* through the use of fog nets [e.g. Schemenauer et al., 1988].

In the south

The southern part of Chile has mostly an oceanic climate (from temperate to subpolar for the southernmost part) and comprises different climate regions. In its northern part comes the Valdivian temperate rainforest (around 40°S) which belongs to the temperate broadleaf and mixed forests biome, abundantly humid due to the wet westerlies condensing on the windward slopes of the Andes, and dominated by forests of evergreen trees. The Magellanic subpolar forests are a temperate broadleaf and mixed forests ecoregion, hosting the world's southernmost forests. Found in the western side of the Andes, this biome extends from the south of the Valdivian rainforest down to the *Tierra del Fuego*. These forests alternate with the Magellanic tundra which is dominated by scrubs and bogs. Further south, the Northern and Southern Patagonian ice fields are located around 47°S to 51°S. They are two remnant parts of the Patagonian ice sheet that used to cover all of southern Chile during the last glacial period. Together their ice mass feeds more than 30 glaciers. These ice fields were formed based on

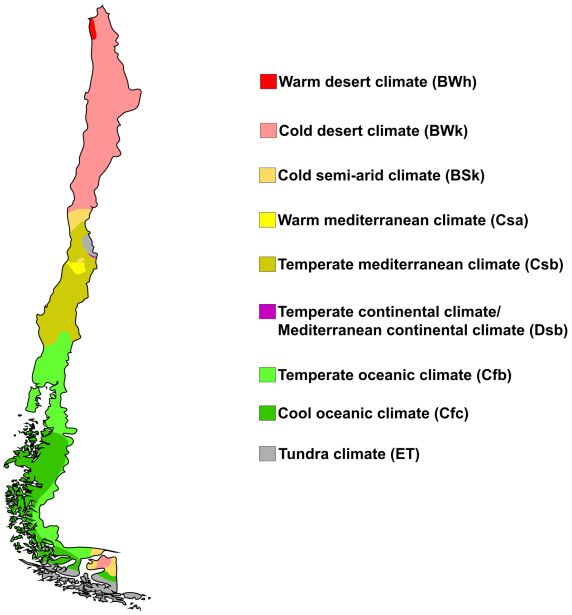

Figure 2.3: Köppen climate classifications of Chile [Peel et al., 2007]

the combination of a high elevation (up to 1,500 m a.s.l.) favorable terrain and a cool, moist, marine climate. The Southern Patagonian ice field alone is the world's second largest extrapolar contiguous ice field.

In the central zone

The Metropolitan Area of Santiago (SMA) is located in the central part of Chile (approximately 32°S to 37°S) which is characterized by a temperate Mediterranean climate, featuring a sharp seasonality in temperature and precipitation as observed in Santiago for instance (Figure 2.4a). Average monthly temperatures are around 20°C during the dry summer months (4 mm accumulated precipitation), and 9°C in winter associated with around 50 mm to 70 mm of rainfall per month. Over the last 50 years, the average yearly temperature rose by approximately +0.8°C in Santiago (Figure 2.4b). According to the IPCC, global warming over the same period was around +0.6°C. The excess warming in Santiago is likely attributable to the sharp increase in urbanization leading to an enhanced urban heat island effect. The persistent negative precipitation anomaly since 2010 (Figure 2.4b) is referred to as a mega-drought and stems from the combined effects of anthropogenic forcings and the Pacific Decadal Oscillation (PDO) phase [Boisier et al., 2016].

Central Chile is located at the convergence zone between the large scale atmospheric circulation Hadley and Ferrel cells, around 30°S. This junction forms the subtropical high-pressure belt, where the general subsident air motion prevents the formation of clouds, thus leading to the prevalence of dry conditions. Another consequence of this high-pressure zone is generally low-intensity winds in the area, with relatively higher wind speeds during summertime. For Santiago in particular, the Andes play a major role in the wind system through the mountain-valley circulation, with down-valley winds (easterlies) in the morning and up-valley winds (westerlies) in the evening, due to differential heating between the wide urban basin and the narrow valleys [Whiteman, 2000].

Interannual variability

The Chilean climate is subject to several variability modes, mostly tied to the state of the Pacific Ocean. At the intra-seasonal time scale, the Madden-Julian Oscillation [Madden and Julian, 1972] (MJO, 40-50 days period) is the leading variability mode. It has been shown for the region of central Chile, that phases of the MJO are correlated with variations in precipitation [Barrett et al., 2012a], strength of temperature inversions and wind speeds and directions, which in turn translate into modulations of particulate matter and ozone concentrations [Ragsdale et al., 2013, Barrett et al., 2012b].

The observed year-to-year variability in precipitation in central Chile is tied to the phases of El Niño Southern Oscillation (ENSO) with positive (negative, respectively) anomalies in wintertime precipitation related to El Niño (La Niña, respectively) phases [Montecinos and Aceituno, 2003]. This teleconnection has impacts on air

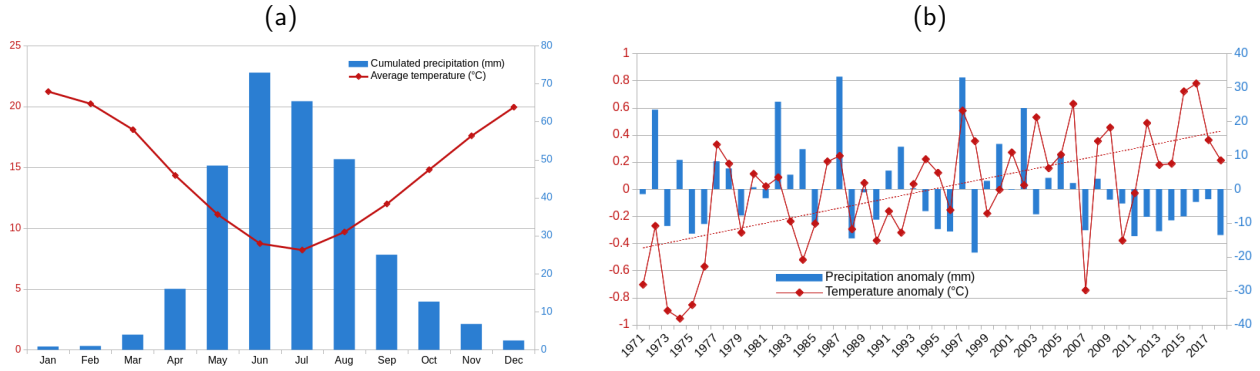

Figure 2.4: Seasonality and evolution of temperature and precipitation in Santiago. (a) Monthly average temperature and precipitation in Santiago. (b) Yearly average temperature and precipitation anomalies in Santiago. Data from [Centro de Ciencias del Clima y la Resiliencia, 2019] for the period 1971-2018.

quality, in relation with the scavening effect of rainfall on particulate matter and the lesser resuspension potential on a wet ground.

At longer time scales, the Pacific Decadal Oscillation (PDO) and Southern Annular Mode (SAM) are the governing variability modes. In particular, as shown in Figure 2.5, shifts in the PDO cold/warm phases correspond to changes in the strength of the ENSO-rainfall teleconnection in central Chile.

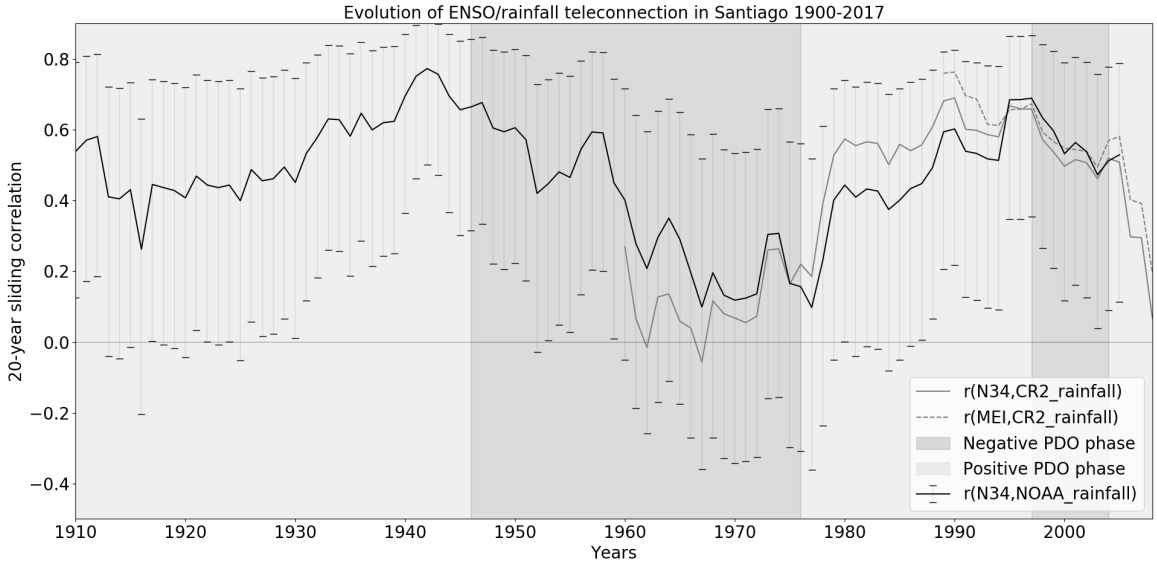

Figure 2.5: 20-year centered sliding correlation between June/July Niño3.4 Index (N34), Multivariate ENSO Index (MEI) and rainfall in central Chile (GHCN version 2 Land Precipitation monthly mean from NOAA/ESRL PSD at the 5° resolution) between 1900 and 2017. Vertical bars represent 95% confidence intervals. Shaded areas represent PDO phases.

2.5 Atmospheric pollution in Chile

Concerns surrounding air quality are particularly strong in Latin America, where 'a more cohesive and sustained community of atmospheric scientists is needed [...] to address the pressing issues of air quality and climate change' [Andrade-Flores et al., 2016]. Historically, São Paulo (Brazil), Mexico City (Mexico) and Santiago (Chile) are the urban areas most affected by anthropogenic atmospheric pollution in this part of the world [Bell et al., 2006]. On the whole, around 25% of the urban population in Latin America (i.e. 81 million people) is exposed to bad air quality as defined by the WHO standards [Romieu et al., 1991]. As mentioned in Section 2.3, the urban basin of Santiago concentrates a large part of the Chilean population so that air quality is paramount in the metropolitan area. What follows will thus mostly focus on the region of the capital city.

A combination of adverse geographical and climate conditions, associated with consequent emission fluxes typical of urbanized densely populated areas have made the air of Santiago and several other cities in Chile among the worst on the continent [Rutllant and Garreaud, 1995, Barraza et al., 2017]. In particular, the capital city regularly faces harmful levels of fine particulate matter pollution [Saide et al., 2016] as well as short-lived peak events [Toro et al., 2019] in wintertime, related to poor ventilation conditions, associated with thermal inversions, trapping and concentrating air masses above the city (Figure 2.6) combined with significant emissions from residential heating and traffic [Mazzeo et al., 2018]. Other cities in Chile are even more affected by wintertime PM pollution, especially in the south (Coyhaique, Osorno, Temuco...) where cold weather leads to large emissions related to wood burning for residential heating, and where the geographical configuration offers a similar confinement between mountains [e.g. Sanhueza et al., 2012].

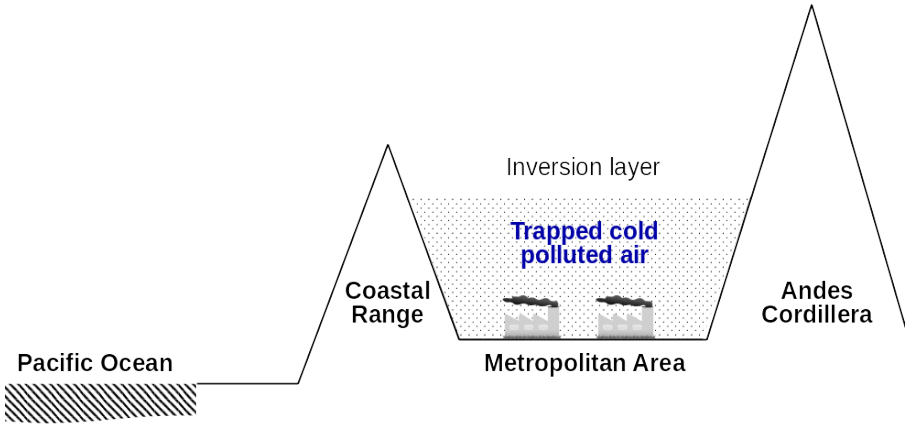

Figure 2.6: Schematic of an inversion layer leading to the accumulation of pollutants over Santiago in wintertime.

In summer and spring, Santiago is subject to the formation of an ozone photochemical smog, related to high emissions of NO_x (from traffic mainly) and volatile organic compounds (emitted by vegetation which is more abundant at this time of the year) and intense solar radiation that enables the photolytic reactions involved in the ozone cycle [Gramsch et al., 2006]. Contrarily, O_3 barely forms in wintertime due to less intense radiation and shorter days. PM concentrations in summertime are a lesser issue compared to wintertime, in relation with smaller emissions and a greater dilution within the deeper more turbulent mixing layer characteristic of summertime [Muñoz and Alcafuz, 2012]. The seasonality of PM and O_3 are clearly visible in Figure 2.7 showing monthly means for three air quality stations in Santiago.

Although the aforementioned characteristics generally apply to the whole metropolitan area, a great spatial variability is observed. In particular, a sharp west/east gradient is observed for $PM_{2.5}$ and O_3: data from Ministerio del Medio Ambiente [2018] shows that western Santiago (e.g. *Pudahuel*) is more prone to elevated $PM_{2.5}$ concentrations in wintertime compared to the eastern part of the city (e.g. *Las Condes*), while in turn summertime O_3 is less abundant in the west compared to the east (Figure 2.7). Downtown Santiago features levels of both pollutants in between, evidencing a zonal pattern. This is partially related to mountain-valley circulation, generating an eastward motion of air masses in the morning and westward in the evening, hence creating zonal gradients [Schmitz, 2005]. However when looking at emission inventories of $PM_{2.5}$ and NO_2 such a pattern is not conspicuous in emission rates: a few districts feature larger emissions of $PM_{2.5}$ mostly related to land-use and higher use of wood burning in winter, while NO_2 emissions mostly follow the main roads network (Figure 2.8). NB: The emissions inventory shown in Figure 2.8 was recently built by colleagues of the University

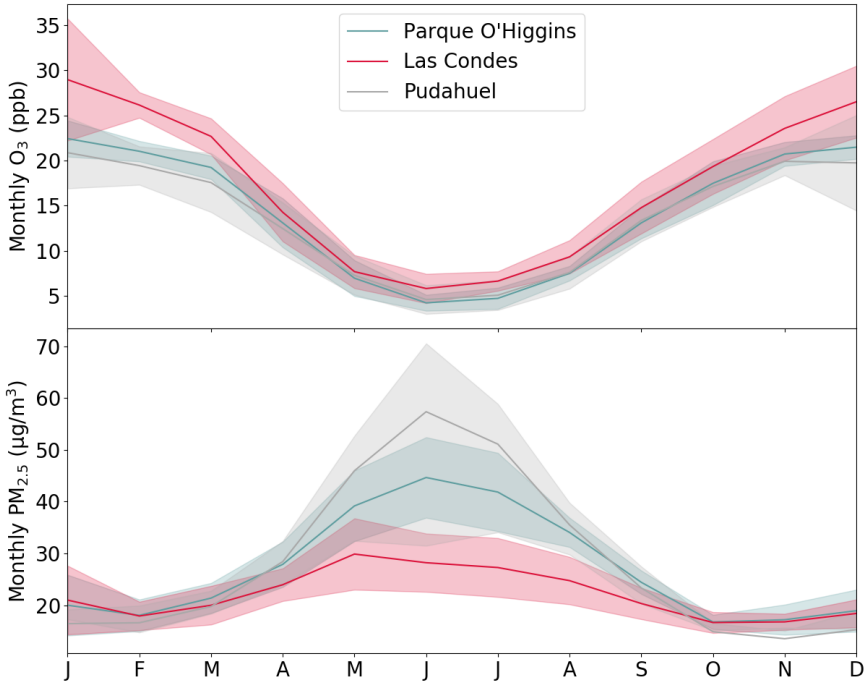

Figure 2.7: Monthly mean $PM_{2.5}$ concentration and O_3 mixing ratio measured at stations *Parque O'Higgins*, *Pudahuel* and *Las Condes* (see Figure 2.8 for their locations) for the period 2010-2018. Solid line is the mean, shades show one standard deviation. Data from Ministerio del Medio Ambiente [2018]

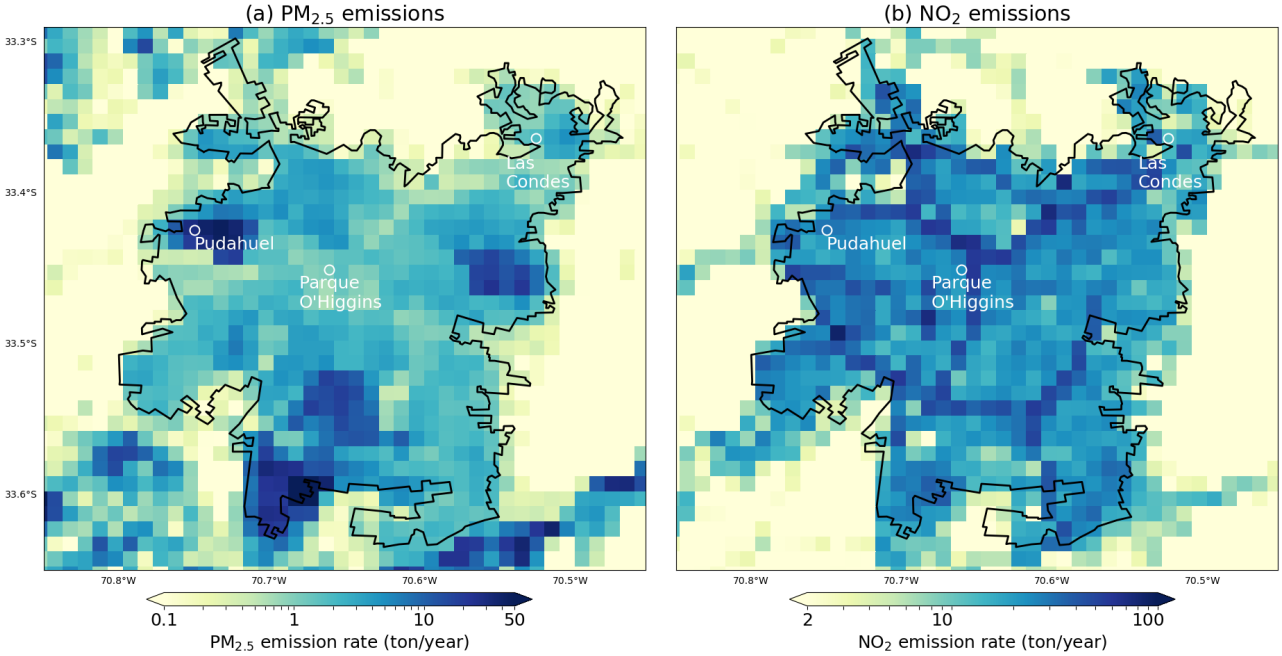

Figure 2.8: Annual emission rates of (a) $PM_{2.5}$ and (b) NO_2 in Santiago as of 2015. Data from the new Chilean emissions inventory at 1 km resolution [Álamos et al., 2021]. Data courtesy of Nicolas Huneeus.

of Chile and will soon be published in Álamos et al. [2021]. It is national, at the 1 km resolution, and will be available for the years 2015 to 2017 for a large panel of particulate and gas species and the main anthropogenic activity sectors of the country (vehicular, industrial, energy, mining and residential sectors). Contrary to global inventories such as HTAP, it is largely based on local observations, and builds upon detailed land information

and up-to-date emissions factors, which improves its accuracy. Unfortunately, as it was not complete at the time, it could not be used in the framework of the studies presented in this manuscript but will likely improve chemistry-transport simulations in the future.

Aware of the necessity to clean the air of Santiago, the local authorities launched the first 'Atmospheric Decontamination Plan' in 1997, 20 years after setting the first air quality standards [Aire Santiago, 2018]. These plans are updated every 5 years, with a progressive lowering of the target thresholds. Air pollution represents a significant burden for the economy of Chile what with the negative effects on health, infrastructures, agriculture, tourism... The authorities estimate that the implementation of the 2012 standards on $PM_{2.5}$ will represent altogether an avoided cost of USD 7.1 billion for the period 2012-2041 [MMA, 2012]. However, although the levels of $PM_{2.5}$ and O_3 have indeed decreased in Santiago by -21% and -12% respectively between the periods 2000-2009 and 2010-2018, mainly because of primary technological mitigation policies addressing vehicle emissions [Gallardo et al., 2018], Figure 2.9 shows a stabilization of average levels in the last decade or so, with a significant inter-annual variability, not evidencing a trend during that period. In this context, $PM_{2.5}$ and O_3 levels remain above the Chilean target and WHO standards: for 2019, the average $PM_{2.5}$ concentration in Santiago, computed over the stations taken into account in the official calculation (namely *Parque O'Higgins*, *Las Condes*, *Independencia* - see Figure 1.12 for their locations), is 23 µg/m^3 i.e. 3 µg/m^3 above the Chilean standard and 13 µg/m^3 in excess of the WHO guidelines [WHO, 2006] (Figure 2.9). Similarly, the criterion for O_3 (99th percentile of maximum 8-hour daily O_3 over the aforementioned stations) is exceeded by 4 ppb (14 ppb, respectively) compared to the Chilean standard (WHO guideline, respectively). Meeting the WHO standards for $PM_{2.5}$ in Chile could save around 1.4 life years per capita [Energy Policy Institute at the University of Chicago, 2017]. The issue of air pollution in Santiago is thus still far from belonging to the past.

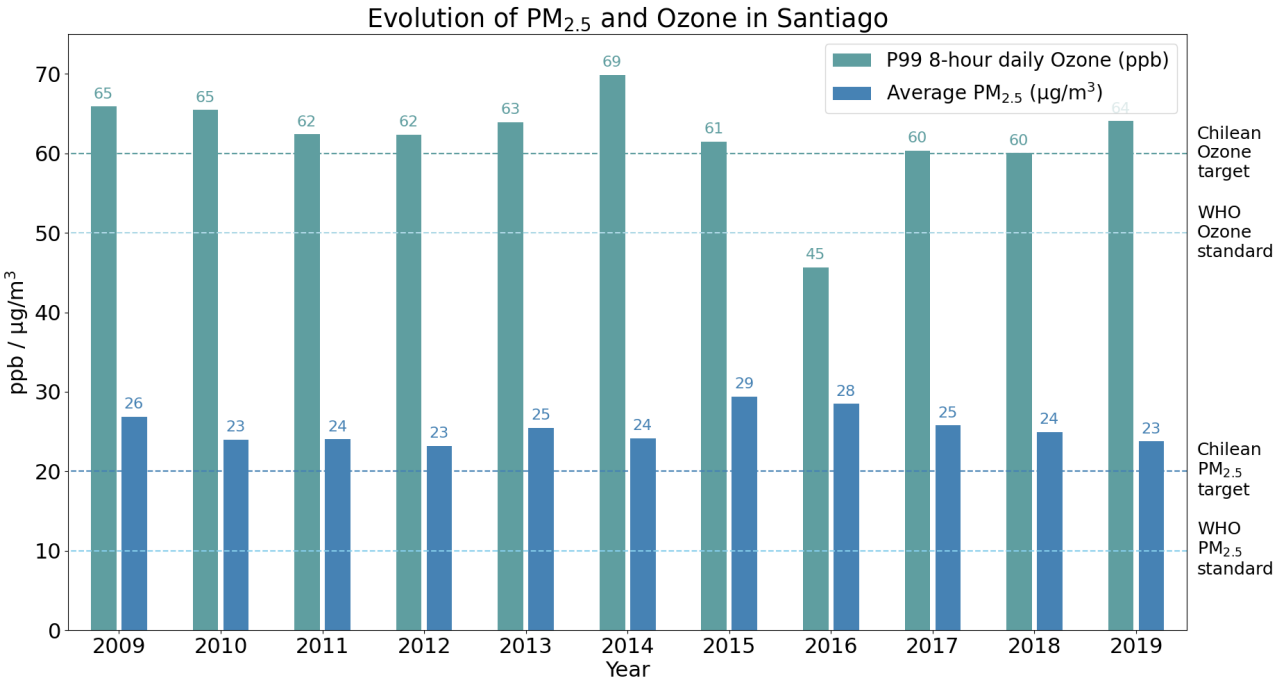

Figure 2.9: Annual evolution of $PM_{2.5}$ and O_3 levels in Santiago with respect to the WHO and Chilean standards. Data from [Ministerio del Medio Ambiente, 2018].

In addition to its health impacts and economic costs, air pollution in Chile also leads to major risks for climate and ecosystems. All along the country (even more so in Santiago), human activities are close to the Andes mountain range. Aerosols and pollutants emitted by these activities may reach the nearby glaciers of the cordillera [Cordova et al., 2016, Gramsch et al., 2020]. In particular, anthropogenic aerosols such as black carbon (BC) deposited on the Andean cryosphere modify the ice albedo and composition, thus leading to accelerated melting [Rowe et al., 2019]. This may contribute to ecosystems destruction and climate change, and jeopardize water resources [Molina et al., 2015]. 'Cookstoves in these urban regions [...] could have a significant impact on the rapid melting of snow and ice shown by the Andean tropical glaciers. Traffic emissions from diesel vehicles may also prove a significant source of black carbon' [International Cryosphere Climate Initiative, 2018].

2.6 Challenges, research questions and thesis plan

Challenges in chemistry-transport modeling applied to Chile

The region of Santiago features a complex topography, which leads to modeling challenges. Indeed, a CTM relies on a grid-based representation, which resolution corresponds to the smallest distinguishable unit. Over areas long of several hundreds of kilometers (which is needed in order to reproduce properly the long-range transport of pollutants), stability and computation time constrain the maximum resolution, which in our case is the order of the kilometer. As a result, over a steep mountainous terrain, properties of the ground might change a lot over 1 kilometer, so that our grid resolution might be insufficient to adequately capture valleys and summits, thus mismodeling air motions by lack of spatial accuracy. Besides, meteorology simulations at such horizontal resolutions, around the kilometer, fall into the 'gray area' of atmospheric modeling, where the resolution of convection and boundary layer processes may be explicitly performed (large-eddy simulation - LES) or parameterized [e.g. Wyngaard, 2004, Shin and Hong, 2015, Doubrawa and Muñoz-Esparza, 2020]. The choice of what to resolve explicitly influences greatly the results of the simulation, but there is no unequivocal rule at kilometer resolutions. Historically, the CHIMERE development team at LMD focuses mainly on Europe and Africa, which are subject to different meteorological features than Chile, and with resolution usually coarser than the highest 1 km resolution I used. Except for one study by Mazzeo et al. [2018] that applied CHIMERE on a short winter period in Santiago, no clues existed at the beginning of my thesis as to what the best parameterization is for Chile. Thus, as a preliminary work, I tested several model parameterizations for WRF-CHIMERE to identify the options that result in the most faithful representation of observations, including for summer periods that were never simulated before for that region.

Another challenge comes from the available emission inventories which are static, based on annual totals, and at a spatial and temporal resolution that is significantly coarser than the grid/time steps considered. In particular, spatial patterns of emissions within Santiago are very heterogeneous, at a finer scale than the available resolution, as evidenced by more recent data shown in Figure 2.8. In addition, the inventory used in this work represents emission fluxes for the year 2010, which is 5 to 7 years prior to the studied periods. Given the air pollution mitigation plans implemented by the Chilean government over the last decades, a time evolution of emissions over the years can be assumed, although average concentrations do not feature a clear downward trend (Fig. 2.9). Downscaling and interpolation are therefore performed on the old, static emission inventories available to improve performance, but they are still a large source of error in the model. In this regard, I had to manipulate these inventories and come up with methods to improve them for the specific cases I studied (e.g. proxy on population density based on high-resolution census data in Santiago, simplified inversion on NO_x and VOC emissions for the proper reproduction of summertime ozone...). Recent publications detail newly built emission inventories of pollutants for Chile, updated for the years 2015 and 2016 [Álamos et al., 2021, Osses et al., 2021]. They reveal discrepancies with the older inventories used in this work, going both ways (under- and over-estimation of fluxes) depending on the pollutant, with compensations across emission sectors that lead to total emitted masses sometimes closer than expected between the data sets. However, for most of the species, the uncertainty range associated with these new inventories is larger than the discrepancy between the old and new versions [Álamos et al., 2021]. In this respect, although switching to the newly available inventories should improve model performance, the uncertainty range does not disqualify our current approach based on older data.

On a similar note, significant sources of natural and biogenic emissions are found throughout Chile, with the Atacama desert in the north generating a lot of dust emissions, the Pacific ocean leading to sea salt aerosols penetrating inland, and more generally the vegetation cover responsible for VOCs emissions. These can account for a large fraction of atmospheric concentrations, even in urban areas, but are quite complex to model as they require detailed information on soil composition and land cover. Biases in chemistry-transport simulations with respect to observations can thus arise depending on the quality of databases of surface data. In the case of Chile, their reliability has not been tested so far. Recent simulations I performed showed that for dust, for example, the model generates too little emissions, in relation with discrepancies in the soil type and soil roughness input databases. Similar to anthropogenic emissions, I analyzed the sensitivity of the simulated fields to surface data and physical parameterizations, and compared to observations, in order to identify possible shortcomings in the input data and devise a working version of the model for dust in the Atacama desert.

In addition, the method commonly used to validate the model outcomes is to compare to on-site observations. Despite a quite well developed ground-level measurement network, vertical profiles are scarce and only the results of specific, time-limited, dedicated campaigns at particular sites. Thus, the validity of the vertical representation of processes by the model can only be assessed over a limited number of days and places. Generally speaking,

the lack of measured data prevents us from extensively validating the simulations. In order to still maximize the validation possibilities, I often reached out to Chilean colleagues to gain access to non-public data in addition to what is readily available in governmental databases.

Despite the aforementioned difficulties with performing chemistry-transport simulations over Chile, this work relies for a large part on modeling with WRF-CHIMERE, which constitutes a still rather novel method to investigate atmospheric composition and its transport in this region. Consequently, a common thread throughout the investigations conducted in this work is the assessment of the ability of WRF-CHIMERE to reproduce observed mean levels and dynamics of atmospheric composition and transport in Chile. Indeed, this model had been run only once over that region before this PhD work, never in summertime. Consequently, in each section, a validation is systematically performed, as thoroughly as possible, and the shortcomings are stated when the performance is deemed insufficient.

Thesis Plan

The title and theme of this PhD thesis is broad and could encompass a large variety of topics and questions. Within the general field of air pollution in Chile, three main research questions were defined and briefly introduced thereafter.

First, seasonal advection patterns of air pollutants are studied to determine the relative contribution of long-range transport of contaminants to and from Santiago, and to provide a broad picture of the fate of emissions in central Chile in summer and winter. Such knowledge is critical for the design of adapted mitigation policies. The approach with chemistry-transport simulations revealed unobserved phenomena.

In addition to a mean seasonal view, policies also need a clarified picture of extreme events. The sources and consequences of sporadic exceptional events that featured skyrocketing concentrations of pollutants in the recent years are thus studied. This is the second research theme I selected for this thesis, connected to wintertime peak events source identification and atmospheric feedback of summertime biomass burning.

Another feedback, that I found was the less well constrained although possibly the most critical, is related to the deposition of anthropogenic light-absorbing aerosols onto glaciers and snowpacks of the Andes. In this regard, I dedicated the third part of this manuscript to identifying the pathways of urban pollutants towards the Andes and quantifying their deposition rate on glaciers.

I selected these topics within the general theme of the thesis because they combine a high level of criticality both in terms of policy design and air pollution feedback, with a relatively small literature so far that is not conclusive on either of the associated questions. I thus deemed the criticality/knowledge ratio of the research questions introduced below was high enough to generate important results and implications. Thereafter, each one of these topics is contextualized, the specific research questions I identified are introduced and the methodology I designed to answer them is briefly described.

1 - Seasonality and consequences of the regional transport of atmospheric pollutants

A fraction of atmospheric pollution in urban centers worldwide comes from medium- to long-range transport [e.g. Vardoulakis and Kassomenos, 2008, Resquin et al., 2018]. Investigations on this topic for Chile and Santiago exist, but mostly rely on statistical analysis through the use of source-receptor models [e.g. Barraza et al., 2017]. Such approaches are not best suited given the sharp spatial gradients in regional emissions, and the complex geographical situation, and do not provide a spatially continuous picture nor the possibility to study the associated dynamics. In addition, the effect of regional circulation on ozone concentrations in summertime had only been partially investigated based on observations [Seguel et al., 2013] but never with a model incorporating the complex underlying chemistry.

Questions that derive from this state of the literature on the regional transport of pollutants in central Chile and that are investigated here include:

- What is the regional footprint of pollutants and precursors emitted in Santiago in summertime and wintertime?
- Conversely, how much of the pollutants in Santiago come from outside the metropolitan basin?
- How does mountain-valley circulation affect ozone dynamics in the vicinity of Santiago?

Chemistry-transport modeling is the appropriate tool to investigate the aforementioned questions. More specifically, a sensitivity analysis to Santiago emissions is performed with CHIMERE, at high resolution, to

identify the relative share of transport to atmospheric composition and the processes guiding the advection. Fine particles in wintertime and ozone in summertime are the variables of interest.

2 - Sources and atmospheric impacts of extreme pollution events

Air pollution is mostly a chronic phenomenon in central Chile, in connection with steady, large anthropogenic emissions [e.g. Mazzeo et al., 2018]. Sporadically however, pollutants concentrations rise to outstanding levels well above alert thresholds for a few hours or a few days. Meteorological conditions can favor and exacerbate the accumulation of contamination, especially in wintertime [Rutllant and Garreaud, 1995], but exceptional emission fluxes are at the core of such events. Although their relevance in public health and economic terms is often overlooked compared to long-term air pollution exposure, peak events such as the ones recorded in June 2016 in Santiago and in January 2017 across central Chile also resulted in a significant increase in hospitalizations [e.g. Bowman et al., 2019]. The origin of the former event, that broke historical records of particulate matter hourly concentrations, remained mysterious before our investigation, while the latter was evidently related to historic forest fires in south-central Chile but the extent of the associated atmospheric impacts was barely touched upon.

In this context, the two aforementioned short-lived extreme air pollution events are investigated, in relation with the following research questions:

- What is the origin of the June 2016 record-breaking fine particles peak events?
- What proxy can help prognose the occurrence of such events?
- What were the effects on atmospheric composition and meteorology of the 2017 mega-fires in southcentral Chile?
- To what extent do they explain the formation of massive clouds along and off the coast of Chile?

For the June 2016 event, the investigation is conducted as follows: (i) estimate, using local measurements, whether other phenomena than massive emissions can explain the observed concentrations, (ii) analyze observed concentration ratios to discriminate between possible emission sources, (iii) model the event with CHIMERE to confirm the relevance of the identified emission source, its magnitude, and its termination.

The study of the 2017 forest fires event relies on a sensitivity analysis using WRF-CHIMERE in fully coupled mode, in order to evidence the impact on atmospheric composition and meteorology of fire-related pollutants. The simulations were extensively validated using (i) data from MODIS, IASI and CALIOP to verify the adequate representation of the plume dispersion, (ii) local measurements of air quality to ascertain the proper reproduction of atmospheric concentrations before and after the event.

3 - Urban black carbon and the Andean cryosphere

Air quality policy design is usually guided by public health considerations. It is acknowledged that air pollution also has adverse effects on climate and environments [e.g. Chung and Seinfeld, 2005]. Even more so when it comes to light-absorbing particles such as black carbon being deposited on the cryosphere, which embeds a positive climate feedback and threatens water supply sustainability [e.g. Rowe et al., 2019]. Despite a growing interest and dramatic stakes, little is known regarding the pathways of export of anthropogenic pollutants from urban centers in central Chile to glaciers and snow covered areas in the adjacent Andes. The magnitude of deposition fluxes on these ecosystems and the contribution of emissions from the Santiago basin are also mostly speculative.

With a view to filling in some of the blanks related to the environmental feedback of particulate matter pollution in central Chile, export and deposition processes of black carbon on glaciers of the Andes are studied, with the following research questions in mind:

- How much black carbon is deposited on Andean glaciers in summertime and wintertime?
- What is the contribution of emissions from Santiago?
- What are the associated pathways and synoptic-scale forcing?

The literature available on this topic exclusively relies on measurements, limited in time and space. As a result, no robust conclusions hold so far. In this regard, our work is oriented towards a modeling approach with high-resolution CHIMERE simulations, providing a more continuous picture both in space and time. The simulations are validated using local air quality and meteorology networks, as well as data from a campaign

dedicated to the investigation of black carbon export, realized in 2015 by our Chilean partners. A set of regional simulations provides estimates of black carbon deposition fluxes, including a sensitivity analysis to assess the role of Santiago emissions in these fluxes. The investigation of wintertime pathways is realized with a very high resolution simulation on a smaller domain near Santiago, and the study of passive tracers trajectories. Finally, our findings are put into a climatological perspective using local observation and reanalysis data, in order to assess their relevance and robustness.

List of publications

Within the framework of this PhD thesis, 5 articles were published and 1 is in preparation at the time of writing this document. These publications are listed hereafter, in chronological order, along with a brief description of their scope. Their contents will be detailed further in the core of the manuscript.

[Lapere et al., 2020]: Soccer games and record breaking $PM_{2.5}$ pollution events in Santiago, Chile, *Atmospheric Chemistry and Physics*, 2020

> The sporadic episodes of record fine particles concentrations in Santiago in recent winters are analyzed using observations and modeling, with a view to identifying their origin.

[Lapere et al., 2021b]: Pathways for wintertime deposition of anthropogenic light-absorbing particles on the Central Andes cryosphere, *Environmental Pollution*, 2021

> The pathways of wintertime export of urban black carbon from Santiago up to the Andes are paramount but far from straightforward, and thus investigated here based on modeling.

[Lapere et al., 2021a]: The 2017 mega-fires in central chile: Impacts on regional atmospheric composition and meteorology assessed from satellite data and chemistry-transport modeling, *Atmosphere*, 2021

> The historic fires of 2017 are investigated from the chemistry-transport modeling perspective, in order to assess their impacts on atmospheric composition and their meteorological feedback.

[Lapere et al., 2021c]: Seasonal variation in atmospheric pollutants transport in central Chile: dynamics and consequences, *Atmospheric Chemistry and Physics*, 2021

> Mean transport mechanisms of pollutants in summer and winter, at the scale of central Chile, are studied based on month-long simulations, with a focus on $PM_{2.5}$ and ozone.

[Huneeus et al., 2021]: Deep winter intrusions of urban black carbon into a canyon near Santiago, Chile: a pathway towards Andean glaciers, *Environmental Pollution*, 2021

> Measurement data from a field campaign are combined with long-term observations and reanalysis to evidence, in wintertime, the relation between synoptic conditions and the export potential of black carbon through canyons connecting Santiago to Andean glaciers.

3 | Seasonality and consequences of the regional transport of atmospheric pollutants

3.1 Seasonal transport of atmospheric pollutants in central Chile

The results presented in this chapter are based on and follow the structure of Lapere et al. [2021c], from which the text and figures were extracted.

3.1.1 Abstract

Central Chile faces atmospheric pollution issues all year long, in relation with elevated concentrations of fine particulate matter during the cold months and tropospheric ozone during the warm season. In addition to public health issues, environmental problems regarding vegetation growth and water supply, as well as meteorological feedback are at stake. Sharp spatial gradients in regional emissions along with a complex geographical situation make for variable and heterogeneous dynamics in the localization and long-range transport of pollutants, with seasonal differences. Based on chemistry-transport modeling with WRF-CHIMERE, this work studies for one winter period and one summer period: (i) the contribution of emissions from Santiago city to air pollution in central Chile, (ii) the reciprocal contribution of regional pollutants transported into the Santiago basin. The underlying 3-dimensional advection patterns are investigated. We find that on average for the winter period 5 µg m^{-3} to 10 µg m^{-3} of fine particulate matter in Santiago come from regional transport, corresponding to 13% to 15% of average concentrations. In turn, emissions from Santiago contribute to 5% to 10% of fine particulate matter pollution as far as 500 km to the north and 500 km to the south. Wintertime transport occurs mostly close to the surface. In summertime, exported precursors from Santiago, in combination with mountain-valley circulation dynamics, are found to account for most of ozone formation in the adjacent Andes cordillera and to create a persistent plume of ozone of more than 50 ppb, extending along 80 km horizontally and 1.5 km vertically, and located several hundred meters above ground, slightly north of Santiago. This work constitutes the first description of the mechanism underlying the latter phenomenon. Emissions of precursors from the capital city also affect daily maxima of surface ozone hundreds of kilometers away. In parallel, cutting emissions of precursors in the Santiago basin results in an increase of surface ozone mixing ratios in its western area.

3.1.2 Introduction

Most urban areas in central Chile (or *Zona central*, extending between 32°S and 37°S), including the capital city Santiago (33.5°S, 70.7°W, 500 m a.s.l.), deal with harmful atmospheric concentrations of fine particulate matter ($PM_{2.5}$) in wintertime [Saide et al., 2016, Barraza et al., 2017, Toro et al., 2019, Lapere et al., 2020], and tropospheric ozone (O_3) in summertime [Gramsch et al., 2006, Seguel et al., 2013, 2020]. Strong anthropogenic emissions of primary pollutants and precursors, combined with the poor ventilation conditions induced by the topography and synoptic-scale circulation, are the core reasons for such air quality issues [Rutllant and Garreaud, 1995]. The main sources of atmospheric pollutants in Santiago are road traffic and industrial activities, with additional contributions in wintertime from wood burning for residential heating [Barraza et al., 2017, Mazzeo et al., 2018]. Such characteristics apply to most urban areas in central Chile, including coastal zones [Sanhueza et al., 2012, Toro et al., 2014, Marín et al., 2017].

The central zone of Chile investigated in this study (referred to as 'central Chile' in the continuation) comprises the six administrative regions of Coquimbo, Valparaíso, Metropolitana de Santiago, O'Higgins, Maule and Ñuble. It is home to more than 12 million people [INE, 2018], who are chronically exposed to $PM_{2.5}$ pollution, leading to respiratory and cardiovascular issues [Ilabaca et al., 1999, Soza et al., 2019]. Chronic and acute exposures to $PM_{2.5}$ pollution also induce a significant economic burden [MMA, 2012, OECD, 2016]. A side effect is the deposition of light-absorbing particulate matter, such as black carbon (BC), on the adjacent Andean snowpack contributing to the observed accelerated melting of glaciers [Rowe et al., 2019, Lapere et al., 2021b]. Aerosols also affect the radiative balance of the atmosphere and influence cloud formation by acting as cloud condensation nuclei [e.g. Chung and Seinfeld, 2005, Koch and Genio, 2010].

Tropospheric O_3 is a secondary pollutant formed by the photochemical oxidation of volatile organic compounds (VOC) in the presence of nitrogen oxides (NO_x). The essential role of photolysis in its production explains that harmful levels are mostly observed in summertime [e.g. Walcek and Yuan, 1995, Seinfeld and Pandis, 2006]. O_3 is noxious for human health, causing respiratory disorders such as asthma [Lippmann, 1991]. Furthermore, its deposition on plant leaves affects their photosynthesis and evaporation ability, hence damaging crop yields [Hill and Littlefield, 1969]. Tropospheric O_3 is also a powerful greenhouse gas (GHG) as well as a photochemical oxidant hence playing a key role in the atmosphere [Ehhalt et al., 2001].

Although anthropogenic urban pollution is mostly a phenomenon affected by local sources and meteorology, interactions with remote emissions and air masses also occur. Depending on the wind system and stability of the troposphere, pollutants and precursors can be transported far from the emission site and reach distant locations. Urbanized areas in Europe [Vardoulakis and Kassomenos, 2008] and South America [Resquin et al., 2018] usually feature a marked contribution of long-range transport to measured concentrations of particulate matter within urban basins. For Santiago, an example can be found in the wildfires occurring frequently in summertime in central Chile, explaining sporadic peaks of particulate matter and ozone in the city although the sources are found more in the South [Rubio et al., 2015, de la Barrera et al., 2018, Lapere et al., 2021a]. In this case, pollutants are not directly of anthropogenic origin, which is out of the scope of the present work and therefore ignored throughout this study. Although specific studies revealed the importance of remote sources such as copper smelters [e.g. Gallardo et al., 2002, Hedberg et al., 2005, Moreno et al., 2010] and marine aerosols [e.g. Kavouras et al., 2001, Jorquera and Barraza, 2012, Barraza et al., 2017] in urban pollution in Chile, generally speaking the processes and patterns underlying pollutants transport are not well known, nor is the amount of advected contaminants.

Chile is a narrow band of land bordered by the Pacific ocean on the western side and the Andes cordillera on the eastern side. Air motions are thus influenced by sea-land atmospheric interactions and mountain-valley circulation, in addition to more synoptic patterns. The intensity of these atmospheric regimes, which are partly governed by radiative processes, are modulated seasonally. So do emissions of primary pollutants and photochemical reactions involved in the creation of secondary pollutants [e.g. Gramsch et al., 2006, Barraza et al., 2017]. Moreover, despite a well developed network of air quality monitoring stations across the country, the spatial and temporal density of the data does not allow for a detailed observation-based study of atmospheric pollutants transport. As a result, chemistry-transport modeling offers a solution to cope with this issue and provide insights regarding the magnitude and mechanisms of advection of pollutants at the regional scale.

The present work studies, for one summer month and one winter month in 2015 in central Chile, through chemistry-transport simulations with WRF-CHIMERE, (i) the contribution of pollutants emitted in Santiago to the regional atmospheric composition, (ii) the reciprocal contribution of regional emissions to air pollution in the capital city basin, (iii) the corresponding 3-dimensional advection patterns of particulate matter and ozone. The methodology and data are described in Section 3.1.3, the relative contributions of transport and the underlying advection processes are presented in Section 3.1.4. These results are discussed in Section 3.1.5 and conclusions are gathered in Section 3.1.6.

3.1.3 Data and methods

3.1.3.1 Modeling setup

The chemistry-transport simulations are performed with the Weather Research and Forecasting (WRF) mesoscale numerical weather model from the US National Center for Atmospheric Research [Skamarock et al., 2008] to simulate the meteorological fields, and CHIMERE to compute chemistry and transport [Mailler et al., 2017]. Anthropogenic emissions are based on the EDGAR HTAP V2 inventory [Janssens-Maenhout et al., 2015]. The simulation domain has a 5 km spatial resolution, extending over 200 latitudinal and 100 longitudinal grid points, and is centered on Santiago (white domain CHILE_5K in Figure 3.1a). The parameterizations and model configuration used for WRF are presented in Table 3.1. WRF is applied to 60 vertical levels up to the highest elevation of 50 hPa. Initial and boundary conditions rely on the NCEP FNL analysis data sets, with a 1° by 1° spatial resolution and 6-hour temporal resolution, from the Global Forecast System [NCEP, 2000]. Land-use and orography are extracted from the modified IGBP MODIS 20-category database with 30 sec resolution [Friedl et al., 2010]. CHIMERE is a Eulerian 3-dimensional regional Chemistry-Transport Model, able to reproduce gas-phase chemistry, aerosols formation, transport and deposition. In this work, the 2017 off-line version of CHIMERE is used [Mailler et al., 2017]. The model configuration is described in Table 3.1, with the same horizontal domain as for WRF, applied on 30 vertical levels up to 150 hPa. Emissions from the EDGAR HTAP V2 inventory are downscaled and split in time down to daily/hourly rates following the methodology of Menut et al. [2013]. Biogenic emissions fluxes in CHIMERE are computed online using the MEGAN (Model of Emissions of Gases and Aerosols from Nature) model [Guenther et al., 2006]. Emission fluxes from the vegetation are based on air temperature, photosynthetic photon flux density and leaf area index. As an example, an emission map of isoprene (C_5H_8, a VOC involved in the formation of O_3 and secondary organic aerosols) as computed in CHIMERE for a given day in January 2015 is shown in Figure 3.11, illustrating the meriodional gradient of vegetation cover.

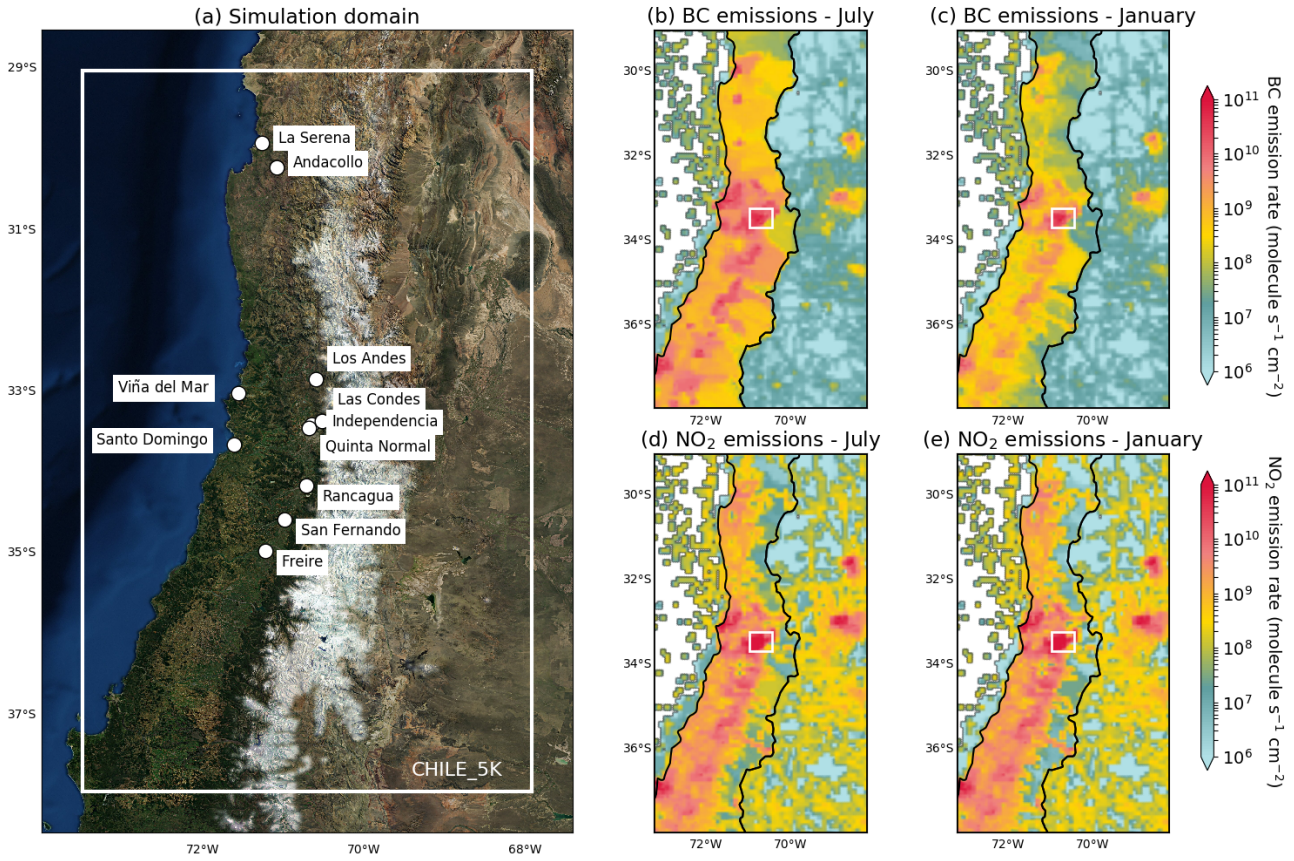

Figure 3.1: (a) Simulation domain at 5 km spatial resolution centered over Santiago. Locations of interest are designated with white dots. Map background layer: Imagery World 2D, ©2009 ESRI, (b) Daily average surface emission rate of black carbon (BC) for July 2015, (c) same as (b) for January 2015, (d) same as (b) for nitrogen dioxide (NO_2), (e) same as (d) for January 2015.

Two different simulation periods are investigated to account for summertime and wintertime differences in atmospheric composition and advection dynamics. "Summertime" hereafter refers to the simulated period 4 January to 3 February 2015. A 20-days spin-up period between 15 December 2014 and 3 January 2015 is used. "Wintertime" refers to the simulated period between 1 July and 31 July 2015. A spin-up period from 15 June to 30 June 2015 is applied. For each of these periods, two simulations are performed. One uses a full emissions inventory including all emissions within the region, referred to as "baseline" henceforth. The baseline simulation for wintertime is named "WB" and the baseline simulation for summertime is denoted "SB". The second simulation corresponds to the case where the city of Santiago would emit no anthropogenic pollutants. In this regard, all anthropogenic emissions within the area corresponding to the white rectangle in Figures 3.1b through 3.1e are set to zero in the simulation referred to as "contribution", hence the designation "WC" and "SC" for the corresponding wintertime and summertime simulations, respectively. The difference in simulated concentrations between baseline and contribution runs shows the proportion of pollutants transported to and exported from Santiago. Aerosol feedback on meteorology is not taken into account here in order to isolate the sensitivity to emission rates only, so that for a given season the same WRF fields are used for both emission cases.

Emissions downscaled from the HTAP V2 inventory and input into CHIMERE are shown in Figures 3.1b through 3.1e. The seasonality of BC emissions is clear, given the major role played by residential heating which takes place mostly in wintertime. Monthly NO_2 emissions are less variable throughout the year, related to the sustained traffic and industrial sources that are nearly constant through time. Figures 3.1b through 3.1e also evidence that Santiago city (represented with a white rectangle) features the highest emission rates for both pollutants and dominates the signal over the simulation domain. In the continuation, given their relevance for the associated seasons, $PM_{2.5}$ in wintertime and O_3 and its precursors in summertime will be considered as the variables of interest, although $PM_{2.5}$ in summertime and O_3 in wintertime can be occasionally discussed. $PM_{2.5}$

include all primary aerosol species (including dust and sea-salt), as well as secondary organic aerosols, but do not incorporate aerosol water.

3.1.3.2 Simulation validation

Surface meteorology and pollutants concentrations are validated using data from the automated air quality and meteorology monitoring network of Chile, known as Sistema de Información Nacional de Calidad del Aire (`https://sinca.mma.gob.cl/index.php/`, last access October 1 2020). Different stations across central Chile are considered depending on data availability for the simulated periods (stations locations can be found in Figure 3.1a). Meteorological vertical profiles in downtown Santiago, for a few days in July 2015, were provided by the Chilean meteorological office, Dirección Meteorológica de Chile.

Simulation scores for surface and vertical profile meteorology are gathered in Tables 3.2 and 3.3. Biases on daily mean temperature range between -1.23 °C and 0.31 °C in wintertime except for the mountainous location of Los Andes where the bias reaches -3.33 °C. In summertime the bias is between 0.07 °C to 0.67 °C. For both periods, correlations on surface temperature vary between 0.7 and 0.89, except for Viña del Mar where it drops to 0.25 in wintertime and 0.18 in summertime, which can be explained by the location of this station near the ocean. The corresponding grid point in the model straddles ocean and land hence featuring a strong gradient, and as a result may not be representative of this coastal city. This remark applies to all meteorological variables at coastal sites. The model shows a negative bias on surface relative humidity with average mean biases of -15% to -20% but shows fair correlations around 0.8 to 0.9. Surface winds are fairly reproduced, with limited biases and wind gusts well captured, although the correlations can be low for some locations. Figures 3.12 and 3.13 compare observed and simulated surface wind distributions for four sites. Summertime shows a good reproduction of wind regimes for all locations, expect for a small positive bias on speeds. In wintertime, winds are more variable and follow less clear patterns, so that the model performance is not as good, especially for the coastal locations of La Serena and Santo Domingo. A positive bias on speed is also observed. Most features of the vertical profiles of temperature, relative humidity and winds are well reproduced, with very good correlations and limited biases for four winter days in downtown Santiago (Tab. 3.3). On the whole, these statistics give confidence in the ability of the model to produce realistic transport events for both seasons.

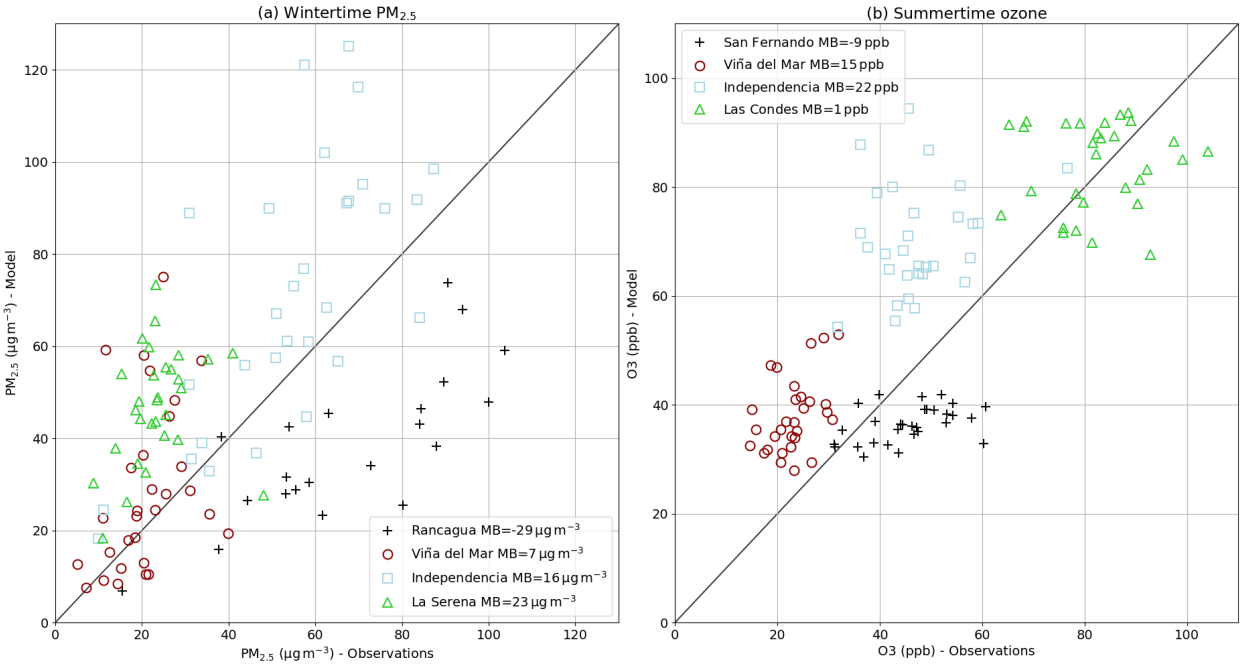

Figure 3.2: Comparison between observation and simulation for (a) wintertime daily average $PM_{2.5}$ concentrations, (b) summertime daily maximum O_3 mixing ratio. Wintertime and summertime correspond to the periods defined in Section 3.1.3.1, respectively. MB is the mean bias.

Figure 3.2 shows a scatter plot of measured and modeled daily mean concentrations of $PM_{2.5}$ in wintertime and daily maximum mixing ratio of O_3 in summertime. For $PM_{2.5}$ the simulation performs better for sites far

inland with correlations of 0.77 and 0.69 for Rancagua and Independencia, respectively. Correlations for the two coastal sites considered (Viña del Mar and La Serena) are more moderate with 0.34 and 0.25, respectively. The same issue of straddling grid points explained previously leads to these degraded statistics: while observations at these sites show a chaotic time series, the model produces a smoother diurnal cycle due to the grid point being partially over the ocean. However for those two sites, biases remain small, while the model systematically underestimates concentrations in Rancagua, and slightly overestimates $PM_{2.5}$ in Santiago (Independencia). For O_3 the picture is similar with a good reproduction of daily peaks in summertime. Despite the relatively coarse resolution of the simulation and strong spatial heterogeneity in precursors emissions, limited biases of a few ppb are obtained on O_3 peaks in summertime, down to only 1 ppb at the most O_3-polluted site of Las Condes (northeastern Santiago). The diurnal cycle of O_3 is also well reproduced with hourly correlations (not shown here) of 0.67 for Viña del Mar and 0.8 to 0.9 for the three other sites. In parallel, summertime NO_x mixing ratios within Santiago city (not shown here) are well captured by the model with mean biases between 0.05 and 1.23 ppb for three stations in Santiago (Las Condes, Puente Alto - southeastern Santiago - and Independencia), associated with decent hourly correlations between 0.43 and 0.59.

The lack of available measurements for NO_x and VOC in central Chile hinders the simulation validation regarding these precursors. However, the HTAP inventory has proved reliable for large urban basins in Argentina and Brazil in terms of magnitude of VOC emissions [Puliafito et al., 2017, Dominutti et al., 2020], and more generally all across southern South America for NO_x [Huneeus et al., 2020]. Consequently, we postulate that emission rates input in the model are appropriate, hence providing adequate chemical regimes when it comes to the simulation of O_3 concentrations. Besides, the known biases of HTAP on these pollutants are critical when it comes to more detailed approaches for policy making but for the purpose of the present work, having the proper total amount is sufficient as we apply our own downscaling methodology, do not discuss very high-resolution processes, and rely mostly on sensitivity analysis.

In conclusion, $PM_{2.5}$ in wintertime and O_3 and its precursors in summertime, the key pollutants for their respective seasons, as well as meteorological conditions, are fairly reproduced by the model for a selection of sites throughout central Chile, which gives confidence in the model outputs that are described and analyzed in the following sections.

3.1.4 Results

Hereafter are described well-known general meteorological features generated by the model, that provide a first clue regarding the advection of polluted air masses in the region, and constitute a reference frame accounting for the results described in the continuation.

The semi-permanent South Pacific High, centered around (30°S, 110°W), along with the elevated Andes cordillera, are two large-scale drivers of the surface wind systems in central Chile. The persistent high induces high velocity southwesterlies blowing along the coast during both daytime and nighttime (Fig. 3.3). These also penetrate deep into land as far as the Andes in summertime during the day, before being blocked by the mountains. On the other side of the Andes, less intensive easterlies coming from Argentina encounter the foothills. Also, the presence of the Andes leads to the development of mountain-valley circulation patterns [e.g. Whiteman, 2000] when the differential heating between narrow valleys and wide plains at the onset and offset of the day lead to the creation of upslope westerlies during daytime (as seen in Fig. 3.3b), and a reversal at nighttime with downslope easterlies (Fig. 3.3d). Although this pattern can be perturbed by clouds or synoptic-scale transient phenomena such as coastal lows, it represents the typical surface wind diurnal cycle for basins along the Andes. From these mean wind fields, the dominant advection pathways of pollutants can be inferred. Polluted air masses are on average blown towards the Andes and the north during daytime in summertime, and have more complex dynamics in wintertime but also transport northward in general. Deeper and more turbulent planetary boundary layer heights during daytime, as observed in summertime (Fig. 3.3a) also enable the vertical export of pollutants up into the free troposphere (FT) where they can be advected farther, while wintertime shallower boundary layers (Fig. 3.3b) imply more stagnation of air masses.

3.1.4.1 Impact of emissions from Santiago on regional atmospheric composition

Wintertime $PM_{2.5}$

Consistently with the mean wind fields and emission rates of pollutants in central Chile discussed previously, anthropogenic emissions in the city of Santiago significantly influence surface atmospheric composition over a large region, over land, the Andes and the Pacific ocean. The following results are based on the analysis of

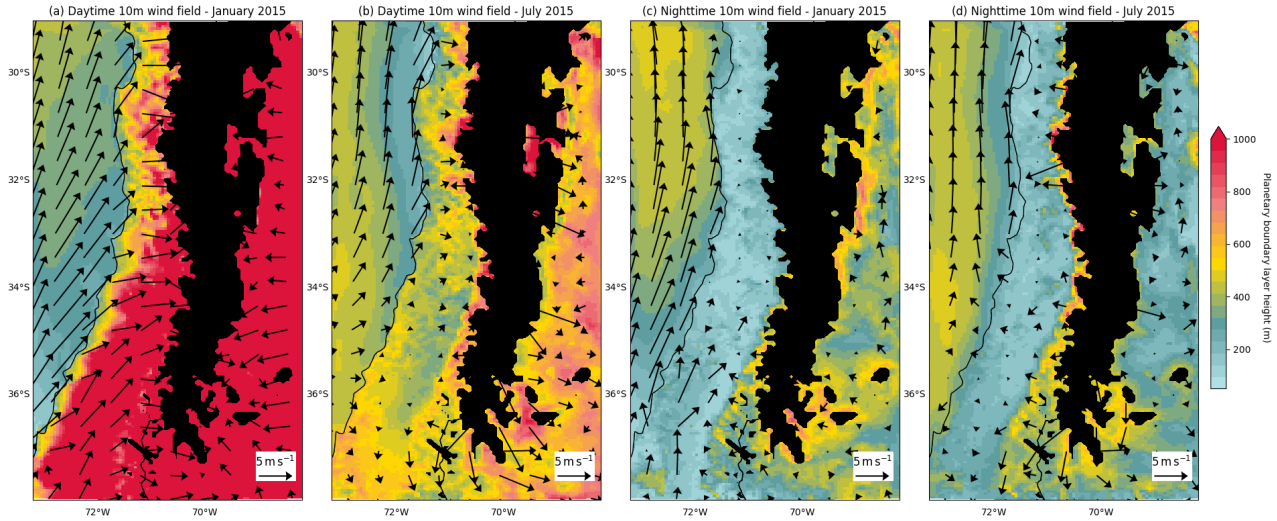

Figure 3.3: Average 10 m wind field (arrows) and planetary boundary layer height (colormap) simulated by WRF (a) during daytime in January 2015, (b) during daytime in July 2015, (c) during nighttime in January 2015, (d) during nighttime in July 2015. Black areas show grid points with elevation in excess of 2000 m a.s.l.

sensitivity to emissions from Santiago described in Section 3.1.3.1: the difference between the simulation with (baseline case) and without (contribution case) emissions from Santiago yields their contribution to atmospheric composition over the domain. Figures 3.4a and 3.4b show the average wintertime $PM_{2.5}$ plume (absolute and relative, respectively) attributable to emissions from the capital city area. The direct western vicinity of the Santiago basin receives, on average $5\,\mu g\,m^{-3}$ to $15\,\mu g\,m^{-3}$ coming from the capital city, a few tens of kilometers from the source, corresponding to more than 30% of the signal simulated in the baseline scenario for this area. At the scale of hundreds of kilometers, the export drops to a few $\mu g\,m^{-3}$, corresponding to 5% to 20%. It is worth noting that the relative contribution of emissions from Santiago remains greater than 5% on a area as large as more than 8° meridionally and 3° zonally, hence stressing the significant impact of the capital city on atmospheric composition for the whole region (Fig. 3.4b). In particular, the southern part of the plume is transported over the Andes down to Argentina with a large spread of several degrees of longitude, whereas the northern part extends mostly along the coast in a narrower manner and transports as far as the boundary of the simulation domain.

More specifically, urban areas along the north-south axis of Santiago (Curicó, San Fernando, Rancagua and Los Andes in Fig. 3.4a) receive $1\,\mu g\,m^{-3}$ to $2\,\mu g\,m^{-3}$ from Santiago on a hourly basis on average, corresponding to 4% to 8% of the baseline concentrations (Fig. 3.4c). Sporadically, up to more than $20\,\mu g\,m^{-3}$ in Rancagua and $9\,\mu g\,m^{-3}$ in San Fernando, Curicó and Los Andes can be attributed to emissions from Santiago. These significant contributions likely lead to alert thresholds crossing for some hours in these cities.

On the eastern side of the Santiago basin is the Andes cordillera. We examine the contribution of Santiago emissions in a mountain locality (San Gabriel, 1250 m a.s.l.) and a summit (Maipo volcano, 5264 m a.s.l.) along the Maipo canyon, southeast of Santiago. We find that for San Gabriel 34% ($1\,\mu g\,m^{-3}$) of $PM_{2.5}$, on average, is transported from the urban basin. This is consistent with the mountain-valley circulation patterns aforementioned, leading to the intrusion of urban air masses deep into the canyon [Lapere et al., 2021b]. We acknowledge that the estimate of 34% is probably larger than reality since the HTAP inventory does not capture properly local emissions in the village of San Gabriel, which likely dominate the signal, especially with wood burning for residential heating being largely used in such villages in wintertime. In the Maipo volcano area, a small contribution in absolute value is found (less than $0.5\,\mu g\,m^{-3}$) although it can reach up to more than $2\,\mu g\,m^{-3}$ occasionally, but this corresponds to 20% of the signal there on average. This area is covered in snow during wintertime, so that despite the small magnitude of the import of $PM_{2.5}$ it can lead to significant radiative effects when deposited [Rowe et al., 2019], especially given the large fraction of BC in $PM_{2.5}$ emitted in Santiago, around 15% according to the HTAP emissions inventory.

The Viña del Mar-Valparaíso area is the second largest populated region of Chile, located on the coast of central Chile, approximately 100 km west of Santiago. In wintertime, it is downwind of Santiago, which leads to an average import of particulate matter from the capital city of $3\,\mu g\,m^{-3}$ (18%) and sporadically up to $18\,\mu g\,m^{-3}$.

Again, air quality in this urban area is worsened by export from Santiago, by a significant share. Further north, at the location of La Serena, which also suffers from bad air quality in wintertime, the contribution of Santiago emissions is more moderate but still remains significant in absolute value although its contribution is only 1%.

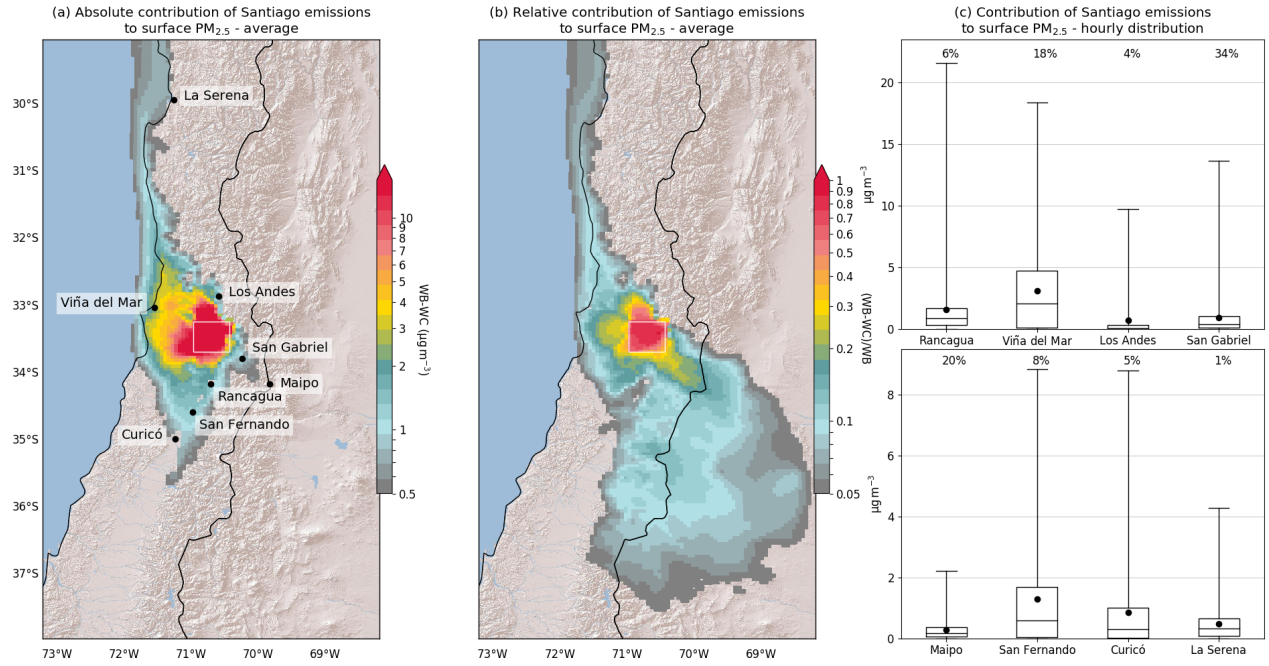

Figure 3.4: (a) Average ground-level $PM_{2.5}$ concentration difference between WB (winter baseline case) and WC (winter contribution case) yielding the Santiago emissions contribution. Concentrations in excess of 0.5 µg m^{-3} are displayed. White rectangle shows the area where emissions are set to zero in WC. Map background layer: World Shaded Relief, ©2009 ESRI, (b) same as (a) in relative contribution i.e. (WB-WC)/WB. Contributions in excess of 5% are displayed. (c) Distribution of Santiago emissions contribution to hourly $PM_{2.5}$ concentration at several sites across central Chile - horizontal lines are quartiles, whiskers show minimum and maximum, dots are the means. All figures are based on hourly concentrations and are for wintertime 2015. In panels (a) and (b) only grid points where the distribution of concentrations in scenario WC is different than in scenario WB at the 90% level, based on a t-test, are shown.

Summertime O_3

In summertime, except for $PM_{2.5}$ emitted by biomass burning events (not considered here), O_3 is the pollutant raising concern. Combined significant emissions of NO_x and VOC are required, in the presence of sunlight, to generate high mixing ratios of O_3. However, a lot of non-linearities are involved in the tropospheric O_3 cycle, so that the sensitivity to its precursors emissions is not straightforward. For instance, imbalances in the ratio of NO_x and VOC decrease O_3 formation. Given the crucial role of photolysis in O_3 formation, it features a strong diurnal cycle, with levels coming back to low values at night. Thus, the important variable to determine whether O_3 pollution is high is its daily maximum mixing ratio, on which we will mostly focus hereafter.

Figure 3.5a shows the average of maximum hourly O_3 mixing ratio at ground-level observed each day in the baseline case (SB). In the baseline scenario, O_3 is mostly found at harmful levels in the vicinity of Santiago, and mainly on its eastern side. Again, mountain-valley circulation accounts for this observation: afternoon westerlies blow O_3 precursors, present in large amounts in urban air masses, towards the Andes. NO_x lifetime is a few hours at most, depending on the reactivity of VOC and NO_2 density [e.g. Laughner and Cohen, 2019], while most VOC have an atmospheric lifetime of several days [e.g. Monod et al., 2001], so that on the way, NO_x are more consumed than VOC. Consequently, while urban air is mostly a NO_x-rich environment, precursors ratios become more balanced along with the export so as to create more favorable conditions for O_3 formation once reaching less urbanized areas. Such a mechanism is observed for Paris and its suburbs for instance [e.g. Menut et al., 2000]. Export by easterlies occur less frequently and mostly at night when O_3 cannot be created due to lack of sunlight, which is why the rural area west of Santiago shows smaller O_3 maxima. This mechanism explains the large concentrations of O_3 mostly found east of Santiago. Except for the center part of the domain

where average daily maxima reach more than 100 ppb, O_3 pollution is less concerning elsewhere in central Chile where they range between 10 ppb and 35 ppb.

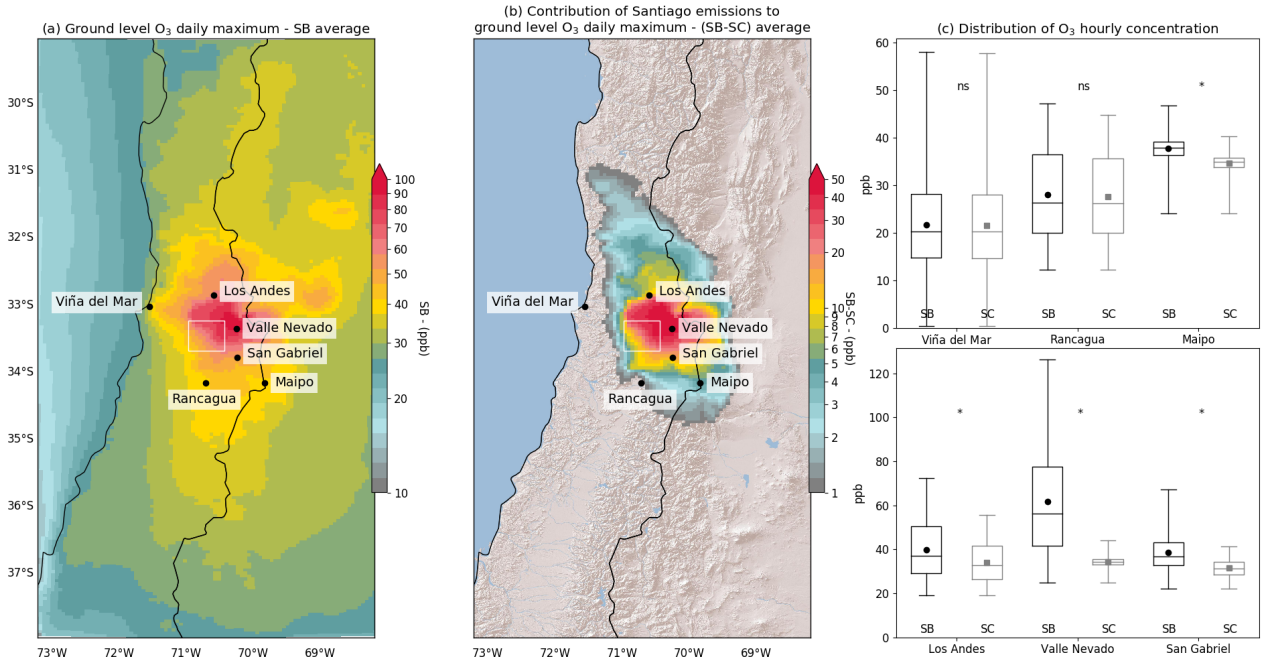

Figure 3.5: (a) Ground-level O_3 average daily maximum of hourly mixing ratio in scenario SB, (b) Difference between SB and SC in ground-level O_3 average daily maximum of hourly mixing ratio. Map background layer: World Shaded Relief, ©2009 ESRI, (c) Distribution of hourly O_3 mixing ratio at six locations in scenario SB (black) and SC (gray) - horizontal lines are quartiles, whiskers show minimum and maximum, dots show the average. "ns" indicates that the distribution in the SB and SC scenarios cannot be distinguished at the 90% level based on a t-test. "*" indicates that they are different at the 99% level based on that same t-test.

Figure 3.5b shows the decrease in O_3 daily maxima induced by eliminating emissions of the Santiago basin. The spatial pattern is again consistent with the mechanism introduced previously: emissions of precursors from Santiago are the main origin for O_3 formation in the Andes and north of the city, with a reduction of more than 50 ppb of the daily maxima over this area when the capital city no longer emits pollutants.

More specifically, the northern city of Los Andes shows a decrease of its daily maxima by 15 ppb on average (Fig. 3.5b) while the average mixing ratio drops from 40 pbb to 33 ppb (Fig. 3.5c). Similarly, at the ski resort site of Valle Nevado (3000 m a.s.l.), which shows concerning levels of more than 60 ppb of O_3 on average in the baseline case, the mixing ratio drops to an almost constant value of 33 pbb and does not go above 43 ppb. This points to O_3 in Valle Nevado being almost exclusively attributable to Santiago emissions. To a lesser extent, the location of San Gabriel shows the same trend although the still wide distribution in scenario SC advocates for a significant contribution of local sources as well. The impact of Santiago emissions in the vicinity of the Maipo summit is small but remains significant with a decrease by 4 ppb of the daily maxima and average mixing ratios. Given the nature of the locations Valle Nevado and Maipo, the narrow distribution of O_3 hourly mixing ratio, averaging at 33 ppb and ranging between 25 ppb and 40 ppb, recovered in scenario SC for those sites is indicative of the background concentration for the region, i.e. the distribution of O_3 mixing ratio that would be observed at a site not influenced by anthropogenic emissions.

On the other hand, the western and southern areas adjacent to Santiago are barely sensitive to its emissions. In Figure 3.5c, the distribution of hourly O_3 mixing ratio at Viña del Mar and Rancagua is nearly the same in both scenarios, except for the maximum at Rancagua which is a few ppb lesser in scenario SC than SB. For those two locations, the difference in O_3 distribution with or without Santiago emissions is not significant at the 90% level, while for all other locations, distributions are significantly different at the 99% level.

3.1.4.2 Contribution of regional emissions to atmospheric composition in Santiago

Similarly to the previous approach, we can, in a symmetric manner, deduce the contribution of transport from remote sources to atmospheric composition in Santiago city. This is achieved by looking at concentrations in the contribution case, that exclusively originate from non-local sources. Hereafter the analysis focuses again on $PM_{2.5}$ in wintertime and O_3 in summertime.

Wintertime $PM_{2.5}$

Figure 3.4b indicated that local emissions largely dominate the wintertime $PM_{2.5}$ signal for Santiago, with 50% to 100% of the mean surface concentration of $PM_{2.5}$ originating locally within the white rectangle. Nevertheless, the contribution of transport is also significant although heterogeneous in Santiago. Figure 3.6a shows that in the baseline scenario, the northern and western parts of Santiago feature higher levels of $PM_{2.5}$, with average concentrations ranging between $30\,\mu g\,m^{-3}$ and $100\,\mu g\,m^{-3}$ for the whole metropolis. In the contribution scenario (Fig. 3.6b), this pattern is partly recovered, with a smoother gradient from west to east. The underlying conclusion is twofold. First, the transport of pollutants in Santiago mostly comes from the west, which is consistent with the presence of the mountain range in the east not featuring many sources of pollution, and the dominant westerly daytime wind direction in wintertime. Second, the districts of Santiago facing the worst air quality are also the ones where the transport of pollutants is larger.

However, the differing patterns between Fig. 3.6a and 3.6b also shows that local sources in these districts are also stronger. If emissions were similar, the observed gradient in WB would be closer to that in WC. Consistently with this observed westward gradient, we define 5 zones of interest, comprising 6 grid points each along a meridional axis (rectangles and dots in Fig. 3.6b). This arrangement ensures that most of the city is covered while maintaining the west-east variability. For each zone we look at the distribution of $PM_{2.5}$, averaged over the 6 grid points, in scenarios WB and WB-WC (Fig. 3.6c) and WC (Fig. 3.6d). When averaged meridionally, the westward gradient is also obtained in scenario WB, and conserved when the contribution of transport is substracted (WB versus (WB-WC) in Fig. 3.6c). On average, the contribution of transport to $PM_{2.5}$ concentration ranges between $10\,\mu g\,m^{-3}$ for the westernmost area and $5\,\mu g\,m^{-3}$ for the easternmost part, with a monotonic spatial variation (Fig. 3.6d). However, this amount always corresponds to 13% to 15% of the WB concentrations. This number is well in line with Barraza et al. [2017] that found 9% of $PM_{2.5}$ in Santiago coming from coastal sources, for the period 2011-2012. It is worth noting that given the observed westward gradient, we also recover that coastal sources are likely the main contributor to imported $PM_{2.5}$. Again, transport is larger in western Santiago, and can sporadically reach up to $30\,\mu g\,m^{-3}$, but does not constitute a greater share than in the east.

This averaged picture provides a first clue as to the main origin of $PM_{2.5}$ transport of Santiago but the picture can be refined by looking at the joint distribution of hourly wind direction and $PM_{2.5}$ concentrations as shown in Fig. 3.7. At the selected southeastern location, mostly clean air comes from the east, i.e. from the Andes where pollutants sources are scarce (less than $5\,\mu g\,m^{-3}$ for almost every hour), while winds blowing from the southwest can transport concentrations as high as more than $20\,\mu g\,m^{-3}$ for some hours, pointing to the southern cities of Rancagua (34.2°S, 70.7°W) or San Fernando (34.6°S, 71°W) mentioned previously, or the southwestern urban location of Melipilla (33.6°S, 71.2°W). At the northeastern site, winds mainly come from the north where only a handful of urban areas are found, hence leading to a transport seldom exceeding $10\,\mu g\,m^{-3}$. In the center of the metropolis, winds are either southwesterlies (from the Rancagua and Melipilla areas) or northwesterlies (from the Viña del Mar-Valparaíso area), with both cases leading to similar amounts of imported $PM_{2.5}$ mostly above $10\,\mu g\,m^{-3}$, i.e. above average. The picture is similar for the northwestern and southwestern sites although wind directions are shifted.

In the northwest, center and northeast, the dominant wind directions also coincide with higher maximum relative contributions of transport over the period along these directions (black diamonds in Fig. 3.7). Sporadically, significant transport events can also come from less frequently observed directions. The maximum relative contribution obtained for the northwest point when winds are from NNE is 75% for example, while such winds occur less than 1% of the time. For southwest and southeast locations, these maximum relative transport episodes are observed when winds blow from the south, in particular in the southeast where it can reach up to 100%.

In summary, wintertime $PM_{2.5}$ concentrations in Santiago are significantly ($5\,\mu g\,m^{-3}$ to $10\,\mu g\,m^{-3}$ on average) and always (at least $1\,\mu g\,m^{-3}$ for every hour) affected by transport, with identifiable origins, and although the different districts are not equally affected in absolute value, the relative burden of imported particulate matter is equivalent.

Summertime O_3

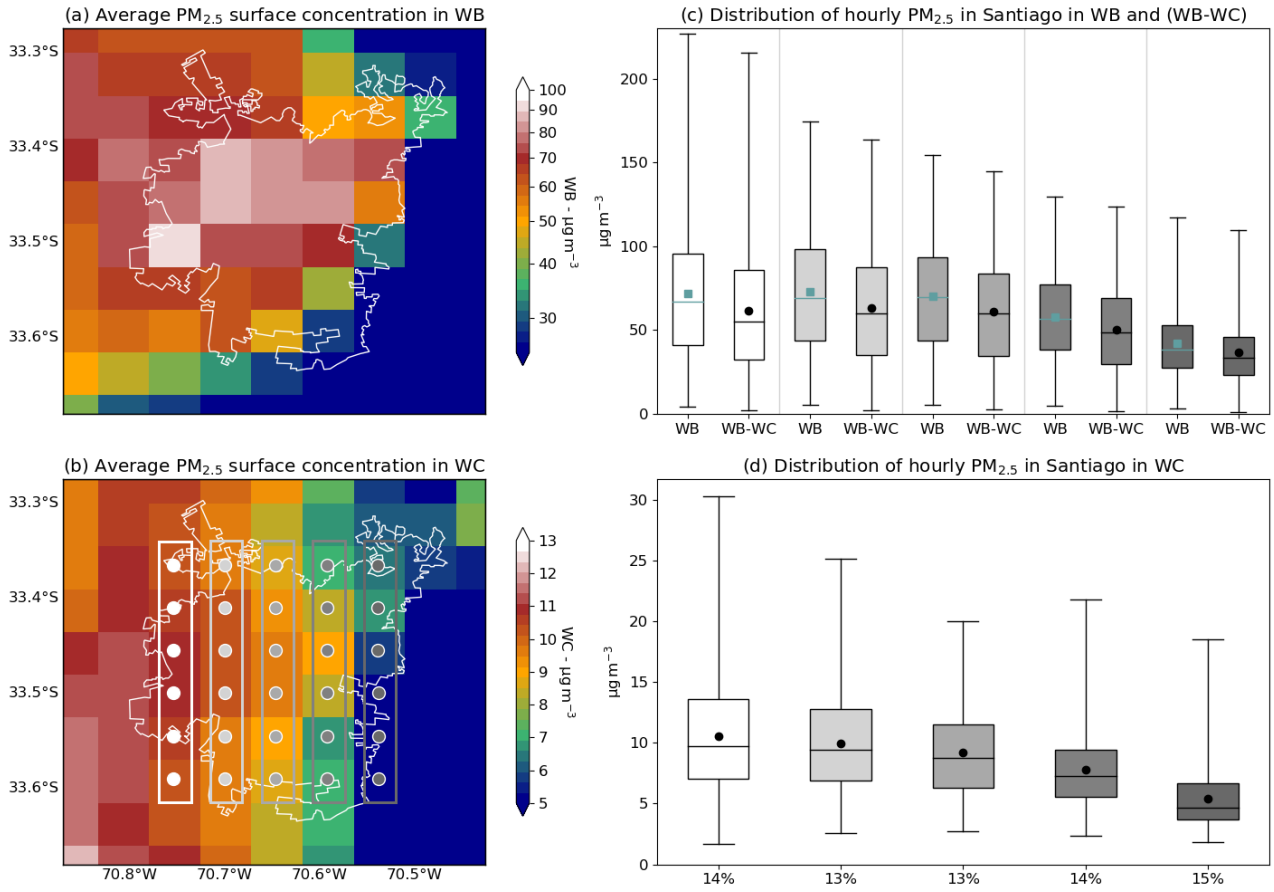

Figure 3.6: (a) Average ground-level $PM_{2.5}$ concentration in scenario WB. White contour shows the boundaries of Santiago city. (b) same as (a) for scenario WC, (c) Distribution of hourly $PM_{2.5}$ surface concentration in WB and (WB-WC). Boxes show the average, median, minimum, maximum, first and third quartiles. Shades of gray correspond to the zones defined in (b) on which an average is made, (d) same as (c) for scenario WC. Percentages indicate the relative average contribution of transport.

Based on the same approach, we find that the summertime transport of NO_x within the Santiago basin never exceeds 0.5 ppb, while average values in the SB scenario are between 5 ppb and 40 ppb, with a similar westward gradient as observed for $PM_{2.5}$ (not shown here). At the 90% level, NO_x transport is thus not significant. Similarly, the transport of VOC is homogeneous over the whole basin at 2 ppb on average, while between 20 ppb and 60 ppb in the SB scenario, which is again not significant at the 90% level. Santiago is thus not affected by the transport of O_3 precursors.

However, the picture within Santiago city in SB and SC scenarios is complex. In the baseline scenario, the eastern area of Santiago is more affected by O_3 pollution compared to the western area (Fig. 3.8a and 3.8c), consistently with observations and the literature [e.g. Menares et al., 2020], due to a more balanced VOC/NO_x ratio than in the western area. At Independencia (center of Santiago), the VOC/NO_x ratio at emission is between 1:1 and 2:1 on average. Contrarily, at Las Condes (eastern Santiago) the VOC/NO_x ratio at emission is around 6:1 on average, in the baseline case (not shown here). A typical O_3 formation ridge line of the VOC/NO_x concentration ratio in urban areas is around 6:1 to 8:1 [e.g. National Research Council, 1991, Sillman, 1999], so that Independencia features a VOC-limited regime, while Las Condes features a balanced regime favorable to O_3 formation, hence the larger amounts found at the latter location.

Figure 3.8b shows the consequences, on O_3 surface mixing ratio, of eliminating emissions within Santiago. Given the configuration described previously, in the baseline case, the VOC-limited districts of western Santiago feature mixing ratios well below the background level due to the titration of O_3 by excess quantities of NO_x, while the eastern districts feature mixing ratios above the atmospheric background level due to excess O_3 formation under a favorable regime. As a result of shutting off emissions, given that there is no import of precursors as evidenced above, the whole area is set to the background O_3 level of around 30 ppb described in Section 3.1.4.1,

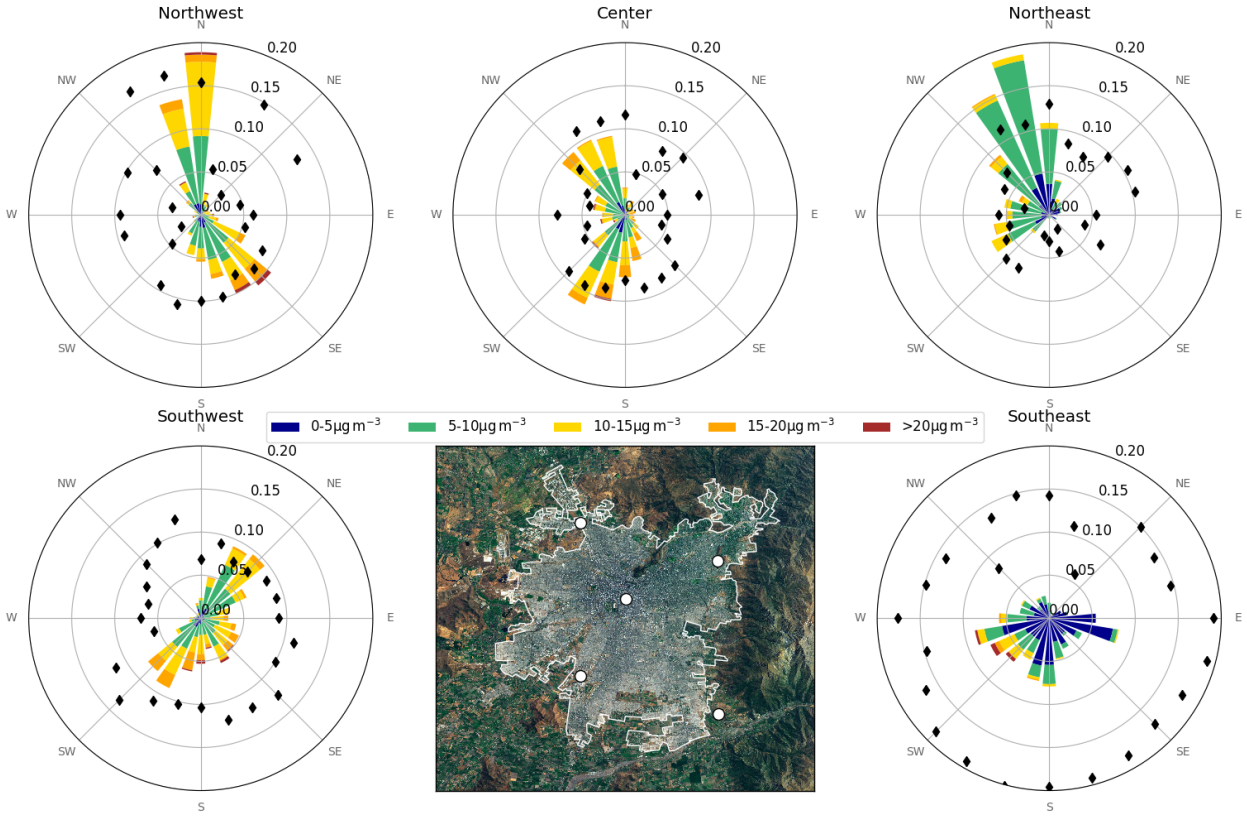

Figure 3.7: Joint distribution of hourly wind direction (length of bar gives the frequency of the corresponding wind direction) and $PM_{2.5}$ concentration (colormap) in scenario WC for 5 locations in Santiago. Black diamonds show the maximum relative contribution of transport (i.e. WC/WB) for each wind direction bin (NB: the scale is the wind frequency scale multiplied by 5, i.e. 0.20 is actually 1.0). The bottom center map shows the location of the considered grid points. Map background layer: Imagery World 2D, ©2009 ESRI.

since there is no influence of anthropogenic pollutants anymore. Therefore, this corresponds to an increase of O_3 in western Santiago and a decrease of O_3 in eastern Santiago, thus explaining the dipole obtained in Figure 3.8b. Such an evolution is also clear in the evolution of the distribution of hourly O_3 mixing ratios across the city between scenario SB and SC (Fig. 3.8c). While in scenario SB the distribution is shifted towards larger mixing ratios when going eastward, in scenario SC all distributions are equal (significant at the 99% level). The leveling of mixing ratios, with no gradient across the city in scenario SC constitutes an additional evidence that O_3 in Santiago is not affected by long-range transport, otherwise heterogeneous patterns similar to what is observed in Figure 3.6b would be obtained.

3.1.4.3 Advection processes

As discussed around Figure 3.3 and observed in Figure 3.4 and Figure 3.5, advection patterns of pollutants differ between wintertime and summertime. So far, the analyses focused on surface fields, but processes along the vertical drive these differences. Figure 3.9 shows an average latitude/altitude transect, along central Chile, of winds, afternoon mixing layer height and pollutants concentrations for the corresponding season, in the baseline scenario and the Santiago isolated contribution case.

In wintertime (Fig. 3.9b and 3.9c), the boundary layer (solid white line) is shallow, and average winds in the FT are strong, consistently with the observed semi-permanent inversion layer in the region. As a result, the $PM_{2.5}$ emitted in large amounts mostly remain trapped within this shallow mixing layer. Injection of polluted air masses into the lower FT can also occur, through mountain venting, as described in Lapere et al. [2021b], explaining why residual concentrations of 1 to 5 $\mu g\,m^{-3}$ are observed higher up in the baseline and contribution scenarios at the latitude of Santiago (Fig. 3.9b and 3.9c). Nevertheless, the long-range export of $PM_{2.5}$ from Santiago observed in Figure 3.4 is mainly driven by advection within the boundary layer, close to the ground, by

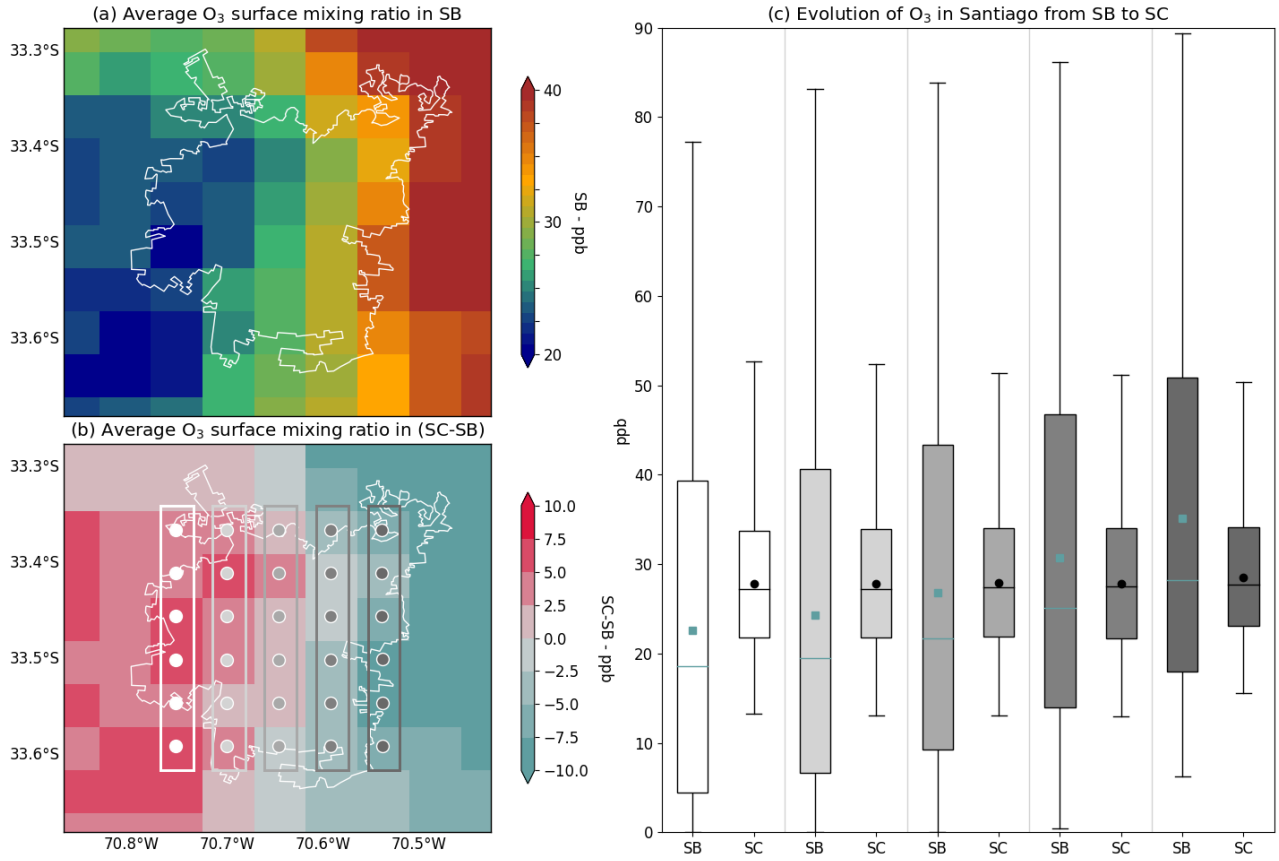

Figure 3.8: (a) Average O_3 mixing ratio at ground level in scenario SB in Santiago, (b) same as (a) for scenario (SC-SB), (c) Distribution of hourly O_3 surface mixing ratio in scenario SB and SC. Boxes show the average, median, minimum, maximum, first and third quartiles. Shades of gray correspond to the zones defined in (b) on which an average is made.

weak winds, as evidenced by Figure 3.9c. Except for a shallow residual layer located above the average afternoon boundary layer, pollutants emitted from Santiago remain within it along the transect from Santiago to Viña del Mar. The pattern changes when reaching the seashore however, with significant wind shears lifting the $PM_{2.5}$ layer above the mixing layer (rightmost part in Fig. 3.9c) thus explaining the wide northward extent of Santiago contribution, due to transport higher up, by intense southerlies.

In this wintertime averaged picture, the patterns underlying the largest transport events are not obvious. In order to identify these advection patterns, four clusters are designed corresponding to episodes of transport from Santiago to the south (Rancagua), from Santiago to the northwest (Viña del Mar), into Santiago from the south, and into Santiago from the northwest. In the case of transport into Santiago, passive aerosol tracers emitted in the model at the locations corresponding to Rancagua and Viña del Mar are used to discriminate the main direction of origin. The composite of these episodes is defined as the hours when the $PM_{2.5}$ (or tracer) contribution to concentration is greater or equal to its 90^{th} percentile over the studied period. The meteorological conditions during these particular hours are then compared to the average for the whole period, in order to compute anomalies in the surface wind and pressure fields. Figure 3.14 shows that southward transport events are associated with lower than average surface pressure by 1 to 3 hPa and large northerly anomalies over most of the wind field, and in particular in the corridor between Santiago and Rancagua. Conversely, northwestward export is associated with positive anomalies in surface pressure and southerly anomaly in surface winds combined with easterly anomaly in the corridor between Santiago and Viña del Mar. The two aforementioned corridors are evidenced by the topographic contours in Figure 3.14. These variations are related to the dynamics of the southeast Pacific high, located near (35°S, 110°W): a weakening or southward/westward displacement of the anticyclone lead to the anomalies observed in Figure 3.14a, while an opposite displacement leads to a situation similar to that of Figure 3.14b. Consistently, transport events into Santiago are related to symmetrical patterns (not shown here), with transport from the northwest featuring similar anomalies as in Figure 3.14a and transport

from the south originating in the same anomalies as in Figure 3.14b.

Interestingly, the summertime transect of O_3 shows a sharp maximum near the latitude of Santiago, several hundred meters above the ground. Figure 3.9d shows the formation of an O_3 bubble of more than 50 ppb on average, i.e. 15 ppb above the 35 ppb background mixing ratio observed in scenario SB (dominant yellow/green levels in altitude in Figure 3.9d), around latitude 33°S i.e. slightly north of Santiago, above the planetary boundary layer, extending between 1.5 km and 3 km altitudes. This additional O_3 plume is mostly attributable to emissions of precursors in Santiago, that account for more than 15 ppb of O_3 on average at the location of the bubble (Fig. 3.9e), i.e. the background level exceedance. Thus, despite a relatively limited area where precursors from Santiago affect O_3 formation near the ground (Fig. 3.5b), their impact on the vertical is more dramatic. The process underlying the formation of this significant O_3 bubble clearly departing from the background, is discussed hereafter. It is also worth noting that even though export of O_3 close to the surface is limited (Fig. 3.5b), it is more widespread higher up, with a residual layer originating from Santiago emissions of a few ppb extending 2 km vertically and transporting northward in the FT along 2° of latitude (Fig. 3.9e).

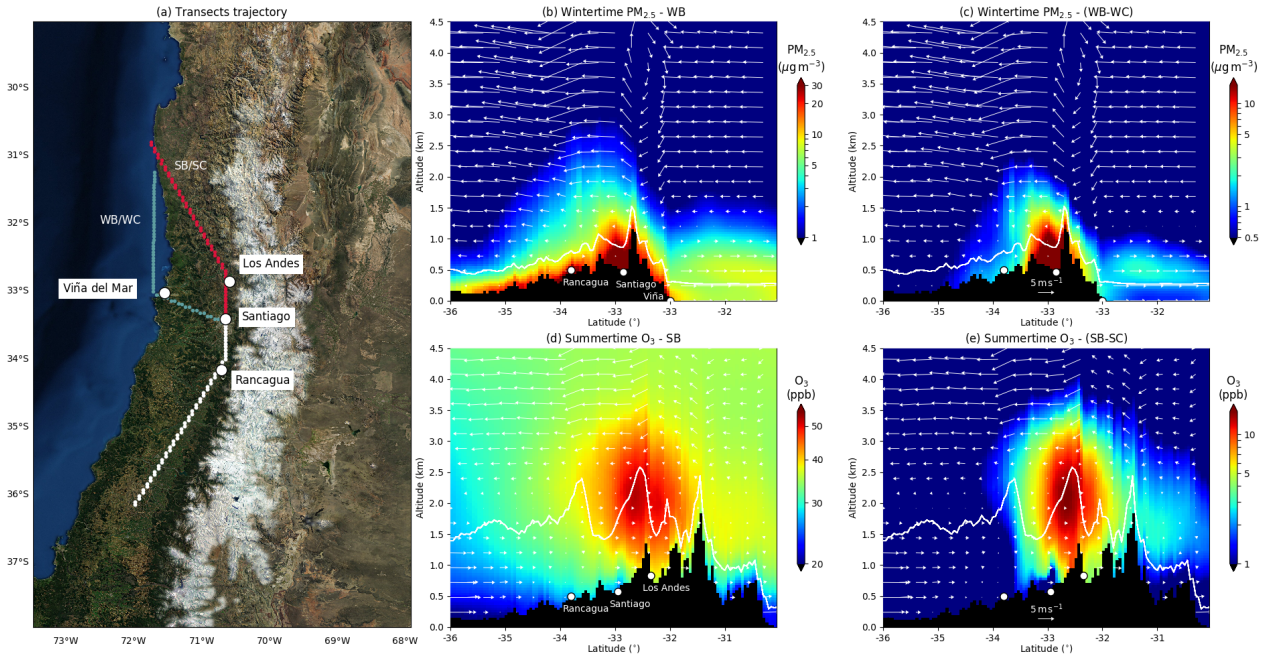

Figure 3.9: (a) Trajectory of the considered latitude/altitude transects and main locations along the way. White dotted line up to Santiago is common for both seasons, blue dotted line is for wintertime, red dotted line for summertime. Values in the transects are not zonally averaged, they correspond to the grid points represented with dots. Map background layer: Imagery World 2D, ©2009 ESRI, (b) Simulated $PM_{2.5}$ concentrations (colormap), wind (white arrows), afternoon boundary layer (white solid line) and terrain elevation (black area), along the white/blue transect. Average for wintertime 2015 - WB scenario. (c) same as (b) for scenario (WB-WC), (d) Simulated O_3 mixing ratios (colormap), wind (white arrows), afternoon boundary layer (white solid line) and terrain elevation (black area), along the white/red transect. Average for summertime 2015 - SB scenario. (e) same as (d) for scenario (SB-SC).

Given the proximity of the Andes cordillera to the Santiago basin, the formation of the aforementioned O_3 bubble finds its origin in the mountain-valley circulation and the associated mountain venting mechanism. Daytime upslope winds, strong in summertime, lift polluted air masses from the atmospheric boundary layer (ABL) over Santiago into the lower FT, possibly above another location depending on the FT winds direction. McKendry and Lundgren [2000] and Lu and Turco [1996] find that this process is a net sink for boundary layer O_3 in British Columbia and the Los Angeles basin, respectively. Henne et al. [2005] find that the effect of venting in an Alpine environment on FT O_3 concentrations strongly depends on initial mixing ratios within the vented ABL, with either net production if ABL mixing ratios of O_3 are high (urban valleys), or net loss if they are low (remote valleys). However, our study case falls into none of the aforementioned. Such a bubble of O_3, detached from the ground, with a mixing ratio much higher than at ground level is not found in the literature to our knowledge. More moderate injections, with O_3 mixing ratios lower to similar to surface levels are usually

observed. In our case, we find that the venting of precursors from the Santiago polluted ABL leads to the net production of large quantities of O_3 in the FT, larger than at the surface. Schematically, there is a larger export of VOC than NO_x in the FT (Fig. 3.15a and 3.15b) which makes for a balanced chemical regime (below 0.5 is NO_x-limited, above 0.5 is NO_x-rich) at around 0.5 at 2 km altitude, while the regime is close to 1 near the surface hence unfavorable to O_3 production, along the whole transect, due to dominant urban NO_x emissions (Fig. 3.15c). Also, the export of Peroxyacetyl nitrate (PAN), which is a NO_x carrier, into the FT, contributes to enhanced O_3 formation (Fig. 3.15d).

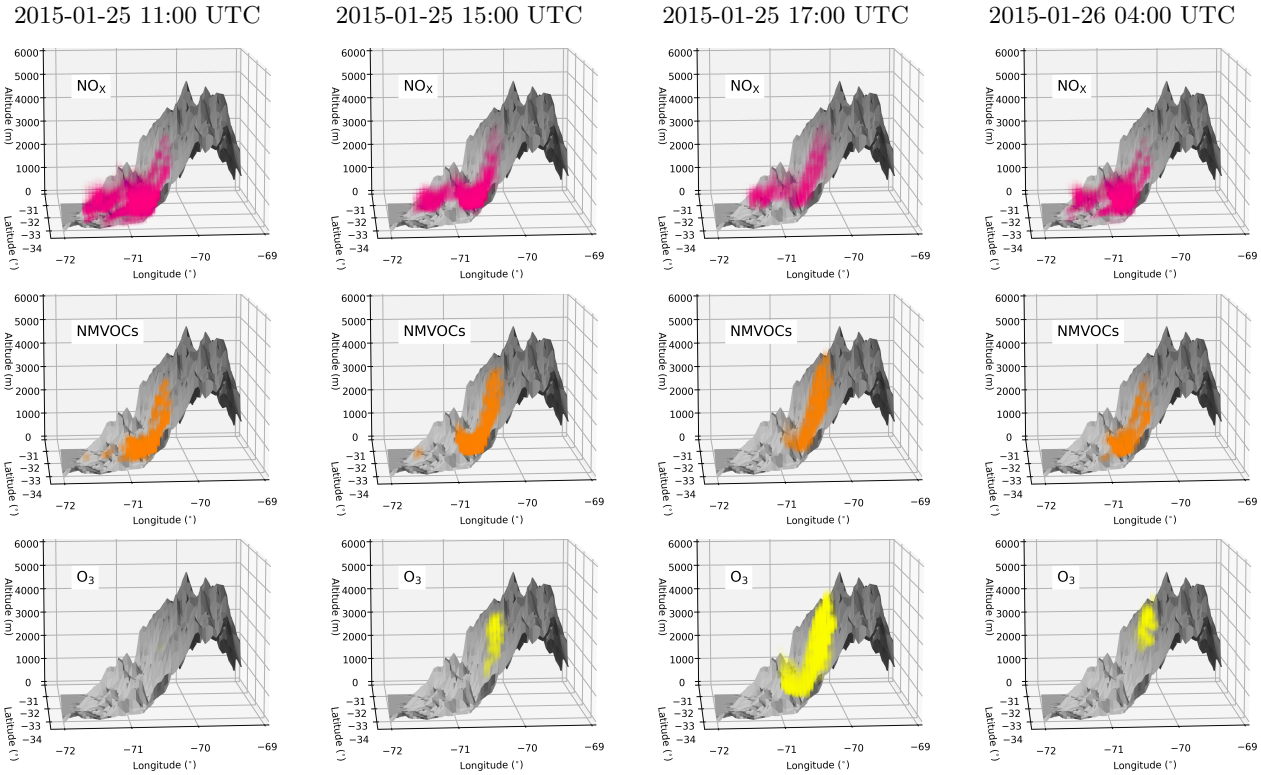

Figure 3.10: Cycle of NO_x (top), NMVOC (middle) and O_3 (bottom) venting in the vicinity of Santiago for a typical day in January 2015. Hourly mixing ratios in excess of 2 ppb, 20 ppb and 60 ppb are shown, respectively. Each panel shows a 3-dimensional view from a longitudinal perspective. Gray surfaces represent the terrain topography. Santiago is UTC-3 for this period.

Figure 3.10 further sheds light on the dynamics of this mechanism. Early in the day, at 11:00 UTC (Chile is UTC-3 in summertime), both NO_x and NMVOC (non-methane VOC) are highly concentrated near the ground (morning peak of emissions from traffic), and start ascending the Andean foothills, but no O_3 is formed in the region given that sunlight is not intense yet (leftmost column in Fig. 3.10). A few hours later, at 12:00 LT (15:00 UTC), the precursors have a similar distribution as in early morning, but the photolysis starts taking place and O_3 is created at the top of the precursors plume, well above the ground.

Two factors explain that O_3 is not formed near the source of precursors. First, given the urban environment of the basin, NO_x are emitted in large quantities so that the VOC/NO_x ratio is adverse to neutral, and O_3 is formed in small amounts (see the related discussion in Sect. 3.1.4.2). But NO_x have a lifetime much shorter than most VOC [e.g. Monod et al., 2001, Laughner and Cohen, 2019], and when the polluted air parcels are lifted up, the ratio becomes more balanced as NO_x is consumed closer to the ground. Due to these asymmetric lifetimes and hence export, at some point on the vertical the ratio becomes favorable (Fig. 3.15c) and O_3 is formed in large quantities. The second factor comes from the increase of photolysis rates with altitude. Several hundred meters above the ground, near or above the mixing layer, photolysis rates of NO_2 are much faster than at ground level [e.g. Pfister et al., 2000] hence favoring the formation of O_3, all other things being equal. In our simulation, on average, the photolysis of NO_2 is 20% faster 1000 m above ground than at the surface. Also, Figure 3.9d shows that at the point where the O_3 plume is denser, winds are weak to null on average, so that precursors stagnate, again allowing for more O_3 creation.

At 14:00 LT (17:00 UTC), the vertical export of precursors is even more important due to the maximum development of the deep mixing layer and the full intensity of upslope winds, with two main consequences. First, NO_x levels in Santiago decrease compared to VOC due to vertical export earlier in the day, leading to a more favorable ratio and O_3 starts forming in the urban basin near the surface. Thus, ventilation of precursors possibly increases O_3 surface concentration in Santiago. Second, the O_3 plume in the lower FT intensifies and extends up to an altitude of 4 km. Finally, at 01:00 LT (04:00 UTC) the next day, the return of a shallower mixing layer and the accumulation of evening traffic emissions make precursors concentrations larger near the ground again. Sun being down, O_3 stops forming, but given the large amounts created during the day, a residual plume remains around 1 km above ground. In parallel, winds along the transect being mostly southerlies, the O_3 plume ends up approximately 50 km north of the Santiago basin.

3.1.5 Discussion

Figure 3.2 revealed moderate biases in the modeled concentrations of $PM_{2.5}$ and O_3 compared to downtown Santiago observations. These discrepancies can stem from (i) the relatively coarse resolution of the simulation compared to the heterogeneity of pollution at the scale of Santiago city, (ii) the static nature of the emissions inventory as of 2010 while air pollution follows a decreasing trend in Santiago hence accounting for the overestimation of primary emissions by the model, (iii) a slight negative bias in the representation of mixing layer height in the simulation contributing to over-concentrate particulate matter. In practice, a combination of the three is likely at play. Although the processes of transport evidenced in this study are not sensitive to such biases, quantitative conclusions can depend on them to some extent. In particular, if case (ii) dominates the discrepancy on $PM_{2.5}$, biases in emissions can be asymmetric between Santiago and other locations given that the trends since 2010 are probably not identical (the model in Rancagua is negatively biased for example). In that case, an overestimation of the relative contribution of Santiago emissions at these locations could be found. If the bias mostly comes from reason (i) or (iii), the quantification should be resilient: the Santiago source is considered at a larger-scale than downtown so that local discrepancies should compensate over the whole area (case (i)), and in case (iii) the bias should concern most locations, and does not have an influence on emissions, and therefore should not modify relative contributions. Regarding the biases on O_3 mixing ratio, case (i) is most likely to be the underlying bias, as levels are better reproduced in the eastern part of Santiago (Las Condes) thus pointing to localized disagreements. More generally, we cannot exclude possible shortcomings of the chemistry-transport model itself to explain the disagreement. Although CHIMERE has been systematically evaluated over Europe, it has not been extensively used over South America so far. In that case, identifying the causes and consequences is more complex.

Only one particular month per season, for one particular year, are analyzed here. Whether the results presented can be extrapolated with a climatological relevance is not straightforward. Climate variability modes such as ENSO, for instance, can lead to inter-annual changes in circulation and meteorology at the scale of central Chile. In particular, El Niño phases are related to above average rainfall in the region in winter [Montecinos and Aceituno, 2003], hence leading to more frequent scavenging of particulate matter, that may imply less regional transport. La Niña years do the opposite, with a dryer winter. In addition, ENSO affects the southeast Pacific anticyclone thus modulating wind speeds alongshore central Chile [Rahn and Garreaud, 2014]. Weaker winds are observed in case of El Niño so that northward transport likely decreases as a consequence. Again, the opposite can be said for La Niña. ENSO also modulates the severity of the fire season in summertime in the region [Urrutia-Jalabert et al., 2018]. However, as pointed out in Section 1, wildfires are not taken into account in our simulation design so that our findings are resilient to this variability. Speculating on the impacts regarding our results of the ENSO-related synoptic-scale variability of atmospheric circulation is even more complex in the context of the last decade, as the ENSO teleconnection in central Chile is weak for that period [Garreaud et al., 2020]. However, although our quantitative conclusions may not exactly hold for other years, the underlying processes described remain valid, particularly when it comes to mountain-valley circulation which is radiatively driven. Variations in primary pollutants and precursors emissions, wintertime precipitation and cloud cover may affect our results, but we do not expect new processes to take place or evidenced processes to stop, nor magnitudes to change entirely. Indeed, the year 2015 was chosen because it recorded no particular extreme pollution event, and corresponds to a neutral ENSO phase for the Chilean climate. In addition, primary emissions in the model are not weather-dependent, and the inventory is static as of 2010, meaning the fluxes of primary anthropogenic emissions would be equal for any simulated year. Therefore, the picture provided by this study is statistically representative of average summer and winter months, despite not being directly extendable.

Section 3.1.4.3 evidences the asymmetric vertical ventilation of pollutants such as NO_x and VOC and its role

in the formation of an O_3 persistent plume. Given the quite unique combination of very high emission rates and close proximity of steep elevated orography featured by the Santiago basin, it is unclear, based on the literature, whether this venting is expected to improve or worsen O_3 pollution at the surface level in the city. To some extent, this asymmetric venting of precursors is similar to the sensitivity analysis performed in Section 3.1.4.2 leading to a change in precursors ratios, except for the magnitude of the variation in pollutants emissions. Thus, one could extrapolate and expect an increase (decrease, respectively) of O_3 mixing ratio in the western (eastern, respectively) districts due to this daily-occurring export of pollutants, compared to a situation where air masses would stagnate. However, there are too many non-linear processes involved to be affirmative on this point.

In addition to being a pollutant, tropospheric O_3 is a strong greenhouse gas, estimated to contribute between 0.2 to 0.6 $W\,m^{-2}$ to present climate global radiative forcing [Myhre et al., 2013]. The process described above may then imply radiative effects, either directly through greenhouse effect, indirectly through its impact on moisture, clouds and atmospheric circulation, or through its interaction with the cycles of other greenhouse gases [Mohnen et al., 1993]. Estimating this impact is however not in the scope of the present work. Nevertheless, it shows that although the venting of pollutants can be beneficial from the urban air pollution perspective, longer-term effects on climate are a corollary worth investigating.

Despite our good confidence in the model, it is not possible to strengthen conclusiveness with observations on the newly evidenced O_3 bubble we find as there are no local measurements of O_3 profiles for our study period. Besides, tropospheric ozone column products from satellite data are usually not fit for analysis in mountainous regions [e.g. Kar et al., 2010]. However, Seguel et al. [2013] conducted ozone profile measurements in the Santiago Metropolitan Region in summer 2011 that match our results quite well. First, they find a similar 35 ppb free troposphere background O_3 mixing ratio. Second, they evidence several occurrences of deep residual layers as intense as 100 ppb of O_3 slightly north of Santiago (at the location of La Colina, between Santiago and Los Andes) in early afternoon, measured between 1.5 km and 2.5 km above ground. Such secondary layers higher up are consistent with our findings. If a vertical profile is taken north of Santiago in Fig 3.9d, a bell shaped profile is recovered, of maximum intensity near 2 km above ground, much like Figure 9 in Seguel et al. [2013]. Thus, our simulation results agree very well with the measurements conducted in Seguel et al. [2013], despite being for a different year, hence strengthening our conclusions on the existence of the newly evidenced O_3 bubble and its seasonal persistence. Similarly to our findings, Seguel et al. [2013] also concluded that the residual layer is coming from pollutants venting from Santiago. However their measurement-based approach did not allow to evidence (i) the exact formation mechanism of this bubble, (ii) its persistent character even through nighttime (measurements presented are only for daytime), (iii) its horizontal extent (measurements are discrete in space). Our modeling approach based on sensitivity analysis confirms the primary role of Santiago emissions and gives a clearer and continuous 3-dimensional picture of the phenomenon, while agreeing with the findings of these previous measurements.

We estimate that 14% of $PM_{2.5}$ in Santiago come from long-range transport in wintertime. Although summertime $PM_{2.5}$ is not discussed within the framework of this paper, it is available in the simulations, and we find its transported contribution to be greater, at 22%, for that period. As a result, we expect the average contribution of long-range transport to $PM_{2.5}$ in Santiago for a whole year to be somewhere between these two numbers, around 18%. It is worth noting that for the year 2019, the exceedance of the $PM_{2.5}$ Chilean standard was 18% for Santiago according to data from the SINCA network. Although for our study year 2015 this exceedance was higher (close to 50%), our findings suggest that if air quality improvement policies are conducted in all urban areas across central Chile, Santiago might be able to meet the national standards more easily due to the large contribution of transported $PM_{2.5}$.

Summertime $PM_{2.5}$ and wintertime O_3 were not studied here given their comparatively lower relevance. A short discussion can be provided however. The simulations show that the regional plume of $PM_{2.5}$ in summertime has a similar extent to the one of O_3 in summertime, i.e. an area of influence lesser than in wintertime, mostly near the surface. O_3 is barely produced in wintertime due to a zenith angle of the sun closer to the horizon and shorter duration of days, resulting in less radiative power and barely active photolysis, so that the question of the export of its precursors at that season is not relevant. The model accordingly yields generally inconsequential mixing ratios in the domain.

3.1.6 Conclusion

Based on chemistry-transport modeling with WRF-CHIMERE, the present work investigates the transport of atmospheric pollutants in central Chile for one winter month and one summer month. Our findings show that emissions from Santiago city greatly affect atmospheric composition in its vicinity and farther, with a

contribution of a few $\mu g\,m^{-3}$ to $PM_{2.5}$ in wintertime corresponding to 5% to 10% of surface concentrations as far as 500 km to the north and 500 km to south. This transport is mostly driven by surface winds within the boundary layer above land, and takes place in the free troposphere over the ocean hence explaining its long northward range. The spatial extent of the effect on surface concentrations of O_3 precursors emitted in Santiago in summertime is lesser. Nevertheless, daily peaks of O_3 in the direct vicinity of Santiago are reduced by up to 50 ppb on average when emissions from the city are eliminated. Conversely, the contribution of long-range transport of $PM_{2.5}$ in wintertime is responsible for $5\,\mu g\,m^{-3}$ to $10\,\mu g\,m^{-3}$ on average in downtown Santiago, corresponding to around 14% of the baseline concentration. While the transport of O_3 precursors to Santiago in summertime is not significant, if emissions of precursors were to be decreased in the city, its western districts would see their O_3 mixing ratios increase on average, despite daily peaks largely dropping, while the eastern area would improve for every quantile. This phenomenon is linked to heterogeneous emissions within the city, which make for currently higher than background levels in the east, and lower than background in the west. When all emissions are cut, the whole area is brought to background, hence the respective variations. The vertical export of precursors above Santiago in summertime, in relation with unperturbed mountain-valley circulation and venting, creates a persistent O_3 bubble of more than 50 ppb on average, around 1000 m above the ground, slightly north of the city. Daytime upslope winds, the heterogeneous lifetimes of precursors, and increasing vertical profiles of photolysis rate account for this formation, which impact should be looked at in greater detail in terms of surface air quality improvement (or worsening), and photo-chemical and greenhouse effects.

3.1.7 Appendix

WRF configuration		CHIMERE configuration	
Horizontal resolution	5km	Horizontal resolution	5km
Vertical levels	60	Vertical levels	30
Microphysics	WSM3	Chemistry	MELCHIOR
Boundary and surface layer	MYNN	Gas/Aerosol Partition	ISORROPIA
Land surface	Noah LSM	Horizontal Advection	Van Leer
Cumulus parameterization	Grell G3	Vertical Advection	Upwind
Longwave radiation	CAM	Boundary Conditions	LMDz-INCA + GOCART
Shortwave radiation	Dudhia		

Table 3.1: WRF and CHIMERE configurations.

	Wintertime							Summertime						
Station	Independencia				Rancagua			Independencia				Rancagua		
	MB	NRMSE	R	:	MB	NRMSE	R	MB	NRMSE	R	:	MB	NRMSE	R
T2	-1.23	0.22	0.87	:	-1.65	0.28	0.7	0.4	0.16	0.75	:	-0.06	0.19	0.73
RH	-0.22	0.39	0.85	:	-0.17	0.35	0.85	-0.12	0.3	0.83	:	-0.12	0.4	0.8
U10	-0.11	0.36	0.52	:	-0.01	0.2	0.77	0.31	0.84	-0.06	:	0.32	0.75	0.09
V10	-0.03	0.27	0.82	:	0.28	0.12	0.87	1.09	2.11	0.65	:	0.03	0.33	0.4
Station	Los Andes				Viña del Mar			Andacollo				Viña del Mar		
	MB	NRMSE	R	:	MB	NRMSE	R	MB	NRMSE	R	:	MB	NRMSE	R
T2	-3.33	0.38	0.89	:	0.31	0.3	0.25	0.67	0.17	0.8	:	0.64	0.42	0.18
RH	-0.17	0.3	0.91	:	-0.17	0.74	0.47	0.0	0.13	0.81	:	-0.06	0.57	0.51
U10	0.29	0.39	0.77	:	-0.12	1.35	0.29	0.85	1.36	-0.08	:	0.83	2.68	0.31
V10	0.74	0.65	0.58	:	2.12	1.54	0.61	2.14	1.14	0.25	:	0.96	1.57	0.64

Table 3.2: Simulation scores for daily average low-level meteorology for wintertime and summertime 2015. T2 is the 2 m air temperature (°C), RH the surface relative humidity, U10 10 m zonal wind and V10 10 m meridional wind speed ($m\,s^{-1}$). MB is the mean bias, NRMSE the normalized root mean square error and R the Pearson correlation coefficient.

Day:	21 July				23 July		
	MB	NRMSE	R	:	MB	NRMSE	R
TEMP	-0.3	0.03	1.0	:	1.13	0.07	1.0
RH	-0.17	0.32	0.79	:	-0.04	0.25	0.48
U	1.29	0.16	0.89	:	-1.65	0.35	0.56
V	-0.46	0.2	0.82	:	3.52	0.31	0.83
Day:	24 July				25 July		
	MB	NRMSE	R	:	MB	NRMSE	R
TEMP	2.36	0.08	1.0	:	1.15	0.06	1.0
RH	-0.03	0.53	0.01	:	-0.04	0.17	0.89
U	-0.52	0.14	0.86	:	-0.51	0.16	0.86
V	0.62	0.13	0.92	:	3.35	0.29	0.86

Table 3.3: Simulation scores for meteorological vertical profiles for four days in July 2015 at noon local time at Quinta Normal station in Santiago. The same notations as in Table 3.2 apply.

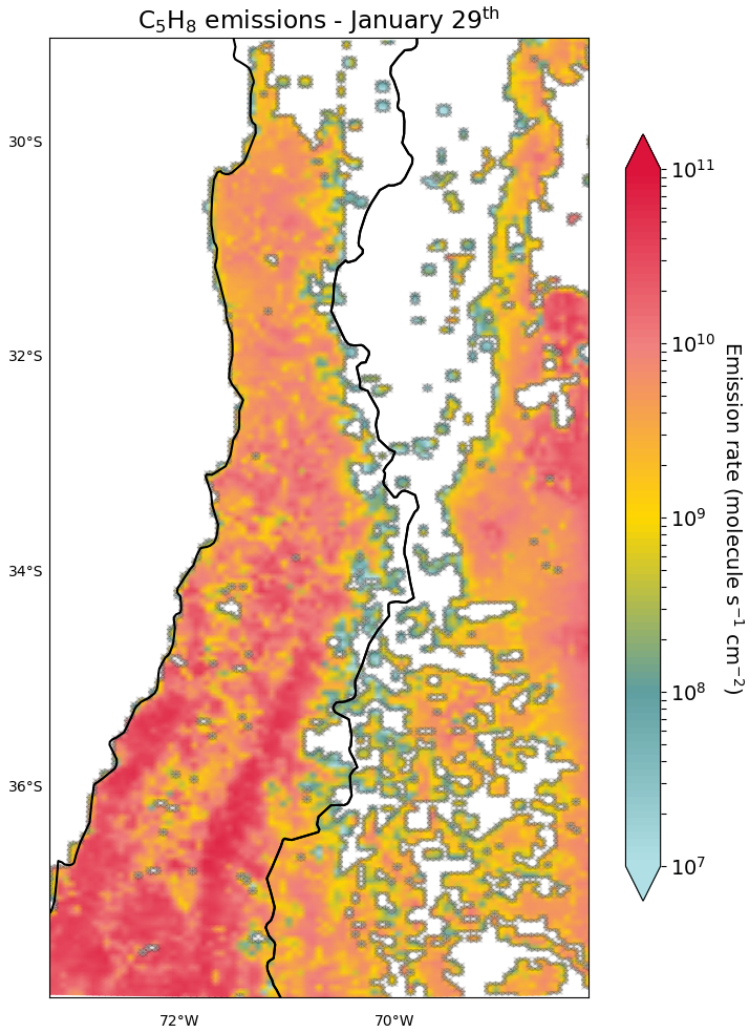

Figure 3.11: Isoprene (C_5H_8) average emission rate from biogenic sources for January 29$^{\text{th}}$ as computed in CHIMERE using the MEGAN model.

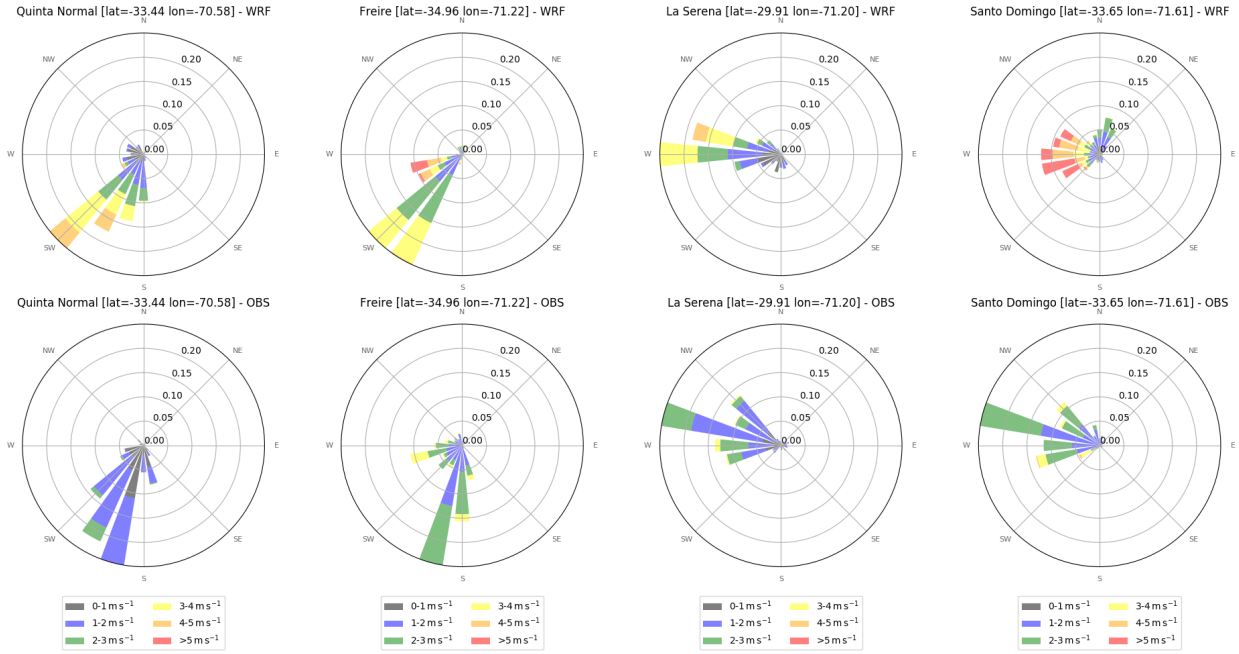

Figure 3.12: 10 m wind distribution in the simulation (top) and observations (bottom) at four locations in central Chile for summertime 2015.

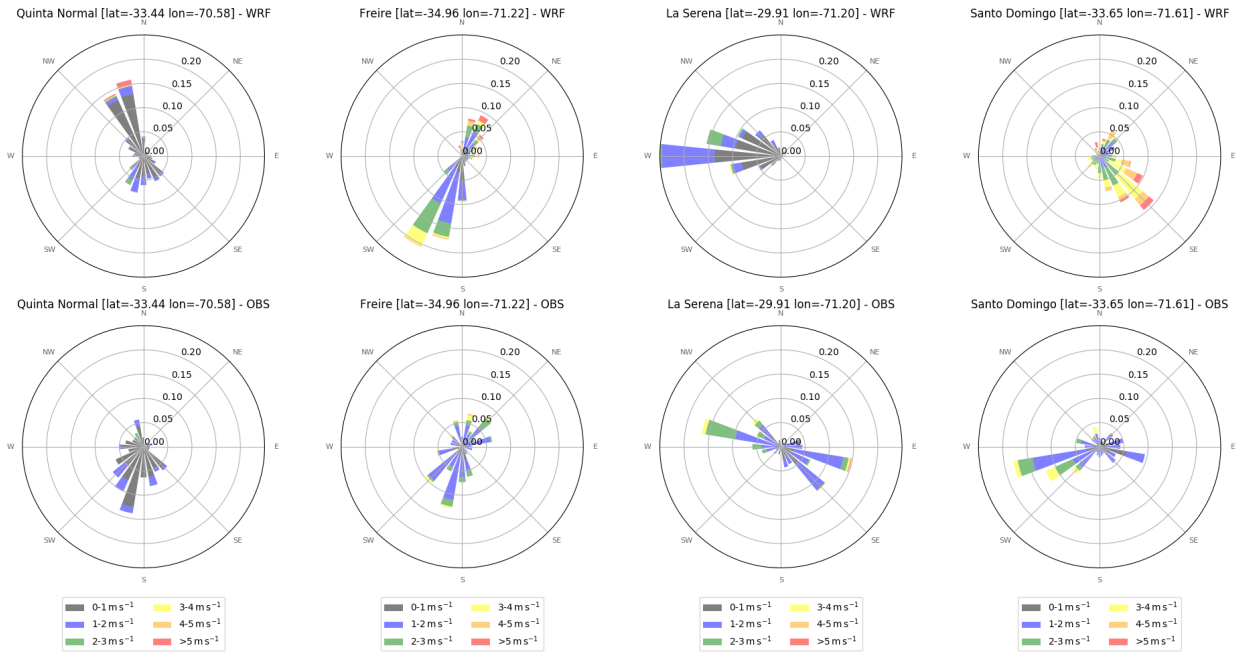

Figure 3.13: Same as Figure 3.12 for wintertime 2015.

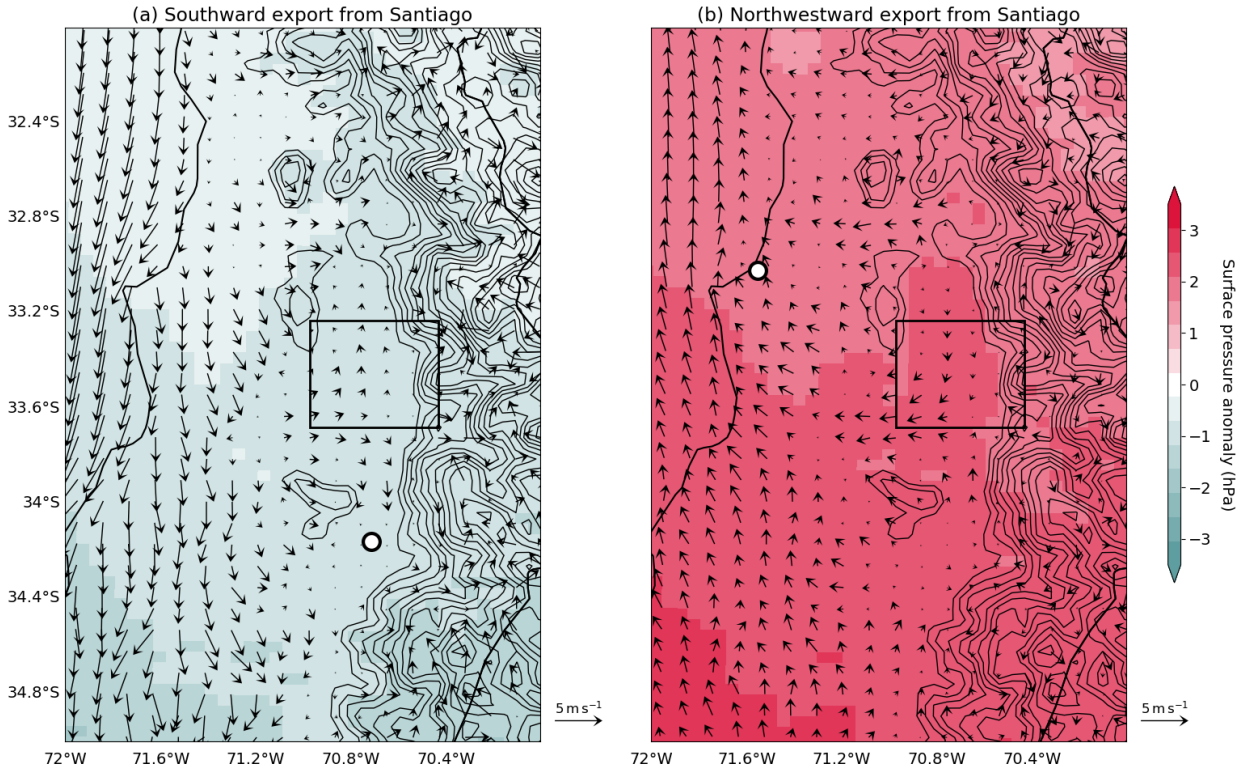

Figure 3.14: (a) Composite of surface wind (arrows) and pressure (colormap) anomalies with respect to the wintertime average, for hours of southward transport episodes, defined as hours when the concentration of $PM_{2.5}$ from Santiago (black rectangle) in Rancagua (white dot) is greater or equal to its 90^{th} percentile for the period. Contours show terrain elevation in excess of 1000 m every 250 m. (b) same as (a) but during hours of northwestward transport, defined in the same manner but with respect to concentrations in Viña del Mar (white dot).

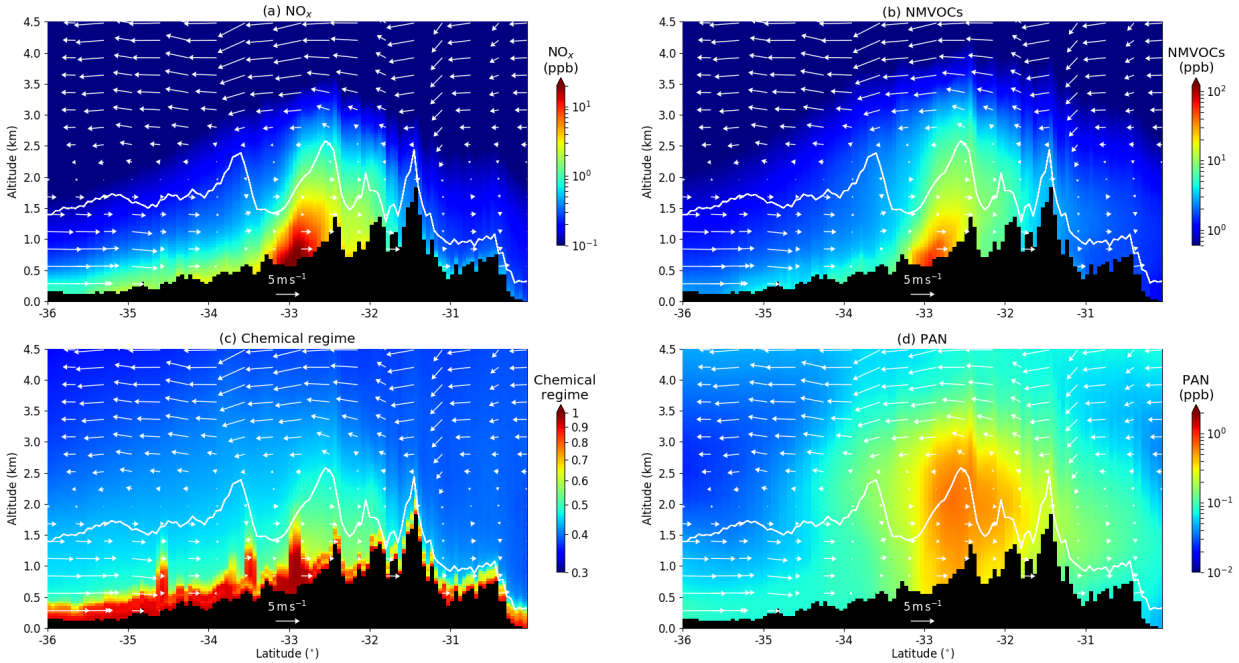

Figure 3.15: (a) Simulated NO_x concentrations (colormap), wind (arrows), afternoon boundary layer (white solid line) and terrain elevation (black area), along the summertime transect considered in Figure 3.9a. Average for summertime 2015. (b) same as (a) for NMVOC, (c) same as (a) for chemical regime, (d) same as (a) for Peroxyacetyl nitrate (PAN).

4 | Sources and atmospheric impacts of extreme pollution events

4.1 The origin of fine particles extreme events in wintertime

This section is based on Lapere et al. [2020] which aims at identifying the source responsible for record-breaking wintertime particulate matter episodes in Santiago in the last decade. The combination of in-situ observations and modeling leads to the conclusion that barbecues (locally known as *asados*) cooked during soccer internationl competitions are the main providers of fine particles leading to these harmful pollution conditions. Given its practical implications and somewhat unusual scope, the underlying article received a bit of media coverage presented in Appendix. The text and figures included hereafter are directly extracted from Lapere et al. [2020].

4.1.1 Abstract

In wintertime, high concentrations of atmospheric fine particulate matter ($PM_{2.5}$) are commonly observed in the metropolitan area of Santiago, Chile. Hourly peaks can be very strong, up to ten times above average levels, but have barely been studied so far. Based on atmospheric composition measurements and chemistry-transport modeling (WRF-CHIMERE), the chemical signature of sporadic skyrocketing wintertime $PM_{2.5}$ peaks is analyzed. This signature and the timing of such extreme events traces their origin back to massive barbecue cooking by Santiago's inhabitants during international soccer games. The peaks end up evacuated outside Santiago after a few hours but trigger emergency plans for the next day. Decontamination plans in Santiago focus on decreasing traffic, industrial and residential heating emissions. Thanks to the air quality network of Santiago, this study shows that cultural habits such as barbecue cooking also need to be taken into account. For short-term forecast and emergency management, cultural events such as soccer games seem a good proxy to prognose possible $PM_{2.5}$ peak events. Not only this result can have an informative value for the Chilean authorities, but a similar methodology could also be reproduced for other cases throughout the world in order to estimate the burden on air quality of cultural habits.

4.1.2 Introduction

Santiago, the capital city of Chile (33.5°S, 70.5°W, 570m a.s.l.) regularly faces high levels of fine particulate matter ($PM_{2.5}$) pollution in winter. The city is located in a confined geographical basin surrounded by the Andes cordillera in the East, a coastal range in the West, and transversal mountain chains in the South and North [Rutllant and Garreaud, 1995]. The induced poor ventilation in wintertime combined with significant anthropogenic emissions lead to high average levels of $PM_{2.5}$ [Barraza et al., 2017, Mazzeo et al., 2018] as well as peak events [Toro et al., 2019]. Hourly surface concentrations can reach up to 600 µg/m^3 in the Western part of the city according to the local air quality monitoring network. Between June and July 2016 records show that the station of Pudahuel saw only seven days with an average $PM_{2.5}$ concentration below the 25 µg/m^3 24-hour mean standard defined by the World Health Organization [WHO, 2006]. 7 million people live in the metropolitan area and are exposed to such atmospheric pollution. The associated life expectancy reduction caused by $PM_{2.5}$ inhalation ranks Chile among the countries with air pollution issues [Energy Policy Institute at the University of Chicago, 2017]. In this respect, atmospheric decontamination plans were designed by local authorities in the recent years [Gallardo et al., 2018, MMA, 2012]. However the source and impacts of extreme peak events as well as the benefits of their mitigation are relatively unknown.

Several studies have been conducted to improve the $PM_{2.5}$ concentration forecast system in Santiago [Rutllant and Garreaud, 1995, Saide et al., 2016, Mazzeo et al., 2018]. However, none of them describe the sharp sporadic peaks observed some years in June and July nor explain their origin, while their impact is substantial. Acute health effects of strong, time-limited $PM_{2.5}$ events are known to be significant in Santiago, with increases in respiratory emergency and pneumonia visits within 2 days after such a peak [Ilabaca et al., 1999]. Government reports also provide evidence that highly polluted conditions affect the local economy, and estimate the net benefit of compliance with PM standards to several millions of US dollars [MMA, 2012]. This study combines the automated air quality monitoring network of Santiago and chemistry-transport modeling to describe and identify the source of recent short-lived $PM_{2.5}$ extreme events occurring in wintertime. The dispersion pattern of such events in June 2016 is also modeled.

Section 4.1.3 presents the data and model configuration used in this study. Section 4.1.4 describes the outcomes of both the data analysis and the chemistry-transport simulations regarding the identification of the origin of the extreme events considered. Section 4.1.5 discusses the hypotheses underlying the conclusions, which are detailed in Section 4.1.6.

4.1.3 Data and methods

4.1.3.1 Observation data

Time series of hourly surface measurements of meteorology and air quality are extracted from the automated air quality monitoring network of Santiago (SINCA - `https://sinca.mma.gob.cl/index.php/region/index/id/M`). The distribution of these urban air quality monitoring stations can be seen in Fig. 4.4 for instance. This network uses beta ray attenuation technology (Met One Instruments' Model BAM-1020) for $PM_{2.5}$ concentrations measurements, gas-phase chemiluminescence (Thermo Scientific Model 42i) for NO_x, and infrared photometry by gas filter correlation (Thermo Scientific Model 48i) for CO. Vertical meteorological profiles used for the validation of the simulations were provided by the Dirección Meteorológica de Chile. Ceilometer back-scattering profiles were measured and provided by the University of Chile.

4.1.3.2 Model set-up

The chemistry-transport simulations are based on the combination of WRF mesoscale weather numerical model, HTAP anthropogenic emissions inventory and CHIMERE chemistry-transport model. The simulation domains are described in Fig. 4.1, with a coarse domain at 15 km spatial resolution comprising most of Chile, and a nested domain focusing on central Chile and centered on Santiago at 3 km resolution. The meteorological conditions are simulated using the Weather Research and Forecasting model from the US National Center for Atmospheric Research [Skamarock et al., 2008]. The model configuration used in this study to simulate and reproduce observed meteorological conditions are presented in Table 4.1. The model was applied to 46 vertical levels up to the highest elevation of 50 hPa, in a two-way nested fashion, with 1-2-1 smoothing. Initial and boundary conditions used are FNL analysis, with a 1° by 1° spatial resolution and 6-hour temporal resolution, from the Global Forecast System [NCEP, 2000]. Land-use and orography are based on the modified IGBP MODIS 20-category database with 30sec resolution [University of Maryland, 2010]. The simulated period is June 1st to July 15th 2016. The starting period from June 1st to June 15th is used for spin-up and will not be analyzed. CHIMERE is an Eulerian 3-dimensional regional Chemistry-Transport Model, able to reproduce gas-phase chemistry, aerosols formation, transport and deposition. In this study the 2017 off-line version of CHIMERE is used [Mailler et al., 2017]. The configuration used for this study is described in Table 4.1. Land-use and orography data is the same as for WRF. For anthropogenic emissions, the HTAP V2 dataset is used which consists of 0.1° gridded maps of air pollutant emissions for the year 2010 [Janssens-Maenhout et al., 2015]. A downscaling is applied to this inventory based on land-use and demographics characteristics, and monthly emissions are split in time down to daily/hourly rates following the methodology of [Menut et al., 2013].

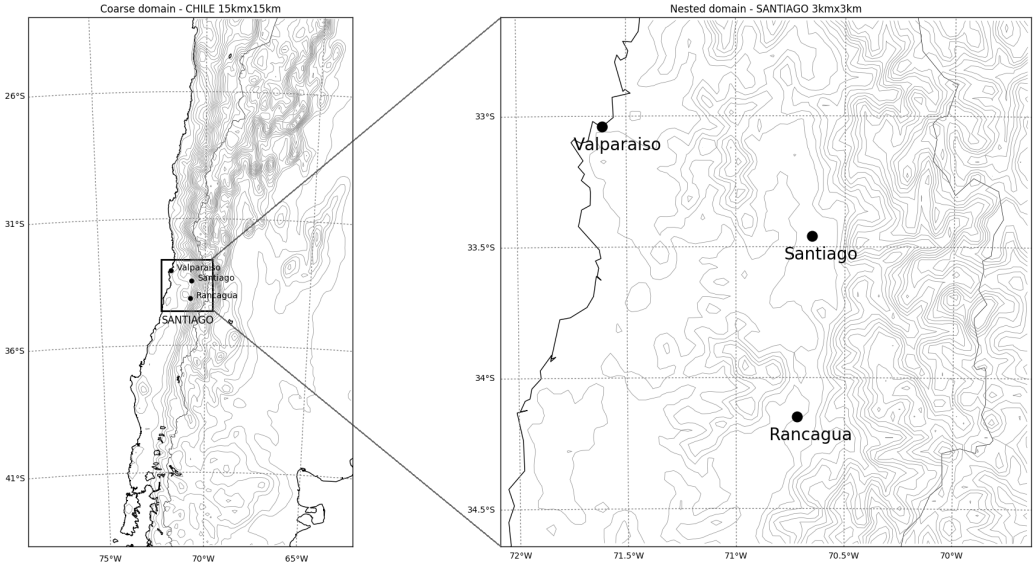

Figure 4.1: Left: coarse simulation domain at 15 km resolution. Right: nested domain at 3 km resolution. 250 m contour levels shown are interpolated from the modified IGBP MODIS 20-category database with 30 sec resolution [University of Maryland, 2010].

WRF configuration		CHIMERE configuration	
Coarse domain resolution	15km	Coarse domain resolution	15 km
Nested domain resolution	3km	Nested domain resolution	3 km
Microphysics	WSM3	Chemistry	MELCHIOR
Boundary and surface layer	MYNN	Gas/Aerosol Partition	ISORROPIA
Land surface	Noah LSM	Horizontal Advection	Van Leer
Cumulus parameterization	Grell G3	Vertical Advection	Upwind
Longwave radiation	CAM	Boundary Conditions	LMDz-INCA + GOCART
Shortwave radiation	Dudhia		

Table 4.1: WRF and CHIMERE configurations.

4.1.3.3 Simulation validation

Simulation scores are gathered in Tables 4.2, 4.3 and 4.4. Two stations downtown are used to validate the simulated near-surface meteorology - Table 4.2. Biases (MB) for temperature are around +/-1 °C with correlations (R) around 0.85. The model is a little too dry with relative humidity biases between -12% and -16% but mostly reproduces the diurnal cycle with correlations of 0.62 and 0.7. 10 m wind speed time series is fairly well reproduced with mean biases of -0.08 m/s (8%) and 0.23 m/s (32%) respectively for observed average values of 1.04 m/s and 0.70 m/s, and correlations of 0.56 and 0.7. Vertical meteorological profiles scores are shown in Table 4.3. For the three days presented the statistics are satisfactory. Typical daily average concentrations of $PM_{2.5}$ are quite well reproduced by the model. Table 4.4 gathers the scores for $PM_{2.5}$ for some stations, between June 28th and July 15th so as to avoid the peaks that do not represent business as usual conditions. Mean biases are less than 5 µg/m^3 to be compared with average hourly levels over the period between 35 µg/m^3 and 55 µg/m^3 for these stations. Corresponding correlations are between 0.45 and 0.63, which are decent values. The representation of wind by the model for synoptic meteorological stations in Santiago, is described in Table 4.3 and Fig. 4.2. Generally speaking the model behaves well for 10 m values and profiles of wind speed and direction, so that transport should be realistically represented.

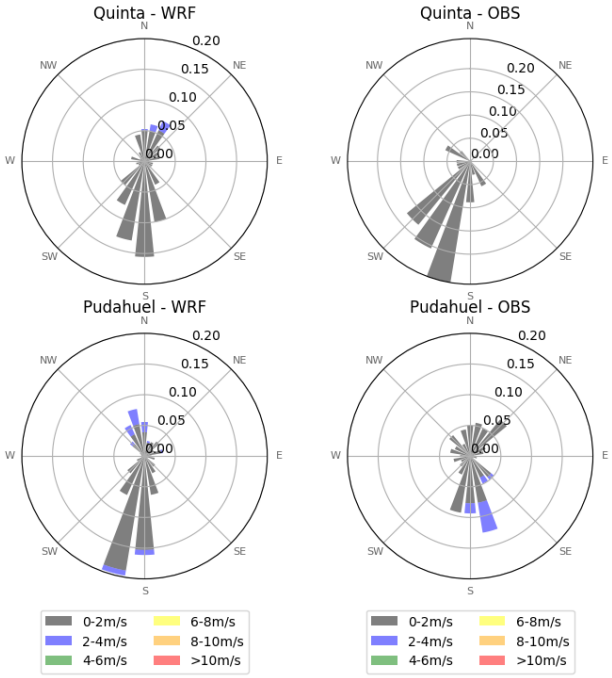

Figure 4.2: Modeled (left) and observed (right) wind rose between June 15th and 30th 2016 - synoptic stations Pudahuel and Quinta Normal

Station:	El Bosque				Independencia		
	MB	NRMSE	R		MB	NRMSE	R
TEMP	1.3	0.34	0.84	:	-1.06	0.2	0.86
RH	-12.7	0.30	0.62	:	-16.6	0.31	0.7
WS	-0.08	0.42	0.56	:	0.23	1.29	0.7

Table 4.2: Simulation scores for low-level meteorology. June 15$^{\text{th}}$ to July 15$^{\text{th}}$ 2016

Day:	June 27$^{\text{th}}$ 2016				June 28$^{\text{th}}$ 2016				June 29$^{\text{th}}$ 2016		
	MB	RMSE	R		MB	RMSE	R		MB	RMSE	R
TEMP	-0.79	2.01	0.99	:	0.51	1.1	0.99	:	0.83	2.4	0.95
RH	7.64	14.3	0.80	:	-1.04	5.88	0.67	:	-7.47	22.2	0.82
WS	-1.92	3.54	0.39	:	1.06	2.71	0.84	:	-3.63	4.38	0.99
WD	-2	4	0.34	:	-4	82	0.71	:	19	85	0.48

Table 4.3: Simulation scores for meteorological vertical profiles for 3 days at DMC station in Santiago.

The modeling setup is based on WRF-CHIMERE, with a horizontal resolution of 3 km, and emissions are downscaled from a dataset originally at a 0.1° resolution. At the scale of a city such as Santiago, which is roughly 20 km by 20 km, such a resolution might seem too coarse to capture the observed heterogeneity. However, the previous analysis shows that the meteorological conditions are well reproduced by the model, and the spatial distribution of $PM_{2.5}$ concentrations also accounts for the observed heterogeneity (see Fig. 4.10 for instance). Mazzeo et al. [2018] used a similar setup with a 2 km resolution for a sensitivity analysis to traffic and residential heating emissions in Santiago, yielding similar performances. Comparable CHIMERE simulations are performed for purposes of air quality operational forecast in France, which performance at small scale is acknowledged in the literature, provided emissions have appropriate magnitudes [Petit et al., 2017, Shaiganfar et al., 2017].

4.1.4 Results

4.1.4.1 $PM_{2.5}$ peaks description

The following analysis is based on the data provided by the "Sistema de Información Nacional de Calidad del Aire" (SINCA) network of surface air quality sensors distributed in the metropolitan area of Santiago [Ministerio del Medio Ambiente, 2018]. The time series of $PM_{2.5}$ concentrations for each of the 11 stations of this network for June and July 2016 are illustrated in Fig. 4.3. Two skyrocketing peaks, up to ten times higher than the average concentration for the season, occurred at several stations during the nights between June 18$^{\text{th}}$/19$^{\text{th}}$ and 26$^{\text{th}}$/27$^{\text{th}}$. These two peaks reached all-time record breaking levels for some stations in the city according to the available SINCA time series. Other stations show less extreme peaks, which is representative of the rich dynamics of particulate matter within Santiago [Toledo et al., 2018]. Understanding the origin and modeling the dispersion of these time-limited, very sharp events is the purpose of this study. For the following analysis, the peak on June 26$^{\text{th}}$/27$^{\text{th}}$ is considered, although the analysis and results are the same for June 18$^{\text{th}}$/19$^{\text{th}}$. Its spatial evolution can be found in Fig. 4.4, showing that the episode starts simultaneously at several air quality stations at around 8pm, levels decreasing back to regular values the next morning. The Western part of the city seems much more affected by the event than the Eastern part. This comes from the diurnal wind cycle in Santiago, that features prevailing easterlies during night time contributing to renew air masses in this part of the city [Rutllant and Garreaud, 1995].

Network	$PM_{2.5}$		
	MB	NRMSE	R
La Florida	-0.45	0.55	0.63
Las Condes	3.31	0.62	0.62
Puente Alto	-3.26	0.72	0.45

Table 4.4: Simulation scores for low-level $PM_{2.5}$ concentrations. June 28$^{\text{th}}$ to July 15$^{\text{th}}$ 2016

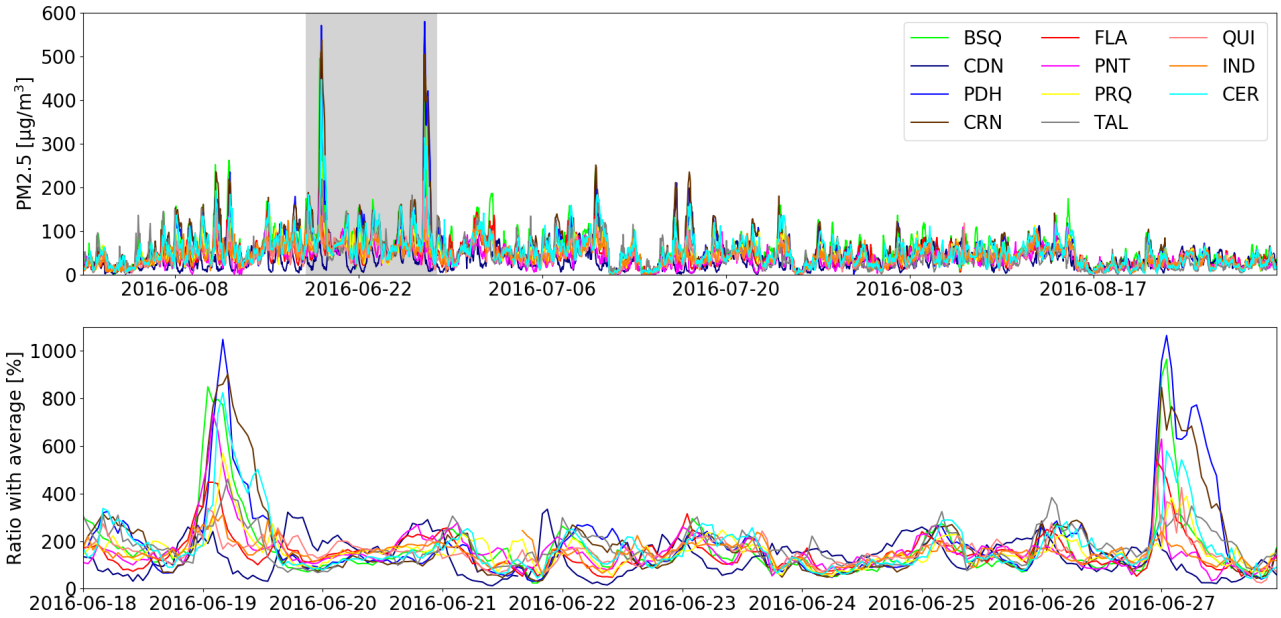

Figure 4.3: Top: time series of hourly $PM_{2.5}$ concentration between June 1$^{\text{st}}$ and August 31$^{\text{st}}$ 2016 for the 11 stations of the air quality network of Santiago. Bottom: ratio between hourly $PM_{2.5}$ and average over the summer, zoomed between June 18$^{\text{th}}$ and June 28$^{\text{th}}$ (shaded period in top graph).

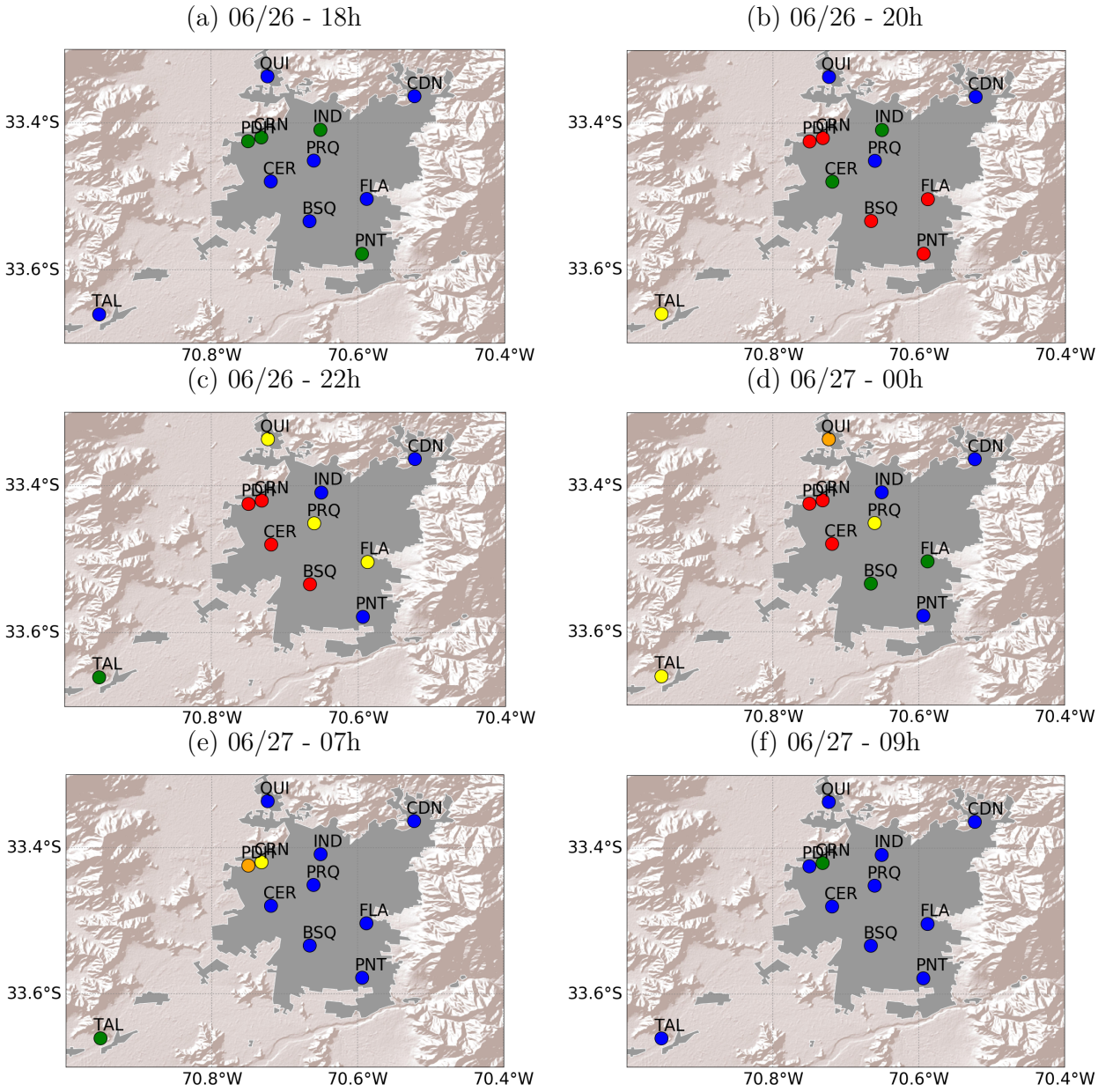

Figure 4.4: Observed $PM_{2.5}$ hourly concentrations during the peak on June 26thcompared to its average over summer 2016 - blue <= 200%, green <= 300%, yellow <= 400%, orange <= 500%, red >500%. Map background layer: World Shaded Relief, ©2009 ESRI.

The meteorological conditions observed at the location of the strongest peak during our period of interest are shown in Fig. 4.5. Red lines correspond to the measurements between June 26th 6 a.m. and June 27th 5 a.m. (local time) which comprises a peak event. Figures 4.5a and 4.5b show that at the location of the strongest $PM_{2.5}$ peak, the surface temperature and relative humidity cycles over the duration of the event are very close to the average over the month (black line). Wind speed - Fig. 4.5c - is a little slower than average on the whole but remains in the range of the 1st and 3rd quartiles of ventilation conditions (dashed white lines). Ceilometer profiles and boundary layer height (BLH) estimation based on the methods from [Muñoz and Undurraga, 2010] derived for each day at 3 p.m. - white diamonds in Fig. 4.5d - indicate that the mixed layer is rather shallow around the peak but not shallower than on the 22nd/23rd for instance, which did not feature such an event. On June 26th, the mixed layer is 430 m high, which is close to the average height over the period, and much higher than the minimum value (260 m) obtained on June 21st.

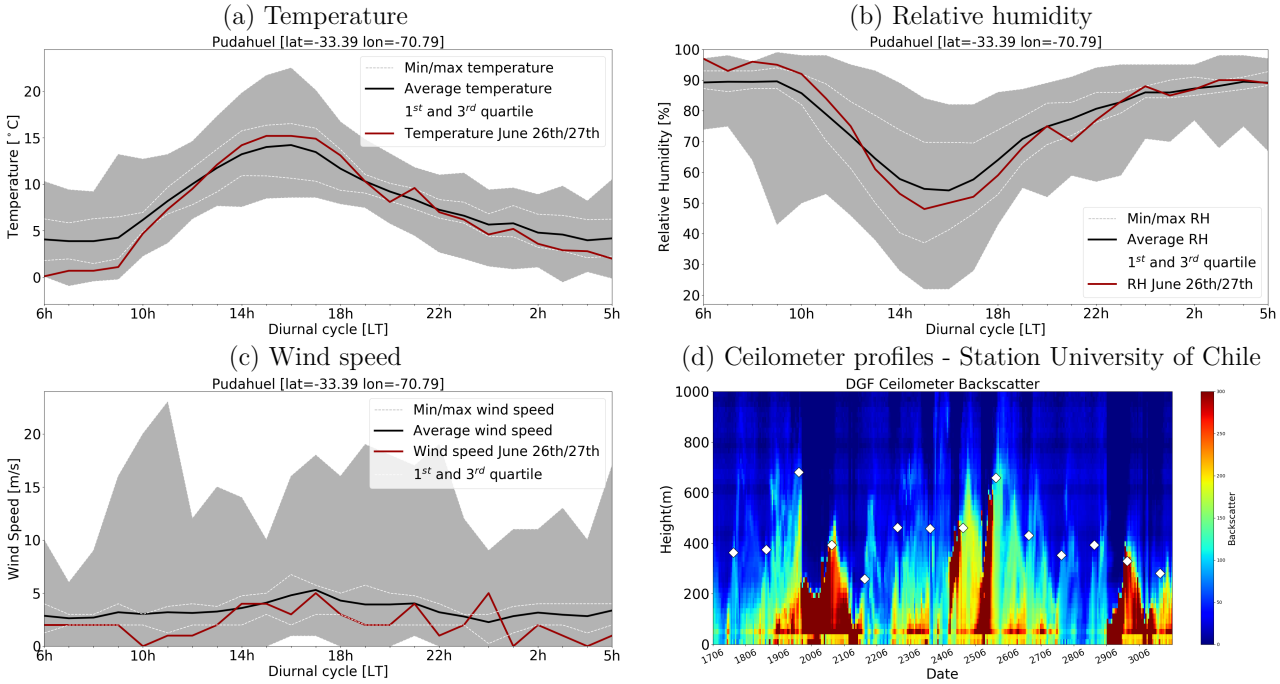

Figure 4.5: Meteorological conditions around June 26$^{\text{th}}$/27$^{\text{th}}$ $PM_{2.5}$ episode for the synoptic station Pudahuel. (a),(b),(c) average (black line), minima and maxima (gray area), 25% and 75% quantiles (white dashed line) between June 15$^{\text{th}}$ and July 15$^{\text{th}}$ 2016. The red lines show the values for June 26$^{\text{th}}$ 6 a.m. to June 27$^{\text{th}}$ 5 a.m. (d) hourly backscatter profiles from June 17$^{\text{th}}$ through June 30$^{\text{th}}$ 2016 and mixed layer height at 3 p.m. (white diamond markers).

Hence, measurements show that the meteorological conditions during the peak are not very different from other days of the period, when no PM peak was recorded. Thus, meteorological conditions are not to consider as the main forcing for the $PM_{2.5}$ event although they are favorable for it to appear, which is usual for the season in the area of Santiago.

Besides meteorology, advection of a PM plume over the city could be a candidate cause for such events. For instance, wildfires occurring in the forests surrounding the city occasionally explain major peaks of particulate matter in Santiago [Rubio et al., 2015, de la Barrera et al., 2018], but these events mostly take place in austral summer, and no such event was reported during our period of study. In addition, the strong concentration gradients observed between nearby stations (Fig. 4.3 and 4.4) makes advection unlikely responsible for these events.

Once meteorology and transport are ruled out as root causes, high local emissions must then be underlying the very strong concentrations recorded.

4.1.4.2 Chemical signature and source identification

In order to identify the type of source involved in the sporadic peaks, Fig. 4.7 shows a scatter plot of $PM_{2.5}$, NO_x and CO hourly surface concentrations from June 15$^{\text{th}}$ to June 30$^{\text{th}}$ 2016, for Pudahuel air quality station. Red dots correspond to $PM_{2.5}$ concentrations higher than 200 µg/m^3, blue dots to concentrations below that value. Out of simplicity, from now on we will refer to the former as PPE (PM peak events) and to the latter as PRS (PM regular situation). Two different regimes can be identified: for PPE, the NO_x/CO ratio is around 4.6%, while for PRS, it is approximately 14%. The same goes for the $NO_x/PM_{2.5}$ ratio, with values around 73% for PPE, and 502% otherwise. Given the short-lived character of the events considered, such different concentration ratios can be related to different emission factors as discussed in Sect. 3.1.5. Thus, two different types of source are involved in the two situations (PPE/PRS) considered.

[Mazzeo et al., 2018] found a $NO_x/PM_{2.5}$ ratio of 526% for Pudahuel station in July 2015, without peak events. Using the same methodology and combining data from July 2015 and 2016, without peak events, we recover a concentration ratio around 557% for this same station. For NO_x/CO we find it is around 14% (see Fig. 4.6). These two values correspond to the average pollution situation in this part of the city, i.e. what is

usually observed in wintertime when no peak event occurs. They are comparable to what can be observed in PRS in Fig. 4.7 with an average ratio of 502% for $NO_x/PM_{2.5}$ and 14% for NO_x/CO. Therefore, the PM regular situation (PRS) fairly corresponds to the average situation in Santiago in winter. Peak events (PPE - red dots) however show very different ratios that do not coincide with the average situation, hence pointing to another specific source. Major contributors to atmospheric pollution in Santiago are traffic (39%), industry (18%) and residential heating (20%) [Barraza et al., 2017]. Based on the current EURO 5 legislation for car engines emissions in place in Chile [Ministerio del Medio Ambiente, 2017] and the vehicles fleet in Santiago [Instituto Nacional de Estadísticas, 2016], the expected emission ratio from traffic yields around 12% for NO_x/CO and 1680% for $NO_x/PM_{2.5}$. Similarly, emission ratios extracted from the HTAP inventory for traffic at the grid point corresponding to Santiago yield 7.5% for NO_x/CO and 1750% for $NO_x/PM_{2.5}$. This does not match with the PPE signal, especially regarding NO_x and $PM_{2.5}$. For residential heating, the HTAP inventory gives emission ratios at the grid point of Santiago of 19% for NO_x/CO and 200% for $NO_x/PM_{2.5}$, also departing from the values observed during PPE. In addition, residential heating by domestic combustion of wood and/or fossil fuel is expected to have slow variations in time, depending essentially on outside temperature [Saide et al., 2016], which as discussed above was not particularly colder on peak days than on other days, permitting to rule out residential heating as the main contribution to these short-lived peaks. Industrial emissions are also generally constant through time, excluding the possibility that they could be the main factor either. HTAP emission ratios for industry also significantly differ from the PPE situation, with 20% for NO_x/CO and 186% for $NO_X/PM_{2.5}$. Other sources than usual must then cause these peaks.

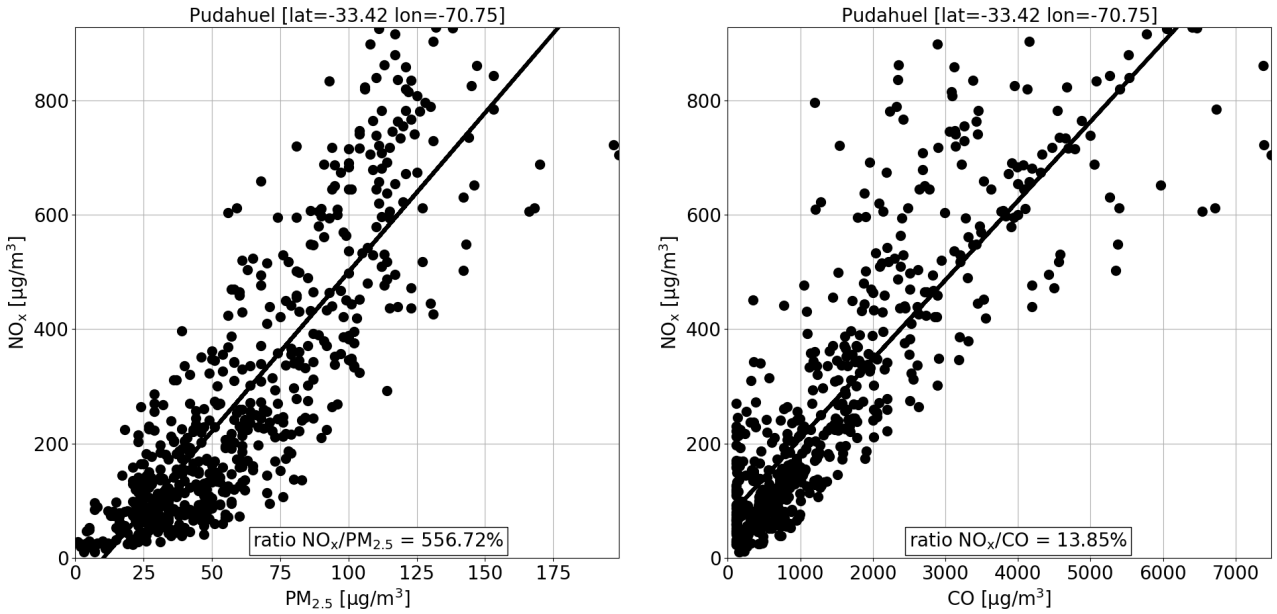

Figure 4.6: Pollutants ratios when no peak event occurs - July 2015 and 2016 - Pudahuel station

Since the peak events considered occurred exclusively during evenings/nights, cooking emissions such as barbecues, which are a cultural habit in Chile, could be a candidate. Different studies estimate emission factors from barbecue cooking (charcoal only and including meat emissions), from which ratios of 1.4% [Vicente et al., 2018] to 2.4% [Lee, 1999] for NO_x/CO and 40.5% [Vicente et al., 2018] to 61.5% [Lee, 1999] for $NO_x/PM_{2.5}$ can be derived. These numbers are not far from the 4.6% and 73% observed during PPE (Fig. 4.7), suggesting that, although the atmospheric composition is likely the result of multiple sources, the main signal in the observed $PM_{2.5}$ concentrations corresponds to emissions from barbecues. As a first order approximation, we use emission ratios and concentration ratios equivalently. This assumption is examined in Sect. 3.1.5. However, one question remains: why would there be peaks of barbecue cooking in the nights of June 18th and June 26th specifically, rather than other nights during the studied period? Even more so given that barbecues are mainly a spring-summer activity in Chile.

Usually, barbecues (or "asados") are cooked when celebrating particular events in Chile. So as to gain statistical significance by including more events, the time period studied is expanded to winter 2015 and 2014 as well. As it turns out, during the month of June of these three years, 8 episodes with hourly $PM_{2.5}$ higher than

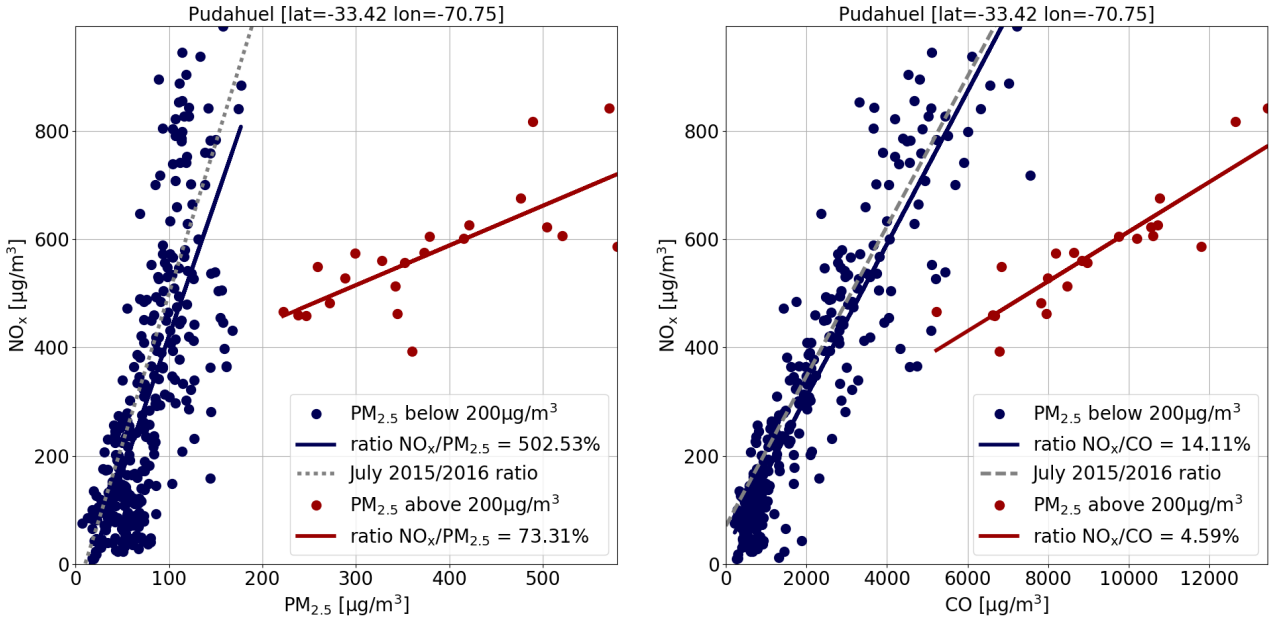

Figure 4.7: Observed NO_x/CO and $NO_x/PM_{2.5}$ concentration ratios at Pudahuel station (PDH). Blue dots are for $PM_{2.5}$ concentrations below 200 µg/m^3 - red dots are for $PM_{2.5}$ concentrations above 200 µg/m^3 - gray line represents the ratio for July 2015/2016 - blue and red lines correspond to linear regressions for each data set.

200 µg/m^3 were recorded at Pudahuel station, 5 of which peaked during international soccer games involving the Chilean national team. The three others were declared within 24 hours after a game. It is even clearer for peaks higher than 400 µg/m^3, all of them occurring at the exact same hour as the kick-off of a soccer game when the next day is not a working day - see Fig. 4.8: red diamonds represent Chile games kick-off during the 2014 world cup, 2015 Copa América and 2016 Copa América. In addition, for the recent years without major soccer championship involving the team of Chile (i.e. 2010, 2012, 2013, 2017), the maximum hourly $PM_{2.5}$ concentration at Pudahuel over the same period of the year was 260 µg/m^3. In 2011 another Copa América was played and values reached up to 360 µg/m^3.

This correlation is likely not coincidental. Over the months of June 2014, 2015 and 2016, the observations show 12 days recording "pre-emergency" conditions (24-hour $PM_{2.5}$ concentration above 110 µg/m^3). Among these 12 days, 10 dates coincide with a soccer game of the national team or the day after such a game (games being played at nights, the peak affects both the game day and the day after). The 3 periods total 90 days, 15 of which were game days. Based on combinatorics, the probability that soccer games and $PM_{2.5}$ pre-emergency levels coincidentally occur with a proportion of at least 10 for 12 can be expressed as in Eq. (4.1). This corresponds to randomly drawing 15 days out of the 90 available, and obtaining at least 10 peaks. As a result, the probability that the correlation between $PM_{2.5}$ peaks and soccer games is purely coincidental is 0.002%. Thus we can be confident that there is actually a significant correlation between these two types of events, through massive barbecue cooking during games.

$$\mathbb{P}_{\text{rand}} = \frac{\binom{12}{10}\binom{78}{5} + \binom{12}{11}\binom{78}{4} + \binom{12}{12}\binom{78}{3}}{\binom{90}{15}} = 2.10^{-5} \tag{4.1}$$

(a) Pudahuel 2016

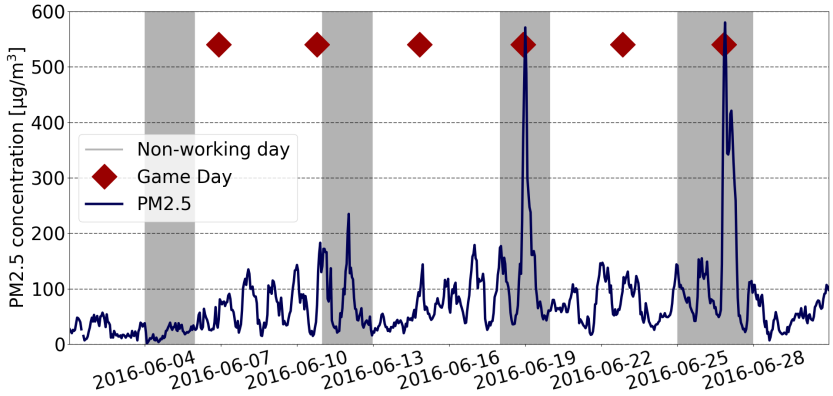

(b) Pudahuel 2015

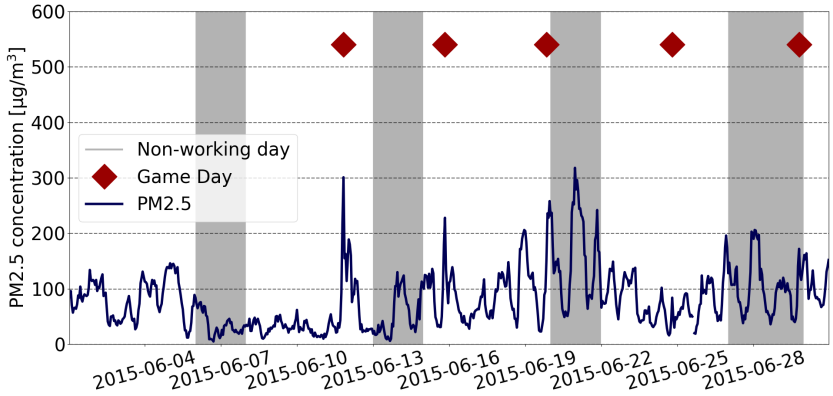

(c) Pudahuel 2014

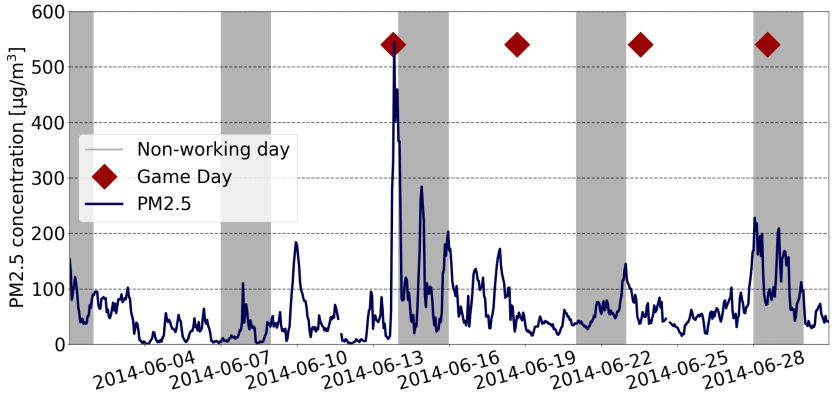

Figure 4.8: $PM_{2.5}$ peak events coincidence with soccer games. (a) Hourly $PM_{2.5}$ concentrations at Pudahuel monitoring station (solid blue line), kick-off hours of soccer games (red diamonds) and non-working days (gray shaded areas) - June 2016. (b) same as (a) for June 2015. (c) same as (a) for June 2014.

The observations made in Fig. 4.7 are also valid for other stations throughout the city. Figure 4.9 shows the NO_x/CO and $NO_x/PM_{2.5}$ ratios for three other locations in Santiago, distinguishing between the hours around the games of June 18^{th} and June 26^{th} (red dots), and the other data for the month (blue dots). Then again, two different regimes are observed, the one during games being attributable to barbecues based on the same analysis as previously done, although barbecues seem to be even more dominant in Pudahuel. In summary, we have shown here that major peak events of $PM_{2.5}$ in Santiago are correlated with soccer games played on the evening before a non-working day, and such conditions can be tied to massive barbecue cooking throughout the city, given the chemical footprint observed at that times.

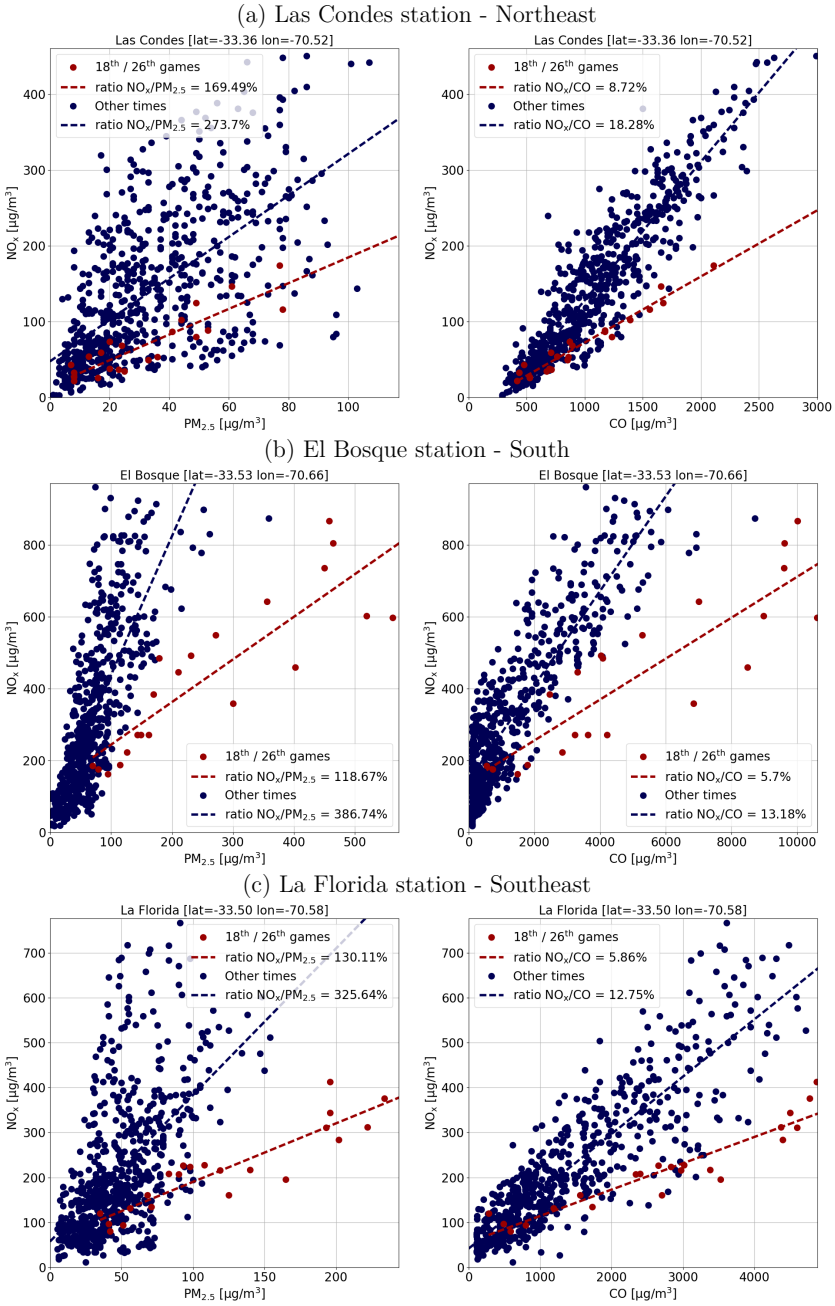

Figure 4.9: Observed NO_x/CO and $NO_x/PM_{2.5}$ concentration ratios at 3 stations in June 2016. Blue dots are observations during the June 18th and June 26th soccer games. Red dots correspond to the rest of the data. Blue and red dashed lines correpond to linear regressions for each case.

4.1.4.3 Transport

These barbecue peaks, although generating large amounts of $PM_{2.5}$, last only a few hours. The termination of one of these events is studied hereafter. A chemistry-transport simulation is run with WRF [Skamarock et al., 2008] and CHIMERE [Mailler et al., 2017] for the austral winter 2016 (see Section 4.1.3 for the details). A first baseline simulation aiming to reproduce observed concentrations of pollutants is performed using HTAP anthropogenic emissions inventory [Janssens-Maenhout et al., 2015]. This inventory does not account for sporadic emissions such as the ones studied here. Despite a good performance in reproducing the observed meteorology and atmospheric composition (see Section 4.1.3, Tables 4.2, 4.3, 4.4), the model does not produce peak events on

June 18$^{\text{th}}$ and June 26$^{\text{th}}$ (dashed black line in Fig. 4.10). This reinforces the idea that strong sporadic emissions are actually at play rather than extreme weather conditions. In a second simulation, all other things remaining equal, strong additional sources of $PM_{2.5}$ are added all over the city based on population density, and plugged into CHIMERE in order to account for barbecues being cooked on June 26$^{\text{th}}$.

A survey conducted before the final game of the 2016 Copa América estimated that 29% of Santiago's inhabitants would cook a barbecue during the game [Panel Ciudadano de la Universidad del Desarrollo, June 26th 2016]. As a first order approximation, considering only the adult population and assuming that this is a group activity gathering on average 7 people, we estimate that this corresponds to 100,000 fires that were lit at the time of the game. Based on PM emission rates estimated by the US Environmental Protection Agency [Lee, 1999] at around 20 g/hr on average, with variations depending on the type of meat cooked, the expected additional emission of $PM_{2.5}$ would be a total of 2 tons per hour for the whole region. In a heavily populated area such as El Bosque, this represents an additional signal 15 times higher than the $PM_{2.5}$ emission rate used in the baseline simulation. We acknowledge the multiple sources of uncertainty in this estimation. However our goal is to explore barbecues as a potential significant source of $PM_{2.5}$ pollution, which only requires orders of magnitude given the strength of the signal. Barbecues are assumed to last 3 hours starting 1 hour before the game kick-off. The estimated additional emissions are plugged in CHIMERE for the peak simulation (gray line in Fig. 4.10).

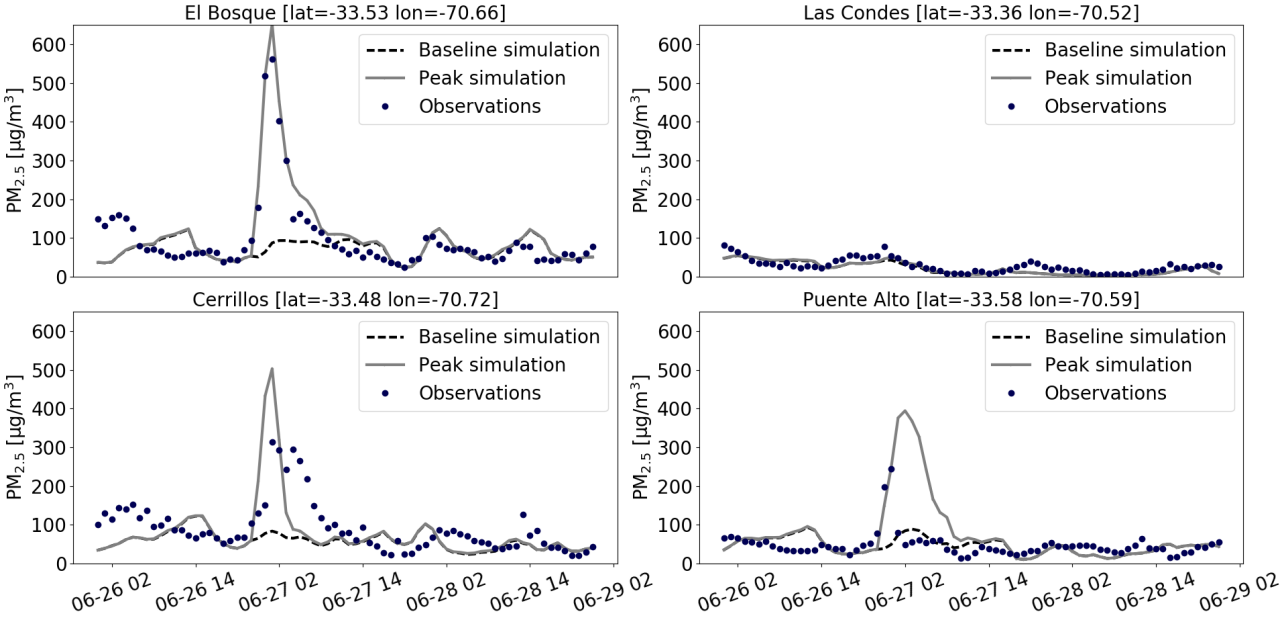

Figure 4.10: Observed (blue dots) and simulated (baseline simulation in black dashed line, peak simulation in gray) $PM_{2.5}$ surface concentrations time series at 4 stations in Santiago, around the peak episode of June 26$^{\text{th}}$ 2016

The resulting $PM_{2.5}$ concentration time series in Fig. 4.10 shows that the observations are well reproduced using this proxy in the South (El Bosque) and Northeast (Las Condes). Although the magnitude is a little overestimated but not far off, the time evolution of concentrations is less well reproduced in the West (Cerrillos) where the peak is too short, and in the Southeast (Puente Alto) where it lasts too long. This is possibly due to the representation of slope winds by the model: too weak easterlies coming from the Andes in the simulation would result in not enough ventilation in the East (i.e. a peak too long) and not enough accumulation in the West (i.e. a too short-lived event). Not many observations are available to investigate this hypothesis. Generally speaking, the peak simulation comforts the magnitude of our estimate of 100,000 barbecues cooked during the game, or an additional 6 tons of $PM_{2.5}$ emitted in total for the area.

Based on this simulation, the transport of the particles generated by the barbecue events can also be studied. Figures 4.11 and 4.12 show the difference in $PM_{2.5}$ concentration between the two simulations aforementioned, for the peaks on July 26$^{\text{th}}$ and July 18$^{\text{th}}$, respectively. Concentrations at 60m above ground level are considered in order to get rid of the signal of emissions. The simulations result in an evacuation of the particles towards the Southwest of Santiago for both events, a few hours after the onset. Then again the episodes are short-lived in

the city, but have impacts on adjacent areas several hours later and several kilometers away from the emission site. For both events the areas impacted by the dispersion of the plume are the South and Southwest regions. Although this result is consistent with mountain-valley circulation, it does not imply that such a dispersion pattern is the only one that can occur during peak events. In addition to the impact within the city, collateral effects outside Santiago must be studied in greater detail, such as a potential deposition of the particles on crops, with effects on yields, or adjacent glaciers, with radiative effects.

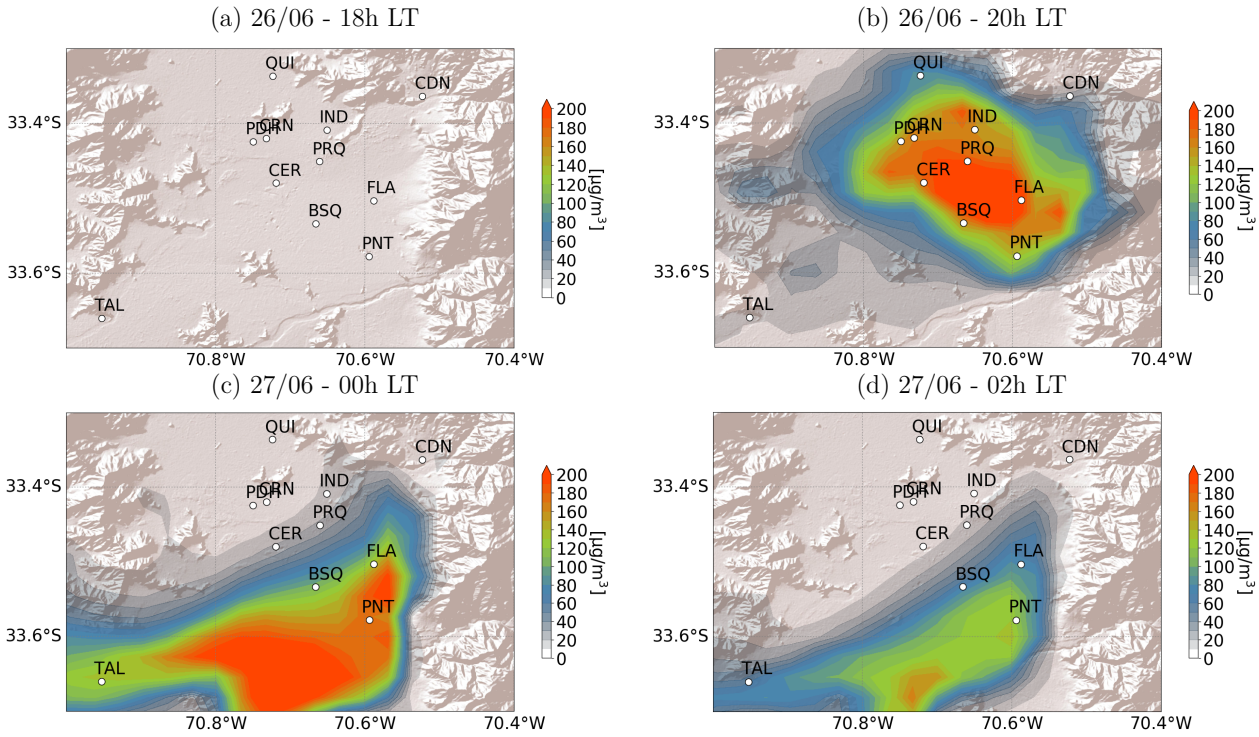

Figure 4.11: $PM_{2.5}$ concentration difference at 60m above surface between the peak event and baseline simulation in June $26^{th}/27^{th}$. Positive values indicate excess concentrations in the peak event scenario compared to baseline. Map background layer: World Shaded Relief, ©2009 ESRI.

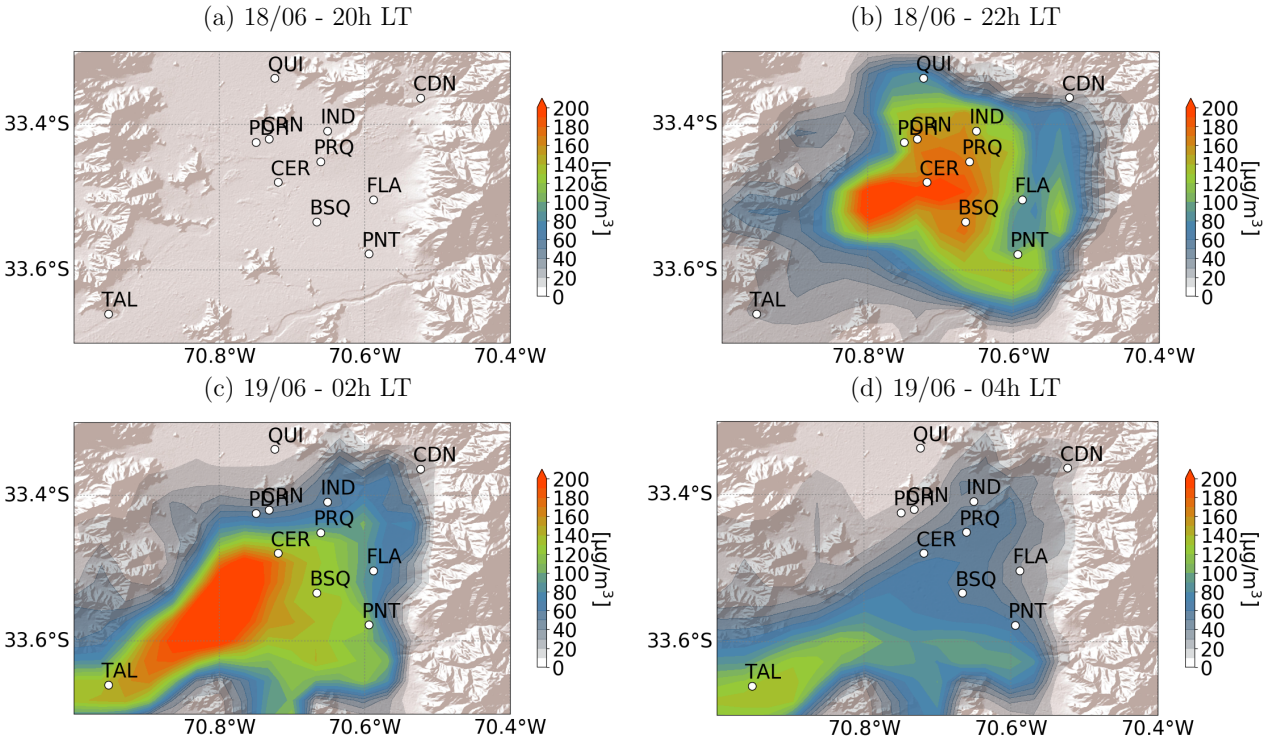

Figure 4.12: $PM_{2.5}$ concentration difference at 60m above surface between the peak event and baseline simulation in June $18^{th}/19^{th}$. Positive values indicate excess concentrations in the peak event scenario compared to baseline. Map background layer: World Shaded Relief, ©2009 ESRI.

4.1.5 Discussion

In Sect. 4.1.4.2, the conclusions are based on the approximation that the concentration ratios observed correspond to the ratios of the underlying emission factors. Chemical processes are at play in the atmosphere that can lead to a difference between these two variables though. However atmospheric lifetimes of NO_x and CO (respectively 1 to 10 days and 1 to 4 months [Seinfeld and Pandis, 2006]) are too long for these species to be significantly removed during the few hours we focus on. The NO_x/CO ratio at emission and concentration ratio are thus expected to be very close. For particulate matter, the discussion is less clear. Secondary PM can form, adding to the emitted $PM_{2.5}$. The nucleation of secondary PM would lead to a $NO_x/PM_{2.5}$ concentration ratio smaller than the emission ratio. However, one order of magnitude separates the two regimes we observe, and the time scale we study does not leave much time for secondary PM to become significant, implying a small contribution to the total PM (for instance the apportionment of secondary versus primary aerosols in our baseline simulation varies between 4% and 63% with an average value of 33%).

4.1.6 Conclusion

In the last decades, decontamination plans in Santiago have mainly focused on decreasing traffic, industrial and residential heating emissions. The chemical footprint of extreme peak events evidenced in this study advocates in favor of also considering more specific and sporadic sources based on cultural habits such as barbecues. Indeed, the mitigation policies currently implemented are helping lowering pollution levels, but based on our study, cannot prevent extreme $PM_{2.5}$ events from happening while their impact can be significant as well. The "game effect" phenomenon has been hypothesized by local authorities but had not been backed up by scientific evidence so far. An analysis of the time characteristics of the events showed that they happen exclusively during soccer games of the national team, played in evenings before a non-working day. The observed concentrations of NO_x, CO and $PM_{2.5}$ at that times, compared with the usual levels, allow to trace back the main contribution to fine particles emitted by barbecue cooking. The amount of barbecues cooked during one peak event is estimated and the associated emissions are plugged into a chemistry-transport simulation, leading to the reproduction of

the observed peaks, which is not the case without these emissions. The model then yields appropriate levels, thus comforting the estimated emissions, and allowing to study the evacuation of the $PM_{2.5}$ plume towards the Southwest of the metropolitan area. The more general question of the fate and impacts of particulate matter plumes generated in Santiago is raised.

Although the results provided here seem to have geographically limited implications, the general methodology can be reproduced and benefit to other places in the world. Indeed, using only a limited set of data, with no speciation of particulate matter, already enables to conclude on the source of extreme events, provided they are tied to cultural habits differing from the usual sources of air pollution. Such type of sporadic habits are usually ignored by air quality plans implemented by cities, due to the lack of scientific evidence.

In addition, a model-based approach allowed to constrain the estimate of number of barbecues cooked during the final game of the 2016 Copa América (around 100,000). Not only this result can have an informative value for local authorities, but such a sensitivity analysis can be reproduced and applied to other cases throughout the world in order to estimate the burden on air quality of specific sources.

4.2 Summertime biomass burning in Central Chile: impacts on air quality and meteorology of the 2017 mega-fires

This section is based on Lapere et al. [2021a] that is designed to investigate the impacts of the 2017 mega-fires that took place in southcentral Chile, on atmospheric composition and meteorology. The text and figures included hereafter are directly extracted from Lapere et al. [2021a].

4.2.1 Abstract

In January 2017, historic forest fires occurred in south-central Chile. Although their causes and consequences on health and ecosystems were studied, little is known about their atmospheric effects. Based on chemistry-transport modeling with WRF-CHIMERE, the impact of the 2017 Chilean mega-fires on regional atmospheric composition, and the associated meteorological feedback, are investigated. Fire emissions are found to increase pollutants surface concentration in the capital city, Santiago, by +150% (+30 $\mu g/m^3$) for $PM_{2.5}$ and +50% (+200 ppb) for CO on average during the event. Satellite observations show an intense plume extending over 2000 km, well reproduced by the simulations, with Aerosol Optical Depth at 550 nm as high as 4 on average during the days of fire activity, as well as dense columns of CO and O_3. In addition to affecting atmospheric composition, meteorology is also modified through aerosol direct and indirect effects, with a decrease in surface radiation by up to 100 W/m^2 on average, leading to reductions in surface temperatures by 1 K and mixing layer heights over land by 100 m, and a significant increase in cloud optical depth along the plume. Large deposition fluxes of pollutants over land, the Pacific ocean and the Andes cordillera are found, signaling potential damages to remote ecosystems.

4.2.2 Introduction

In summertime, air quality in central Chile (32°-38°, S, 70°-73°, W) is mostly affected by ozone (O_3) pollution in urban and sub-urban areas, with hourly maxima reaching typically up to 55 ppb in downtown Santiago [Seguel et al., 2013]. This phenomenon originates in the combination of large emissions of nitrogen oxides (NO_x) from traffic and industry (typically around 60 ppb daily maxima in downtown Santiago), volatile organic compounds (VOCs) from anthropogenic sources and vegetation (typically around 70 ppb on average in downtown Santiago), with increased photo-chemistry [Gramsch et al., 2006, Seguel et al., 2013]. The latter is made possible by long days and intense solar radiation. On the contrary, particulate matter (PM_{10}) pollution is usually lesser than in wintertime, due to less residential heating and hence less wood burning emissions of fine particulate matter ($PM_{2.5}$), together with deeper mixing layers diluting pollutants to a greater extent [Gramsch et al., 2006]. However, PM concentrations can sporadically reach or exceed wintertime levels for a few days in summertime, in association with massive forest fires in the region [de la Barrera et al., 2018]. The production and transport of O_3 by these events also exacerbate air pollution in the affected urban areas [Rubio et al., 2015].

The nature of gas and particulate emissions from forest fires varies depending on the burned species, but a subset of key pollutants are dominant and common to most fires [e.g. Andreae, 2019]. Greenhouse gases such as CO_2, CH_4 and N_2O find a significant part of their worldwide emissions originating from forest fires. As is the case for BC and primary organic aerosols, for which biomass burning is believed to be the main source of emission globally. Other gaseous pollutants such as CO, NO_x and VOCs are also part of the key emitted species during forest fires. NO_x and VOCs undergo photochemistry right after emissions in the smoke plume, under daylight conditions, leading to the production of secondary pollutants such as O_3, which has impacts on plants productivity and threatens human health [Hill and Littlefield, 1969, Lippmann, 1991]. The increase in fine particulate matter concentrations from the transport of fire emissions to remote and urban areas also raises concerns regarding respiratory issues for human beings [Ilabaca et al., 1999]. Acidic aerosols such as sulfuric acid (H_2SO_4) similarly generate pulmonary inflammations when inhaled [Amdur, 1989]. In this study, analyses will focus on a selection of pollutants based on their level of harmfulness to human health, although many others could be relevant to look at.

Central Chile is characterized by a temperate Mediterranean climate so that wildfires occur every year in summertime although their magnitude is variable. Since the 1970's, forest fires in the region have been continuously growing in number and affected surface area, from 2000 fires per year corresponding to a 350 km^2 burned area for the period 1970-1979 on average to a mean 6000 fires and 1180 km^2 for the 2010-2019 period [Corporación Nacional Forestal, 2020]. Multi-factorial changes underlie this evolution such as climate, biogeography, land use, and fire management [Holz et al., 2017, McWethy et al., 2018, Bowman et al., 2019]. In particular, the recent

mega-drought recorded in central Chile aggravated the hydrological deficit in the region and partly explains the exceptional severity of fires observed over the last decade in the region [CR2, 2015, Garreaud et al., 2017, González et al., 2018].

In late January 2017, a record-breaking biomass burning event started in south-central Chile, destroying more than 5000 km^2 of plantations, native forests and shrublands in a few days. Although the number of wildfires observed in summer 2016/2017 is close to the decadal average, the total burned area is more than 5 times larger than any other year [Corporación Nacional Forestal, 2020], hence their designation as mega-fires. The associated emissions and atmospheric transport of O_3 and PM_{10} affected air quality over most of the region and as far North as Santiago, the capital city, with significantly increased concentrations recorded throughout the air quality monitoring networks [de la Barrera et al., 2018]. A wide range of social, economic, and environmental impacts result from these fires [Castillo et al., 2020, Sarricolea et al., 2020], in addition to an estimated 76 premature human deaths and 209 additional hospital admissions for respiratory conditions in the region [Bowman et al., 2019]. To date, studies investigating the atmospheric impact of the 2017 fires rely on local measurements and satellite data analysis rather than modeling, which does not provide a comprehensive, spatially continuous analysis nor permits a scenario approach regarding atmospheric composition modifications induced by the 2017 mega-fires.

Chemistry-transport modeling (CTM) offers a solution to cope with such limitations, hence the extensive use of CTM scenario approaches to describe and assess the transport and impact of biomass burning emissions on atmospheric composition at the global [e.g. Szopa et al., 2007, Jacobson, 2014, Cussac et al., 2020] and regional scale [e.g. Lu and Sokolik, 2018, Vara-Vela et al., 2018, Haslett et al., 2019]. In particular, the CHIMERE model [Mailler et al., 2017] is extensively used for the study of atmospheric impacts of large biomass burning events in several areas of the world, with examples of application in Africa [Menut et al., 2018], Russia [Konovalov et al., 2011, Péré et al., 2014, Konovalov et al., 2015], and the Mediterranean [Hodzic et al., 2007, Majdi et al., 2019, 2020].

Given the forecast increasing frequency of summertime droughts in the region for the years to come, identifying the climate feedback linked to biomass burning in central Chile is of significant importance. Examples of such feedback arise throughout the world. In the long run the radiative impact of aerosols emitted by biomass burning over the Amazon rainforest is found to improve the net primary productivity of biomass located downwind, due to changes in the more scattered nature of the light reaching the canopy, which in turn induces modifications in biochemical processes [Malavelle et al., 2019]. In South Africa, a Niña-like climate response to biomass burning is found, affecting the Walker circulation in the tropical Pacific through atmospheric teleconnections [Amiri-Farahani et al., 2020]. In the Southeast Atlantic region, biomass burning aerosols create a cyclonic anomaly over the ocean but enhance tropospheric stability over the continent [Mallet et al., 2020]. Russian wildfires in summer 2010 decreased solar radiation significantly for a few days, resulting in a surface cooling of the region contributing to stabilize and shallow the boundary layer, the latter leading to an increase in surface PM_{10} concentrations [Péré et al., 2014]. However, despite the 2017 mega-fires in Chile representing a major biomass burning event, the associated climate feedback is not known.

In this context, the present work aims to study and provide insight on the effects on atmospheric composition and meteorology of the 2017 mega-fires in central Chile. To do so, chemistry-transport modeling with WRF-CHIMERE is used, in fully coupled mode, to perform a sensitivity analysis to the fire emissions. Section 4.2.3 describes the data used and the modeling methodology adopted for the chemistry-transport simulations. Performance of the simulation compared to satellite data and local measurements, impacts on air quality and meteorological feedback are presented in Section 4.2.4. Section 4.2.5 discusses the findings and Section 4.2.6 elaborates on the conclusions of this work.

4.2.3 Materials and methods

The adequacy of the simulations performed using the WRF-CHIMERE chemistry-transport model is assessed by comparison to surface measurements and satellite data, which are presented hereafter. The model setup and configuration as well as the fire emissions parameterization are also described here.

4.2.3.1 Observational data

Time series of hourly measurements of atmospheric pollutants surface concentrations in Santiago are provided by the Chilean automated air quality monitoring network named SINCA (for spanish Sistema de Información Nacional de Calidad del Aire - `https://sinca.mma.gob.cl/index.php/region/index/id/M` (accessed on 2020,

October 1st)). Local measurements of Aerosol Optical Depth (AOD) and Single-Scattering Albedo (SSA) are extracted from the Santiago Beauchef station of the Aerosol Robotic Network (AERONET [Holben et al., 2001] - `https://aeronet.gsfc.nasa.gov/` (accessed on 2020, October 1st)). AOD at the regional scale is taken from MODIS Terra (`http://dx.doi.org/10.5067/MODIS/MOD04_L2.061` (accessed on 2020, October 1st)) and Aqua (`http://dx.doi.org/10.5067/MODIS/MYD04_L2.061` (accessed on 2020, October 1st)) level 2 aerosol products. Lidar satellite cross sections are taken from the CALIOP Lidar Level 2 Vertical Feature Mask Data, V4-20 (`https://doi.org/10.5067/CALIOP/CALIPSO/LID_L2_VFM-STANDARD-V4-20` (accessed on 2020, October 1st)) onboard the CALIPSO satellite. Carbon monoxide (CO) total column and O_3 tropospheric column satellite observations are taken from the IASI level 2 products [Clerbaux, 2018].

4.2.3.2 Modeling setup

The simulation domain comprises central and south-central Chile, between 15° S to 42° S and 63° W to 86° W (white domain in Figure 4.13b), at the 15 km spatial resolution. On the vertical, 30 levels are used up to the pressure of 300 hPa. CHIMERE v2020r1 is used, in fully coupled mode, integrating aerosols direct and indirect effects. CHIMERE is a Eulerian 3-dimensional regional Chemistry-Transport Model, able to reproduce gas-phase chemistry, aerosols formation, transport and deposition [Mailler et al., 2017, Bessagnet et al., 2020]. The v2020r1 version used in this work also provides a full coupling with the Weather Research and Forecasting (WRF) mesoscale numerical weather model from the US National Center for Atmospheric Research [Skamarock et al., 2008].

The simulated period is 15 to 31 January 2017, preceded by a spin-up period from 1 to 14 January 2017. Temperature anomalies and wind fields during the most intense fire period are described in Figure 4.13a, showing a large positive anomaly in surface temperature favoring the development of the fires, along with strong southerlies near the coast of central Chile that prefigure the general shape of the smoke plume. Parameterizations and schemes choices for CHIMERE and WRF are shown in Table 4.5. Fire emissions are extracted from the Copernicus Atmosphere Monitoring Service (CAMS) Global Fire Assimilation System daily data sets [Copernicus Atmosphere Monitoring Service, 2016] and adapted to the CHIMERE format (see Section 4.2.3.2). Emissions of CO for this fire event reach up to several hundreds tons per day per grid point (Figure 4.13b), with more than 10 t/day/km^2 for the most affected locations. Anthropogenic emissions are based on the HTAP v2.2 inventory [Janssens-Maenhout et al., 2015], downscaled and split down in time to hourly rates following the methodology of Menut et al. [2013]. Initial and boundary conditions rely on the NCEP FNL analysis data sets, with a 1° by 1° spatial resolution and 6-hour temporal resolution, from the Global Forecast System [NCEP, 2000]. Land-use and orography are extracted from the modified IGBP MODIS 20-category database with 30 s resolution [Friedl et al., 2010].

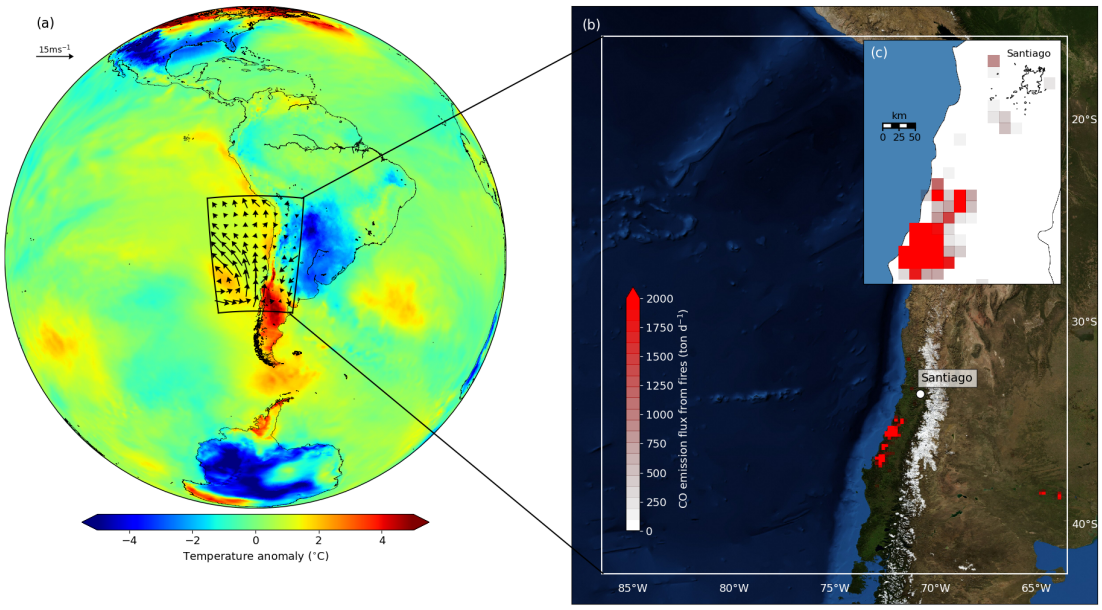

Figure 4.13: (**a**) Temperature anomaly between 25 and 29 January w.r.t. January 2017 average, and associated mean wind field. Data from ERA5 hourly surface reanalyses [Copernicus Climate Change Service, 2017]. (**b**) Simulation domain (white boundaries) and CO emissions from the main fire areas on 29 January. Emission data from CAMS GFAS [Copernicus Atmosphere Monitoring Service, 2016] pre-processed for CHIMERE. Map background layer: Imagery World 2D, ©2009 ESRI. (**c**) Zoom on the region of Santiago.

A first simulation is performed without considering emissions of pollutants from the fires (hereafter 'control case'), and a second one including these emissions (hereafter 'fire case'), so as to be able to perform a sensitivity analysis and isolate the effects stemming from the fire emissions. In the control case, all fire emissions are switched off, regardless of their location and magnitude, even during spin-up, as if the model were oblivious to fires.

Fire emissions parameterization

Emission rates of gases and particulate matter from fires are extracted from the CAMS GFAS daily emissions product and spatially downscaled to our simulation domain. A parameterized diurnal cycle is applied, with a daytime increase in emission rates until early afternoon (maximum at 16:00 UTC i.e., 13:00 LT) and low emission rates during nighttime (Figure 4.21a), consistently with what is usually observed for mid-latitude wildfires [Hodzic et al., 2007, Andela et al., 2015].

The vertical parameterization is similar to what is carried out in Menut et al. [2018]. Fire emissions are injected between ground level and the injection height H_p which is computed after the methodology of Sofiev et al. [2012] as Equation (4.2):

$$H_p = \alpha H_{ABL} + \beta(\frac{P_f}{P_{f0}})^{\gamma} \exp(-\frac{\delta N_{FT}^2}{N_0^2}) \tag{4.2}$$

where α=0.24 and H_{ABL} is the atmospheric boundary layer (ABL) height, so that the first term represents the fraction of the ABL that is passed 'freely', $\beta = 170\,\mathrm{m}$, P_f and P_{f0} are the fire radiative power (FRP) and reference FRP (10^6 W), respectively, $\gamma = 0.35$, $\delta = 0.6$, and N_{FT}^2 and N_0^2 are the Brunt-Väisälä frequency of the free troposphere and of reference ($2.5 \times 10^{-4}\,\mathrm{s}^{-2}$), respectively. The second term hence corresponds to the available convective potential energy diagnosed based on the FRP. NB: P_f is empirically corrected according to Veira et al. [2015] as $P_f^* = P_f \times \sqrt{H_p/1500}$.

The injection profile between the surface and H_p follows a K_z-like shape based on the approach from Veira et al. [2015]. The emission factor (EF) for a given altitude z is expressed as Equation (4.3):

$$\begin{cases} \text{if} \quad z/H_p \leq 1, EF(z) = z(1 - z/H_p)^2 \\ \text{if} \quad z/H_p > 1, EF(z) = 0 \end{cases} \tag{4.3}$$

In our simulation this corresponds to emissions being distributed throughout the mixing layer with a maximum emission rate typically around 500 m above ground level, i.e., about halfway through the ABL. Figure 4.21a shows an example of diurnal cycle and vertical profile for January 29 at a strong emission grid point.

Results are expected to be sensitive to these parameterization choices: the choice of diurnal distribution of emissions affects the injection height given its dependence on meteorological conditions. In turn, the simulated transport depends on this injection altitude [Majdi et al., 2019]. We acknowledge this source of uncertainty, although our modeling choices correspond to proven performing configurations with CHIMERE in the literature. Besides, the continuation shows that the model reproduces adequately surface and satellite observations, strengthening confidence in these choices.

CO_2 and H_2O not being included in our emissions inventory, carbon monoxide (CO) is by far the dominant emitted species (81% of the molecules), followed by methane (CH_4-5%), organic carbon (OC-2%) and non speciated fine (PPM_fin) and coarse (PPM_coa) particulate matter (1.8 and 1.3% respectively). It is worth noting that despite its criticality regarding radiative effects, black carbon (BC) constitutes only a limited fraction (0.2%) of emissions (Figure 4.21b).

4.2.4 Results

4.2.4.1 Fires impact on atmospheric composition

In this section, the adequacy of the model in reproducing the observed changes in atmospheric composition due to the fire events is assessed. A quantitative estimate of the fires emissions burden on air quality at the local and regional scales is then proposed.

In Santiago

Figure 4.14a shows the distribution of observed and simulated hourly concentrations of $PM_{2.5}$, PM_{10}, O_3 and CO at ground level over the SINCA network in Santiago, during the intense fire period of 22 to 30 January. Except for O_3, the control case simulation yields largely underestimated concentrations, confirming the significant transport of biomass burning pollutants towards Santiago during the 2017 event, as was inferred from statistical analyses of observations in de la Barrera et al. [2018]. In the fire case, simulated concentrations are much closer to observations, especially for $PM_{2.5}$ and CO although the spread is larger in the simulation. The discrepancy between the mean and median can be accounted for by the generation of spikes with excessive intensity in the model, while the observed distribution shows limited skewness. Apart from skewness, the distribution quartiles are adequately reproduced by the model for these two pollutants.

Contrary to $PM_{2.5}$, PM_{10} is significantly underestimated by the model, even in the fire case, meaning the coarse fraction of particulate matter is not adequately emitted and/or transported. Although the model and observations are consistent for average PM_{10} surface concentration during the event (driven by intense peaks like for $PM_{2.5}$), the distribution is shifted toward lower values in the simulation. The discrepancy comes from a negative bias in the model even before the fire event. For the period preceding 22 January, i.e., without the influence of fires in Santiago, $PM_{2.5}$ is consistently reproduced by the model in the capital city (not shown here), but the coarse fraction of PM (PM_{10}-$PM_{2.5}$) is significantly underestimated: between 14 and 22 January, observations over the automated network of Santiago recorded a $PM_{2.5}/PM_{10}$ ratio of 0.4 on average, while the model yields 0.7 (not shown here). The underestimation of the coarse fraction of PM can stem from either too low emissions of coarse particles in the HTAP anthropogenic emissions inventory, or excess dry deposition as (PM_{10}-$PM_{2.5}$) are substantially more deposited than $PM_{2.5}$ due to their greater mass. The latter point is sensitive to the choice of the deposition scheme, sometimes resulting in significantly different fluxes [e.g. Beegum et al., 2020]. However, emissions of aerosols by fires are usually mostly found in fine mode as is consistently shown both by the simulations and measurements: when the fire event starts, the $PM_{2.5}/PM_{10}$ ratio increases in both the model and observations, to around 0.8 and 0.6, respectively, (not shown here). Figure 4.22b also illustrates the dominance of fine mode aerosols transported from the fires. The lesser performance for PM_{10} thus does not jeopardize the present analysis regarding the influence of fires on atmospheric composition in Santiago, as it is mostly expected to affect the fine fraction of PM, which is well reproduced.

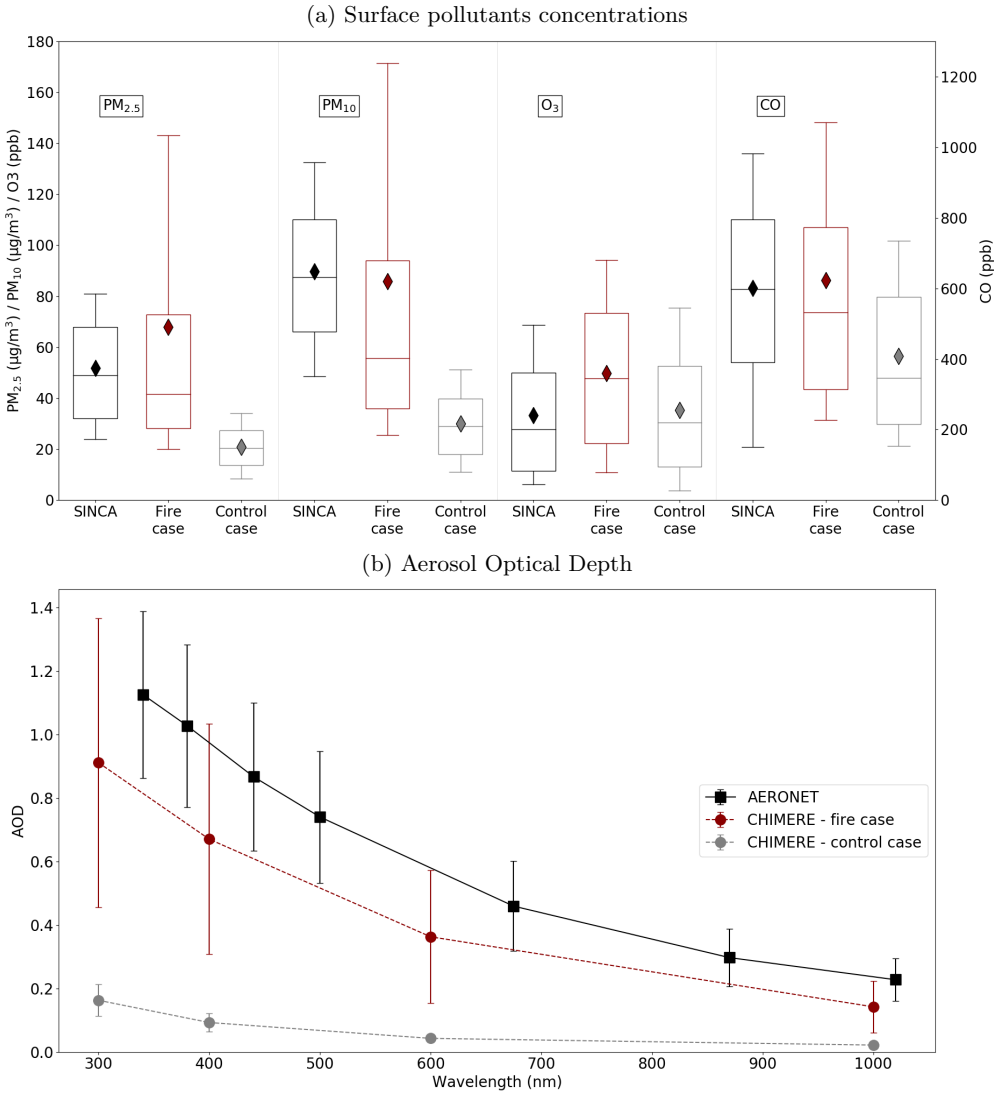

Figure 4.14: (**a**) Observed (black), and modeled (fire case in red, control case in gray) distribution of surface pollutants hourly concentrations in Santiago between 22 and 30 January. Distribution over 9 stations of the SINCA network (Parque O'Higgins, Las Condes, Independencia, Puente Alto, Pudahuel, La Florida, El Bosque, Cerrillos, Quilicura). Boxes show the median and first and third quartile, whiskers show 10% and 90% percentiles, diamonds show the mean. (**b**) AOD distribution by wavelength for the period 22 to 30 January for Santiago Beauchef AERONET station (same color code). Whiskers show one standard deviation.

For O_3, the simulations show an increase of mixing ratio by more than 10 ppb on average in the fire case compared to the control, which is consistent with the findings of Rubio et al. [2015] that showed significant O_3 transport to Santiago during the 2014 fires. However, the model is positively biased as the control case matches the observations while the fire case yields mixing ratios well above. Given the non-linearity of O_3 chemistry such a discrepancy can come from several uncertainty sources and does not allow to extract a quantitative estimate of the excess concentrations attributable to fires.

AOD in downtown Santiago also features a clear change in the signal when fire emissions are included (Figure 4.14b). During the days of strong fire intensity the observed AOD at 380 nm reaches elevated values as high as 1.5 on the daily average and up to 3 for one hour. Such levels are even higher than what is usually observed in wintertime when emissions from wood burning for residential heating strongly increase the aerosol load over the Metropolitan Area. Before the fire period, the usual summertime AOD daily mean of around 0.25 is recorded (not shown here). For the period between 22 and 30 January, in the control case, AOD at all wavelengths show average values between 0.01 and 0.2, while observations and simulation in the fire case indicate AOD around 1 at 300 nm and 0.3 at 1000 nm. The model shows a small negative bias and more spread

AOD distribution compared to observations from AERONET, at all wavelengths (mean bias of −0.12 and Pearson correlation coefficient of 0.45 at 340 nm on the hourly time series). For the larger wavelengths, the underestimation is consistent with the previous statement that the simulation is negatively biased regarding the coarse fraction of PM, even in the control case preceding the fire events. Furthermore, Santiago being near the edge of the main dense plume, the simulated signal at this grid point is tangential so that a small error in the transport or the magnitude of emissions will result in a relatively large bias there, which partly explains degraded performance, although standard deviations still overlap for every wavelength. Unfortunately, other AERONET stations in south-central Chile did not record any data for the period so that other comparisons are prevented.

A comparison of the volume size distribution of aerosols before and during the fires (Figure 4.22b) shows that both fine (diameter smaller than 2.5 µm) and coarse (diameter between 2.5 and 10 µm) mode are reinforced by the smoke plume, with a significantly larger increase in the fine mode, tied to the transport of BC and OC. In parallel, the SSA becomes more spread across wavelengths when fires start to kick in, with its values decreasing in the longer wavelengths (Figure 4.22a). Again, this relates to BC and OC being brought over to Santiago as these two species have SSA of around 0.5 and 0.8, respectively, when emitted from biomass burning [Bahadur et al., 2012], hence driving down the scattering efficiency compared to absorption. Again, fires affect aerosols properties measured in Santiago.

In summary, simulations and observations both point towards a large contribution of fire emissions to air pollution and modification of atmospheric composition in Santiago during the 2017 event. The model allows to quantify the burden induced by the transport of fire-emitted pollutants towards Santiago on $PM_{2.5}$ and CO concentrations in the capital city, as well as AOD, with excess concentrations of 30 µg/m^3 (+150%) and 200 ppb (+50%), respectively, and an increase of AOD by a factor between 6 and 8 for all wavelengths, on average for the period 22 to 30 January, and a peak at 2.5 in AOD at 500 nm recorded by AERONET during the event. However, the degraded performance on O_3 and PM_{10} in the capital city only allows for qualitative conclusions for these pollutants.

At the regional scale from satellites

Figure 4.15 compares satellite observations from IASI (Metop-b CO total column and O_3 partial column) and MODIS (AOD at 550 nm) to the corresponding simulated variables in CHIMERE. The satellite panels are gridded at 0.5° resolution and composited averaging all available data for each grid point over the period 25 to 29 January of high fire intensity. Simulation values are extracted at the corresponding passage times of Metop-b and Terra/Aqua, so as to recreate what the satellites would see if they observed the model.

(a) CO total column

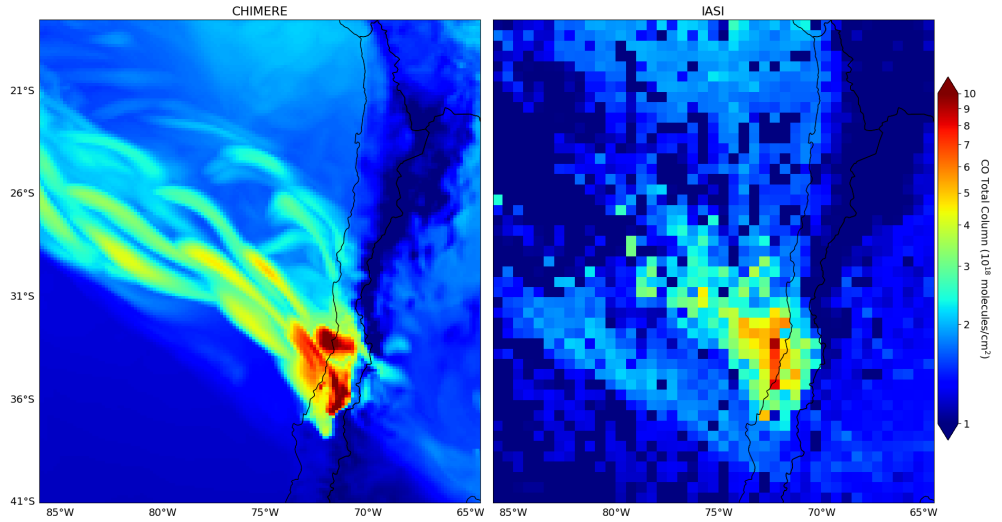

(b) O3 partial column

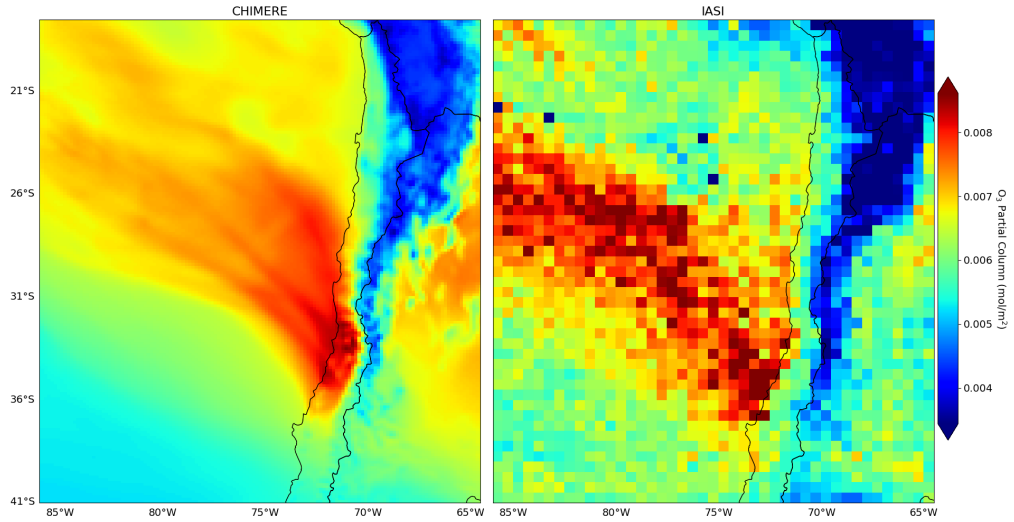

(c) Aerosol Optical Depth

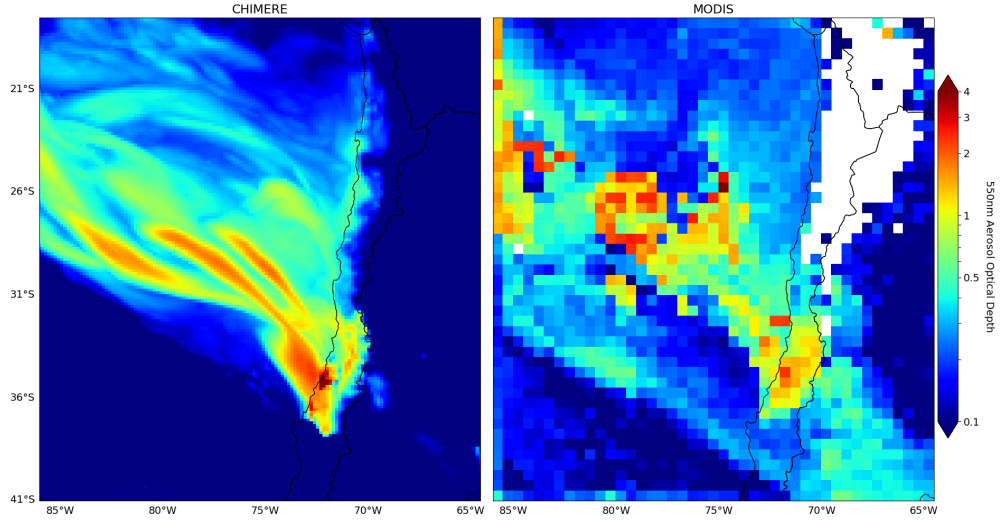

Figure 4.15: (**a**) CO total column composite as simulated by CHIMERE (**left**) and recorded by IASI Metop-b (**right**). (**b**) O_3 tropospheric column between 0 and 8 km altitudes composite as simulated by CHIMERE (**left**) and recorded by IASI Metop-b. (**c**) 550 nm Aerosol Optical Depth composite as simulated by CHIMERE (**left**) and recorded by MODIS Terra and Aqua level 2 products (**right**). All panels show composited averages for the period 25 to 29 January.

The simulation yields a CO total column slightly more intense than IASI near the emission area and a more extended plume. These discrepancies come from the discrete and partial nature of the data from IASI that feature many indeterminate values for the area and the period. However the shape of the plume and magnitude of the total column are well in accordance between measurements and modeling, showing a dense CO load up to 80° W and a blocking effect by the Andes cordillera towards the east (Figure 4.15a). O_3 partial columns also compare quite well in terms of the shape and extent of the plume, while the model mostly underestimates the O_3 load by a few percents. Again, the scarcity of valid measurements from satellite data leads to a bias where some grid points only have one value for IASI while CHIMERE shows an average for the period, hence shaving more the peak values. Nevertheless the magnitudes are still in good agreement, and both show an O_3 plume extending diagonally northwestward across 15° of longitude and latitude, i.e., around 2000 km (Figure 4.15b). Similar observations can be made for the comparison with MODIS data. The area of high intensity and downwind of the fires recorded AOD at 550 nm as high as 4 on average over the 5 days period (Figure 4.15c) and locally higher than 5 at a given point in time, suggesting significant direct radiative effects as explored later on in this work. Such AOD levels are comparable to what was recorded by MODIS during the fires in Australia in early 2020 and in Siberia in summer 2020 (see the NASA Worldview application for instance `https://worldview.earthdata.nasa.gov` (accessed on 2020, October 1st)), stressing again the exceptional character of the 2017 Chilean fires studied here. In summary, the combination of all panels in Figure 4.15 shows the large extent and high density of the plume generated by the 2017 mega-fires and the good performance of the simulation in reproducing the emissions and horizontal transport of fire-emitted pollutants over the region for this event.

The Vertical Feature Mask (VFM) product of CALIOP provides information on the altitude and nature of dominant aerosols along vertical transects [Winker et al., 2010]. CHIMERE outputs from the fire case are transformed so as to recreate what CALIOP would see from that perspective if it observed the model, as shown in Figure 4.16 for January 26 and 29 in the morning. For these two transects, the vertical shape of the plume is consistent between satellite and model data, except for the nature of the high elevation plume between 35° S and 30° S on 29 January, where CALIOP sees mostly polluted dust with a bit of elevated smoke, while CHIMERE simulates only elevated smoke, according to the VFM classification. Given the biomass burning nature of the event, the simulation's output and CALIOP records both make sense in this regard. Generally speaking there is good agreement on the vertical transects compared here, giving confidence in the model's ability to reproduce the vertical distribution of pollutants. CALIOP and CHIMERE both consistently show that the plume of aerosols was injected as high as 6 km above ground, the highest altitudes being reached above the ocean, for the plume downwind of the main fire locations. On 26 January over land, both find the smoke plume getting vertically more extended as it moves northward, indicating a possible ramping effect of the topography along that direction, combined with a channeling effect of the Andes cordillera.

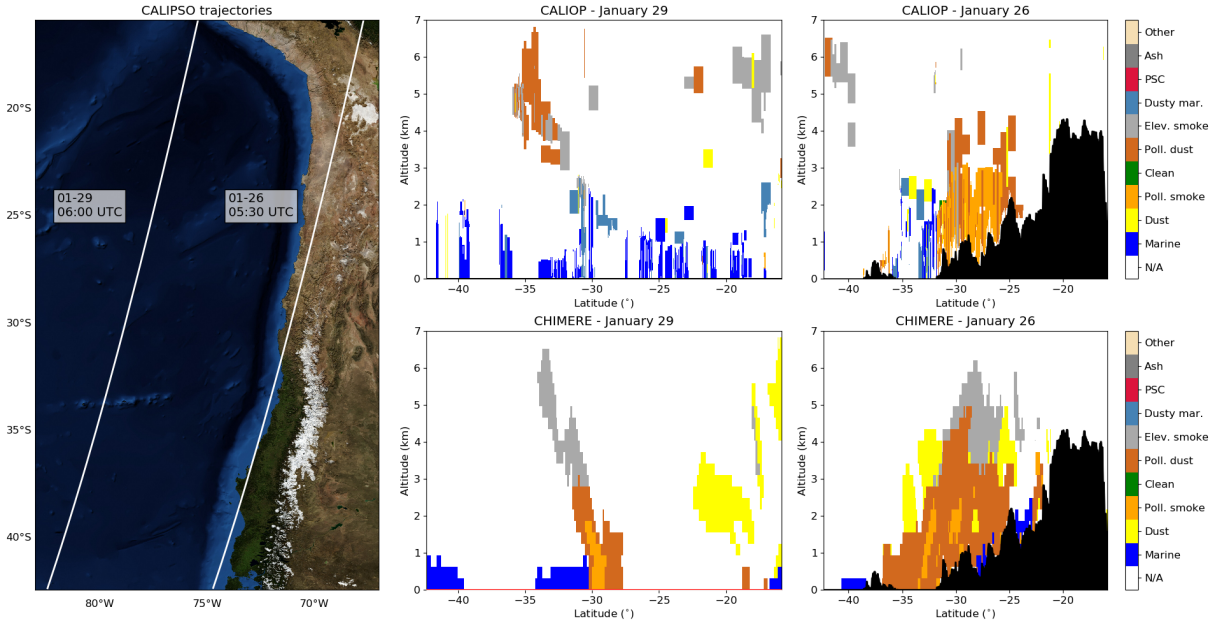

Figure 4.16: (**Left**) Trajectories of the CALIPSO legs for January 26 and 29 at 05:30 and 06:00 UTC, respectively, (white lines). Map background layer: Imagery World 2D, ©2009 ESRI. (**Middle** and **Right**) Vertical feature mask from CALIOP (top) and corresponding vertical feature mask extracted from CHIMERE for 29 and 26 January, respectively. Black filled contour shows terrain elevation along the transect.

A limitation to the previous comparison is the choice made for the translation from CHIMERE concentration fields into the VFM classification. The structure of the transect is somewhat sensitive to the mapping used between CALIOP optical indices and CHIMERE aerosol concentrations. In this work, an approach similar to Menut et al. [2018] is adopted to establish the correspondence and cope with the difficulties raised in the literature regarding CALIOP's detection algorithm [Omar et al., 2009, Chen et al., 2012, Winker et al., 2013].

In addition to a description at the regional scale of different aspects of the pollutants plume emitted by the 2017 biomass burning event, the previous analysis provides confidence in the model behavior both on the horizontal and the vertical, over land and the ocean. This legitimates the impact analysis on air quality and meteorology over the region that is carried on later on in this work.

At the regional scale from the model

Figure 4.17 shows the average excess surface concentration of CO, BC, O_3 and particle phase H_2SO_4 due to the fire activity, as well as two vertical transects (one along each main advection direction) of said concentrations, during the 2017 mega-fires peak intensity period (25 to 29 January). NB: In CHIMERE, 'particle phase H_2SO_4' is to be understood as 'sulfate aerosols', i.e., H_2SO_4 crystals and all sulfate in particle phase (ions, molecules, precipitates) deriving from the condensation of gas-phase H_2SO_4. The species considered are transported in significant amounts as far as 20° northward and 15° westward before vanishing or reaching the simulation domain boundaries. According to the vertical transects in Figure 4.17, the Andes act as a barrier, channeling pollutants on a meridional axis, and preventing their eastward dispersion, especially in the northern part of the cordillera where elevations are higher (transects (a) in Figure 4.17). In the south, summits are lower so that a fraction of the pollutants, particularly the gases, can travel above the mountains (a few ppb for O_3 and a few tens of ppb for CO). In that case, the Andes act as a ramp, injecting the pollutants higher up compared to the plume that goes westward over the ocean, in relation with mountain-valley circulation patterns governed by upslope winds during the afternoon. However, for fine particulate matter such as BC, even the lower Southern Andes act as an efficient barrier as the simulated concentrations near the summits are less than 1 µg/m^3.

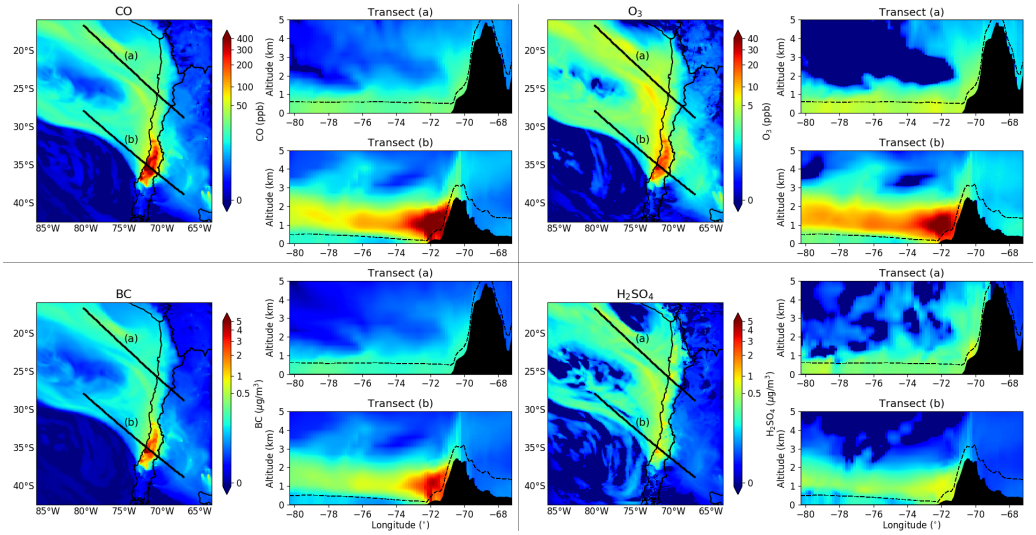

Figure 4.17: Excess concentrations of CO, O_3, BC and H_2SO_4 (particle phase) due to the contribution of fire emissions. Average for 25 to 29 January at the surface level and along two vertical transects. Each panel is composed of a map of surface concentrations (**left**), a northern transect along trajectory (a) shown in the surface map (**top right**), a southern transect along trajectory (b) shown in the surface map (**bottom right**). Black dashed line in the transects is the average mixing layer height along the transect. Black filled contours show terrain elevation.

The plume near the locations of higher fire intensity (transects (b) in Figure 4.17) is mainly contained in a layer between 1 km and 3 km altitude, above the mixing layer, rising steadily as it transports farther. Inside this plume, concentrations of CO, BC, O_3 and H_2SO_4 can reach values as high as a several hundreds ppb, tens of µg/m^3, several tens ppb and a few µg/m^3, respectively, with mean levels between100 and 1000 ppb, 1 and 10 µg/m^3, 10 to 50 ppb, and 0.5 to 1 µg/m^3, respectively. The other leg of the plume, in the north (transects (a) in Figure 4.17), is less dense and more homogeneous, mostly contained within the planetary boundary layer, except for the venting effect of the Andes that injects residual concentrations higher up and forms a secondary layer around 3500 m altitude near 72° W. It is worth noting that along this northern transect, O_3 above 2 km is slightly depleted in the fire case compared to the control case, by around 1 ppb on average. The main lower plume, where mixing ratios increase in the fire case is composed of O_3 formed close to the fires then advected, but in this depleted region, little O_3 is transported while simultaneously other gases such as CO or CH_4 reach this area. Although in minor quantities, the addition of these compounds slightly modifies the photochemical state of the atmosphere in this zone, reducing the availability of O_3 precursors, hence lowering the background mixing ratio. It is also interesting to see that the plume of H_2SO_4 is more homogeneously spread than the three other pollutants considered in Figure 4.17, without a sharp peak of concentrations near the fires location. This observation is consistent with the fact that the formation of H_2SO_4 (gas and particle phase) is favored in an ageing biomass burning plume compared to a fresh one [e.g. Fiedler et al., 2011]. The conversion rate of its precursor SO_2 is determined by the hydroxyl radical (OH) concentration. However, OH is primarily consumed by NO_2, also emitted in large amounts by the fires, one order of magnitude faster than by SO_2 [Seinfeld and Pandis, 2006], hence leaving little OH available for the latter. Accordingly, the plume of HNO_3 observed in the simulation and formed by the reaction of NO_2 against OH, shows a large spike near the fires origin as is observed for BC or CO (not shown here), corroborating the dominance of consumption of OH by NO_2 over SO_2 near the fires origin. As a result, although SO_2 is liberated in larger quantities near the fires origin (the SO_2 plume is similar in shape to that of CO - not shown here), the ability of H_2SO_4 to form increases as the plume moves further away and NO_2 levels decrease, hence leaving more OH available. The consequent H_2SO_4 plume is thus more homogeneous as quantities of SO_2 decrease as the plume ages but available OH quantities increase simultaneously.

Figure 4.18 highlights significant deposition fluxes of the considered species throughout the fire event. BC is deposited in large amounts over land near the fires origin with up to more than 500 µg/m^2 in a few days. Fluxes of BC are also important over the Andes mountain range. H_2SO_4 deposition is mostly observed over the ocean, far from the Chilean coast, with up to more than 2 mg/m^2 in the area [30° S; 80° W-25° S; 85° W]. Over the ocean, we find that both BC and H_2SO_4 are dominantly deposited via wet processes, while dry deposition occurs mostly near the fires origin over land. For these two species, the scattered deposition pattern

on the eastern side of the Andes north of the domain is artificial and due to a perturbation of precipitation in that region between the two simulation cases, and should not be attributed to the fire event as in this area dipoles of negative/positive changes in deposition cancel out eventually. O_3 is dominantly deposited over land, as its primary deposition process comes from the uptake by plant leaves. The model yields a total deposition of more than 50 mg/m^2 between 37° S and 32° S over the fires period for this pollutant. Possible impacts of the significant deposition fluxes of pollutants observed in Figure 4.18 associated with the particular locations they affect are further discussed in Section 4.2.5.

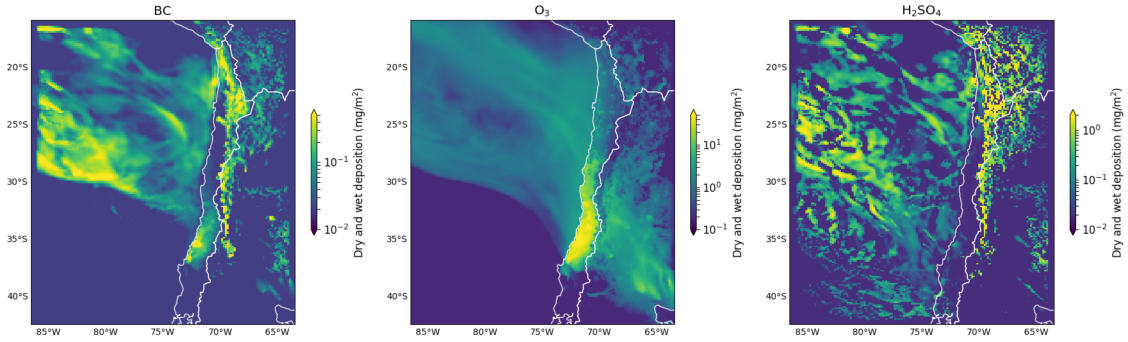

Figure 4.18: Accumulated deposition (dry+wet) of BC, O_3, and H_2SO_4 (particle phase) attributable to fires (fire-control) from 25 to 31 January. NB: deposition colormaps use a log scale.

In summary, biomass burning emissions from the 2017 mega-fires induced a dramatic input of pollutants into the atmosphere, with effects on health and possibly on ocean water, crop yields and glaciers albedo. In addition to such environmental feedback, impact on the regional meteorology are also at stake, as described hereafter.

4.2.4.2 Fires impact on meteorology

At the global scale, the atmospheric burden of gases and particles emitted by forest fires result in perturbations that have important consequences on climate. In particular, aerosols, especially light-absorbing particles, have a direct effect, scattering and absorbing solar radiation hence changing its nature and intensity when it reaches the ground. In addition to the modification of biogeochemical processes, this change in radiation affects temperature profiles and can in turn have an influence on atmospheric circulation. Indirect consequences of the release of such aerosols include the modification of the amount and properties of clouds, which has an impact on precipitation and albedo and thus radiation, entering a positive feedback loop [Andreae, 2019]. These direct and indirect effects, although conceptually accessible, are complex and hard to measure and model, hence being one of the main uncertainties in climate projections according to IPCC [2013]. Hereafter, we estimate the aforementioned effects attributable to the 2017 mega-fires on the regional climate of central Chile.

Indirect effects

Satellite imagery during a day of the period of intense fires (27 January) shows the formation of clouds above the Pacific ocean, downwind of fires, along the coast of central Chile (Figure 4.19a). Given the mixed brown/white colors of the cloud cover recorded by MODIS, the aerosols found in the fire smoke plume likely play a role in its formation. This hypothesis is tested using the simulation's sensitivity analysis. For that particular day, CHIMERE is consistent with MODIS regarding the location of the main fires (red spots in Figure 4.19a,b), and produces a cloud cover comparable to that observed by MODIS, with denser clouds along the plume (red contour in Figure 4.19b). Averaged over three consecutive days (27-29 January), we find that most of the cloud cover is found over the ocean along the aerosols plume (Figure 4.19c). For that smoke-affected region, defined by the light brown filled contour in Figure 4.19c, the difference in distribution of hourly cloud cover, between the fire and control case, is shown in Figure 4.19d for the three days aforementioned and compared to a previous period featuring limited fire activity.

During that latter period, given the very limited fire activity, emission rates are close between the fire and control cases, so that meteorological fields should not change significantly from one simulation to another. However, small changes are observed in the cloud OD distribution, symmetrical to zero, that are induced by the slight perturbation in emissions, resulting in a slightly different state of the atmosphere, inducing an artificial displacement of clouds. During the fire days however, the cloud OD distribution is significantly shifted

towards larger values in the fire case, indicating the thickening and creation of clouds due to the presence of fire-emitted aerosols acting as cloud condensation nuclei (CCN). Nevertheless, the simulated increase in cloud OD is significantly smaller than the average for the three days (up to 12 hourly in Figure 4.19d while the average is mostly above 20 in Figure 4.19c), so that according to the model, the cloud cover mostly preexists regardless of the presence of fires and is solely strengthened. This observation is further discussed in Section 4.2.5.

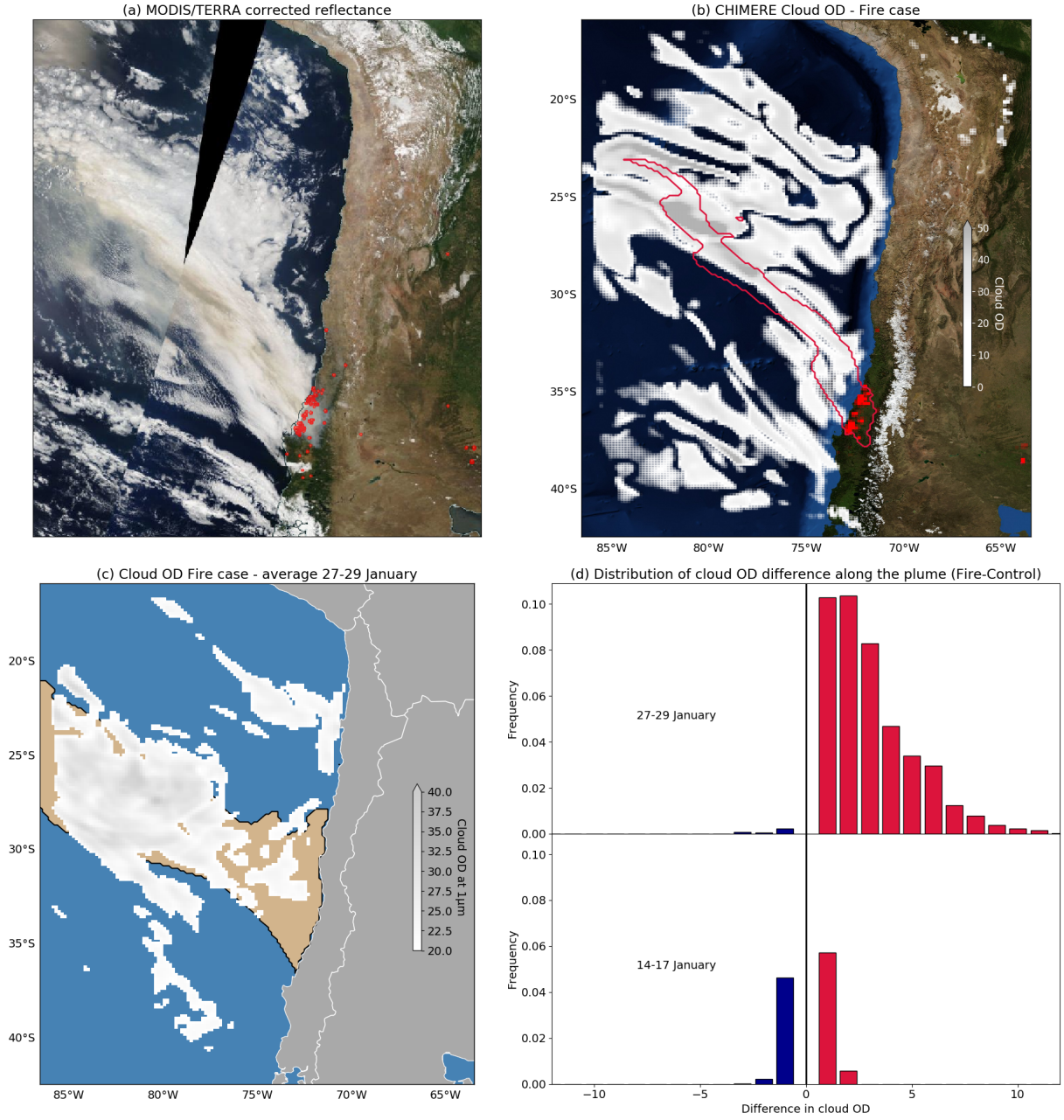

Figure 4.19: (**a**) Corrected reflectance product from MODIS/TERRA on 27 January provided by the NASA EOSDIS Worldview platform. Red spots show the fire and thermal anomalies as retrieved by MODIS. (**b**) CHIMERE simulated cloud OD at 1 µm at the passage time of MODIS on 27 January. Red spots correspond to the main emission sites at that time in the simulation. Red contour shows the shape of the aerosol plume originating from the fires. Map background layer: Imagery World 2D, ©2009 ESRI. (**c**) Cloud OD at 1 µm in the fire case averaged for 27 to 29 January (colormap). The light brown shade shows the extent of the PM plume originating from the fires. (**d**) Distribution of the cloud OD change in the fire case compared to the control case, over the region defined by the light brown shade in (**c**), for a fire period (27-29 January) and a non-fire period (14-17 January). NB: the central $[-0.5, 0.5]$ bin is removed for improved readability.

Combined effects

In addition to the aforementioned indirect effects, direct effects superimpose, tied to radiation perturbation by the scattering and albedo effects of the particles themselves. In particular, under clear-sky conditions the addition of light-absorbing particles in the atmosphere reduces the downwelling solar radiation reaching the ground. The interaction between aerosols and radiation leads to rapid adjustments over land, which are even more marked with dark aerosols such as BC [Boucher et al., 2013].

Figure 4.20a shows a large reduction, on average over four intense fire days, of ground shortwave radiation by up to more than 100 W/m^2 locally, especially over land near the fires origin and over the ocean in the region of denser cloud cover. A direct consequence over land is a decrease in surface air temperature by up to 1 K on average (Figure 4.20b). Over the ocean on the contrary, a slight warming is observed near the coast. The heat capacity of the ocean is high, so that it has a strong thermal inertia. Thus, the response to the change in daytime radiation is limited, while at night the layer of aerosols yields back heat and traps outgoing radiation at the same time so that the ocean cools less than normally. All combined, this results in the observed surface air slight warming over the Pacific shore contrasting with the cooling over land. Similarly, the reduction in surface radiation limits the development of the planetary boundary layer, making it lower by up to 100 m over land on average over the period. In turn, this shallower mixing layer implies that pollutants are even more concentrated, since diluted in a smaller volume, hence evidencing a positive feedback loop. Furthermore, given the radiation-driven nature of surface winds in mountain environments, the decrease in solar energy reaching the ground leads to slightly lower wind speeds over the south-central Chilean land (Figure 4.20d). During daytime, the differential heating of air masses between plains and valleys usually gives rise to westerlies blowing towards the Andes. However, during the fire event, the lesser fraction of radiation reaching both environments prevents this phenomenon of mountain-valley circulation from happening, as would be the case during cloudy days [Whiteman, 2000]. Over the ocean no clear pattern is observed in this regard. Numerous small perturbation dipoles appear in Figure 4.20 especially far from the fire event. The displacement phenomenon mentioned previously is responsible for this noisy appearance.

The standard deviation associated with the mean effects presented in Figure 4.20, is generally speaking of the order of magnitude of the mean for the whole domain (not shown here). This indicates that the feedback is variable in time, with a large heterogeneity depending on the activity of the fires and with a strong diurnal cycle, although it is significant based on statistical tests.

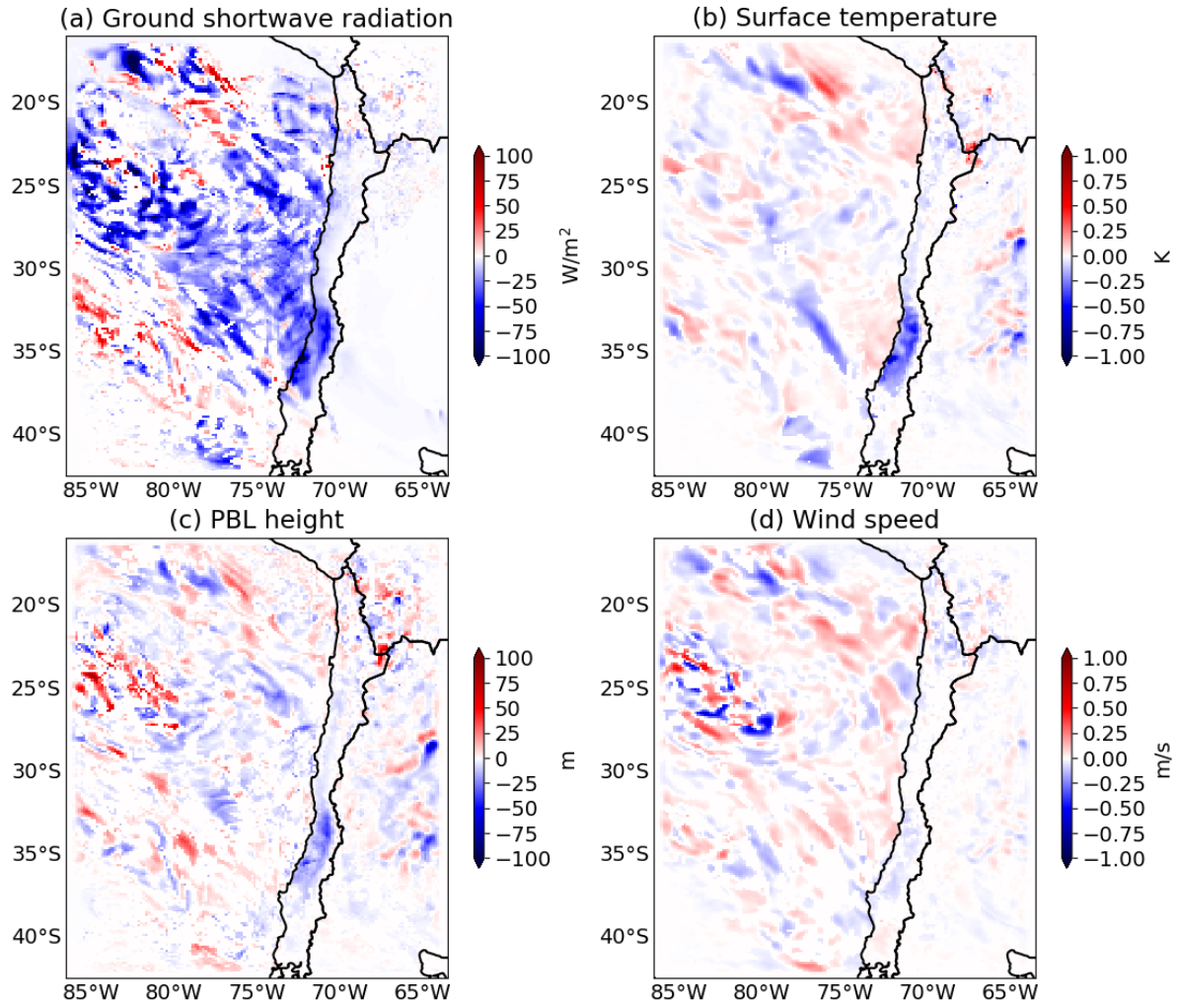

Figure 4.20: Effect of fire emissions on (**a**) surface shortwave radiation, (**b**) planetary boundary layer height, (**c**) surface air temperature, (**d**) 10 m wind speed. Difference between the fire case and control case. Average for 26-29 January. Only grid points where the distribution of concentrations in the fire case is different than in the control case at the 99% level, based on a Wilcoxon test, are shown.

4.2.5 Discussion

Significant deposition of pollutants originating from fire emissions were observed in Figure 4.18, which potential environmental impacts are discussed hereafter. Although the effects of BC deposition on vegetation is still debated - partly fertilizing when deposited on the ground [Shrestha et al., 2010], partly detrimental when deposited on the leaves [Anda and Illes, 2012] - the large deposition fluxes at stake might be of importance. Such deposition also occurs on high altitude areas in the Andes, with possible impacts on glaciers albedo [Zhang et al., 2017, Kang et al., 2020]. Furthermore, BC is known to be an important carrier of phosphorus into the ocean at the global scale, hence stimulating bacterioplankton and influencing microbial diversity [Weinbauer et al., 2017]. However, the Humboldt current along the coast of Chile and Peru being already a thriving ecosystem, with an abundance of marine plants and animals, the input from forest fires through BC as evidenced in Figure 4.18, is not large enough to be expected to provide a significant change in the biodynamics of the area in terms of nitrogen, phosphorus, iron and silicon intake. Sulfuric acid (H_2SO_4) formed through SO_2 oxidation is highly soluble in water and tends to acidify the solution. Although ocean acidification is dominated by the dissolution of excess atmospheric CO_2 at the global scale, the deposition of sulfuric acid as observed in Figure 4.18 might locally and sporadically contribute to the decrease of ocean water pH and alter its alkalinity and inorganic carbon storage [Doney et al., 2007], with consequences on the ocean's viability for native plants and animal species. O_3 is known to have detrimental effects on plants yield when deposited on the leaves [Hill and Littlefield, 1969].

The large deposited quantities of this compound over land found by the model may thus suggest a potential loss in crop yields in 2017 although this hypothesis does not seem to have been investigated so far.

When looking at satellite images (Figures 4.19a and 4.23) one could arguably imagine that the observed coastal clouds near the fires would not have been formed without the CCN input stemming from those fires, as the rest of the region features mostly clear skies pointing towards conditions not favorable for cloud formation. The model says otherwise though, evidencing only a thickening of these clouds, but on the other hand seldom generates the clouds closest to the coastline that appear in the satellite images, while cloud cover far from the coast is adequately reproduced throughout the simulation in both the fire and control case. Several sources of bias in the simulation can explain the absence of coastal clouds (injection height of emissions, CCN activation parameterization, dry bias on humidity...). According to MODIS Terra cloud top height product (MOD06), the investigated coastal clouds were found mostly below 800 m above ground level. Our simulation consistently generates a CCN maximum number at around 500 m in the area of interest, although no clouds are formed near the coast due to unsaturated water vapor (relative humidity is around 0.95). Thus, the argument can be made that such coastal clouds indeed originate in the condensation of water vapor on fire-emitted nuclei, but small biases in the state of the atmosphere prevent them from being generated in the simulation. Furthermore, important processes are not yet taken into account in CHIMERE when in comes to biomass burning, such as the release of water vapor and heat by the fire, which can affect relative humidity. The representation of pyroconvection in coupled mode is also a development point of the model, as we would expect the phenomenon to lead to air masses convergence near ground-level hence affecting 10 m wind speed, which we showed is moderately changed and mostly due to the aerosol direct effect. Whether the observed coastal clouds would have existed without the fire event is thus not obvious, despite major implications in terms of meteorological feedback. In order to investigate this question on a climatological time scale, a long-term analysis based on clusters of MODIS cloud cover/height data with/without fire activity could be conducted, although it is out of the scope of this work.

4.2.6 Conclusions

This study investigated the impacts on air quality and meteorology of the early 2017 historic mega-fires in south-central Chile. Based on a chemistry-transport modeling approach with the fully coupled WRF-CHIMERE model, a set of two simulations was performed to assess the sensitivity of atmospheric variables to the occurrence of the aforementioned fires. Surface and satellite observations were used to describe the event and assess the quality of the simulation. The pollutants plume originating from the fires spread across more than 2000 km, and up to 7 km above sea level on the vertical, causing AOD at 550 nm over the Pacific ocean off the coast of Chile to rise up to 4 on average for the most intense days. As a result, surface concentrations of pollutants in Santiago rose by +150% for $PM_{2.5}$ (+30 µg/m^3) and +50% for CO (+200 ppb), and a multiplication of AOD at all wavelengths by a factor 6 to 8 (+0.2 to +0.9 on average) was induced in the capital city, with a peak at 2.5 in AOD at 500 nm, explaining the serious health impacts of these fires recorded in the literature. Pollutants were also consequently deposited in large amounts over the land, the Andes cordillera and the Pacific ocean. Detrimental as well as fertilizing impacts can arise and should be further investigated. In addition to atmospheric composition and environmental impacts, the fire event showed a meteorological feedback with enhanced cloud formation over the ocean (aerosol indirect effect), as well as decreased surface radiation by up to 100 W/m^2, surface temperature by up to 1 K and mixing layer height by up to 100 m, on average, with disparities between land and ocean. Such modifications are substantial and should be taken into account in future projection scenarios, that foresee an increased frequency of biomass burning events of this magnitude in the region.

4.2.7 Appendix

WRF configuration		CHIMERE configuration	
Horizontal resolution	15 km	Horizontal resolution	15 km
Vertical levels	33	Vertical levels	30
Time step	30 sec	Physical time step	15 min
Microphysics	Thompson aerosol-aware	Chemistry	MELCHIOR2
Boundary and surface layer	MYNN	Land Use	USGS
Land surface	Noah LSM	Horizontal Advection	Van Leer
Cumulus parameterization	Grell G3	Vertical Advection	Van Leer
Longwave/Shortwave radiation	RRTMG	Boundary Conditions	LMDz-INCA

Table 4.5: WRF and CHIMERE configurations.

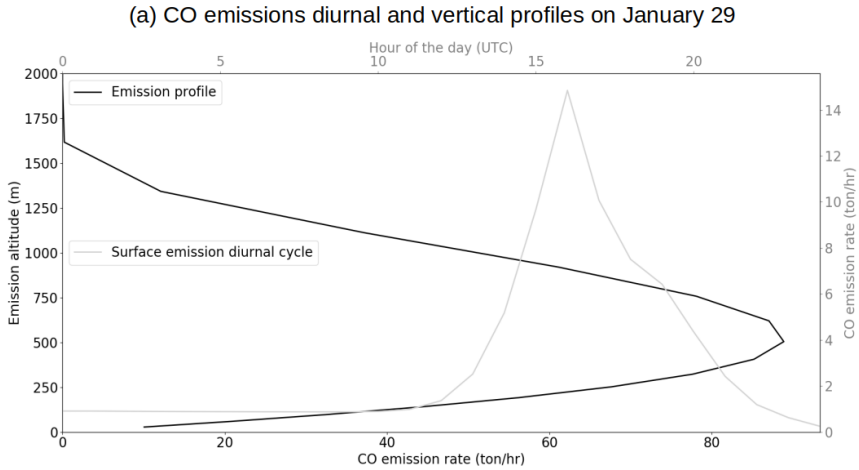

(b) Chemical composition at emission

Species		Ratio at emission
C2H4	Ethene	1.1%
C2H6	Ethane	0.4%
C3H6	Propene	0.9%
CH3CHO	Acetaldehyde	0.4%
CH3COE	Methyl Ethyl Ketone	0.1%
CH4	Methane	5.2%
CO	Carbon monoxide	82%
HCHO	Formaldehyde	0.9%
NC4H10	n-Butane	0.3%
NH3	Ammoniac	1.6%
NO	Nitrogen monoxide	1.5%
NO2	Nitrogen dioxide	0.2%
SO2	Sulphur dioxide	0.2%
TOL	benzene, toluene and other mono-substituted aromatics	0.1%
OC	Organic carbon	2.1%
BC	Black carbon	0.2%
PPM_fin	fine PPM	1.8%
PPM_coa	coarse PPM	1.3%

Figure 4.21: (**a**) CO emissions diurnal (gray line) and vertical (black line) profile on 29 January at the grid point of maximum intensity. (**b**) Molecular ratio of fire-emitted species at emission for the same grid point. Percentages give the number of molecules of each species over the total number of all molecules emitted by the fires.

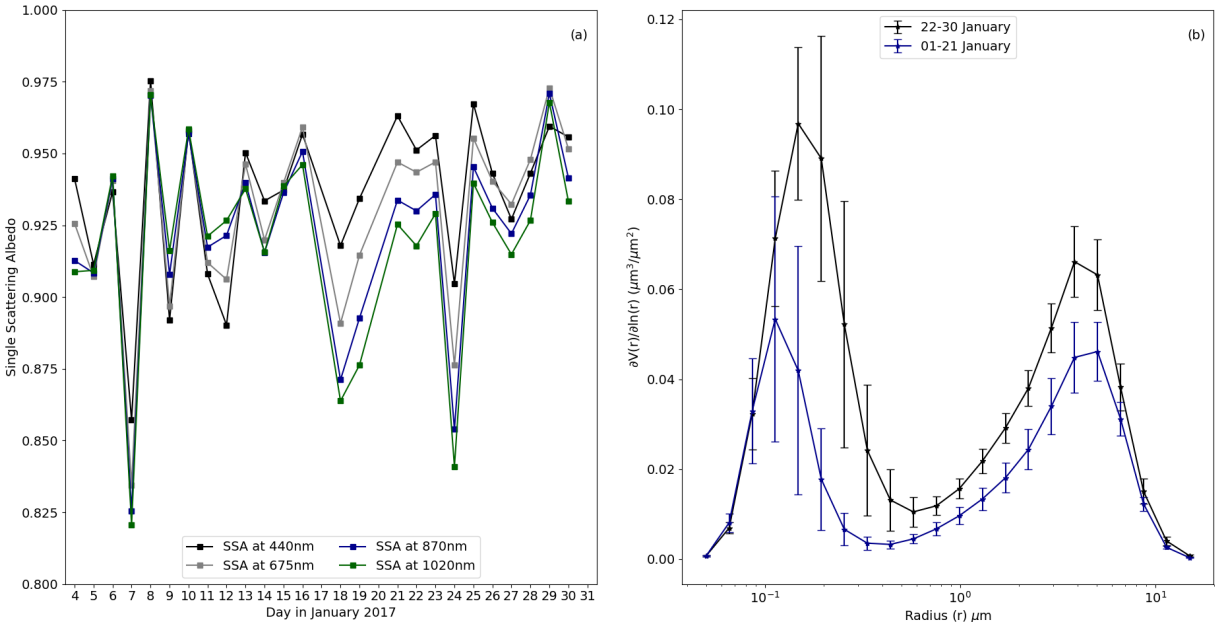

Figure 4.22: (**a**) SSA at 20:00 UTC recorded by AERONET (440, 675, 870 and 1020 nm) in January 2017. (**b**) Volume size distribution of aerosols before and during the fire events. Whiskers show one standard deviation. Observations from Santiago Beauchef AERONET station.

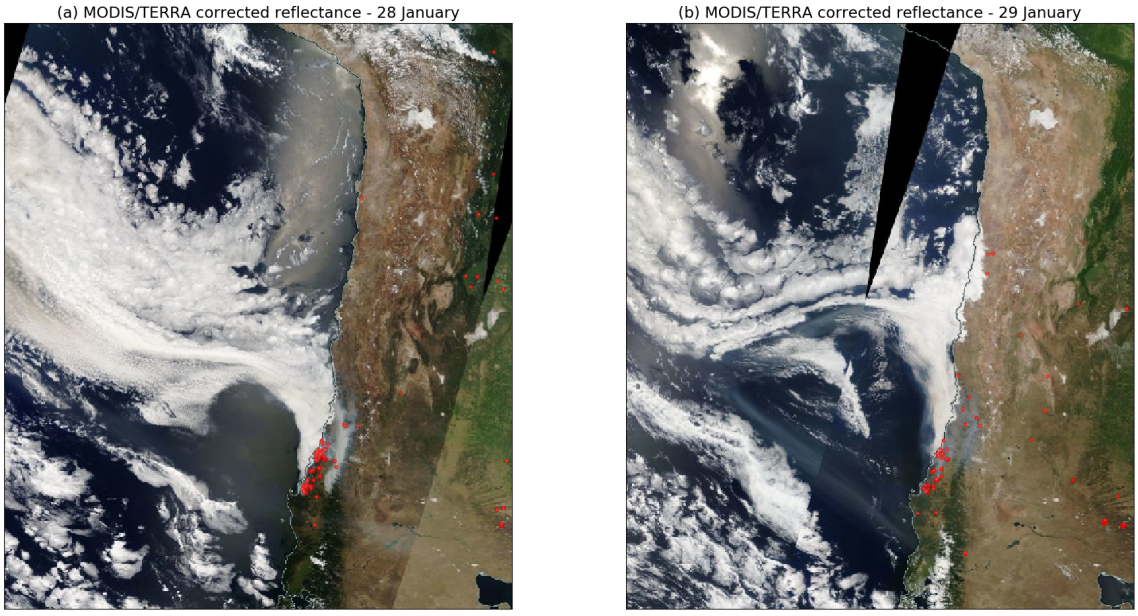

Figure 4.23: (**a**) Same as Figure 4.19a for 28 January. (**b**) Same as (**a**) for 29 January.

5 | Urban black carbon and the Andean cryosphere

5.1 Pathways for wintertime deposition of black carbon on the Central Andes cryosphere

This section combines results from Lapere et al. [2021b] and Huneeus et al. [2021], that focus on the wintertime transport mechanisms of urban pollutants from Santiago towards the Andes, using high-resolution CHIMERE simulations for the former, and data from a dedicated measurement campaign and reanalysis for the latter. Although the structure of the contents hereafter merges Lapere et al. [2021b] and Huneeus et al. [2021], text and figures are directly extracted from the corresponding articles.

5.1.1 Abstract

Ice and snow in the Central Andes contain significant amounts of light-absorbing particles such as black carbon. The consequent accelerated melting of the cryosphere is not only a threat from a climate perspective but also for water resources and snow-dependent species and activities, worsened by the mega-drought affecting the region since the last decade. Given its proximity to the Andes, emissions from the Metropolitan Area of Santiago, Chile, are believed to be among the main contributors to deposition on glaciers. However, no evidence backs such an assertion, especially given the usually subsident and stable conditions in wintertime, when the snowpack is at its maximum extent. Based on high-resolution chemistry-transport modeling with WRF-CHIMERE, the present work shows that, for the month of June 2015, up to 40% of black carbon dry deposition on snow or ice covered areas in the Central Andes downwind from the Metropolitan area can be attributed to emissions from Santiago. Through the analysis of aerosol tracers we determine (i) that the areas of the Metropolitan Area where emissions matter most when it comes to export towards glaciers are located in Eastern Santiago near the foothills of the Andes, (ii) the crucial role of the network of Andean valleys that channels pollutants up to remote locations near glaciers, following gentle slopes. A direct corollary is that severe urban pollution, and deposition of impurities on the Andes, are anti-correlated phenomena. Finally, a two-variable meteorological index is developed that accounts for the dynamics of aerosol export towards the Andes, based on the zonal wind speed over the urban area, and the vertical diffusion coefficient in the valleys close to ice and snow covered terrain. Numerous large urban areas are found along the Andes so that the processes studied here can shed light on similar investigations for other glaciers-dependent Andean regions.

5.1.2 Introduction

The chapter on High Mountain Areas, from the IPCC's Special Report on the Ocean and Cryosphere in a Changing Climate (SROCC) [Hock et al., 2019] highlights the threats posed by the feedback associated with deposition of light absorbing particles on snow and glaciers, that induce surface air warming along with accelerated snow cover reduction. Recent studies over the Tibetan Plateau show that light-absorbing particles are responsible for about 20% of the albedo reduction of glaciers at the end of winter, corresponding to a radiative forcing of up to hundreds of $W\,m^{-2}$, hence accelerating their melting during the warmer season [Zhang et al., 2017, Kang et al., 2020]. In addition to a positive radiative feedback on climate, local impacts on water resources, population security, ecosystems, infrastructure and tourism are also at stake.

Glaciers in Chile have been shrinking over the recent decades, in particular in the Central Chilean Andes (32°S to 36°S) where large glaciers feed valleys rich in agriculture and large populated centers such as Santiago, Chile's capital [Pellicciotti et al., 2013]. Although the role of anthropogenic black carbon (BC) on the retreat of glaciers has not been established for South American glaciers, previous studies suggest that deposition of BC on snow can affect the length of the snow cover season in the Northern hemisphere reducing its duration by up to 10 days in boreal and temperate regions [Ménégoz et al., 2013] and up to 8 days in the Himalayas [Ménégoz et al., 2014]. The current mega-drought in Central Chile exacerbates the retreat of the Central Andean glaciers and threatens the sustainability of water resources in the region [Garreaud et al., 2017, 2020]. The stakes are thus high for urban areas neighboring the Andes cordillera. In this context, BC deposition on the Central Andes glaciers represents an additional burden, and as the management of water resources becomes paramount in the region for the coming years, a detailed knowledge of the processes and sources leading to the presence of BC in glaciers is essential.

A likely contribution of anthropogenic pollution to the observed retreat of glaciers in the Central Andes was found [Molina et al., 2015, Rowe et al., 2019]. In particular, the significant amount of atmospheric pollutants emitted in Santiago, Chile is hypothesized to influence ice composition in nearby glaciers [Cereceda-Balic et al., 2012, Rowe et al., 2019]. Indeed, the city regularly faces high levels of fine particulate matter pollution, of which

BC, in wintertime, mainly due to massive emissions from wood burning for residential heating and diesel-fueled vehicles [Barraza et al., 2017], but also to episodic strong emissions from barbecue cooking [Lapere et al., 2020]. Nevertheless, no evidence was found so far to confirm that BC emissions from Santiago are able to deposit on the Central Andes glaciers, particularly given the subsident conditions associated with a shallow stable boundary layer and a persistent inversion over the city observed during winter months [Garreaud, 2009], when most residential wood burning emissions occur and snow extent is at its maximum. Furthermore, Santiago is only 500 m above sea level, while nearby Andean mountains reach altitudes as high as 5800 m, which represents a huge obstacle to go over for these stable, non-convective air masses. In particular, Cordova et al. [2016] found that at the beginning of spring 2014, air masses reaching an Andean valley southeast of Santiago barely interacted with urban air from the city. On the other hand, Gramsch et al. [2020] has shown recently that for the northern part of Santiago, emissions from the urban area can contribute significantly to atmospheric concentrations observed higher up in the cordillera, with limited export in wintertime compared to summertime.

Studies over the Himalayas and the Alps show that an effective pathway for deposition of anthropogenic particles on glaciers is channeling through valleys [Ming et al., 2012, Diémoz et al., 2019a]. However, wintertime conditions lead to a minimum intensity of this phenomenon [Diémoz et al., 2019b]. Also, during fair weather convective days, vertical export of air masses from the boundary layer into the free troposphere can occur through topographic venting [Henne et al., 2004]. Again, this mechanism is less active under stable cold conditions. Holmes et al. [2015] suggest enhanced vertical mixing over complex terrain in wintertime under cloudy conditions, in the western United States. Nonetheless, given the quite unique configuration of the Andes cordillera, the processes at play for a potential wintertime export of pollutants from Santiago basin up to the Andean glaciers are not well known, and are investigated in this study.

The objective of this work is to provide a first assessment of the burden of Santiago's emissions on BC deposition over the Central Andean snowpack, and to understand why this contribution can be significant while the mainly stable meteorological conditions observed in wintertime would lead to think that the export of pollutants is prevented. To do so, a combination of observations and chemistry-transport modeling with WRF-CHIMERE is used to determine the amount of BC deposition on glaciers attributable to emissions from Santiago and the associated pathways.

5.1.3 Data and methods

The present work relies for a large part on chemistry-transport modeling with WRF-CHIMERE. Atmospheric composition and meteorological measurements are also used, for analysis purposes as well as for assessing the quality of the simulations. These two components are described hereafter.

5.1.3.1 Observational data

Time series of hourly surface measurements of meteorology and air quality are extracted from the automated air quality monitoring network of Santiago (SINCA - `https://sinca.mma.gob.cl/index.php/region/index/id/M`, last access 28 April 2020). Climatological daily rainfall and temperature data at DMC is issued from the Chilean Weather Service (DMC, from Spanish *Direccion Meteorológica de Chile*) and accessible from the Chilean Center for Climate Science and Resilience through their online database *Explorador Climático* (CR2 - `http://explorador.cr2.cl/`, last access 28 April 2020). For the analysis of the model's ability to reproduce a specific transport event with complex topography, additional data from a dedicated one-week campaign carried out in Santiago and the adjacent Maipo canyon, including vertical profiles of BC, have been used. This campaign was conducted from Monday 20 until Sunday 26 July 2015. In each one of the three sites defined during the campaign (locations DMC downtown Santiago, VZC at the entrance of the Maipo canyon, and GYC inside the meridional branch of the canyon - a map is provided later on), hourly surface measurements of standard meteorological parameters and PM_{10} concentration were conducted. In addition, vertical profile measurements of BC (via a mini-aethalometer) and standard meteorological parameters are available up to 1 km above ground, from tethered balloon, every 3 hours.

5.1.3.2 Modeling setup

The chemistry-transport simulations use the Weather Research and Forecasting (WRF) mesoscale numerical weather model [Skamarock et al., 2008] to simulate the meteorological fields, and CHIMERE to compute chemistry and transport. Anthropogenic emissions are taken from the EDGAR-HTAP inventory. Two simulation domains are considered and described in Figure 5.1 and Table 5.1, with a coarse domain at a 5 km spatial resolution

including Central Chile (referred to as CC5 hereafter), and a nested domain focusing on Santiago area at a 1 km resolution (referred to as STG1 hereafter). The model configuration used in this study is presented in Table 5.2. WRF is applied to 46 vertical levels up to 50 hPa, in a two-way nested fashion. Initial and boundary conditions used are from the NCEP FNL analysis, with a 1° by 1° spatial resolution and 6-hour temporal resolution, from the Global Forecast System [NCEP, 2000]. Land-use and orography are based on the modified IGBP MODIS 20-category database with 30 sec resolution [Friedl et al., 2010]. CHIMERE is a Eulerian 3-dimensional regional Chemistry-Transport Model, able to reproduce gas-phase chemistry, aerosols formation, transport and deposition. In this study the 2017 version of CHIMERE is used [Mailler et al., 2017]. The configuration is described in Table 5.2. The EDGAR HTAP V2 dataset provides the anthropogenic emissions inventory, which consists of 0.1° gridded maps of air pollutant emissions for the year 2010 [Janssens-Maenhout et al., 2015]. A downscaling is applied to this inventory based on land-use characteristics, and monthly emissions are split in time down to daily/hourly rates following the methodology of Menut et al. [2013].

Domain	Horizontal resolution	Purpose	Key output
CC5	5km (100x200 grid points)	Scenario on BC urban emissions	Contribution of BC from Santiago to deposition on glaciers
STG1	1km (100x100 grid points)	High resolution transport of tracers without chemistry	Pathways of aerosols from Santiago to the glaciers

Table 5.1: Description of CC5 and STG1 domains and their purposes. Both are centered on Santiago.

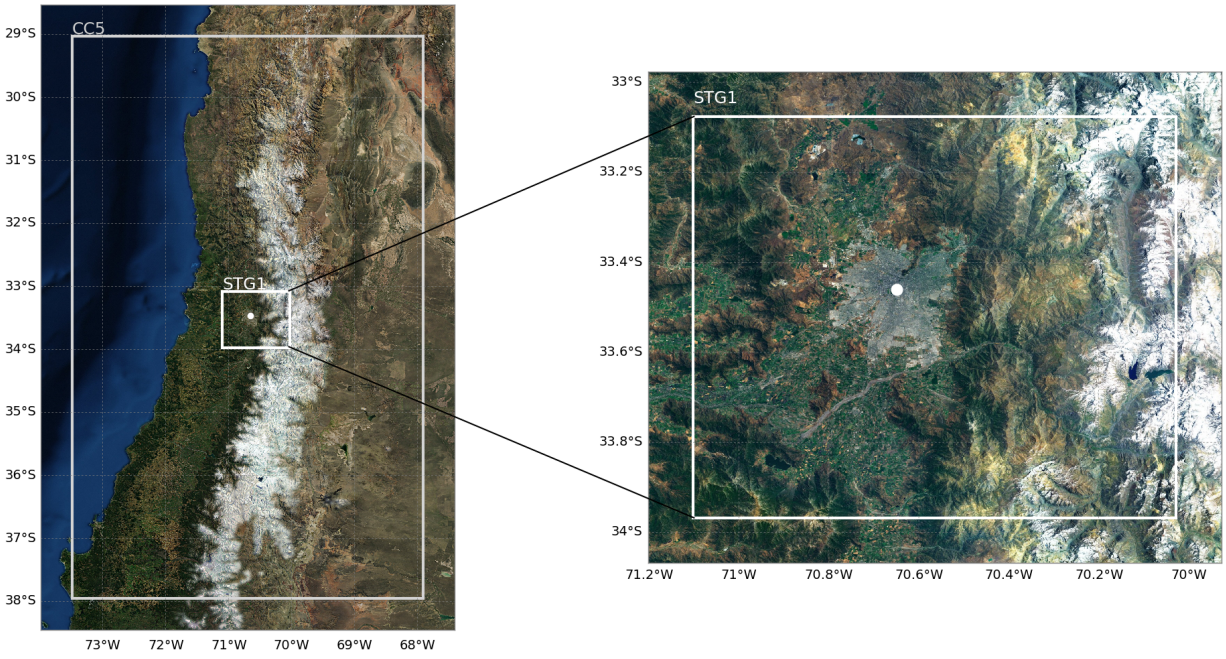

Figure 5.1: Left: coarse simulation domain at 5 km resolution - CC5. Right: nested domain at 1 km resolution - STG1. In both maps the white dot shows the location of downtown Santiago. Map background layer: Imagery World 2D, ©2009 ESRI.

The simulated period is 16 June to 31 July 2015. The period from 16 June to 30 June is used for spin-up and thus not analyzed. The choice to simulate the month of July 2015 is justified by the availability of dedicated measurements evidencing some of the processes studied here on the one hand, and on the other hand this month of the year is interesting for its combination of a large snow cover and high pollutants emissions at the same time. In June, pollution levels are similar but the extent of the snow cover is lesser, while August shows a more developed snowpack but less pollution in the city. In addition, meteorological conditions for July 2015 are

climatologically typical of July, with daily mean, maximum and minimum temperatures in downtown Santiago of 9 °C, 12.6 °C and 5.5 °C, respectively, to be compared with the 2000-2019 median values of 8.4 °C, 12.1 °C and 4.3 °C respectively (Fig. 5.19a). Precipitation in Santiago is also well in the range of the 21st century values with a daily mean at 1.2 mm close to the recorded 1.1 mm median over the last 20 years (Fig. 5.19a). As for the wind regime, the mountain-valley circulation induced dipole of south-westerlies and easterlies in Santiago is consistent, with similar average wind speeds along these two main directions for the climatology and July 2015 (Fig. 5.19b and 5.19c, respectively). Simulation scores for meteorology and atmospheric composition, against observations at stations of the urban area, can be found in Tables 5.3, 5.4 and 5.5. Surface wind and temperature, as well as vertical profiles for these two variables decently reproduce observations for several locations in Santiago. Thermal inversions are also successfully captured. Concentrations of $PM_{2.5}$ simulated in the CC5 case are in reasonable agreement with surface observations in the Metropolitan Area of Santiago.

For the CC5 domain, two simulations are performed. One with a full emissions inventory - referred to as baseline case or BS in the continuation - and one with an inventory setting emissions from Santiago area to zero - contribution case or CS. The comparison of these two simulations yields the share of emissions from Santiago in the atmospheric composition and deposition of pollutants in the region. As an example, the emission inventory extracted from EDGAR HTAP used for BC is provided in Figure 5.2a. The black rectangle on the inventory map defines the limit of the grid points belonging to the Metropolitan area of Santiago. The model points inside this zone see their emission rates of BC set to zero in the CS simulation so as to perform the sensitivity analysis. The nested STG1 domain is designed for the finer study of pollution export processes and corresponds to the black square in Fig. 5.2b (which is a slightly different area than the black rectangle in Fig. 5.2a). Chemistry is not activated in this domain since the studied compounds are reduced to passive aerosol tracers (fine mode, density of 1.7 g cm^{-3}), distributed over the Santiago Metropolitan Area according to Figure 5.2b. Tracers emission rates are the same for every location, and can be found in Figure 5.2c. Emission rates are adapted from HTAP data so as to emit the same total mass of BC as a typical 1 km^2 grid point of the urban area. A daily cycle is then applied on these emission rates to be as close to actual emissions dynamics as possible. Such a configuration allows for the study of the pathways of pollution depending on their origin in the basin, and assess the preferred origin of polluted air masses reaching elevated, snow-covered sites. The nesting between STG1 and CC5 is only used for meteorological conditions simulation purposes in WRF but deactivated for CHIMERE, as the targets in terms of atmospheric composition study differ between the two domains.

5.1.4 Contribution of emissions from Santiago to BC deposition

The following analysis estimates the contribution of emissions from Santiago to BC deposition on the nearby Andean snow or ice-covered areas in wintertime. The influence and reach of pollutants emitted in different districts within Santiago is also studied.

5.1.4.1 Contribution of the Metropolitan Area

The following analysis is based on the 5 km CC5 CHIMERE simulations. Details of their configuration and validation can be found in Section 5.1.3 and 5.1.10. Two simulations are compared, one with a full emissions inventory (BS), one where emissions from Santiago area are set to zero (CS). The difference yields an estimate of the share of Santiago's emissions in the atmospheric composition of the region. Snow measurements from Rowe et al. [2019] estimate the surface deposition rate of BC at the *Yerba Loca* site near Santiago (33.33°S, 70.33°W - see YBL in Figure 5.2b) in July 2016 to around 5.2 mg m^{-2} for the month. For the same location, the baseline simulation (BS) yields 8.7 mg m^{-2} for July 2015, which is comparable in terms of magnitude although these numbers are not for the same years, and despite the relatively coarse resolution of the simulation. We also acknowledge the absence in the EDGAR HTAP emission inventory, of the significant BC source linked to the nearby mining activity at *Los Bronces* (33.15°S, 70.28°W), which may be a source of discrepancy between measurements and modeling, although there is no evidence these emissions reach the site of *Yerba Loca*. Nevertheless, in addition to the good reproduction of meteorology and atmospheric composition observed in Santiago, and despite several sources of uncertainty, having the proper order of magnitude for deposition at this location gives confidence in the behavior of the simulation.

Figure 5.3 shows the amount (a and b) and proportion (c and d) of the total BC deposition attributable to Santiago emissions for July 2015. This is achieved by representing the difference between the total deposition in the BS case and in the CS case (BS-CS), and the ratio (BS-CS)/BS. Clearly, BC emissions from Santiago mainly affect low elevation areas nearby, particularly regarding dry deposition, with a contribution to BC deposition of

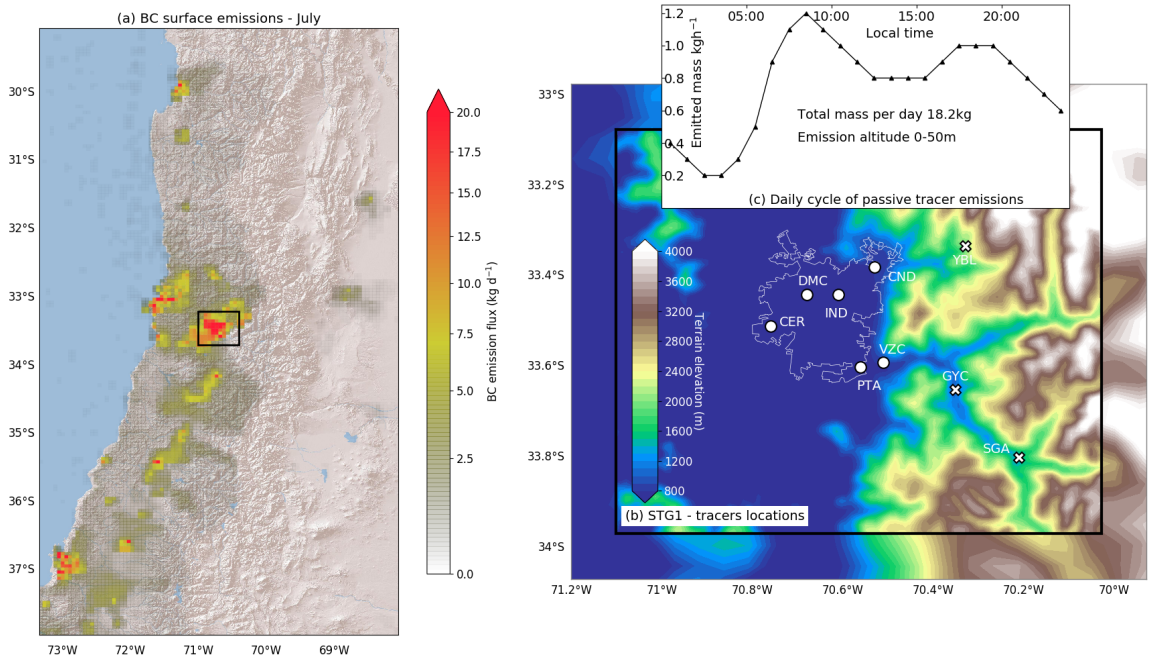

Figure 5.2: (a) Surface emissions of BC for the CC5 simulation. The black box represents the area where emissions are set to zero for the contribution case. Map background layer: World Shaded Relief, ©2009 ESRI (b) Location of passive aerosol tracers used in the SGT1 simulation (circles) and topography of the basin (colormap). Crosses indicate other relevant locations mentioned in the study. GYC is for *Guyacan*, YBL for *Yerba Loca*, SGA for *San Gabriel* (c) Daily cycle of emission for each tracer.

60% to 100%. A significant amount of BC also reaches much higher summits, where it can contribute to up to 40% of the deposition for the period, especially in the southeast of Santiago. Wet deposition is more scarce at this time of the year, and in our case seems driven by orographic precipitation. According to Figure 5.3b a plausible pattern could be that pollutants from Santiago are blown towards the southeast cordillera consistently with the afternoon westerlies induced by mountain-valley circulation, and are precipitated when moist air masses encounter the foothills and cloud droplets scavenge the air below.

Based on Figure 5.3, the Andean area most affected by Santiago's emissions during the month of July 2015 is located at the southeast of the city. Accordingly, a focus is made on the terrain in this zone that is permanently snow or ice-covered during the whole month of simulation (grid points shown in white stars in Figures 5.3c and 5.3d), to study the temporal evolution of deposition. From now on, this area is referred to as the target area. The simulated time series of BC dry and wet deposition averaged over the target area is shown in Figures 5.4a (2-hour deposition) and 5.4b (accumulated deposition). Dry deposition occurs continuously over the target area during the simulated month, with a marked diurnal cycle but maintaining non-zero values throughout the whole 24-hour cycle, the minimum 2-hour value being $0.2\,\mu g\,m^{-2}$. When the rate of dry deposition is near its minimum, the contribution of emissions from Santiago is very small (solid and dashed line cannot be distinguished), pointing to a domination of local and less intensive sources of BC such as road traffic, mining or wood burning for residential heating in the valley villages. On the other hand, when deposition rates are higher (19 July and 27 July for instance) the contribution of emissions from Santiago becomes more significant reaching up to 50%. BC emissions from Santiago thus seem to play a role mainly during stronger deposition episodes. On the whole, the emissions from the city lead to an accumulated additional dry deposition of $126\,\mu g\,m^{-2}$ (33%) over the target area (Figure 5.4b). Contrarily to dry deposition which occurs on a continuous basis, only a few precipitation episodes, concentrated between 12 July and 15 July, account for all wet deposition during the month of July 2015. Given the spatial pattern of wet deposition seen in Figure 5.3b and also the increase in dry deposition right before the precipitation events, this episode likely corresponds to convective moist air masses coming from the northwest, importing BC, and leading to orographic precipitation which in turn scavenges pollutants to the ground. Although slightly weaker than dry deposition, wet deposition of BC from Santiago still accounts for $75\,\mu g\,m^{-2}$ (26%) of total deposition (Figure 5.4b) and is much more concentrated in time (Figure 5.4a). As a result, precipitation in wintertime, which have a positive influence on air quality in Santiago

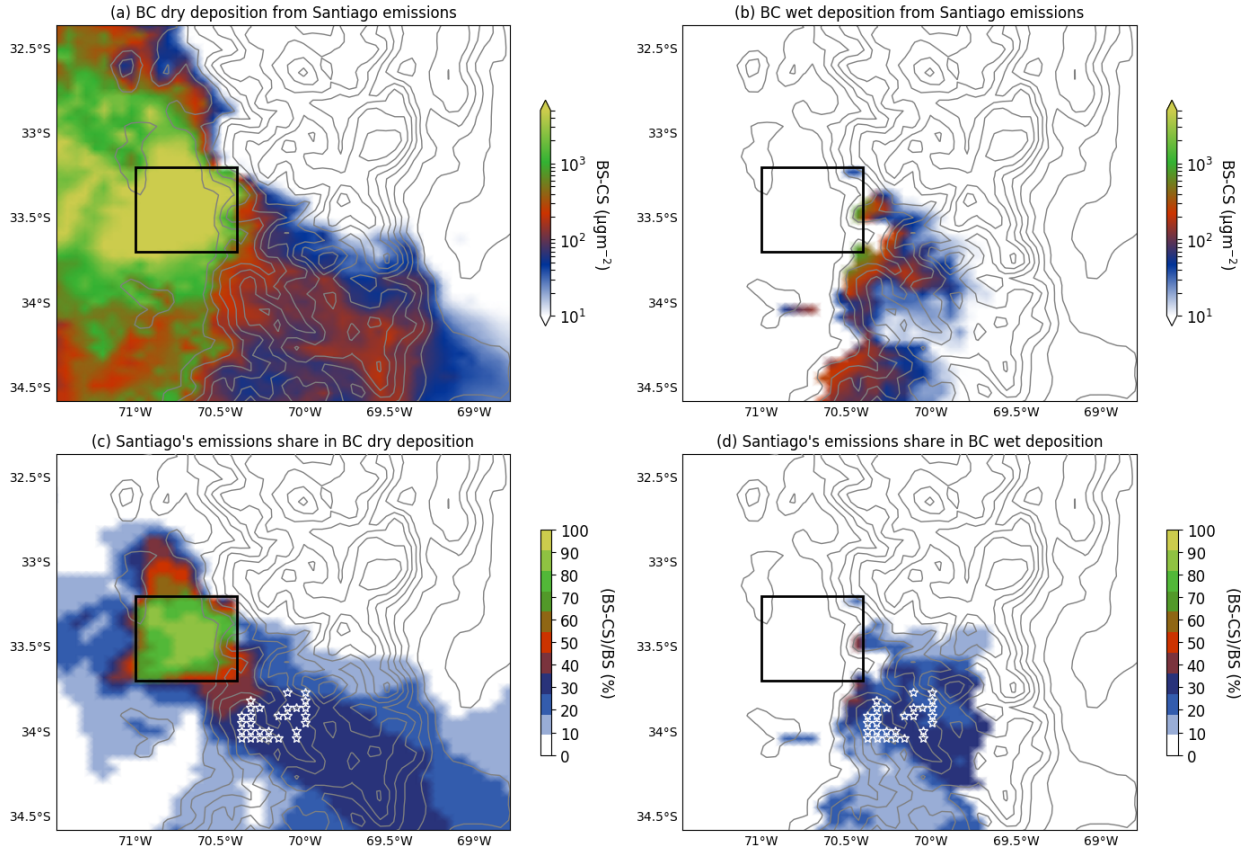

Figure 5.3: (a) BC dry deposition originating from Santiago's emissions, (b) same as (a) for wet deposition, (c) proportion of BC dry deposition originating from Santiago's emissions, (d) same as (c) for wet deposition. Total over July 2015 - CC5 simulation. The black box corresponds to the area where emissions are set to zero in the CS case. Grey contour levels are every 500 m starting from 1000 m a.s.l. White stars in (c) and (d) show the snow or ice-covered grid points considered in the continuation.

because of the associated scavenging of particles, lead at the same time to a higher deposition of light-absorbing particles on snow via wet deposition. Local effects - air quality in Santiago - and global consequences - radiative forcing leading to accelerated melting of glaciers and snow - compete in this regard.

In Figure 5.4a, the period between 21 to 25 July shows a clear minimum in deposition rate compared to the rest of the time series. In connection, the onset of a coastal low along the subtropical west coast of South America is observed around that period. Figure 5.5 shows the evolution of the mean sea-level pressure and 925 hPa wind fields between 22 July to 25 July. The patterns correspond well to d-2, d-1, d0 and d+1 of a coastal low event as described in Garreaud et al. [2002]. One of the effects of this shallow, warm-core low pressure cell disrupting the synoptic circulation is a strengthening of the easterlies flowing above the Andes (not visible in this large-scale figure) and a strengthening of the persistent inversion layer above Santiago for a few days [Rutllant and Garreaud, 1995, Garreaud et al., 2002]. These coastal lows can also affect surface winds through the formation of strong easterly katabatic winds locally known as *raco* [Muñoz et al., 2020, e.g.]. As an example, *raco* events were observed on 21 and 24 July (not shown here), during the coastal low development and extinction, and resulted in no deposition coming from Santiago on the Andes, as can be seen in Figure 5.4a. As a consequence of both phenomena - strong easterlies above the Andes and *raco* - air masses from Santiago are blown in the opposite direction of the Andes when above the mixing layer, and hence do not affect the target area during that period. In parallel, stagnation is favored in the basin, above the urban area. Most wintertime pollution events in the city occur under such synoptic-scale conditions [Rutllant and Garreaud, 1995]. Again, conditions favoring urban pollution in Santiago imply minimal export of BC towards the cryosphere.

It is clear in these simulations that urban emissions from the capital city of Chile have a significant influence on deposition of light-absorbing particles on Central Andean snow and ice, with an average total deposition of around 200 $\mu g\,m^{-2}$ (corresponding to 30% of the total) on the snow or ice-covered areas southeast of Santiago for

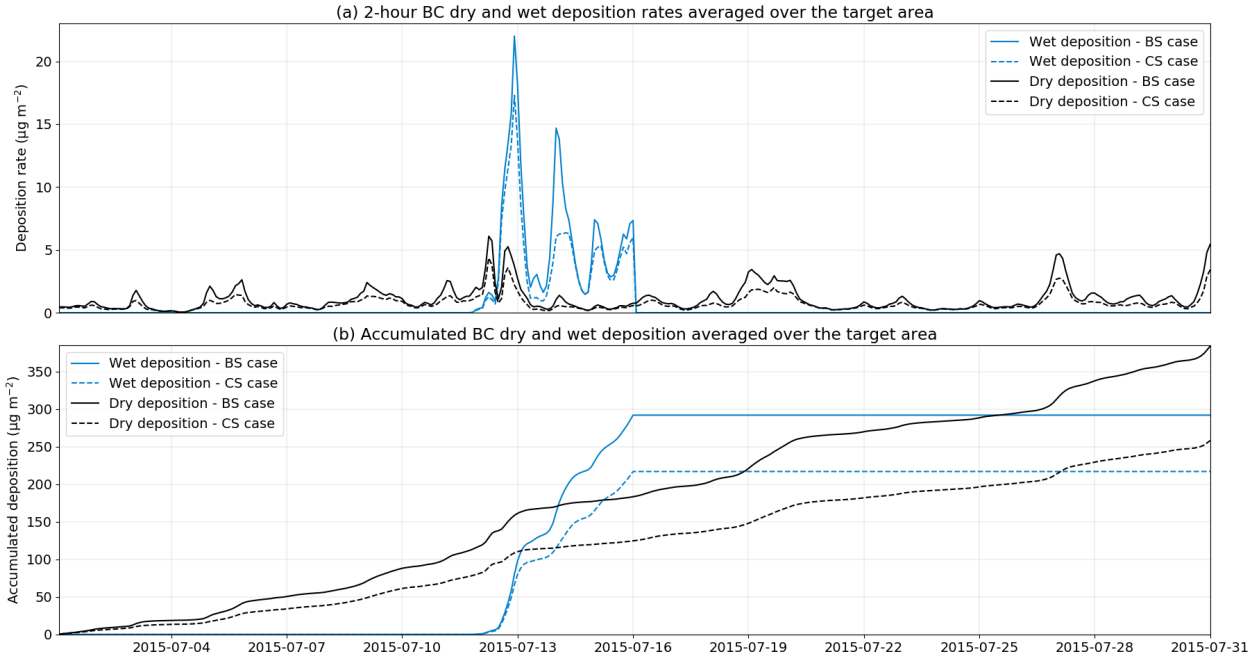

Figure 5.4: (a) Simulated time series of BC deposition over the target area in the BS case (solid line) and CS case (dashed line), (b) same as (a) but accumulated.

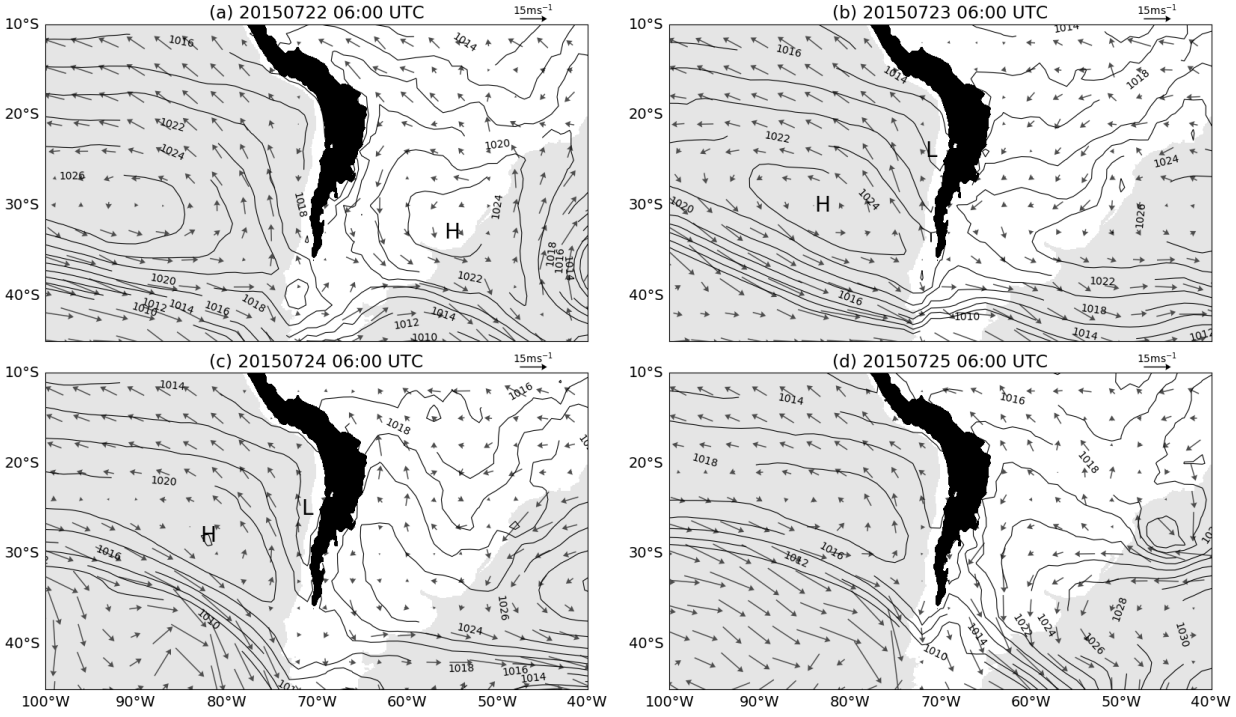

Figure 5.5: Mean sea-level pressure (contours every 2 hPa) and 925 hPa winds (arrows) at 06:00 UTC from 22 July to 25 July. Data is from the NCEP FNL analysis used as boundary conditions for the CHIMERE simulations. Black area indicates terrain elevation exceeding 2500 m. H and L indicate high and low centers, respectively.

the month of July 2015 (Fig. 5.4). The effect on ice and snow albedo, and thus the associated radiative forcing are not straightforward to estimate. However, the field measurement campaign conducted in the snowpack of the Central Andes by Rowe et al. [2019] found that the regional average vertically-integrated load of BC in snow

samples near Santiago was 780 µg m^{-2}, corresponding to a mean radiative forcing of 1.4 W m^{-2} during winter. We find that around 30% of this BC is likely to have been emitted in Santiago (Fig. 5.4). Hence, a significant fraction of the excess radiative forcing measured in snow samples is attributable to emissions from Santiago, although it is not quantifiable here.

In the above analyses, the metropolitan area of Santiago was considered as a unit block of BC emissions, but this urban area is wide (640 km^2), with large gradients in the spatial distribution of emissions. In addition, the surrounding topography of the Andes makes air masses circulation complex. In this respect, the locations within the Santiago area that have the most impact when it comes to deposition on the Andes, i.e. where pollutants are more likely to reach the glaciers once emitted, are not straightforward. The continuation looks at the locations within Santiago where emissions reductions would imply a significant decrease in BC deposition on the cryosphere.

5.1.4.2 Contribution of different districts of Santiago

Using the 1 km resolution STG1 simulation with passive fine mode aerosol tracers, and integrating over the target area (snow or ice-covered - red stars in Figure 5.6a), the contribution of air masses from different districts of the Santiago Metropolitan Area to atmospheric composition and pollutants deposition on the Andean cryosphere can be studied.

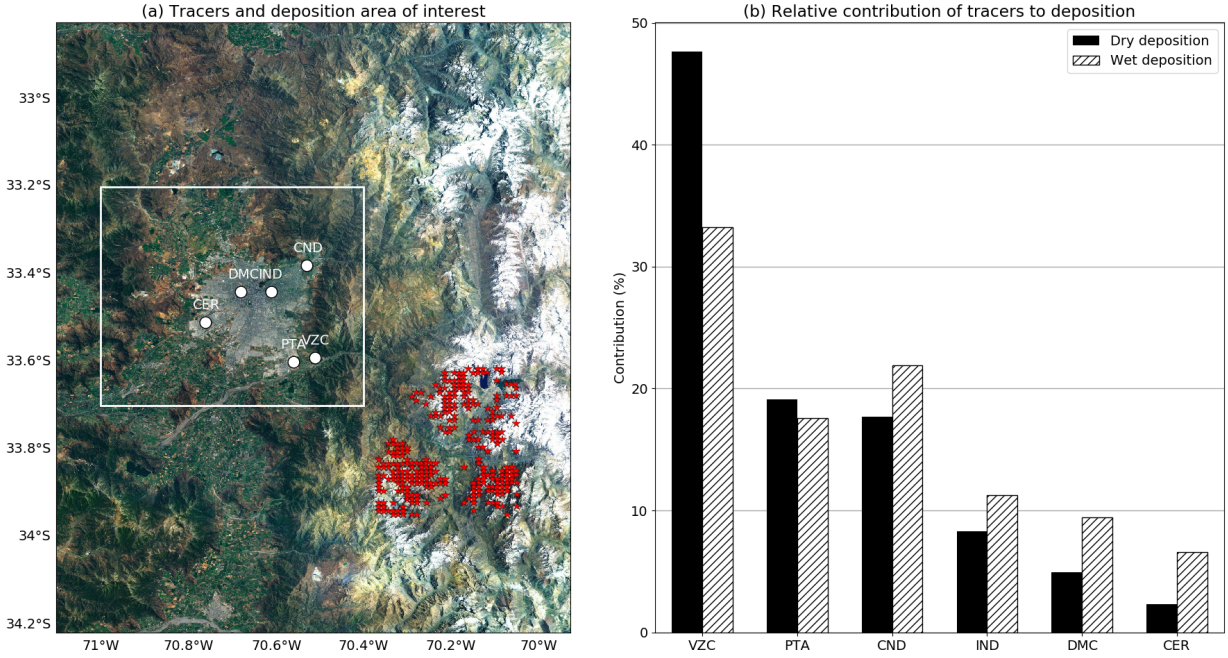

Figure 5.6: (a) Locations of considered passive tracers (white dots), and target area (red stars) influenced by emissions from Santiago (white box). Map background layer: Imagery World 2D, ©2009 ESRI (b) relative share of each tracer to dry and wet total deposition on the target area for July 2015.

Dry deposition mainly originates from emissions at VZC location (47% of accumulated dry deposition over the month of July), at the entrance of the Maipo canyon (Fig. 5.6b). Less intuitively, emissions from the northeast (CND - 17%) weigh almost as much as the ones from a site much closer to the target area (PTA - 19%). The other parts of the city considered here, especially downtown, have a lesser role in dry deposition (2% to 8%). Regarding wet deposition, locations of origin are slightly more evenly distributed, indicating a probable role of large-scale convection over the city mixing pollutants and generating clouds. However, only a few precipitation events are simulated over the period, so that concluding on it is not relevant. Generally speaking, Figure 5.6 shows that the closer the location is to the Andes, regardless of the latitude, the more likely its emitted particles will deposit on the target area. More than proximity to the target area, the interaction of air masses and the foothills and valleys of the cordillera is then of major relevance. Figure 5.7 shows the pathways of tracers VZC and CND during the periods 17-20 July and 21-24 July. The former episode features significant deposition on the Andes while the latter shows very little (Fig. 5.4a). For VZC, an efficient pathway is through the Maipo

canyon, southeast of Santiago, that acts as a funnel guiding particles towards the summits during the 17-20 July period (Fig. 5.7a). The 21-24 July period (Fig. 5.7c) shows a less marked intrusion in this valley, and the tracer barely reaches high elevation. For CND (Fig. 5.7b and d) the Mapocho canyon, northeast of Santiago plays a similar role, enabling polluted air masses to enter the network of valleys and eventually access high elevation sites during the 17-20 July period, which occurs much less during the 21-24 July period.

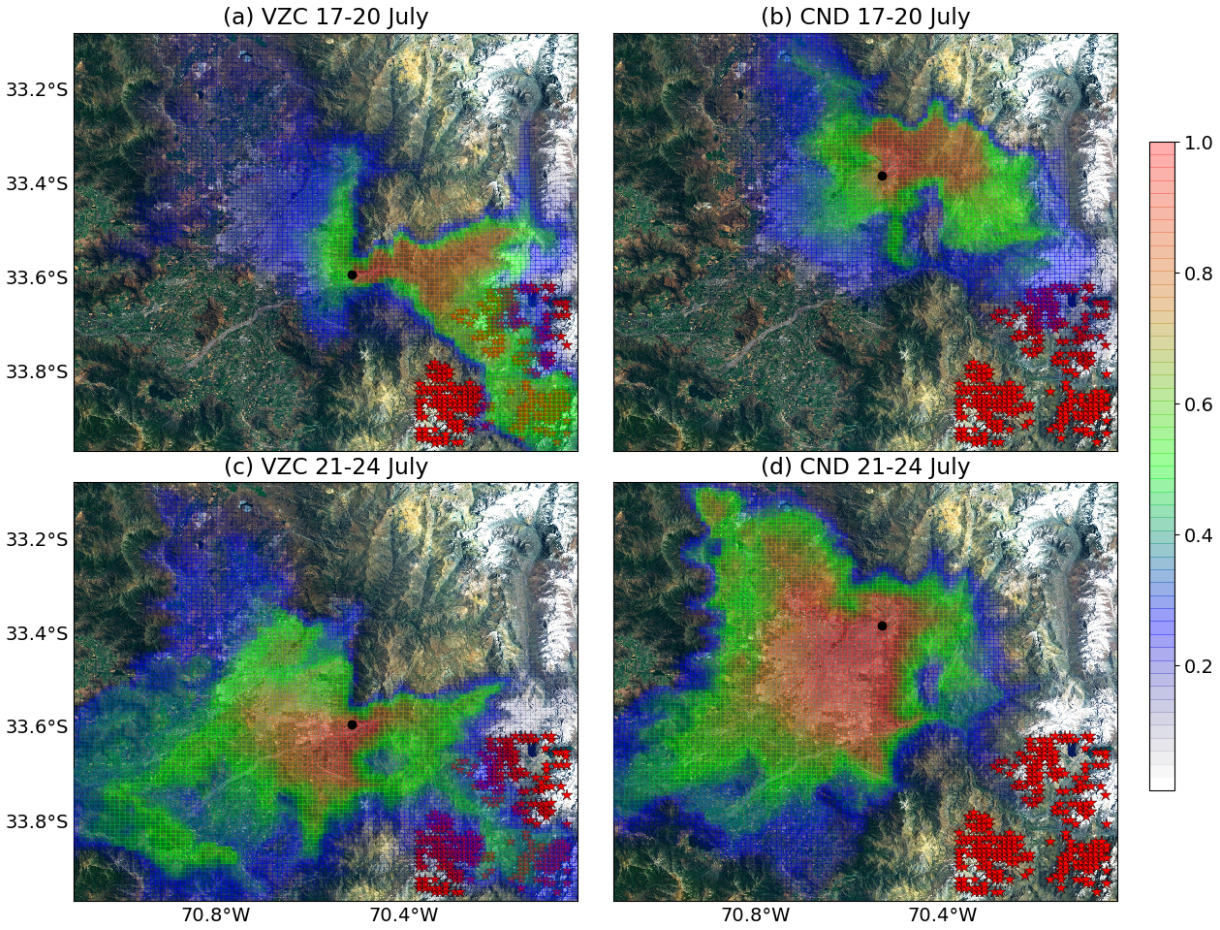

Figure 5.7: Frequency of tracer surface concentration above 0.2‰ of the maximum concentration at the source for two periods with distinct synoptic circulation (a) VZC for 17-20 July, (c) VZC for 21-24 July, (b) CND for 17-20 July, (d) CND for 21-24 July. Red stars show the target area, black dots the emission site. Map background layer: Imagery World 2D, ©2009 ESRI.

It is important to keep in mind that the results in Figure 5.6b are based on equal emission rates at every tracer locations. However, actual measurements from the air quality network of Santiago show that the CND location emits much less particulate matter than PTA for instance. The circulation dynamics imply that for each emitted particle at both locations, they have approximately the same likelihood to end up deposited on the cryosphere, but in actual conditions, regulating emissions at PTA would have a much more dramatic impact on deposition given the higher emission rate. Similarly, VZC is found to be at the optimal location, but is also less densely populated and emits less, in total amount, than PTA.

Given the usually stable and subsident conditions in wintertime, and the elevated height of the mountains that are within reach of air masses coming from Santiago (the urban area is only 500 m a.s.l while summits in the southeast, where deposition is observed, can reach up to 4000 m), the processes leading to such a high elevation deposition are not straightforward. Given the previous analysis, a first natural explanation would involve mountain-valley circulation and the so-called mountain venting phenomenon. The latter corresponds to the horizontal advection of air masses from elevated areas towards flat terrain that, when encountering a shallow mixing layer, leads to the export of boundary layer air into the free troposphere [Kossmann et al., 1999, Henne et al., 2004].

5.1.5 Role of the mountain-valley circulation

5.1.5.1 Injection of BC into the free troposphere

Circulation and interaction between Santiago and the Maipo canyon, south of Santiago, is studied here. Mountain-valley circulation patterns are clear at this location, with a first part of the canyon being almost zonally oriented (Fig. 5.6 eastward of VZC), and the second part almost along a meridional axis. Schematically, under usual wintertime conditions, the differential heating of air masses by sunlight between the Santiago basin and the Andean slopes generates an ascending motion of air from the city into the valley during the afternoon, and a reversal of this motion, from the valley towards the city, during nighttime (Fig. 5.8 and Whiteman [2000]). Since the boundary layer above the city is even shallower at night than during the day, a direct consequence of this circulation pattern is that polluted air masses coming back towards the urban area, if given enough momentum, will likely be injected into the free troposphere (Fig. 5.8). As a result, pollutants found in this secondary layer above the boundary layer can be exported much farther, and become available on the next day to be transported higher up when the daytime circulation resumes.

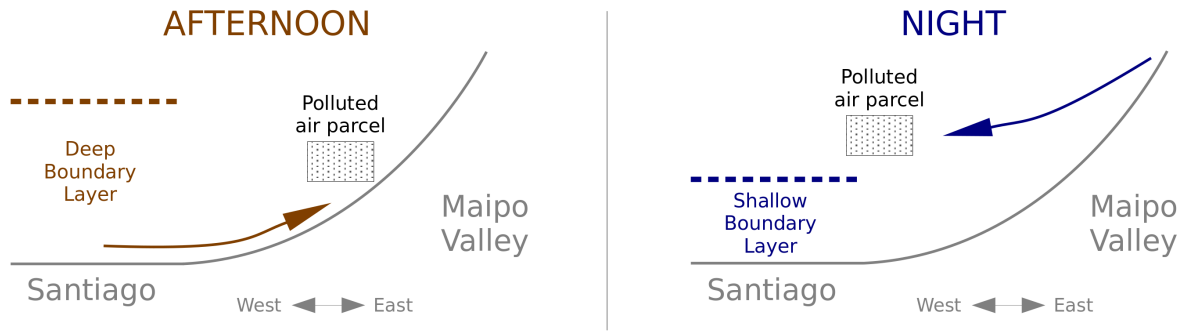

Figure 5.8: Schematic of the usual mountain-valley circulation along the zonal part of the Maipo canyon and associated venting mechanism.

Such a mechanism was clearly recorded during the 2015 campaign described in Section 5.1.3.1, on 22 July at the entrance (VZC) and farther (GYC) in the Maipo canyon (Fig. 5.2). The combination of a positive zonal wind at VZC and a negative meridional wind at GYC allows for the intrusion of polluted air masses deep into the valley during the afternoon (Fig. 5.9a). At night, these air masses come back down into the basin (positive meridional wind at GYC and neutral zonal wind at VZC). At 18:00 local time (LT), pollutants at VZC are still contained and well mixed within the boundary layer, while at 21:00 a secondary layer of BC can be observed above the boundary layer (Fig. 5.9b). The fate of this secondary layer was not observed though, so that validating the hypothesis of injection of the BC higher up as the origin of its transport towards the mountains is not possible with observation only. Our STG1 simulation bridges this gap. It is worth noting that the model (solid lines) agrees reasonably with the observations (dashed lines), both for surface winds at the two locations, and for the shape of the aerosol profile at night, especially regarding the formation of a secondary layer in the free troposphere (Fig. 5.9). The model generates a shallower mixing layer than observed, but the pattern is consistent.

This event can be further described with the STG1 simulation, following along-valley transects of tracers concentrations and wind profiles. At 16:00 LT, particle pollutants, mainly originating from the VZC location, have penetrated deeply into both branches of the Maipo canyon, mostly within the boundary layer (Fig. 5.20). This intrusion is mainly driven by low-level winds in both valleys, while a wind shear at the end of the southern valley disconnects the polluted air masses from the surface. 5 hours later (Fig. 5.21) low-level winds have reversed, consistently with mountain-valley circulation, and blow tracer-containing air masses back towards the Santiago basin. However, while the intrusion was governed mostly by surface winds, winds above the boundary layer now dominate the advection. As a result, particles are injected into the free troposphere over Santiago, as already evidenced in Figure 5.9. Thus, despite stable conditions and a shallow boundary layer, the mountain valley circulation allows for the export of pollutants higher up.

However, when tracking the secondary layer of BC injected into the free troposphere, it does not appear to go back into the direction of the Andes, but rather continue its path towards the west of Santiago, and eventually

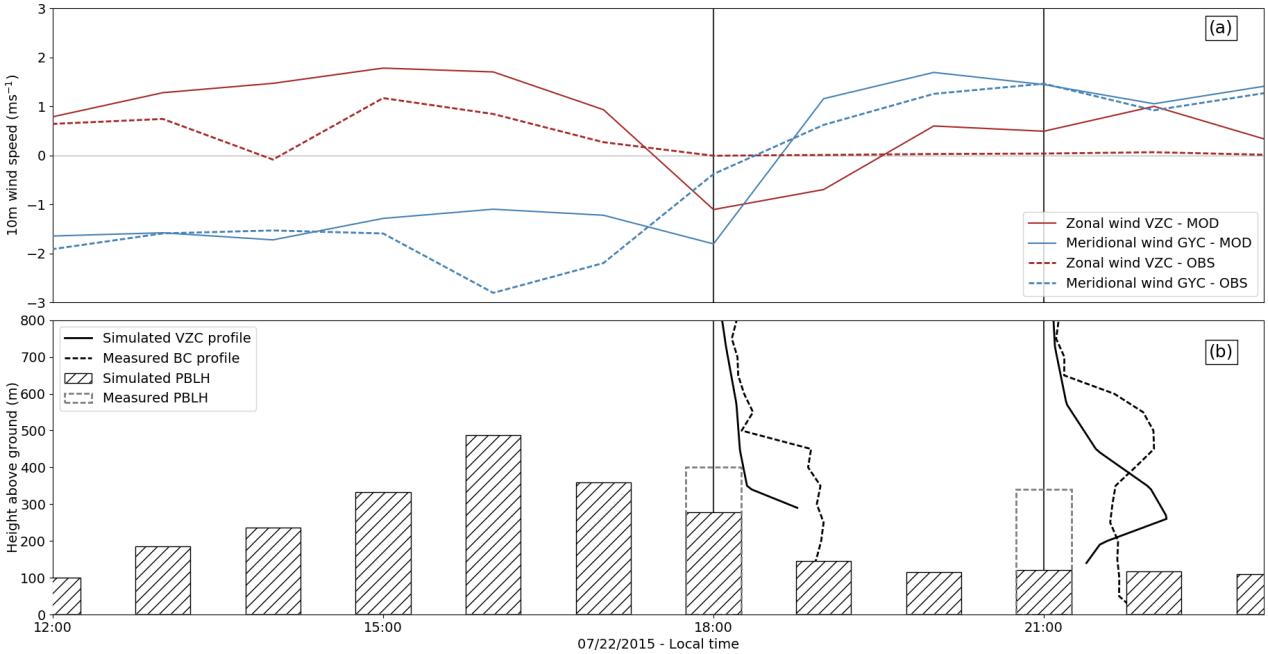

Figure 5.9: Observed (dashed lines) and modeled (solid lines - STG1 simulation) intrusion episode of 22 July. (a) Observed and modeled zonal wind at VZC and meridional wind at GYC. (b) Boundary layer height and vertical profiles of BC (observed) and VZC tracer (simulated). For the sake of comparability, only the free troposphere profiles are shown for the model. Boundary layer heights from the campaign are derived from vertical profiles based on the methodology described in Stull [1988]

be diluted without being recovered higher up despite winds above 2000 m blowing in the favorable direction (Fig. 5.22). This result is consistent with the time series in Figure 5.4a, where almost no deposition occurs on the target area in the few hours following the 22 July venting episode. In fact, the whole period between 22 July and 25 July in Figure 5.4a features very little deposition. This can be traced back to the onset of the coastal low, as discussed in Section 5.1.4.1. The hypothesis of the observed secondary layer of pollution in the free troposphere as a source of export and deposition of BC, does not apply in this case. Nevertheless, while the nighttime venting may not be relevant, the daytime mechanism of injection of pollutants into the Andean valleys is critical.

5.1.5.2 Valley intrusion of air masses and vertical export

When comparing the two contrasted periods mentioned in Section 5.1.4.2, although the total deposition over the whole domain remains similar (7% difference on the accumulated deposition of tracers), the spatial patterns greatly differ. As seen in Figure 5.7, during the 21-24 July period, pollutants are advected towards the city and the southwest region mainly, while during the 17-20 July period they are found in the northwest, the east of Santiago adjacent to the cordillera, and over the Andes. Section 5.1.5.1 points towards two key meteorological components of the mountain-valley circulation driving the fate of polluted air masses: the low-level zonal wind above the city, and the vertical motions at the end of the southern valley. Schematically, the weak vertical mixing associated with wintertime conditions forces the pollutants to follow a pathway along gentle slopes near the ground to reach or get closer to the snow or ice-covered areas. Furthermore, even though events of polluted air intrusion into the Maipo canyon occur, these air masses do not necessarily reach the snow or ice-covered areas of the Andes. Based on the above, we identify three possible transport alternatives which are schematically represented in Figure 5.10: (1) easterly winds dominate and urban polluted air masses are transported away from the Andes, (2) westerlies enable intrusion into the canyon but pollutants cannot reach the Andean cryosphere and (3) deep intrusion occurs and air masses are successfully transported to the Andean summits. The latter is the case where we expect large deposition.

We derive now a parameterization indicating the likelihood that one of the aforementioned alternatives occur and we use the simulated daily deposition of tracers in July 2015 to examine its validity. Given the fact that

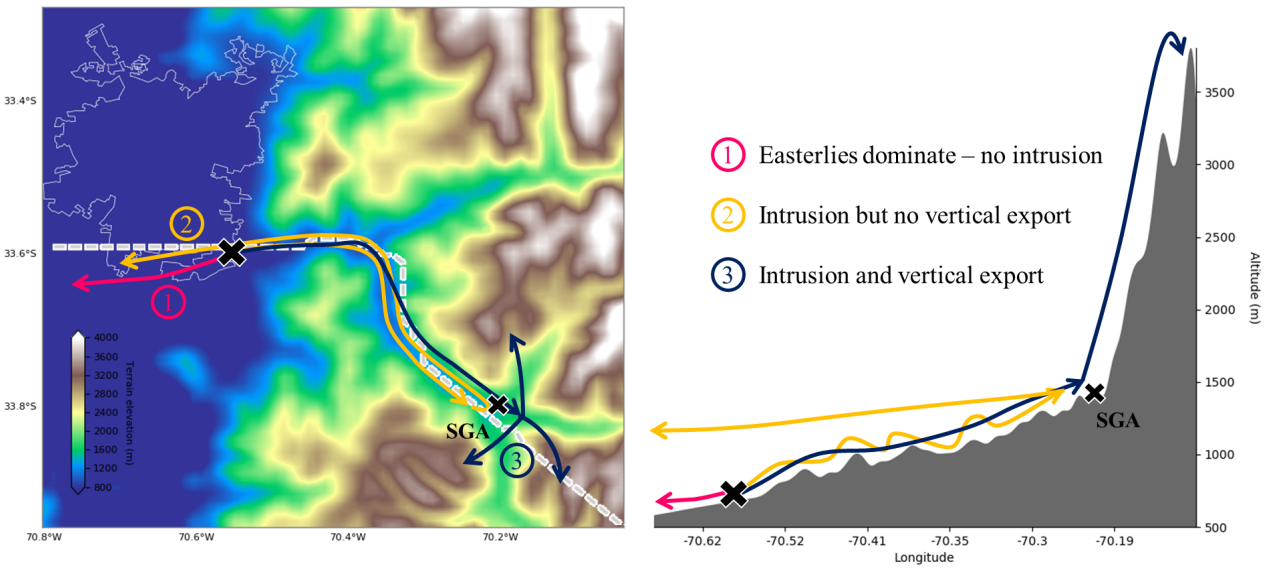

Figure 5.10: Schematic of the 3 export situations from a latitude/longitude (left) altitude/longitude (right) perspective. The transect followed in the right-hand panel is shown in white dashed line in the left-hand panel.

the chance of an air mass reaching the Andean cryosphere is linked first to the occurrence of a zonal wind transporting the air parcels into the canyon and then lifting it to the Andean summits, we choose the simulated near-surface zonal wind (u) over the Santiago basin in the afternoon to represent the former and the simulated vertical diffusion coefficient (K_z) near the surface in the valley, close to the summits, at the same time of day to express the magnitude of vertical motion. The combination of these parameters evidences that large deposition occurs for significant zonal winds and vertical diffusion (large circles in Fig. 5.11a). For strong zonal winds only or strong updrafts only, deposition is moderate. For situations with both weak winds and vertical diffusion, almost no deposition occurs.

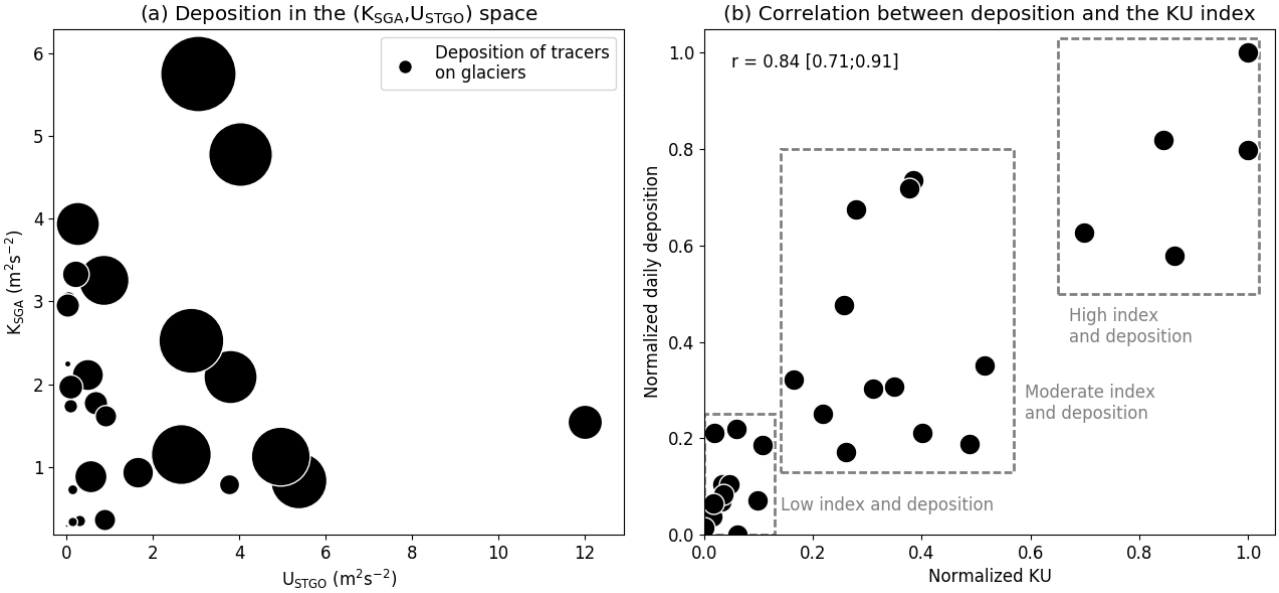

Figure 5.11: (a) Tracers dry deposition on the target area dependency on K_{SGA} and U_{STGO}. Circles areas are proportional to deposition. (b) Relationship between the normalized daily dry deposition and the normalized index $KU/\max(KU)$. The correlation is given with a 95% confidence interval.

The parameterization combining these two variables, representing the above and thus expressing the likelihood

of occurrence of deposition is defined in Eq. 5.1. For the K_z term we choose the vertical diffusion coefficient at 40 m above ground level at the location of San Gabriel (K_{SGA} - see SGA in Figures 5.2 and 5.10) averaged between 14:00 and 20:00 LT. San Gabriel is considered because of its location at the end of the main southern valley where the pollutants are lifted from the ground to the Andean summits (Fig. 5.20b). For the zonal wind component (u) we choose the zonal wind at 40 m above ground level, squared and averaged over the urban area of Santiago and between 14:00 and 20:00 LT (hereafter U_{STGO}). The zonal wind is squared so as to be homogeneous to a kinetic energy per unit mass of air, which is what physically provides momentum for the intrusion of air masses. Both U_{STGO} and K_{SGA} are capped, related to the fact that above a certain threshold, increasing wind speed or vertical motion does not bring any more deposition if the other parameter is too small, as evidenced in Figure 5.11a. The thresholds are empirically set to $1\,\mathrm{m\,s^{-1}}$ for u and $3\,\mathrm{m^2\,s^{-2}}$ for K_z. The correlation of this index with dry deposition is illustrated in Figure 5.11b. The deposition term considered here is limited to the target area summed for all tracers between 14:00 and 04:00 LT, and normalized by the maximum deposition over the period. The resulting correlation is not very sensitive to the choice of the threshold values for U_{STGO} and K_{SGA} as long as they are not taken too small, and such thresholds are necessary to have a consistent result. This index accounts for (i) intrusion of urban BC into the Maipo canyon via significant zonal winds over the city in the afternoon (ii) the possibility for air masses to be exported from the bottom of the valley up to the summits at the same time, before being distributed and diluted into several smaller valleys. Combining (i) and (ii) leads to large deposition a few hours later (hence the consideration for the total deposition between 14:00 and 04:00 LT). Having only one of the two induces moderate deposition, having none leads to limited to no deposition. This justifies the choice of multiplying the two variables, accounting for a logical *and* relationship, although the meteorological meaning of the resulting index is not obvious. The correlation between the normalized deposition and normalized KU is 0.84 [0.71;0.91] at the 95% confidence level, showing that the combination of positive zonal winds in the basin and vertical diffusion in the deep valley accounts for most dry deposition episodes (top right corner box in Figure 5.11b). It is worth noting that the contribution of each tracer source in high deposition days follows the average distribution found in Figure 5.6b, with dominance from VZC, and CND and PTA playing similar roles at round 20%. Conversely, when both wind and K_z are low, almost no deposition occurs (bottom left corner box in Figure 5.11b). For intermediate values of the two variables, deposition is more scattered but remains within median values. A corollary of this strong correlation is that the detachment of pollutants from the surface is driven by mixing and turbulence processes deep in the valleys network, rather than by organized circulation patterns.

$$\begin{aligned} KU &= K_{SGA} \times U_{STGO} \\ &= \min(< Kz_{SGA} >_{14-20}; 3) \times \min(< u^2{}_{STGO} >_{14-20}; 1) \end{aligned} \tag{5.1}$$

5.1.6 Observations from the 2015 measurement campaign

Three measurement sites were defined for this campaign (red crosses in Fig. 5.12a). One site was set in downtown Santiago in the dependencies of the Chilean weather service (33.45 °S, 70.68 °W, 530 m a.s.l. - hereafter DMC). A second site was located at the entrance of the canyon in the *El Almenar* school (33.59 °S, 70.51 °W, 790 m a.s.l. - hereafter VZC) and a third site was defined 17 km into the Maipo River canyon in a military hotel (33.619 °S, 70.351 °W, 930 m a.s.l. - hereafter GYC) and 4 km north of San José de Maipo, a town with around 6000 inhabitants. We will not dive into the specifics of the field campaign hereafter, only the key messages revealed by the observations, but more detail on the campaign's configuration and available measurements can be found in Huneeus et al. [2021].

On July 23^{rd} (Fig. 5.13), winds at VZC are westerlies in the ML and easterlies above, between 12:00 and 18:00, with a well-defined BC layer and PM_{10} concentrations at the surface above $50\,\mu g/m^3$. Such a configuration at VZC should lead to the intrusion of air pollutants into the Maipo canyon. However, winds at GYC are southerlies throughout the column during the whole day, preventing intrusion into that section of the canyon. In this case, urban PM transiting at VZC are likely advected into the Colorado river canyon instead. The lack of any observations along the northern branch prevents verifying this hypothesis. As a result, surface PM_{10} concentrations in the evening remain limited at GYC, at around $25\,\mu g/m^3$. It is worth noting that after 19:00, surface PM_{10} concentrations at VZC drop to nearly $0\,\mu g/m^3$ in relation with strong easterlies throughout the whole column, blowing from the canyon and hence bringing cleaner air. On the previous day (July 22^{nd} - Fig. 5.14), similar afternoon conditions were recorded at VZC with relatively high surface PM_{10}, westerlies in the ML and a significant BC layer at 18:00. However, simultaneous measurements at GYC show northerlies dominating the mixing layer, with the development of a deep BC layer at 18:00 revealing favorable conditions for

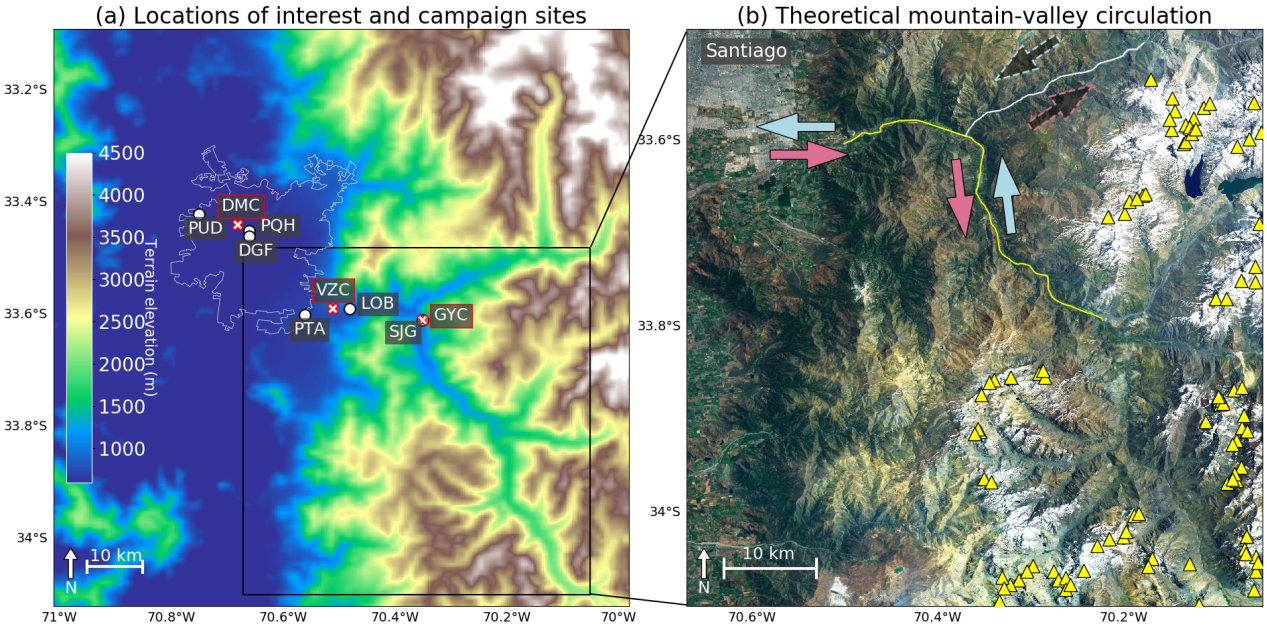

Figure 5.12: (a) Location of the three measurement sites used during the July 2015 campaign (red crosses); one in downtown Santiago (DMC), a second one at the entrance of the Maipo canyon (VZC) and a third in the southern branch of the Maipo canyon (GYC). Automated network (white circles) of air quality monitoring (Pudahuel, PUD; Parque O'Higgins, PQH; Puente Alto, PTA) and weather stations (Departamento de Geofisica, DGF; La Obra, LOB; San José de Guayacan, GYC). (b) Theoretical wind directions (arrows) in the morning (blue) and afternoon (red) along the Maipo (yellow line) and Colorado (white line) canyons. Triangles indicate the coordinates of glaciers according to WGMS and National Snow and Ice Data Center (comps.) [1999, updated 2012].

air pollutants intrusion from Santiago into the southern section of the canyon. Surface PM_{10} records show that concentrations at VZC peak at 14:00 at around 80 $\mu g/m^3$ and consistently decrease afterwards down to 40 $\mu g/m^3$ at 21:00. In parallel, said concentrations at GYC follow the exact opposite trend: from modest concentrations at 14:00 (around 40 $\mu g/m^3$) they consistently increase to peak at 21:00 at 80 $\mu g/m^3$. These mirrored trends, combined with the recorded wind at both sites strongly advocate for a PM transport event from the urban basin (VZC), far into the Maipo canyon (GYC), as theoretically expected. The retrieval of similar concentrations at GYC a few hours after VZC shows that most of the PM at the entrance eventually travels through the canyon suggesting high transfer rate.

Figure 5.15 provides insight on the effect of winds on surface PM_{10} concentrations at the two Maipo canyon sites of the campaign. At GYC, lowest PM_{10} concentrations are recorded when winds blow from the south bringing clean air from upslope and evacuating local emissions. This configuration occurred most often during the campaign. Contrarily, when winds blow from the north, i.e. air masses from the urban basin are brought up to GYC, concentrations reach values close to maximum, emphasizing again the major role of air pollutants from Santiago in atmospheric composition in the canyon. Interestingly, when winds are weak and with a direction different than the valley orientation (i.e. easterlies, rightmost region in the figure) corresponding to stagnant conditions, PM_{10} concentrations are high, pointing to a predominance of local emissions, although such conditions are seldom observed. At VZC, winds sporadically coming from the foothills (i.e. the region above the NW-SE axis in Figure 5.15) mostly bring clean air. Southerlies lead to moderate concentrations of PM_{10} by carrying relatively clean air and/or marginally evacuating local emissions through weak wind speeds. Highest concentrations are observed when westerlies are recorded. Again, depending on wind speed, such concentrations either correspond to stagnation of local emissions or transport from the denser more polluted urban basin (PTA for instance).

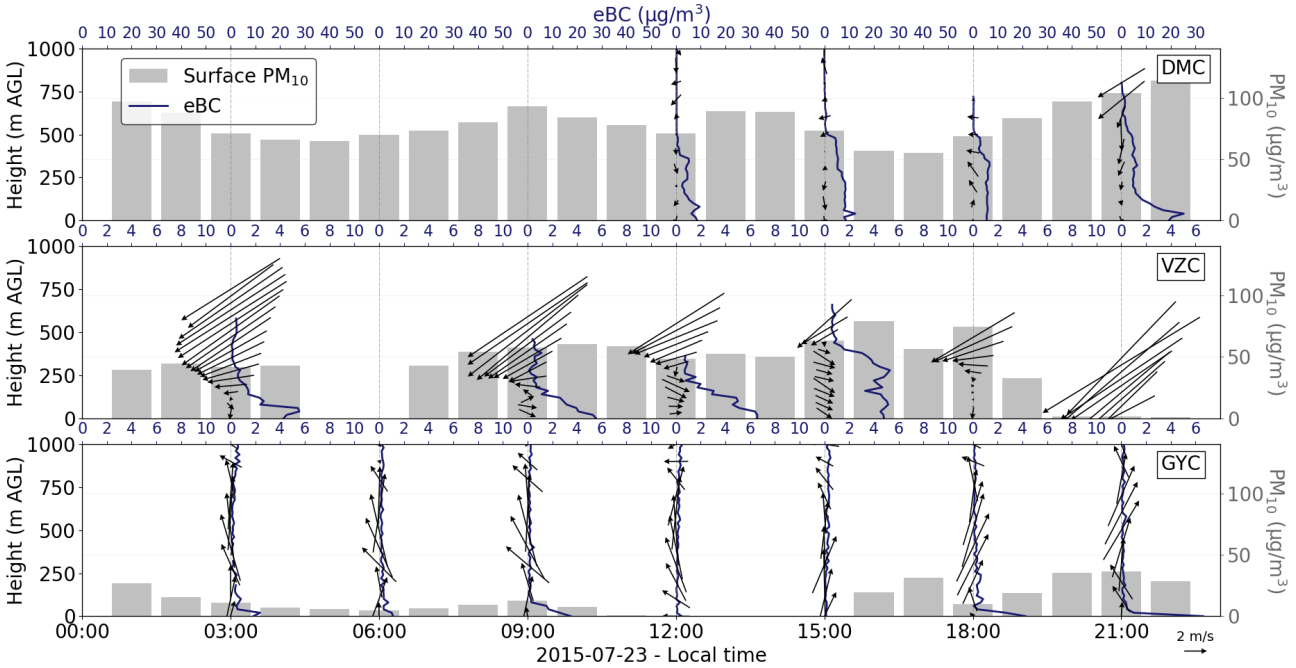

Figure 5.13: Surface PM_{10} concentration (bars) and 3-hourly vertical distribution of BC (blue line) and horizontal winds (wind vector) at DMC (top), VZC (middle) and GYC (bottom) for July 23^{rd}. We highlight that different scales are applied for BC in DMC than for VZC and GYC. Wind data at DMC and GYC are from tethered balloons, while at VZC sodar data is used. No data is available in the morning for DMC due to icing on the balloon caused by low temperatures.

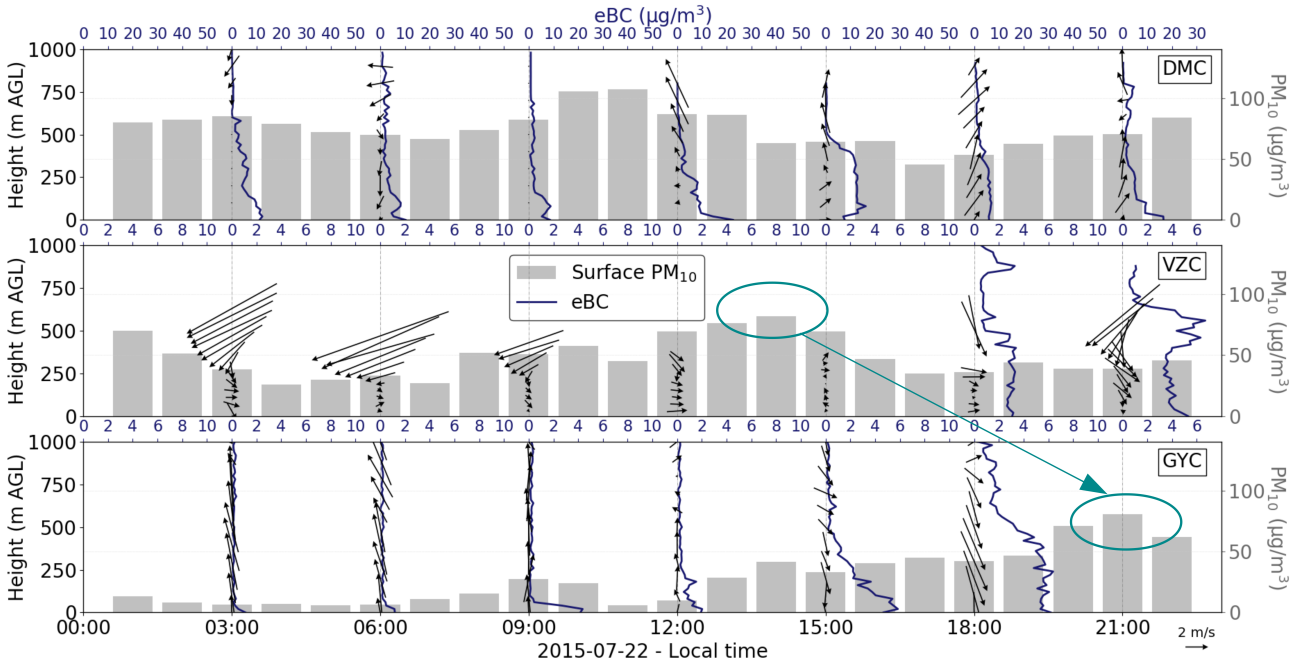

Figure 5.14: Same as Figure 5.13 but for July 22^{nd}.

5.1.7 Extension to climatological time scales

As a result of the zonal axis of the first part of the canyon (Fig. 5.12), clear and sharp patterns of mountain-valley circulation are expected [Whiteman, 2000]. The differential radiative heating and cooling between the wide

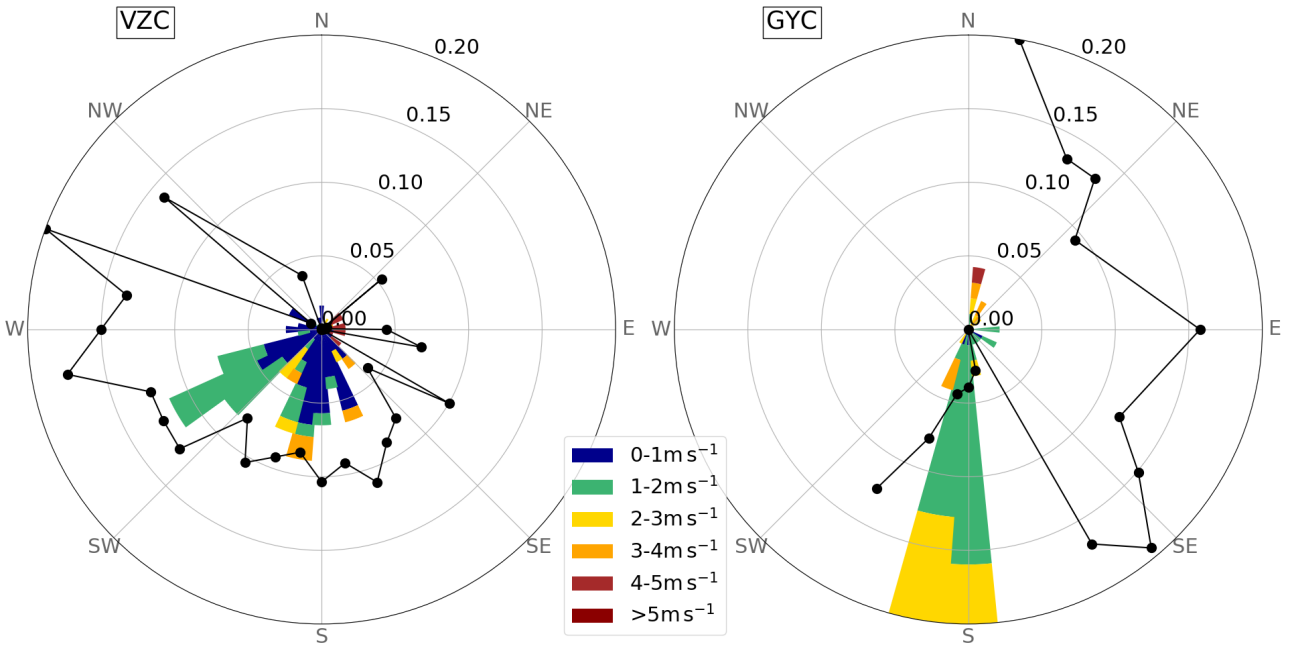

Figure 5.15: Surface wind distribution (colormap) and associated average PM_{10} surface concentration normalized by the maximum over the period (black line) at VZC and GYC during the campaign. The scale for PM_{10} is the wind frequency scale multiplied by 5, i.e. 0.20 for wind corresponds to 1 for PM_{10}.

urban basin and narrow Andean canyons leads to down-valley winds towards the urban area in the early morning and nighttime, while in the afternoon (approximately 14:00 to 19:00) winds reverse and go up-valley at LOB (Fig. 5.12), near the entrance of the canyon (Fig. 5.16a and 5.16b). In parallel, winds in the southern branch of the canyon (location GYC in Fig. 5.12) follow the valley axis with mostly southerlies during night and morning time, and northerlies during afternoons (Fig. 5.16c and 5.16d). It can be noted in Figure 5.16a the occurrence of strong down-valley *Raco* winds at the valley entrance (north-easterlies in red), mostly in the early morning [Muñoz et al., 2020]. The aforementioned climatologically recurring patterns are valid for the whole winter 2015 season, pointing to afternoon conditions being usually favorable for BC export from Santiago deep into the Maipo canyon.

The campaign showed that deep intrusion events, which are theoretically expected under mountain valley circulation conditions, do not occur systematically. Figure 5.17 provides a climatology of such conditions by showing the joint frequency distribution of wind directions at the entrance (Station PTA) and inside the canyon (station GYC) for the 00-07 and 14-19 LT hours of June-July-August in years 2013-2019. The hour periods were defined so as to avoid the transition times between the two main phases of the mountain-valley circulation. According to Figure 5.17, conditions combining westerlies/northerlies (up-valley daytime phase) and easterlies/southerlies (down-valley nighttime phase) are very frequent, with 67% of afternoons and 78% of mornings featuring such canonical conditions, and hence the conspicuous dipole in Figure 5.17 at the lower-middle and upper-left quadrants. However, some perturbations can occur, leading to a second though less frequent opposite dipole in the wind direction distribution (upper-middle and lower-left quadrants). In particular during the campaign, only one day features the usual afternoon combination all along (July 22^{nd} - the clearest case of deep intrusion of PM into the canyon during the campaign) although all mornings are unperturbed (campaign morning hours are black circles, campaign afternoon hours are black squares in Fig. 5.17). All the other campaign days have at least one hour departing from the canonical circulation. In the context of air pollutants export, afternoon perturbations are critical, and can be threefold: (i) southerlies instead of northerlies in the meridional part of the canyon, which can still lead to transport of air masses towards the mountains, but through the Colorado river canyon (upper-middle quadrant - 23% of the time climatologically), (ii) easterlies instead of westerlies at the entrance of the canyon which prevents any intrusion of urban air pollutants into the valley (lower-left quadrant - 5% of the time), (iii) reversal both in the valley and at its entrance (5% of the time). The last two perturbed cases prevent the export of air pollutants towards the Andes whereas the first case suggests that the main pathway of urban BC to the Andean cryosphere is through the Colorado canyon instead of the

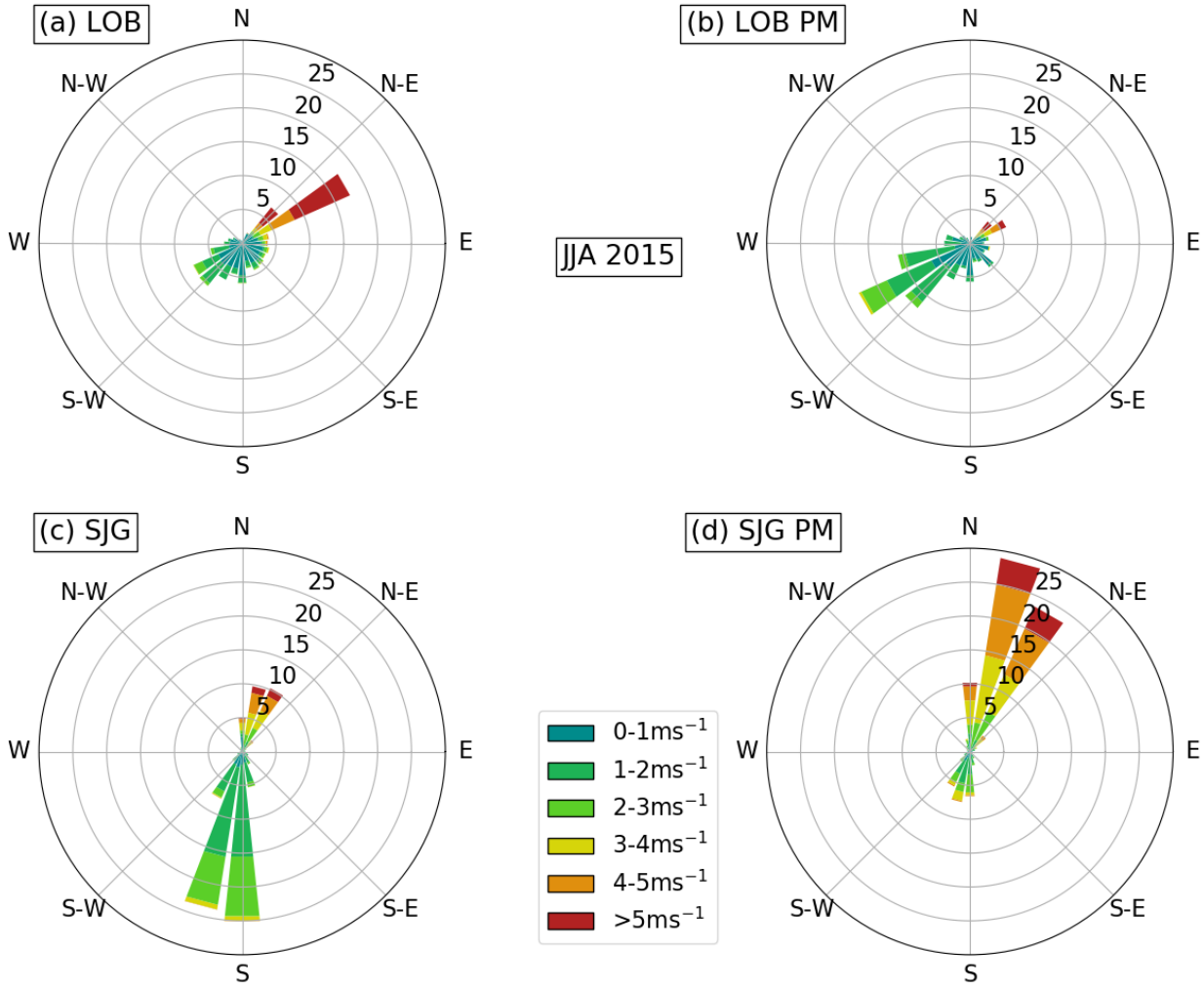

Figure 5.16: 10 m wind distribution at La Obra (LOB in Fig. 5.12) and San José (GYC in Fig. 5.12) for June-July-August 2015 (left) and restricted to 14:00 to 19:00 LT (right). The length of the section corresponds to the frequency of the wind direction (in %), colors correspond to the wind speed from that direction. Source DMC for GYC and Muñoz et al. [2020] for LOB.

Maipo Canyon.

In order to identify the meteorological conditions leading to the perturbation of the mountain-valley circulation in the afternoon, a composite analysis is performed using ERA5 reanalysis data [Copernicus Climate Change Service, 2017]. We consider perturbed the days in which at least two consecutive hours in the afternoon are found to disrupt the intrusion of air masses from Santiago into the Maipo canyon, i.e. correspond to one of the three combinations departing from the westerly-northerly one mentioned previously (represented by the upper-middle, lower-left and lower-middle quadrants in Figure 5.17). Then, for each perturbation type the large-scale daily mean sea-level pressure, 1000 hPa winds, geopotential height at 500 hPa and cloud cover are temporally averaged for the composite analysis. Figure 5.18 shows a similar large-scale picture for the perturbation of zonal winds at the entrance of the canyon (easterlies instead of westerlies) whatever the perturbation on meridional winds inside the canyon - Fig. 5.18a and 5.18b): position of the South Pacific High (SPH) at around 100 °W far from the Chilean coast, moderate westerlies coming from the ocean and full cloud cover over the Santiago basin in relation with a trough coming from the south. This pattern corresponds to pre-frontal (BPF) coastal lows, with overcast skies and low surface pressure that foster convergence and hence widespread downslope easterlies. The perturbation due to the influence of cloud cover is theoretically expected, mountain-valley circulation being radiatively driven. Daytime upslope winds develop under the influence of sunlight, so that a persistent cloud cover prevents this phenomenon from occurring [Whiteman, 2000].

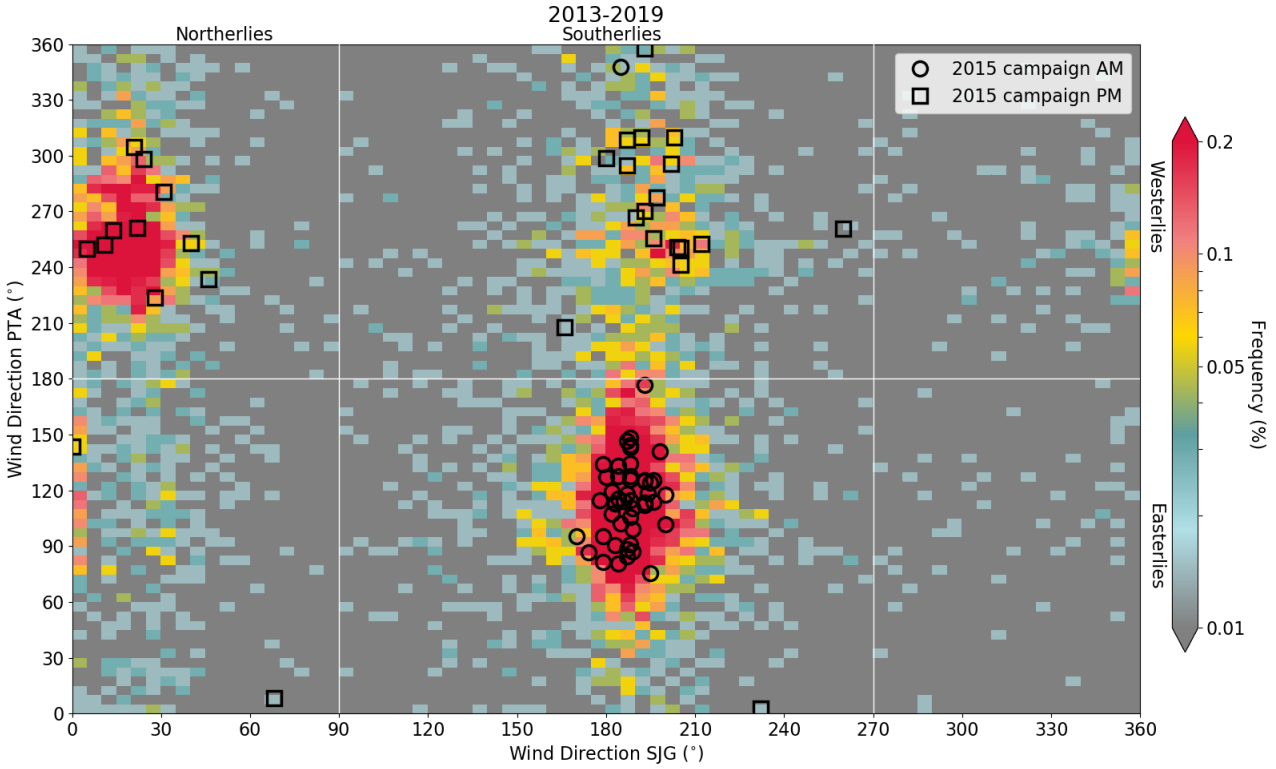

Figure 5.17: Joint distribution of hourly 10 m wind directions at PTA (data from SINCA) and GYC (data from DMC). JJA 2013 to 2019 except 2017. Restricted to hours between 00:00 to 07:00 and 14:00 to 19:00. Circles (squares) indicate the campaign hours in the morning (afternoon).

Contrarily, in the case of a perturbation of meridional wind in the canyon only, with westerlies at its entrance, clear skies are observed associated with an incoming mid-tropospheric ridge and a SPH closer to the continent around 85 °W (Fig. 5.18c). This reversal of meridional winds in the canyon appears to be related to synoptic conditions corresponding to a class A coastal low (see Section 5.1.4.1), a well-known consequence of which is the strengthening of easterlies blowing down the Andean slope. Given the southeastern orientation of the canyon, anomalous afternoon easterlies thus lead to anomalous southerlies inside the valley. Under such conditions, although the intrusion of atmospheric pollutants into the southern branch of the canyon is unlikely, the Colorado river branch (towards the north) probably receives urban PM instead, thus still potentially contributing to the transport of BC towards the Andean glaciers.

5.1.8 Discussion

Although this study looks into one particular month, there are reasons to believe that the results are more general. Indeed, Figure 5.19 shows that July 2015 is climatologically relevant given the usual character of its meteorological conditions for winter months. Besides, although a quantitative analysis is performed specifically for July 2015, the qualitative results determining the critical meteorological variables and the pathways associated with export and deposition of pollutants on the cordillera can be generalized to all winter months. In addition, the year-to-year variability in BC emissions is not significant for Santiago at the monthly level, except for particular peak events such as the ones described in Lapere et al. [2020]. However those peak events occur at night so that air masses cannot be exported into the Andean canyons. Traffic and residential heating provide most of the BC. The former does not change much from year-to-year and the latter is mainly connected to outside temperatures, for which July 2015 is not an outlier. Thus, the magnitude of exported and deposited BC on the cryosphere every year is likely around the estimate given in Section 5.1.4.1 for dry deposition. Wet deposition might be more variable from one year to another. The pathways identified here for a particular valley likely apply for other valleys in the area, although this calls for further research.

The present work focuses on wintertime conditions because they combine high BC emissions due to residential heating with wood burning, and a large extent of snow covered areas. However, it is worth

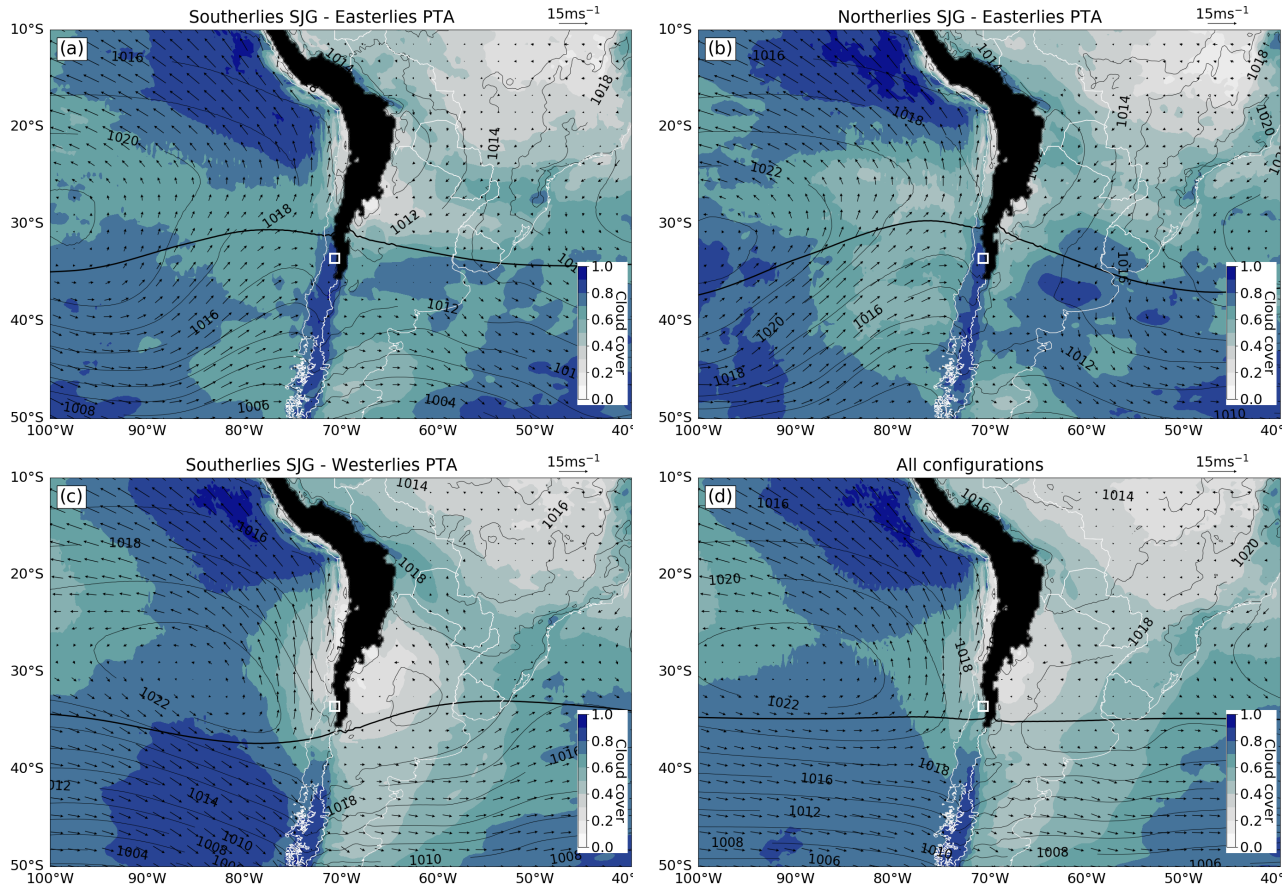

Figure 5.18: Composite of mean sea-level pressure (contours every 2 hPa), 1000 hPa winds (arrows), geopotential height at 500 hPa (5680 m contour - thick black line) and cloud cover (colormap). Black area represents the Andes where elevation is higher than 2500 m. White square shows the location of the Santiago area. Data from ERA5. Average of daily means for (a) SE perturbation (5% of cases), (b) NE perturbation (5% of cases), (c) SW perturbation (23% of cases), (d) all days. June/July/August 2013 to 2019.

briefly discussing what could be expected for other seasons in terms of export pathways and deposition. May/June/July/August concentrate most of the annual precipitation in Central Chile with an average 59 mm month^{-1} while November/December/January/February only see precipitation of 3.5 mm month^{-1} on average in downtown Santiago (data for the period 1950-2019 from the CR2 database for station *Quinta Normal* - see Section 5.1.3.1 for the data source). As a result, wet deposition is not expected to be a recurring process of export and removal of BC from the atmosphere in spring and summer seasons. Regarding atmospheric export and dry deposition, the warmer periods of the year feature a more turbulent atmosphere, with a much deeper mixing layer. A consequence is the greater ability for BC particles to be exported higher up and reach more elevated areas so far as to travel over the Andes towards Argentina more easily. Also, given the lack of precipitation and hence diminished cloud cover in summertime, we expect that mountain-valley circulation is barely disturbed, so that the export of pollutants is more regular and thus deposition more periodic. This is just a glimpse at what we expect since other seasons are not within the scope of this work, but these are the features that should be investigated.

To obtain the deposition rate estimate, a 5 km resolution chemistry-transport simulation is performed. Such a resolution is relatively coarse given the sharp orography of the studied area. Valleys are not necessarily well reproduced, and mountain ranges are flattened, appearing lower than they are because of sub-grid averaging. Nevertheless, Section 5.1.3.2 showed that the performance of the model is still good, and in particular it has the ability to capture well the deposition rate of BC on snow measured at an Andean site. Still, the quantitative results from simulation CC5 are not to be taken as definitive, but we have good confidence that the order of magnitude is realistic. This is only a first step and more work needs to be done, but the results obtained so far

show that the model reproduces deposition fluxes and that the approach is promising to extend them and to examine other valleys and periods of the year.

Throughout the study, the idea emerged that the conditions preventing BC deposition on the Andes are the ones that lead to high urban pollution in the city and vice versa (coastal lows strengthening inversions versus enhanced zonal winds). Although a qualitative explanation was given, it is also possible to quantify this relationship with the CHIMERE simulation data. In the model outputs, the correlation between the daily average BC concentration at IND location (downtown Santiago - see Figure 5.2), and the daily average deposition of BC on the target area is -0.58 [-0.63;-0.51] at the 95% level. This number illustrates the idea that urban pollution and deposition on the cryosphere are anti-correlated despite their sharing the same sources. This phenomenon is explained by the fact that if the meteorological conditions do not allow for the export of pollutants (i.e. no wind and/or presence of a coastal low) then particulate matter accumulates over Santiago without the possibility of export. A result of such conditions is (i) high concentrations of pollutants in Santiago due to accumulation (ii) no deposition on the glaciers for the period that follows because pollutants are not able to export and remain above the urban area and hence cannot reach the Andes. More favorable export conditions result in the exact opposite with a renewal of air masses in Santiago when polluted ones are exported, thus explaining the observed anti-correlation.

5.1.9 Conclusions

In wintertime, light-absorbing particles such as BC are massively emitted in the metropolitan area of Santiago. Measurements in the literature show significant amounts of BC in snow in the Andes near Santiago, but the contribution of the city was never estimated. Based on chemistry-transport simulations, we show that urban emissions can contribute to up to 40% of BC deposition on southeastern snow or ice-covered areas of the Central Andes, corresponding to $200\,\mu g\,m^{-2}$ for the month of July 2015, with a potential dramatic radiative impact. Despite rather stable conditions in wintertime, we show that an essential role is played by up-slope winds, i.e. mostly zonal winds, in the afternoon, that carry polluted air masses deep inside the Maipo and Mapocho canyons. If the vertical motions in the valley allow for the export of these polluted masses, they can then access higher elevations and deposit on the snowpack and glaciers. Quantitatively speaking, as soon as zonal winds over Santiago exceed $1\,m\,s^{-1}$ on average in the afternoon, and the vertical diffusion coefficient at the tip of the Maipo valley is higher than $3\,m^2\,s^{-2}$, large amounts of BC are expected to deposit on snow or ice-covered areas. Contrarily, large scale strengthening of easterlies over the Andes, as generated during coastal lows and associated with enhanced subsidence, are linked with decreased export and deposition of pollution towards the mountains. All districts of the Metropolitan Area do not have the same influence on air masses reaching the Andes. As a result, great attention must be paid to emission control policies in this respect. Finally, we show that urban pollution and deposition on the cryosphere are anti-correlated: large BC concentrations at downtown Santiago coincide in general with weak deposition fluxes on the target area and vice versa. These results provide additional information to enrich mitigation policies allowing them not only design measures improving air quality in Santiago but also to mitigate the urban impact on the nearby cryosphere. Although the present study focuses on the area of Santiago, such a configuration involving large urban basins close to the Andean slopes can be found at numerous latitudes along the cordillera. As a result, our conclusions provide a basis to guide further investigation, over a broader area, particularly in the context of the critical need for a thoroughly-informed management of water resources in all Andean countries.

5.1.10 Appendix

WRF configuration		CHIMERE configuration	
Coarse domain resolution	5 km	Coarse domain resolution	5km
Nested domain resolution	1 km	Nested domain resolution	1km
Vertical levels	46	Vertical levels	30
Microphysics	WSM3	Chemistry	MELCHIOR
Boundary and surface layer	MYNN	Gas/Aerosol Partition	ISORROPIA
Land surface	Noah LSM	Horizontal Advection	Van Leer
Cumulus parameterization	Grell G3	Vertical Advection	Upwind
Longwave radiation	CAM	Boundary Conditions	LMDz-INCA + GOCART
Shortwave radiation	Dudhia		

Table 5.2: WRF and CHIMERE configurations

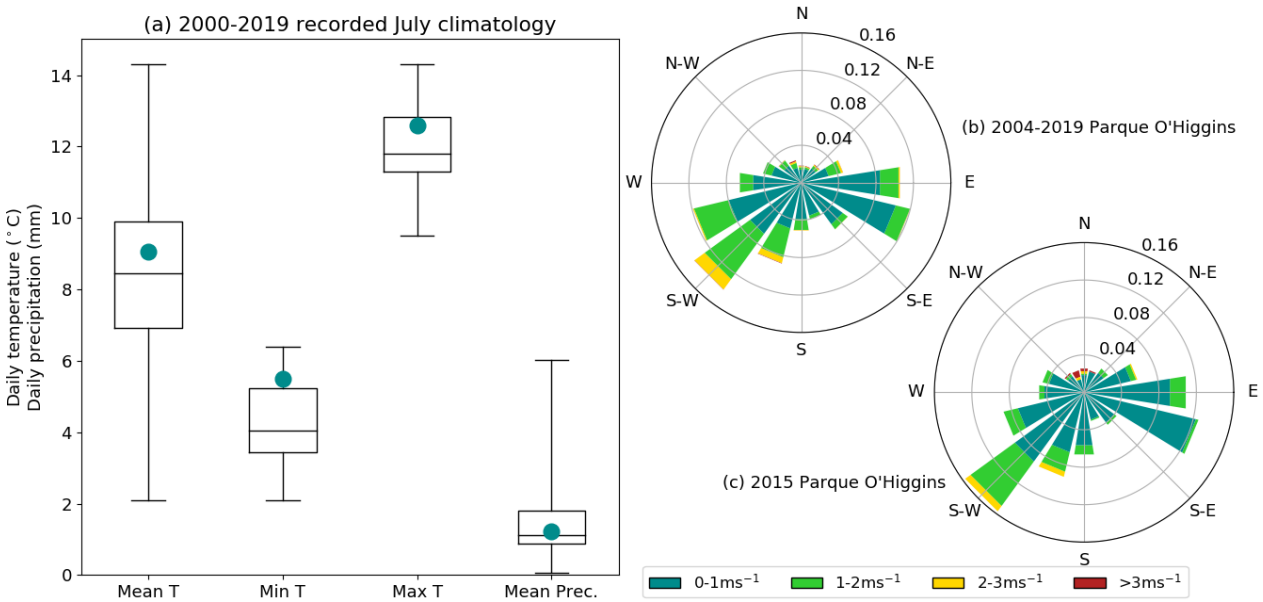

Figure 5.19: (a) Daily 2 m air temperature (average, minimum and maximum) and precipitation (average) distribution for 2000-2019 at DMC (33.44°S,70.68°W). Values for 2015 are shown in blue dots. Source CR2. (b) Hourly 10 m wind speed at Parque O'Higgins (33.45°S,70.66°W), 2004-2019. Source SINCA. (c) Same as (b) for 2015 only.

Station:	Las Condes							Independencia					
	MB		NRMSE		R			MB		NRMSE		R	
TEMP	NA		NA		NA		:	-0.17	-0.18	0.08	0.08	0.91	0.91
RH	-20.64	-18.07	0.28	0.25	0.83	0.86	:	-19.84	-19.60	0.27	0.26	0.83	0.83
U10m	0.39	0.81	0.15	0.21	0.54	0.25	:	-0.31	-0.13	0.74	0.64	0.41	0.41
V10m	-0.01	-0.12	0.18	0.22	0.54	0.53	:	0.46	0.55	0.14	0.15	0.60	0.62
Station:	Pudahuel							Puente Alto					
	MB		NRMSE		R			MB		NRMSE		R	
TEMP	-0.30	0.06	0.09	0.09	0.92	0.92	:	2.12	2.31	0.11	0.12	0.93	0.93
RH	-21.05	-22.18	0.31	0.32	0.76	0.77	:	-19.29	-19.83	0.27	0.28	0.83	0.83
U10m	-0.40	-0.36	0.22	0.22	0.27	0.19	:	-0.40	-0.44	0.14	0.14	0.73	0.71
V10m	0.11	0.32	0.11	0.12	0.66	0.64	:	0.06	0.21	0.12	0.12	0.39	0.41

Table 5.3: Simulation scores for hourly surface meteorology. 1 July to 31 July 2015. Left column values are for CC5, right ones for STG1. MB is mean bias, NRMSE is normalized root mean square error and R is Pearson correlation. TEMP is the 2 m air temperature, RH is relative humidity, U10m and V10m are zonal and meridional wind speed at 10 m, respectively.

Day:	21 July 2015				24 July 2015				25 July 2015		
	MB	RMSE	R		MB	RMSE	R		MB	RMSE	R
TEMP	-0.23	0.03	1.0	:	2.44	0.09	1.0	:	1.19	0.07	1.0
RH	-13.12	0.27	0.84	:	-1.65	0.39	-0.13	:	-2.39	0.19	0.87
U	1.76	0.19	0.9	:	-0.57	0.13	0.92	:	0.48	0.17	0.88
V	0.21	0.17	0.84	:	-0.44	0.11	0.95	:	1.91	0.17	0.95

Table 5.4: Simulation scores for meteorological vertical profiles at 12:00 LT for 3 days at DMC station in Santiago. STG1 simulation.

Station:	Las Condes				Independencia		
	MB	NRMSE	R		MB	NRMSE	R
Daily $PM_{2.5}$	-8.71	0.32	0.11	:	12.68	0.27	0.69
Hourly $PM_{2.5}$	-8.45	0.17	0.33	:	12.74	0.25	0.57
Station:	Pudahuel				Puente Alto		
	MB	NRMSE	R		MB	NRMSE	R
Daily $PM_{2.5}$	16.69	0.32	0.53	:	-6.62	0.27	0.57
Hourly $PM_{2.5}$	16.77	0.22	0.37	:	-6.45	0.17	0.32

Table 5.5: Simulation scores for surface $PM_{2.5}$ concentrations for CC5. 1 July to 31 July 2015.

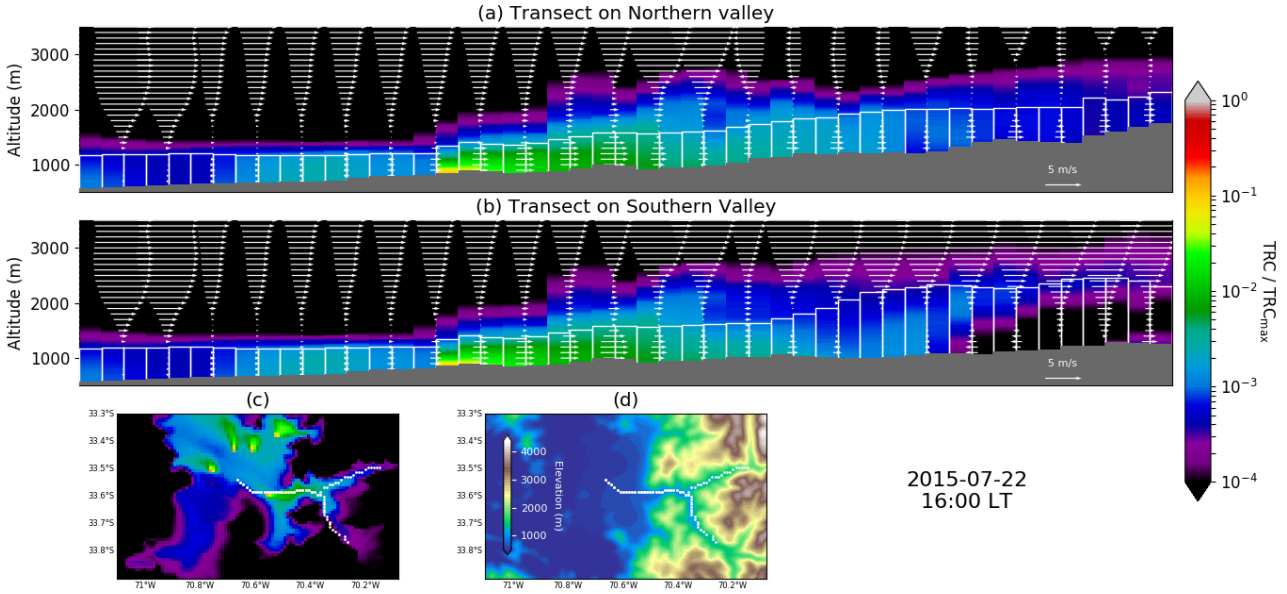

Figure 5.20: (a) Transect of normalized tracers concentration (colormap), along-valley horizontal wind profiles (white arrows) and boundary layer height (white bars) along the northern part of the Maipo canyon. (b) Same as (a) for the southern part of the Maipo canyon. (c) Ground level normalized concentrations of all tracers. White dots show the transect paths. (d) Terrain elevation map. Snapshot on 22 July at 16:00 LT.

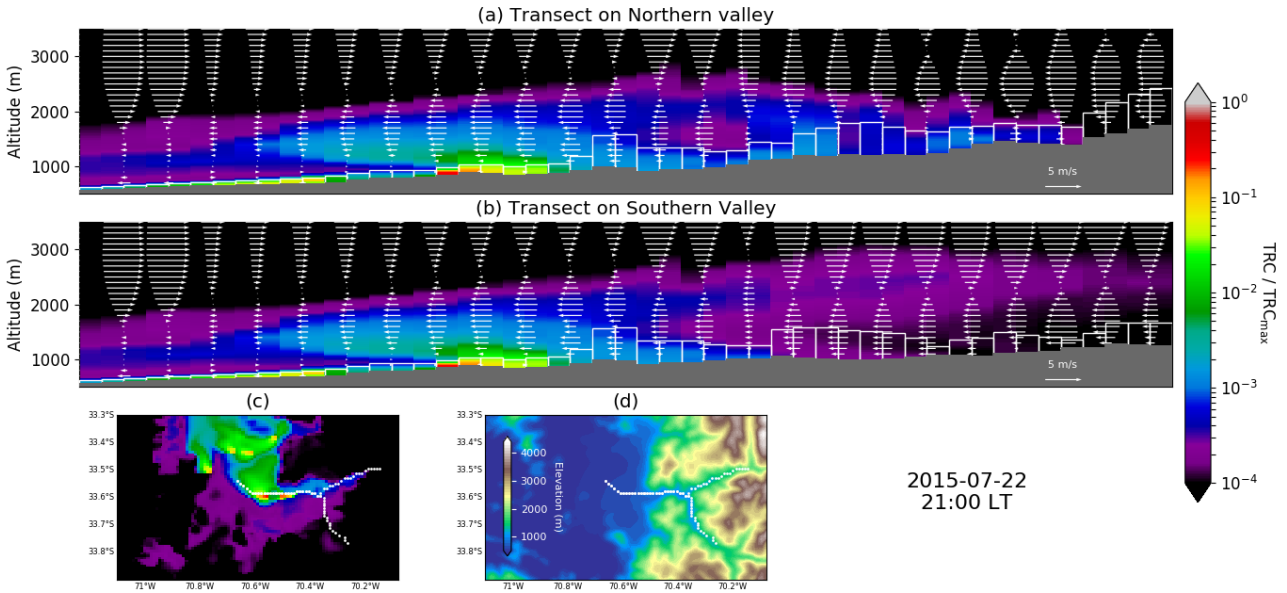

Figure 5.21: Same as Figure 5.20 but on 22 July at 21:00 LT.

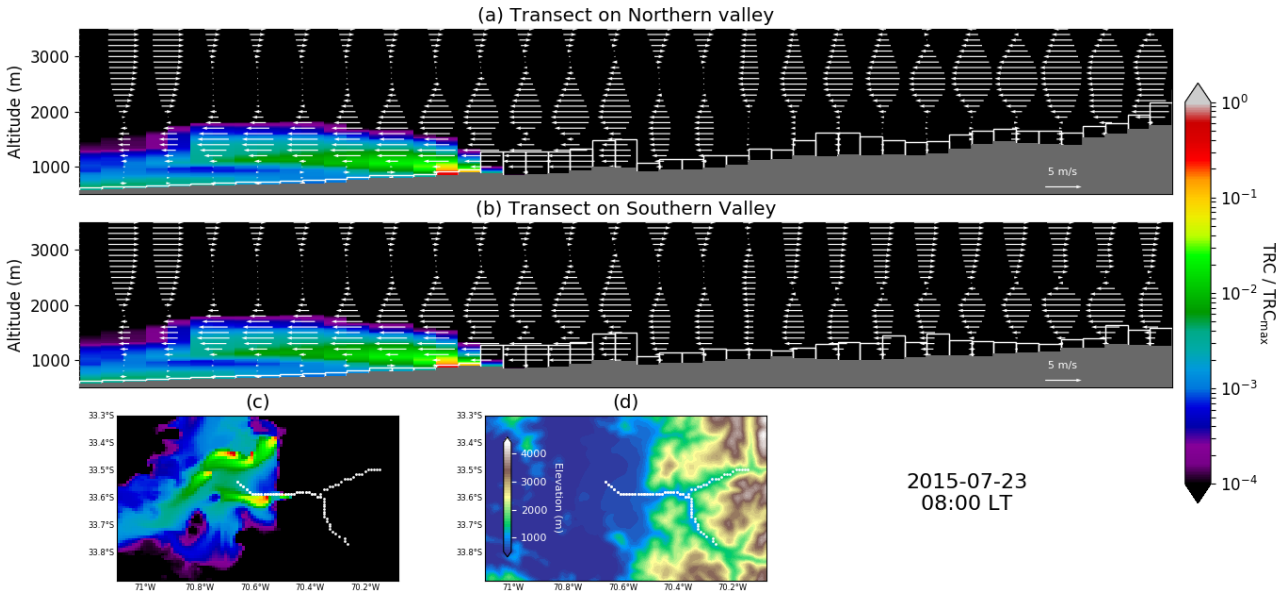

Figure 5.22: Same as Figures 5.20 and 5.21 but on 23 July at 08:00 LT.

5.2 Summertime/Wintertime dichotomy

The previous Section was focused on wintertime periods, as they combine larger emission fluxes of BC and mostly stable atmospheric conditions. Nevertheless, emissions are also significant in summer, and different pathways should be involved. The following section investigates the comparative export mechanisms and deposition fluxes between winter and summer, using chemistry-transport modeling, long-term local observations, and reanalysis.

5.2.1 Abstract

Air pollution in the central zone of Chile not only is a public health concern, but also threatens water resources and climate, in connection with the export and deposition of black carbon from urban centers onto the glaciers of the Andes Cordillera. Chemistry-transport simulations reveal a seasonal dichotomy in the flux and latitudinal pattern of black carbon deposition on central Chilean Andean glaciers. The average deposition flux on glaciers between 30°S and 37°S is 4 times higher in winter, affecting mostly low elevation glaciers, whereas the smaller summertime flux affects glaciers evenly, irrespective of their elevation. The simulated fluxes are comparable to what is found in the literature for glaciers of the Tibetan Plateau. The contribution of emissions from Santiago city is dominant in summertime with more than 50% along the Andes, but minor in wintertime with less than 20% even close to the capital city. In the vicinity of Santiago, a northward gradient in the deposition flux is found in summertime, while it is southward in wintertime. This can be related to the superimposition of synoptic-scale circulation and local mountain-valley circulation in the Santiago basin, with a climatological relevance. Future emissions and climate projections suggest that the summertime/wintertime asymmetry in BC deposition on glaciers will be exacerbated under scenario RCP8.5, while scenario RCP2.6 does not display a significant trend in this regard. This new insight can help better design modeling studies and field campaigns interested in black carbon in the Andes.

5.2.2 Introduction

Urban areas in the central region of Chile (extending roughly between 30 and 37°S) face concerning air pollution issues, especially regarding fine particulate matter ($PM_{2.5}$) [e.g. Saide et al., 2016, Barraza et al., 2017, Lapere et al., 2021c]. Strong anthropogenic emissions of primary particulate matter and precursors mostly stem from road traffic and industrial activities all year round, and a large additional contribution from wood burning for residential heating in wintertime [Marín et al., 2017, Mazzeo et al., 2018]. Among these emissions, black carbon (BC) particles constitute a large fraction, in relation with incomplete combustion of fossil fuel and biomass [Shrestha et al., 2010]. Dense traffic and wood burning for residential heating are dominant sources of BC in central Chile, particularly in the capital city, Santiago [Barraza et al., 2017].

Besides the health issues associated with air pollution [Ilabaca et al., 1999], light-absorbing particles such as BC have a dramatic radiative impact once deposited on snow and ice, inducing a reduction in their albedo, hence accelerating their melting [e.g. Kang et al., 2020]. BC was found in significant amounts in snow and on glaciers of the central Chilean Andes, with an estimated radiative forcing of $1.4\,\mathrm{W\,m^{-2}}$ [Rowe et al., 2019]. The region faces a hydrological deficit since the last decade in relation with the recent mega-drought [Garreaud et al., 2017] so that the additional contribution to accelerated glaciers melting coming from BC leads to an even higher tension on water resources. In this context it is paramount to expand the knowledge on BC transport towards, and deposition on, glaciers of the Chilean Andes.

Central Chile is a narrow strip of land surrounded by the Pacific Ocean in the West and the Andes Cordillera in the East. As a result, the atmospheric circulation is driven both by synoptic-scale conditions related to the position of the South Pacific High (SPH) over the Pacific Ocean, and by mountain-valley circulation dynamics. Mountain-valley circulation is related to the differential heating and cooling between narrow canyons and wide basins under radiative forcing, that generate up-slope and up-valley winds during daytime and a reversal at night with down-slop and down-valley winds [e.g. Whiteman, 2000]. A direct corollary is a strong seasonality in wind regimes, particularly inland in the Santiago basin, in connection with the latitudinal displacement of the SPH and contrasts in solar radiation between winter and summer affecting the mountain-valley circulation.

Several atmospheric measurement campaigns have been conducted in the vicinity of Santiago aiming to investigate the transport of urban BC into the adjacent Andean valleys, each focusing on a different canyon and/or time period [Cordova et al., 2016, Gramsch et al., 2020, Huneeus et al., 2021]. Modeling studies also provided insight on this topic, again focusing on specific periods and/or canyons [Gramsch et al., 2020, Lapere et al., 2021b]. Although the aforementioned studies complement each other to refine the knowledge on BC transport near

Santiago, a more holistic approach both temporally and spatially, with a regional and climatological relevance is missing, to the best of our knowledge.

It is now well established that particulate matter emitted in Santiago has the ability to reach high-elevation areas in the nearby Andes both in summer and winter periods, with transport times of a few hours [Gramsch et al., 2020, Huneeus et al., 2021]. Nevertheless, the aforementioned works focus on atmospheric concentrations but do not investigate deposition on snow or ice covered terrain, which is ultimately the issue at stake. Rowe et al. [2019] measured wintertime BC deposition rates in the high Andes but cannot conclude on source attribution. Symmetrically, Lapere et al. [2021b] used a model-based approach enabling to trace back the origin of deposited BC on the Andean crysophere but only for one winter and a limited area.

The objective of this work is to provide a more complete picture in terms of space, time and drivers of urban BC export towards the Andes Cordillera. In this work, we use chemistry-transport modeling with WRF-CHIMERE to evidence asymmetries in BC deposition on central Chilean Andes glaciers between summertime and wintertime, for a given year. Then, based on local observation and reanalysis the underlying processes driving these differences are identified and extended on a climatological time scale. Finally, CORDEX simulation data is used to have a glimpse at the future trend, under RCP scenarios, in the seasonal asymmetry in BC export from Santiago leading to deposition on the Andes. The methodology adopted and data sets used in this work are described in Section 5.2.3. Results regarding BC deposition fluxes, their meteorological drivers and climatological relevance are presented in Section 5.2.4. The perspectives and shortcomings of these results are discussed in Section 5.2.5, before concluding on this work in Section 5.2.6.

5.2.3 Data and methods

5.2.3.1 Modeling setup

The chemistry-transport modeling setup adopted in this work is the same as in Lapere et al. [2021c]. The same set of simulations is used, despite a different perspective. Hereafter are presented only the most important features of the model. For full details and validation of meteorology and pollutants concentrations, the interested reader is invited to refer to Lapere et al. [2021c]. Simulations are performed with the CHIMERE chemistry-transport model [Mailler et al., 2017], forced by meteorological fields simulated with the Weather Research and Forecasting (WRF) mesoscale numerical weather model from the US National Center for Atmospheric Research [Skamarock et al., 2008]. Anthropogenic emissions only are considered for BC (i.e. biomass burning events are ignored), and are adapted from the EDGAR HTAP V2 inventory [Janssens-Maenhout et al., 2015] using the methodology from Menut et al. [2013]. The simulation domain as shown in Figure 5.23 comprises the central zone of Chile, at the 5 km spatial resolution. A set of four simulations is performed: one month in January 2015 with and without emissions from Santiago city (as defined by the white shaded box in Figure 5.23), and one month in July 2015 considering the same sensitivity analysis. Based on this set of simulations, typical deposition fluxes of BC, including the contribution of emissions from Santiago, for summertime and wintertime can be derived.

The aerosol dry deposition scheme used in CHIMERE for this work is based on Zhang et al. [2001], that relies on a resistance analogy where the deposition velocity v_d can be written as in Eq. 5.2.

$$v_d = v_s + \frac{1}{r_a + r_s} \tag{5.2}$$

where v_s is the the settling velocity related to the particle mass upon which gravity acts to bring it back to ground level, r_a is the aerodynamic resistance that accounts for turbulence and surface friction and roughness, and r_s the surface resistance including Brownian diffusion, impaction and interception terms. More details and formulas for the different components of Eq. 5.2 can be found in the CHIMERE model documentation (`https://www.lmd.polytechnique.fr/chimere/docs/CHIMEREdoc_v2020r1.pdf`).

5.2.3.2 Observational, reanalysis and future scenario data

Local observational data of wind speed and direction in the Santiago area comes from the Chilean air quality monitoring network [Ministerio del Medio Ambiente, 2018], referred to as SINCA in the continuation, and the Chilean weather service [Dirección Meteorológica de Chile, 2019], referred to as DMC hereafter. In order to analyze the large-scale circulation and vertical wind profiles, we use reanalysis data from ERA5 at the 0.25° resolution [Copernicus Climate Change Service, 2017]. In particular, monthly averaged reanalyses of zonal and meridional winds on pressure levels, together with mean sea-level pressure, cloud cover and 10 m zonal and meridional winds are incorporated to the analysis.

The analysis of future trends in surface winds in Santiago is based on outputs from the CORDEX project [Gutowski Jr. et al., 2016] on the South America domain at the 22 km resolution (SAM-22), for two regional climate models (REMO2015 and RegCM4-7) driven by three different general circulation models (MOHC-HadGEM2-ES, MPI-M-MPI-ESM and NCC-NorESM1) under two future scenarios (RCP2.5 and RCP8.5). The variables of interest were downloaded through the Earth System Grid Federation (ESGF) data platform [ESGF, 2014]. Wind speeds are considered as the ensemble mean of the six realizations for each scenario. Wind direction is not available in REMO2015 outputs so that RegCM4-7 data only is used for this variable. These trends in the regional climate are put into perspective with regard to expected changes in BC emissions in Santiago area. For that, RCP2.6 [van Vuuren et al., 2007] and RCP8.5 [Riahi et al., 2007] emissions scenarios are considered. The data was downloaded from the RCP Database `https://tntcat.iiasa.ac.at/RcpDb/`.

For ERA5, CORDEX and RCP emissions data, when graphs show results for Santiago, the nearest grid point to downtown Santiago (33.5°S, 70.65°W) is considered, without interpolation.

5.2.3.3 Analysis methodology

The methodological approach adopted in this study follows three steps. First, using chemistry-transport modeling for a summer month and a winter month in 2015, an estimate of the deposition flux of BC on the glaciers of central Chile is derived, as well as the share attributable to emissions from Santiago city. These time-limited simulations are designed to provide insight on the seasonality, magnitude and areas most affected by BC deposition. Then, differences in circulation explaining the seasonal and spatial asymmetry in deposition observed in the simulations are identified using multi-annual time series from reanalysis and local observation, in order to account for the climatological relevance of the chemistry-transport results. Finally, future projections of this circulation are analyzed using CORDEX data under RCP scenarios.

Throughout this work, the locations of glaciers are defined based on WGMS and National Snow and Ice Data Center (comps.) [1999, updated 2012] and the corresponding nearest grid point in the CHIMERE domain is used to compute the deposition flux. Rock glaciers are excluded from the analysis as the main concern regarding BC deposition on glaciers is the impact on their albedo. Several localities and canyons in the vicinity of Santiago are considered throughout this work. For more detail on their exact locations, the reader is invited to refer to Figure 5.30.

5.2.4 Results

5.2.4.1 Seasonal asymmetry in BC deposition

In connection with the radiatively-driven mountain-valley circulation and synoptic wind regimes driven by the position of the SPH, summertime and wintertime ventilation conditions in central Chile are significantly different, as will be further investigated in Section 5.2.4.2. In parallel, anthropogenic emissions of primary pollutants such as BC also feature a pronounced seasonality, as shown in the HTAP inventory (colormap in Figure 5.23). In particular, this inventory evidences that in summer (January) BC emissions are concentrated in large urban centers such as the Santiago basin (white shaded box in Figure 5.23) and the Valparaíso (33°S,71.5°W) and Concepción (37°S,73°W) regions. In contrast, wintertime (July) emissions of BC are more evenly scattered across the domain, in relation with the widespread use of wood burning for residential heating purposes during that season, all along central Chile. This additional emission source in wintertime leads to a monthly total flux of BC over the domain 62% lesser in summer compared to winter, with 123 ton month^{-1} for January and 324 ton month^{-1} for July.

As a result of the combination of the seasonality both in emissions and circulation, deposition fluxes of BC greatly differ between January and July 2015 at the scale of central Chile. In particular, the glaciers-averaged BC deposition flux between 30 and 37°S is four times larger in winter, at 634 µg m^{-2} month^{-1}, compared to summer with 158 µg m^{-2} month^{-1} (blue boxes in Figure 5.23). In these totals, the contribution of Santiago emissions is dominant in summertime with 50% of the BC particles deposited coming from the capital city, while it accounts for only 14% in wintertime (gray boxes inside the blue boxes in Figure 5.23). The seasonality in spatial patterns of BC emissions aforementioned, with emissions found mostly in large urban centers in summer but more scattered in winter, accounts for this observation.

In the direct vicinity of Santiago city, the seasonality is less pronounced regarding the monthly total deposition flux with 292 µg m^{-2} month^{-1} in summer and 322 µg m^{-2} month^{-1} in winter. Emissions in the capital city being dominated by traffic and industrial sources throughout the year, the additional contribution from wood burning for residential heating in winter only induces a minor increase. However, in terms of relative contribution from

Santiago emissions, the seasonal difference is even greater close to the urban basin, with 74% of deposition in summer whereas only 18% in winter. In this case, seasonal variations in regional emissions only cannot explain this large difference.

The aforementioned absolute deposition fluxes are considerably larger than what is modeled regionally for the Tibetan Plateau (maximum deposition rate in the monsoon season around 120 $\mu g\,m^{-2}$) [Ji, 2016] and comparable to the results of measurement campaigns on specific glaciers in that same region (between 2.4 and 62.6 $\mu g\,m^{-2}\,day^{-1}$ [Wang et al., 2017] and between 2.6 and 34.6 $mg\,m^{-2}\,year^{-1}$ [Yan et al., 2019] i.e. 72 to 2,883 $\mu g\,m^{-2}\,month^{-1}$). The implications of this comparison are discussed in Section 5.2.5.

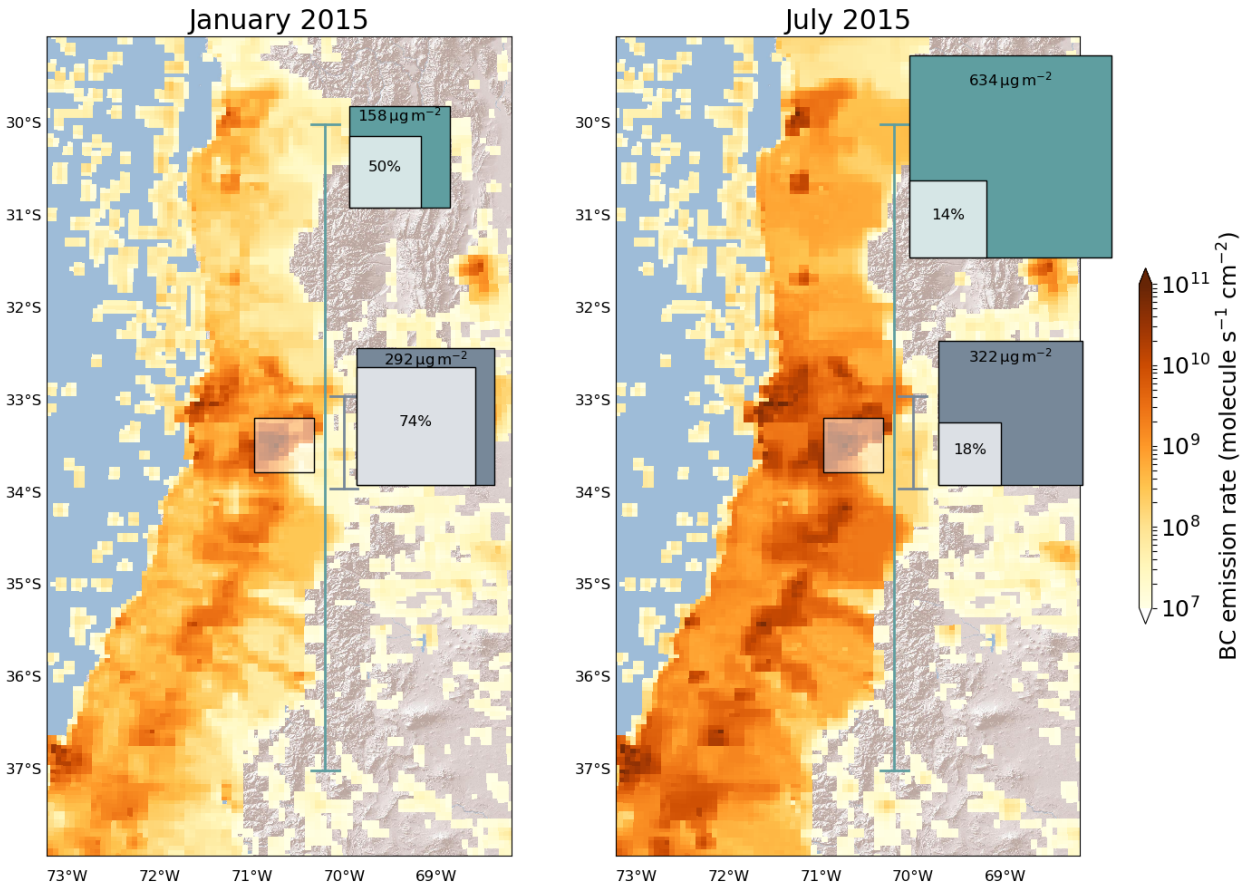

Figure 5.23: Simulated emissions of BC and accumulated deposition on glaciers of the central Chilean Andes in January and July 2015. Color map shows BC emission rates. White shaded box represents the Santiago city area. Colored boxes indicate the average monthly accumulated BC deposition on glaciers (outer box, in $mg\,m^{-2}$) and contribution from emissions in Santiago (inner box, in percent). Blue boxes correspond to glaciers between 30°S and 37°S as indicated by the blue lines, whereas grey boxes (associated with the grey lines) are for the direct vicinity of Santiago (33°S to 34°S). Box areas proportions correspond to the total deposition proportions. Map background layer source: World Shaded Relief, ©2009 Esri.

In order to further investigate the large difference in the contribution of Santiago emissions to BC deposition of Andean glaciers in the vicinity of the capital city, Figure 5.24 provides a more detailed picture with glacier-by-glacier simulated BC deposition rates and relative contribution for that region. In absolute value, deposition rates feature a large spatial heterogeneity in both seasons, with affected areas varying between summer and winter (Figure 5.24a and b). In summertime, deposition is larger on glaciers closer to the longitude of Santiago and decreases eastward, with a smooth gradient both in the west-east and north-south directions. It reaches a maximum slightly north of the city, along the Olivares river canyon and near the tip of the Mapocho river canyon, at more than 1 $mg\,m^{-2}$ for the month of January (red circles in Figure 5.24a). In winter, the BC deposition flux is spatially more erratic (Figure 5.24b), in line with the previous comment on emissions being scattered across the region. Maximum values are obtained near the south of Santiago, particularly near the tip of the Maipo

river canyon, where deposition rates rise up to $1\,\mathrm{mg\,m^{-2}}$. Deposition hot spots are also found further south in connection with other large urban areas such as Rancagua (34.2°S,70.7°W), San Fernando (34.6°S,71°W) and Curicó (35°S,71.2°W).

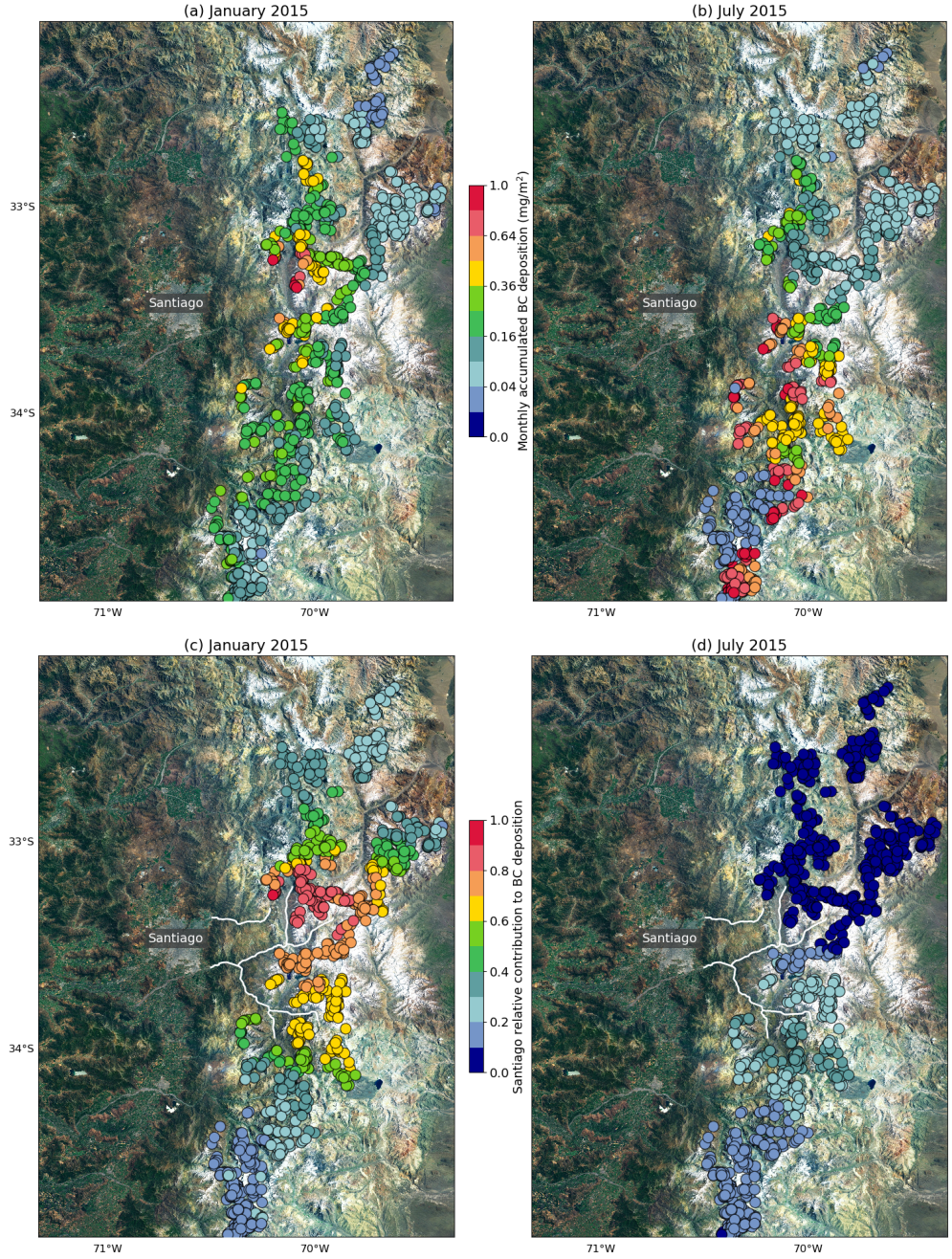

Figure 5.24: (a) Monthly accumulated BC deposition on glaciers in the vicinity of Santiago (colored circles) for January 2015. (b) same as (a) for July 2015. (c) Relative contribution of emissions from Santiago to accumulated BC deposition on glaciers for January 2015. (d) same as (c) for July 2015. White lines indicate the main canyons connecting Santiago to the glaciers. Map background layer source: Imagery World 2D, ©2009 Esri.

The more heterogeneous picture in wintertime is consistent with the underlying time dynamics of deposition. In summer, the glaciers-averaged BC deposition time series features a pronounced, smooth diurnal cycle, with a steady daily deposition rate varying between 4 and $13\,\mathrm{\mu g\,m^{-2}}$ for the month of January, associated with a relative standard deviation of 26%. In contrast, the same time series for July is more chaotic, featuring no clear variability mode and daily deposition rates between 2 and $37\,\mathrm{\mu g\,m^{-2}}$ with a relative standard deviation of 109%.

The winter time series also includes a wet deposition component that exacerbates its erratic behavior. This component is absent in summertime due to essentially dry conditions in the region for that season.

Regarding the relative contribution of emissions from Santiago, Figures 5.24c and d also reveal contrasting patterns between January and July. In the direct vicinity of the capital city, the contribution ranges from 50% to 100%, with a northward gradient. Above 33°S and below 34°S the contribution decreases around 30%. Contrarily, in July the contribution from Santiago emissions does not exceed 40% and is concentrated in the south, near the Maipo river canyon (southernmost white line connecting Santiago to the Andes in Figure 5.24d). This finding is consistent with Lapere et al. [2021b] that evidenced the export mechanism of pollutants from Santiago to the Andes in wintertime and revealed the critical role of mountain-valley circulation in the Maipo river canyon. In comparison, all major canyons seem to significantly channel BC higher up in large amounts in summer (at least 50% in the vicinity of the white lines in Figure 5.24c). In particular, in the area of the Mapocho river canyon (northernmost white line in Figure 5.24c), moderate BC deposition fluxes are found in July, originating mostly from outside Santiago, whereas they are larger in January and mostly attributable to Santiago emissions. This finding is consistent with Gramsch et al. [2020] that observed more transport of BC inside this canyon in summer than in winter.

Variations in emissions alone do not account for the differences in summertime and wintertime deposition patterns. The theoretically more intense mountain-valley circulation in summer provides a first additional driver for these differences. Nonetheless, this phenomenon does not account for the reversed gradient in the contribution of Santiago emissions (northward in summer, southward in winter, as observed in Figure 5.24c and d) given that the magnitude of emissions only changes between seasons in our modeling experiment, not their spatialization in the Santiago basin. Besides, based on the findings of Lapere et al. [2021b], mountain-valley circulation driven export of BC should primarily affect lower elevation glaciers. However, Figure 5.25 shows that in summertime, the BC deposition flux on glaciers between 30°S and 37°S does not seem elevation-dependent (orange line in Figure 5.25), although it does indeed decrease with altitude in wintertime (blue line in Figure 5.25) confirming the dominant role of mountain-valley circulation for that season.

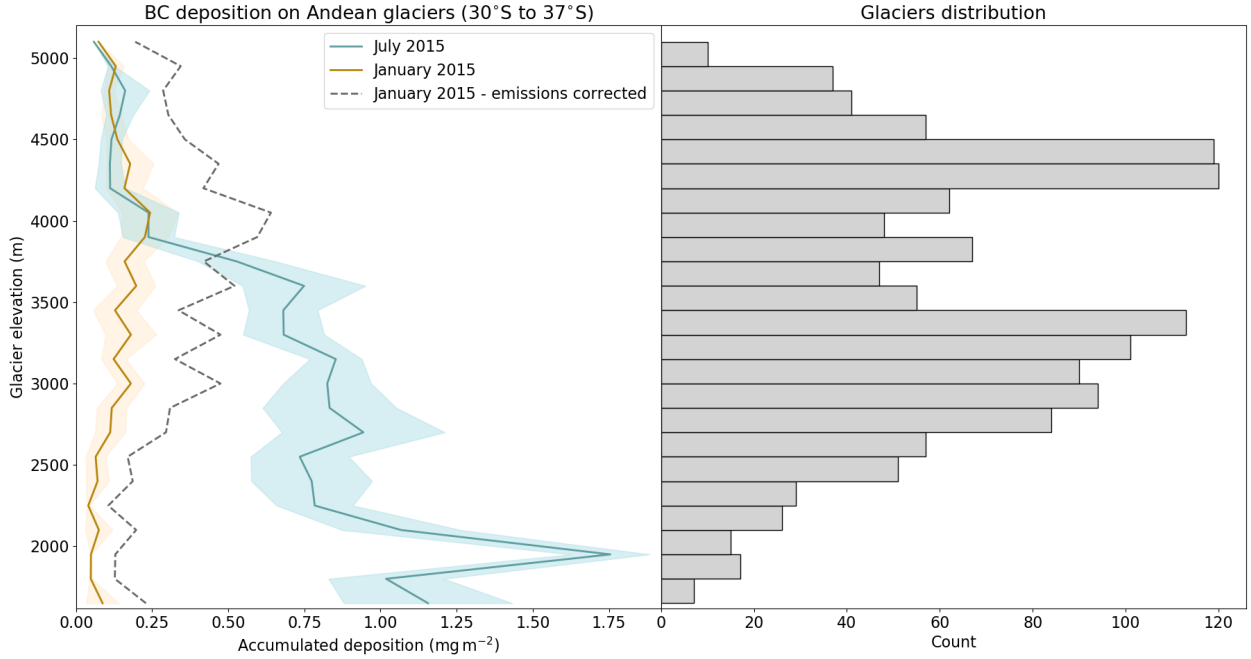

Figure 5.25: BC accumulated deposition on glaciers between 30°S and 37°S depending on their mean elevation, and corresponding number of glaciers for each elevation bin (grey bars). Average for January 2015 (brown line) and July 2015 (blue line). Colored shades show one standard deviation. Dashed grey line is for January 2015 but multiplying the deposition flux by a factor accounting for the difference in emissions compared to July. Glaciers are clustered every 250 m of elevation.

Assuming a simplified linear relationship between emission and deposition fluxes, the gray dashed line in Figure 5.25 shows the deposition profile in summertime multiplied by the wintertime/summertime emission ratio. In that case, a maximum in the deposition rate is obtained near 4000 m elevation, more than twice as

large as compared with the lowest glaciers, and significantly greater than in wintertime for glaciers at the same elevation. In parallel, even after multiplication, summertime deposition at low elevation is still largely smaller than in wintertime for the same altitude. In summary, BC is primarily deposited on low-elevation glaciers in wintertime, while BC has the ability to deposit on higher-elevation glaciers in summertime where it finds its maximum deposition flux.

It is worth noting that this asymmetry on the vertical profile does not stem from a statistical bias, since many glaciers are found both in altitude zones of high and low deposition rates in both seasons as shown in the histogram in Figure 5.25. Between 30°S and 37°S, glaciers are predominantly found around 3000 m (large deposition in wintertime, small in summertime) and 4500 m (small deposition in wintertime, large in summertime) elevation.

In conclusion, the chemistry-transport modeling experiment evidenced strong differences in the horizontal and vertical patterns in BC deposition between winter and summer, as well as in the underlying time dynamics. As a result, the following hypothesis regarding the processes driving the export of urban BC towards the Andes can be derived: in wintertime, erratically occurring mountain-valley circulation driven export dominates the deposition flux, while in summertime the mountain-valley circulation amplifies but a synoptic-scale motion superimposes, leading to BC export higher up and in a different direction than in wintertime. The next sections investigate the validity of these hypotheses, within a climatological framework through the analysis of ERA5 data and local observations of atmospheric circulation.

5.2.4.2 Role of local and synoptic-scale circulation

Synoptic-scale circulation in the central zone of Chile is driven by the position of the SPH, in conjunction with the passage of migratory anticyclones regularly leading to the formation of coastal lows disrupting circulation for a few days [e.g. Garreaud et al., 2002]. In particular, the contours in Figure 5.26 shows that for the period 2010-2020, the SPH is located near (35°S,100°W) in January and 5° northward in July near (30°S,100°W), resulting in strong southwesterlies along the Chilean coast at the latitude of Santiago in January, whereas weaker southerlies are observed in July. This synoptic forcing results in dominant southerwesterlies inland as far as Santiago (black box in Figure 5.26) in January but no established regime in July. The summertime synoptic wind direction is thus consistent with the orientation of the Mapocho and Olivares canyons neighboring the glaciers where maximum deposition and contribution from Santiago are observed in the chemistry-transport simulations. This points to synoptic winds playing a key role in the export of BC from the urban basin towards the Andes.

Simultaneously, cloud cover is mostly nonexistent above Santiago in January with less than 10% cloud cover on average, while the months of July exhibit a 50% cloud cover (colormap in Figure 5.26). Consequently, solar radiation fully reaches the ground in summertime, resulting in very active mountain-valley circulation. In contrast, surface radiation is weaker and more variable in wintertime, leading to a comparatively weaker mountain-valley circulation and by extension less BC export through this process. Therefore, in addition to synoptic winds, mountain-valley circulation also governs BC export in summertime and superimposes on large scale motions. Otherwise, the large deposition rates obtained in the chemistry-transport simulations along the Maipo river canyon, which has a NW-SE orientation perpendicular to the synoptic wind direction, would not be observed if only the synoptic scale played a role. This finding is consistent with Zängl [2009] for instance, that observed an influence of synoptic forcing on valley-wind circulation when the associated direction matches the direction of the considered valley. It is worth noting that mountain-valley circulation is naturally stronger in summertime regardless of cloud cover considerations, due to longer days and smaller solar zenith angles. The difference in cloud cover evidenced here thus exacerbates this phenomenon.

The previous analysis considered surface winds. Vertical wind profiles also advocate in favor of a strong contribution of synoptic forcing to wind conditions in Santiago thereby influencing the export of BC. Figure 5.27 reveals that the aforementioned SPH-generated southwesterlies not only dominate near the surface but also throughout the mixing layer up to 825 hPa in summertime, with average wind speeds between 2 and 3 $\mathrm{m\,s^{-1}}$. Above the mixing layer, a smooth transition towards stronger winds of 6 to 8 $\mathrm{m\,s^{-1}}$ is observed, with a primary northerly component. The picture is different in wintertime. Average wind speed in the mixing layer up to 900 hPa do not exceed 1 $\mathrm{m\,s^{-1}}$ and do not feature a preferred direction. Winds aloft however are much stronger, well above 10 $\mathrm{m\,s^{-1}}$, with a similar direction as in summertime, and create a strong wind shear at the interface between the mixing layer and the free troposphere around 800 hPa.

Therefore, advection of BC by southwesterlies consistently takes place throughout the mixing layer in summer, and the smooth transition towards free troposphere winds does not exclude vertical export outside the mixing

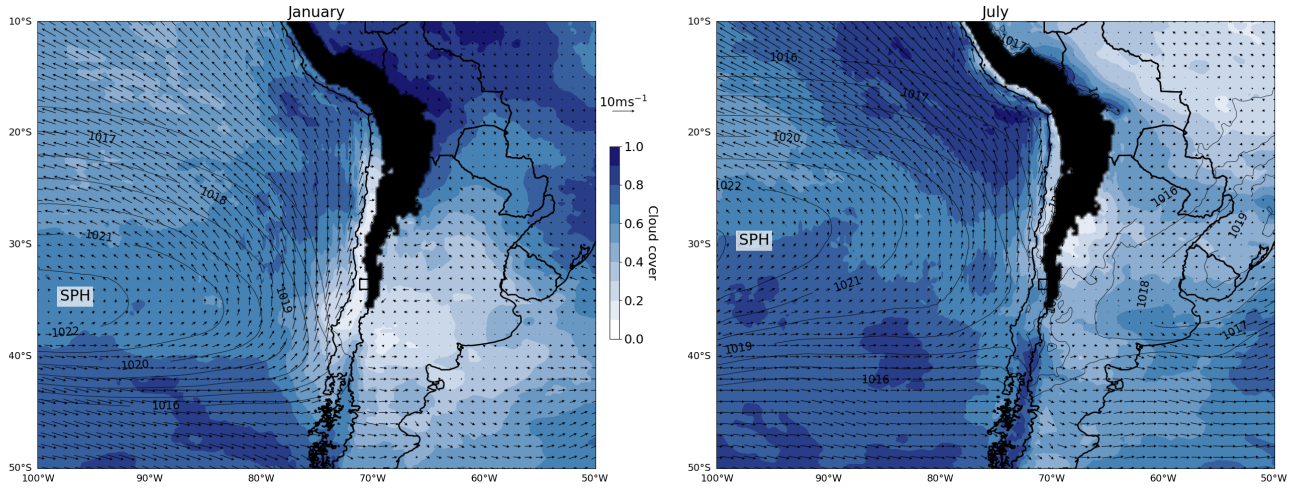

Figure 5.26: Composite synoptic scale circulation for January (left) and July (right) months for the period 2010-2020. Contours indicate mean sea-level pressure (hPa), colormap corresponds to cloud cover, arrows show 10-meter wind speed. Black area represents the Andes where elevation is higher than 2500 m. Black box indicates the location of Santiago. Data from ERA5 single level reanalysis.

layer of a fraction of emissions. In comparison, wintertime emissions are contained within a shallower, stable mixing layer, with no homogeneous horizontal motion. These observations reinforce the idea that the summertime BC export is governed by synoptic winds and mountain-valley circulation combined, while only mountain-valley circulation only dominates the export in wintertime, with no synoptic component.

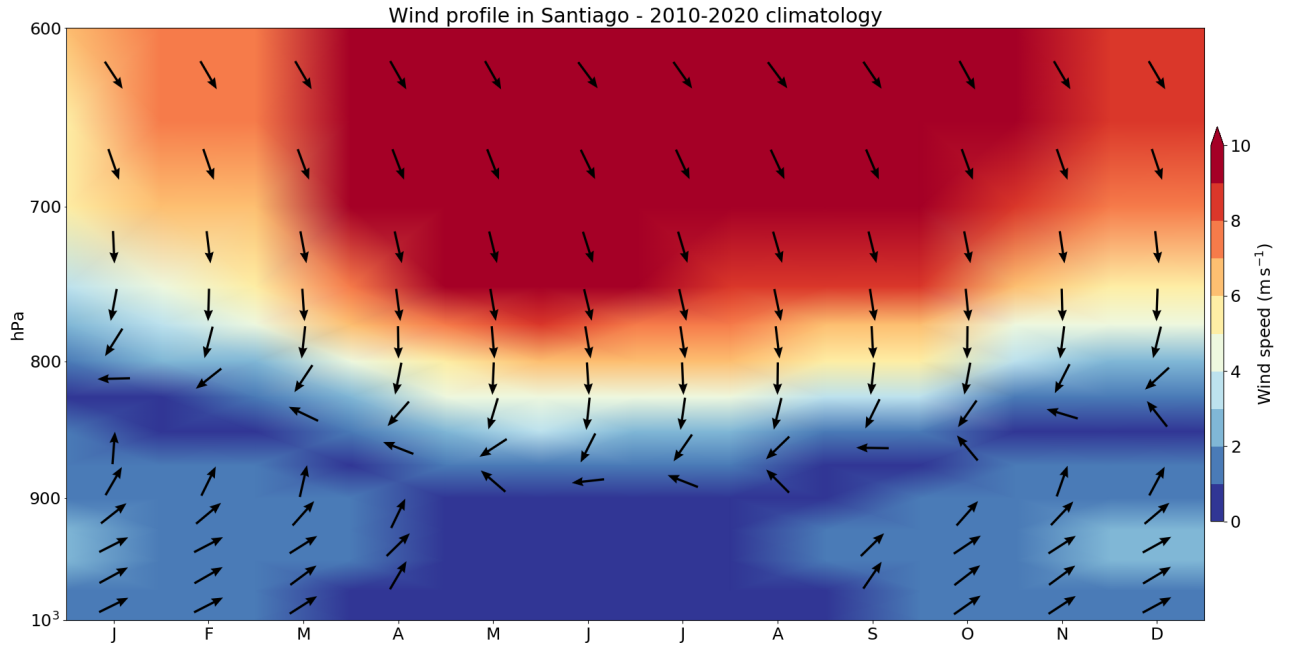

Figure 5.27: Monthly climatological wind profile in Santiago for 2010-2020. Colors indicate wind speed, arrows indicate wind direction. Directions are displayed for average wind speeds above 1 m s^{-1} only. Average of monthly means from ERA5 pressure-levels reanalysis.

The previous results in this section are based on ERA5 data. Although reanalysis data are state-of-the-art when it comes to the representation of large-scale fields over climatological time scales, their resolution is not suitable for the study of local-scale phenomena. Therefore, in order to confirm the processes identified above, a similar analysis is conducted hereafter based on local observation.

Surface wind observations at different sites in the Santiago basin and inside nearby canyons show a good agreement with the proposed BC export mechanisms. Figure 5.28 compares wind roses in January and July for four sites: Parque O'Higgins (PQH) in the center of the city (Figure 5.28a), Las Condes (CND) in the northeast near the Mapocho river canyon entrance (Figure 5.28b), Puente Alto in the southeast near the Maipo river canyon entrance (Figure 5.28c), and San Jose de Guayacan inside the meridional branch of the Maipo river canyon (Figure 5.28d). A map designating the aforementioned locations and associated canyons can be found in Figure 5.30.

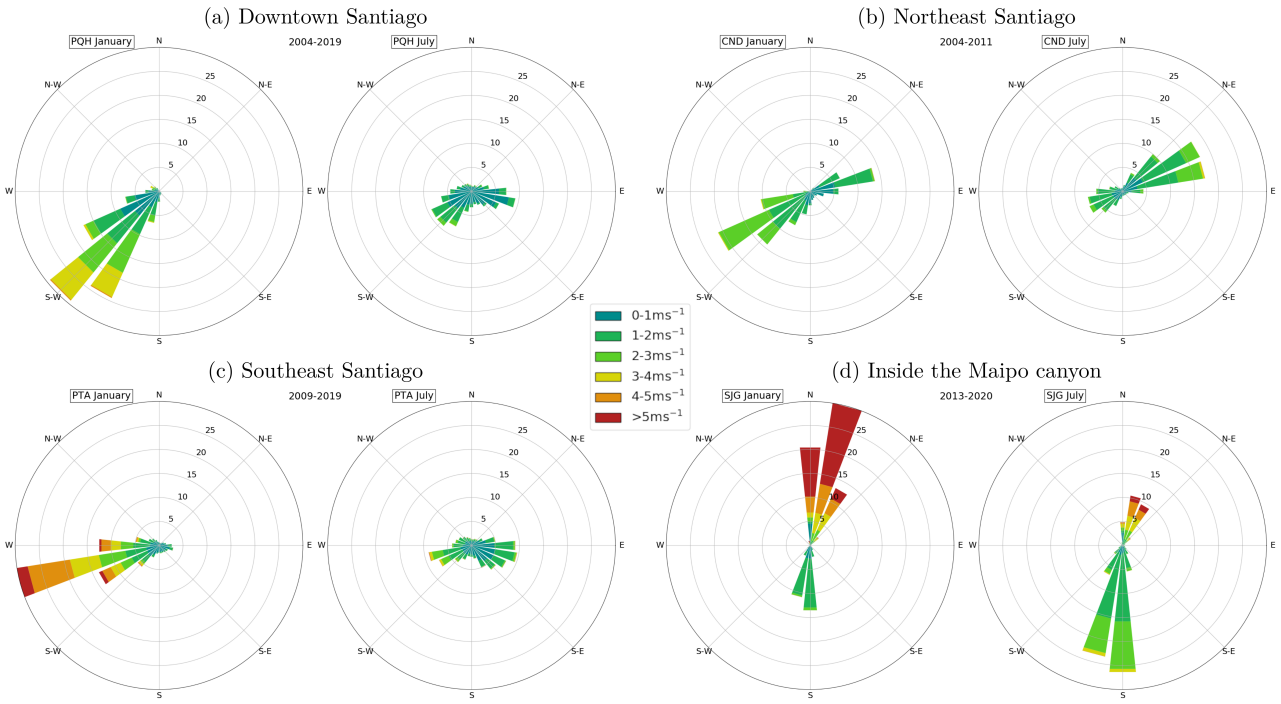

Figure 5.28: Climatological wind speed and direction distribution at (a) Parque O'Higgins (PQH - downtown Santiago), (b) Las Condes (CND - northeast Santiago, near the entrance of the Mapocho canyon), (c) Puente Alto (PTA - Southeast Santiago, near the entrance of the Maipo canyon), (d) San Jose de Guayacan (SJG - deep into the Maipo canyon). Lengths of the underlying time series vary depending on data availability. Wind roses display the distribution of hourly data. Source SINCA for (a), (b), (c), source DMC for (d).

In downtown Santiago (Figure 5.28a), there is a clear dichotomy between January and July months winds over the last 15 years. January months feature a predominant southwesterly component in wind direction and wind speeds frequently above $3\,\mathrm{m\,s^{-1}}$. This is consistent with the synoptic forcing observed in Figure 5.26. Wind speeds are much slower in July, barely exceeding $2\,\mathrm{m\,s^{-1}}$, and wind directions exhibit a clear southwesterlies/easterlies dipole consistent with mountain-valley circulation patterns of winds blowing towards the Andes during the day (westerlies) and back towards the urban basin during the night (easterlies). For this location however, there is no easterly component in January, meaning that mountain-valley circulation is inhibited by the strong synoptic winds.

The observation at the PTA site near the Maipo river canyon entrance is similar: strong westerlies well above $4\,\mathrm{m\,s^{-1}}$ dominate in January, and weaker winds forming a mountain-valley dipole are recorded in July. Nonetheless, for this location a summertime easterly component indicative of down-valley winds is observed contrary to downtown, thus evidencing the occurrence of mountain-valley exchanges despite the dominance of synoptic westerlies.

The records show a different situation at PTA's counterpart site, CND, near the entrance of the Mapocho river canyon (Figure 5.28b). The mountain-valley dipole is observed both in January and July, with a shift from more frequent occurrences of southwesterlies in January to more frequent northeasterlies in July. Nevertheless, both components of the dipole remain significant and wind speeds are in the same range for both seasons. It is worth noting that the shift in the dominant wind direction explains the limited deposition flux in absolute and relative value observed in July compared to January in the area of the Mapocho river canyon (Figure 5.24). In

July, mostly down-valley winds (northeasterlies) are observed with consequent wind speeds, thus preventing intrusion of BC into the canyon for a majority of the time. In January, wind conditions are the other way around hence favoring the export of BC from Santiago into the canyon.

Unfortunately, wind speed data inside the canyons are available for only one site, SJG, located in the meridional branch of the Maipo river canyon (Figure 5.30) so that a comparison with what occurs in other canyons is prevented. Nonetheless, it is interesting to observe that at the SJG site, northerlies greater than $5\,\mathrm{m\,s^{-1}}$ dominate the summertime winds, still with a significant component from the south but related to moderate wind speeds. In wintertime, northerlies are still the strongest winds in terms of speed but they are less frequent than southerlies that occur the majority of hours, again associated with moderate wind speeds. Given the configuration of the canyon, northerlies are associated with air masses coming from the urban basin, thus bringing BC deep into the canyon as evidenced in Huneeus et al. [2021]. These winds are the counterpart of westerlies at PTA. As a result, Figure 5.28d accounts very well for the larger contribution of Santiago emissions to BC deposition fluxes in summertime compared to wintertime near the Maipo river canyon observed in Figure 5.24c and d: the westerly at PTA / northerly at SJG combination is the most favorable for urban BC intrusions into the canyons, and is recorded much more frequently in January than in July. Absolute deposition fluxes in that area are still larger in winter than in summer (Figure 5.24a and b) despite advection conditions being more favorable in summer, but emissions are also significantly larger in wintertime, thus explaining the larger share from Santiago but smaller absolute total in summer.

In summary, chemistry-transport simulations, reanalysis and local observations consistently evidence and explain that (i) summertime conditions are more favorable for the export of urban BC but lower emission rates in Santiago lead to less deposition, (ii) synoptic winds influence the summertime export throughout the mixing layer, combining with mountain-valley circulation dynamics, while only the latter govern wintertime deposition. The next section briefly explores whether and how this summertime/wintertime dichotomy is likely to evolve under climate change and emission scenarios.

5.2.4.3 A glimpse at future trends

Figures 5.29a and b show the time series of future wind speed in Santiago under RCP2.6 and RCP8.5 scenarios, as downscaled within the CORDEX framework (see Section 5.2.3.2 for details on the data and models used). In the context of the RCP2.6 scenario, the ensemble mean does not contain a significant trend (in the sense of a Mann-Kendall test) for either season (gray lines in Figures 5.29a and b). Similarly, no trend is observed in the wind direction in that scenario (Figure 5.29c). Oppositely, the RCP8.5 scenario leads to significant trends in wind speed in January and July and in wind direction in January, with $+0.02\,\mathrm{m\,s^{-1}\,dec^{-1}}$, $-0.03\,\mathrm{m\,s^{-1}\,dec^{-1}}$ and $-1.38\,^{\circ}\,\mathrm{dec^{-1}}$, respectively. In other words, under RCP8.5 scenario hypotheses, summertime wind speeds will increase while wintertime wind speeds will decrease in Santiago area. Although the trends have a limited magnitude, based on the findings of Section 5.2.4.2 the summertime/wintertime dichotomy in BC export potential will thus be exacerbated in the future, with even more (less, respectively) favorable conditions for export in summer (winter, respectively). The slight trend in wind direction for January months observed in Figure 5.29c should not influence dramatically the areas where deposition occurs. Neither scenario indicate a trend in wind direction for July months (not shown here).

Along with climate, anthropogenic emissions of greenhouse gases and pollutants also evolve in RCP scenarios. Interestingly, the scenario limiting climate change (RCP2.6) is associated with a lesser reduction in BC emissions compared to the business-as-usual scenario (RCP8.5) for Santiago, with almost no emissions as of 2100 in RCP8.5 but still more than $200\,\mathrm{ton\,yr^{-1}}$ in RCP2.6 by the end of the century. This comparison is reversed at the global scale where BC emissions remain higher in RCP8.5 (not shown here). The reason for the RCP8.5 featuring lesser BC emissions than RCP2.6 is that the latter is a climate-focused scenario where BC emissions reductions are mostly a co-product of policies on greenhouse gases emissions, while the former assumes that in regions of the world with high exposure to atmospheric pollution, the effort is focused on designing stringent air quality policies [van Vuuren et al., 2011]. This category of regions comprises Santiago, hence accounting for comparative trends in emissions in both RCP scenarios.

However, RCP emission scenarios do not provide infra-yearly detail. No information is available on whether the seasonal cycle of emissions will change under such scenarios. Nevertheless, RCP8.5 likely leads to increasing average temperatures in the Santiago area. In that case, one can assume that the need for residential heating will decrease as a result, thereby limiting wood burning for that purpose in wintertime, generally speaking. Since the difference in BC emissions between summer and winter mostly stems from the contribution of this source, it is likely that under RCP8.5 scenario, summertime BC emissions become closer in magnitude to wintertime

emissions.

In conclusion, although BC emissions in Santiago will likely drop in the coming decades regardless of the scenario, under RCP8.5 assumptions, summertime emissions will catch up on wintertime emissions, and the more favorable export conditions in summertime will be exacerbated. Consequently, despite currently larger BC deposition fluxes on glaciers in wintertime, summer will likely become the important season in the future in this respect.

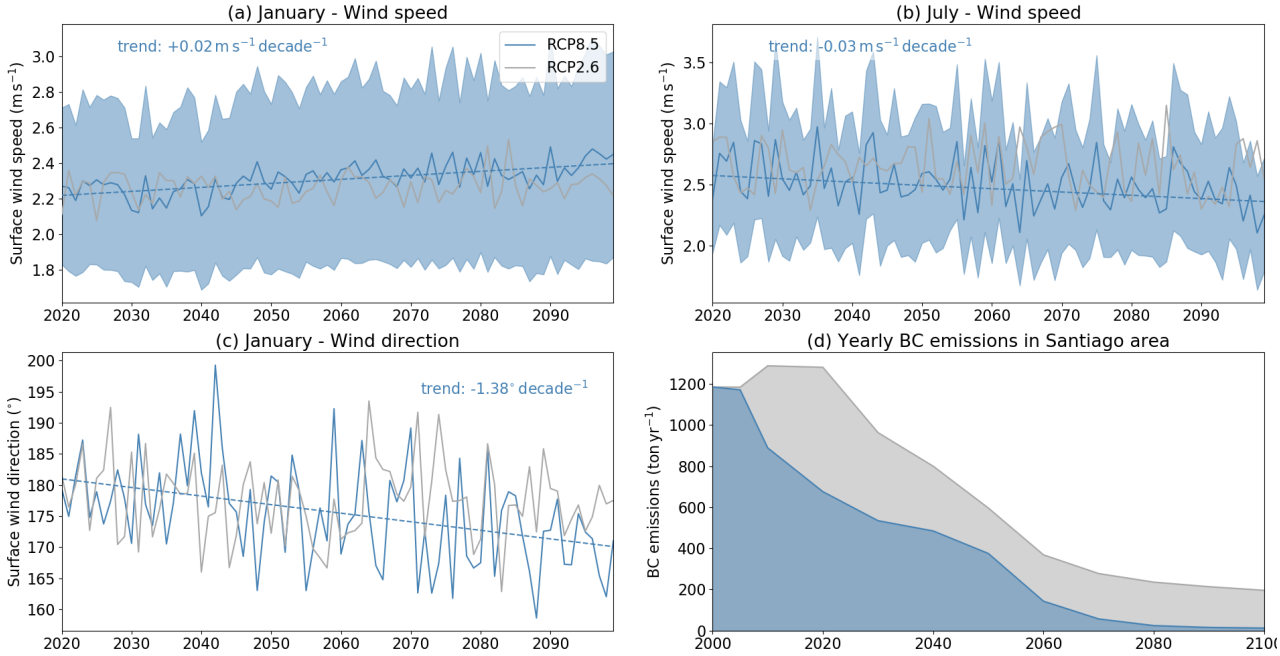

Figure 5.29: (a) Times series of future monthly wind speed in Santiago under scenarios RCP8.5 (blue) and RCP2.6 (gray) for the months of January. Blue shade shows one standard deviation for the RCP8.5 scenario. (b) same as (a) but for the months of July. (c) same as (a) but for wind direction. Ensemble mean of 6 model realizations. Trends significant based on a Mann-Kendall test are shown in dashed line. (d) BC emission scenarios for Santiago under RCP8.5 (blue) and RCP2.6 (gray) scenarios. See Section 5.2.3.2 for more detail on the data.

5.2.5 Discussion

The CHIMERE simulations dedicated to estimating the deposition flux of BC on Andean glaciers are performed using a 5 km resolution domain. Given the sharp topography of the region, the sub-grid variability in elevation is large. The altitude of the glaciers as represented in the model might thus be too low due to the grid-point averaging. This may result in excessive deposition fluxes, especially in wintertime when deposition is found to be altitude-dependent. Over the 845 glaciers found in the simulation domain, the comparison with data from WGMS and National Snow and Ice Data Center (comps.) [1999, updated 2012] yields a mean bias of -287 m in the model, associated with a normalized root-mean-square error (NRMSE) of 11% and a Pearson correlation coefficient of 0.85. Thus, the glaciers altitudes are not exact but well reproduced by the model and the bias induced by the representation of the topography is not expected to affect the results presented earlier on.

Another large source of uncertainty in the simulations stems from the BC emission fluxes. The HTAP inventory is static as of 2010, and with a relatively coarse resolution compared to the processes studied in this work. Simulated $PM_{2.5}$ concentrations could not be extensively validated across the domain except for a few cities where automated air quality networks are present, and no validation on the BC fraction of $PM_{2.5}$ could be performed either (see Lapere et al. [2021c] for more detail on the validation). As a result, BC deposition fluxes presented in this work are to be understood as indicative of the order of magnitude rather than precise estimates of the actual fluxes.

In addition, deposition is among the less well represented processes in chemistry-transport models. Consequently, there is a significant margin for error in the deposition fluxes obtained and presented in Section 5.2.4.1. However, a comparison of dry deposition rates simulated by the model and measured by

Rowe et al. [2019] for a snowy site in the Andes near Santiago in winter results in a good agreement between both. Monthly BC deposition rates for the months of July are well in line as presented in Lapere et al. [2021b]. Although this is only for one site due to lack of more available data, this comparison gives confidence in the model's accuracy in the representation of deposition in this topographically complex area. Conducting multiple simulations, using different deposition parametrizations could help estimate the variability of our results related to this choice. However, Beegum et al. [2020] showed, for instance, that the compared performance of both deposition schemes available in CHIMERE depends on the season and location considered. Thus, including a second set of simulations with the other deposition scheme would not result in more confident results.

Deposition fluxes of BC obtained with CHIMERE are in line with observed and modeled fluxes in the Tibetan Plateau. This region however receives a comparatively much greater attention from the research community. The deposition fluxes in Ji [2016] over the Tibetan Plateau, lower than what we found for the Chilean Andes, were estimated to correspond to a radiative forcing of 3 to 6 $\mathrm{W\,m^{-2}}$. In consequence, this comparison might point to possibly larger impacts on the central Andes than the 1.4 $\mathrm{W\,m^{-2}}$ first estimated in Rowe et al. [2019]. Although uncertainties are attached to our results, the magnitude of the deposition revealed by our simulations suggests a current underestimation by a factor 2 to 4 of the radiative impact of BC on the central Chilean Andes glaciers.

5.2.6 Conclusion

This work presented comparative estimates of typical BC deposition fluxes on glaciers of the central Chilean Andes for a summer month and winter month, using chemistry-transport modeling. At the regional scale, this flux is found to be four times larger in winter (634 $\mathrm{\mu g\,m^{-2}\,month^{-1}}$) than in summer (158 $\mathrm{\mu g\,m^{-2}\,month^{-1}}$), in connection with the use wood burning for residential heating purposes. Such fluxes are comparable to that observed in glaciers and snow over the Tibetan Plateau. While deposition is strongly elevation-dependent in winter with glaciers below 3500 m featuring the largest fluxes, it is vertically less variable in summer although its maximum is found near 4000 m elevation. The summertime flux is proportionally larger than in winter assuming equal emissions, pointing to more favorable export conditions. This can be critical because glaciers melt in summertime, providing fresh water to valleys down the way. If their melting is even faster at that season due to BC, water resources will be depleted even sooner.

Based on a sensitivity analysis, the share of deposition attributable to emissions from the Santiago basin was estimated at 50% in summer and 14% in winter, related to more scattered BC sources across central Chile in winter. In the vicinity of the capital city, the areas primarily affected by deposition vary significantly from one season to the other, with the north of the city most affected in summer and the south most affected in winter. The rationale for this difference comes from divergent transport mechanisms. Reanalysis and local observation data revealed that synoptic winds and mountain-valley circulation combine in summertime to create ventilation conditions conducive to the transport of BC emissions from urban centers in central Chile towards the Andes, reaching even the highest elevations. In contrast, wintertime only features a more moderate mountain-valley circulation driven export but no synoptic forcing.

In summary, large emissions and moderate mountain-valley circulation lead to large but localized BC deposition fluxes in winter, while lower emissions but suitable export conditions lead to more widespread BC deposition in summer. Air pollution in the region is mostly investigated in wintertime due to larger emissions and concentrations, but our findings imply that when it comes to the feedback of BC pollution on glaciers albedo and in turn on climate and water resources, summertime is also a season of interest and should not be overlooked.

In the future, under RCP8.5 scenario, this dichotomy is likely to fade however. First, summertime emissions will likely catch up on wintertime ones. Second, the favorable summertime export conditions will likely become even more favorable. Third, the stable unfavorable export conditions in wintertime will likely become even more stable and unfavorable.

This study provides a wider picture in terms of space and time, completing the existing literature on BC export and deposition in the central zone of Chile. We hope these results can help guide future measurement campaigns carried out in the region on this topic in terms of areas and periods of interest.

5.2.7 Appendix

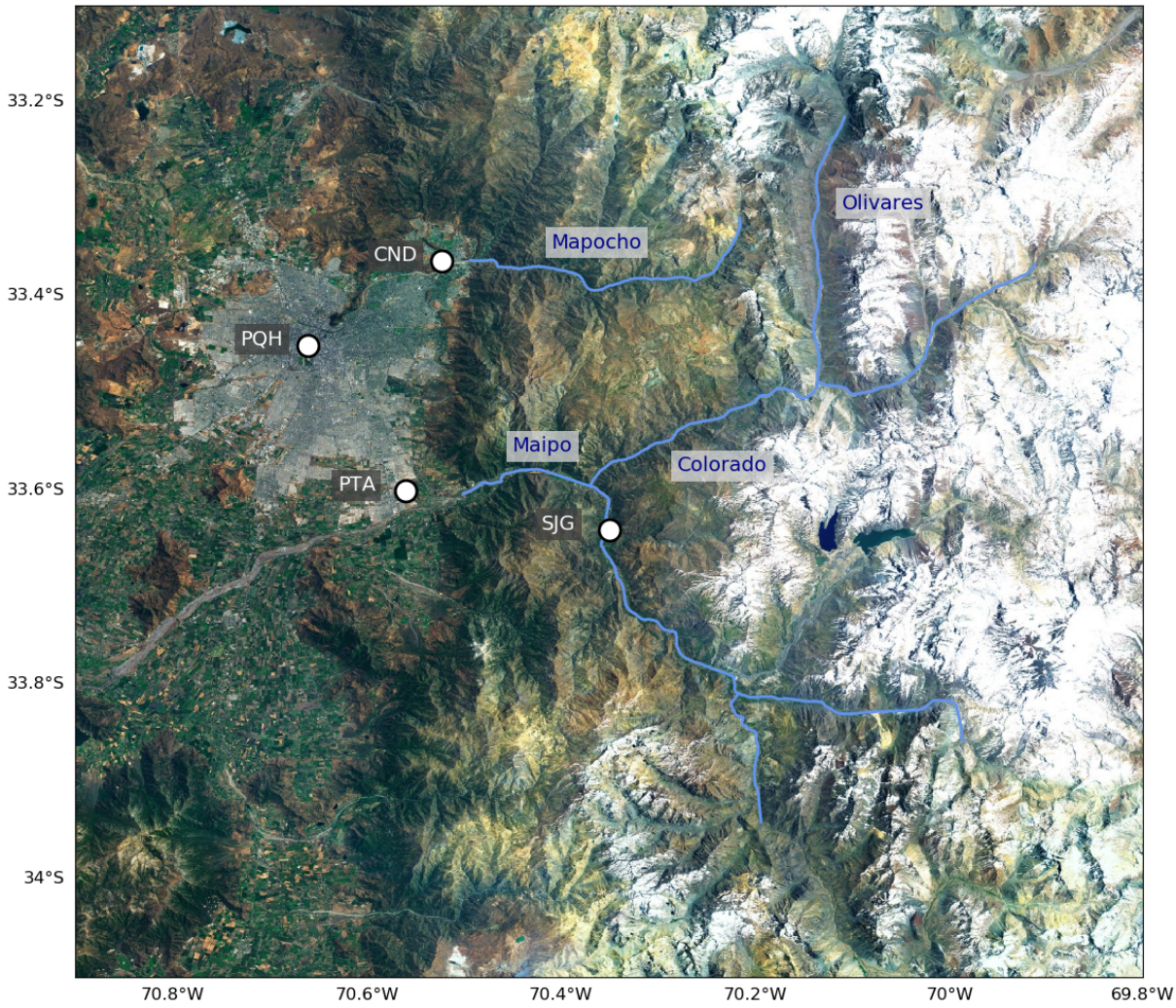

Figure 5.30: Localities and canyons of interest in the vicinity of Santiago. Measurement stations are designated with white circles. Canyons of interest are evidenced with blue lines. Map background layer source: Imagery World 2D, ©2009 Esri.

Conclusions and perspectives

Hereafter are wrapped up the major findings of this 3-year work, along with the gaps in knowledge they helped fill. Nevertheless, some of the questions addressed in this thesis deserve to be further investigated, expanded or confirmed, or have generated related interrogations. Follow-up questions and research work deriving from the studies presented in the previous chapters are thus also discussed in the next few paragraphs.

Conclusions

The rationale of this thesis work stemmed from several previously unanswered questions related to atmospheric pollution in Chile. They are briefly summarized below, along with the contribution from this PhD work to bridging the corresponding gaps in knowledge, and the underlying implications.

• **Where do atmospheric pollutants transport across central Chile?**

Although statistical models based on observations and chemical analyses partially discuss the topic in the literature, no spatially nor temporally highly resolved results were available. As an illustration, typical results explore the contribution of different emission sources to concentrations observed in Santiago, and deduce by extension that transport is partly responsible due to the presence of marine aerosols or copper smelters related particles, for which sources do not exist in the capital city. Prior to this thesis however, there was no knowledge on the mean advection patterns and magnitudes, nor the burden of Santiago emissions on air quality in remote locations in central Chile. Based on CHIMERE simulations, these features of regional pollution transport were evidenced in Lapere et al. [2021c]. **The plume of fine particles emitted in Santiago was found to extend over 500 km towards the northwest and 500 km towards the southeast, on average for a winter month**, with advection processing in shallow layers close to the ground. The contribution of Santiago emissions can be as high as 50% on average in its direct vicinity. In turn, **regional transport from other urban centers accounts for 15% of wintertime particulate matter in the capital city**. The relationship between strong mountain-valley circulation dynamics in summertime and the export of ozone and precursors from Santiago had never been investigated. However, Lapere et al. [2021c] **revealed an important, newly evidenced mechanism leading to the formation of a persistent ozone bubble of 50 ppb on average, extending over 80 km horizontally and 1.5 km vertically, detached from the ground several hundred meters above Santiago**.

A better understanding of pollutants transport dynamics at the scale of central Chile is key for policy design, especially given the large fraction of wintertime particulate matter in Santiago attributable to advection from remote locations that was estimated in this work. It is also important to raise awareness on the fact that air pollution is not only a local phenomenon in Chile, especially given the vast extent of the area under the influence of Santiago emissions that was estimated. Furthermore, the existence of a persistent ozone layer in the lower free troposphere, if confirmed by dedicated measurements, can have major implications. As of the current situation, emission ratios of ozone precursors in Santiago are such that their venting corresponds to an evacuation of ozone molecules and contributes to lowering concentrations and thus exposure in Santiago. However, in a scenario of changing emission ratios, this may not hold anymore and, depending on the emission sources targeted by policies, the ozone maximum could be found directly over Santiago near ground-level instead, due to the heterogeneous lifetimes of nitrogen oxides and volatile organic compounds.

• **What is the root cause of recent record-breaking peak events of fine particles in Santiago?**

The 'soccer game effect' on air quality in Santiago was a controversial question, mostly debated in the political sphere but never looked at from a scientific perspective. So much so that politicians defending the idea that barbecues led to bad air quality were usually not taken seriously. Based on readily available observations and CHIMERE simulations, I was able to **provide solid evidence that wintertime fine particles record peak events in Santiago in 2016 and 2014 were attributable to massive barbecue cooking during soccer games of the national team**. In particular, I have estimated that 100,000 barbecues were cooked in Santiago during the final game of the 2016 Copa América, emitting an additional 2 ton/hour of fine particulate matter, thus explaining around 95% of the observed concentrations.

Our definitive proof of the role of barbecues in these peak events had direct implications right away. Indeed, the results from Lapere et al. [2020] were first released in the Chilean press in June 2019, before their publication in ACP. From the exposure of those findings a few days before the start of the 2019 Copa América, resulted a public debate that led to a ban, by local authorities, on barbecues during the games of the Chilean team. Even though the chemical signature of barbecues can still be distinguished in observations, no peak event was recorded during the 2019 Copa América despite conditions being favorable, meaning that my work helped improving air quality in Santiago. The relatively simple methodology developed for this study is easy to replicate to other locations and could benefit the analysis of peak events in urban centers worldwide.

• **What were the atmospheric impacts of the 2017 mega-fires in central Chile?**

The historic fires of 2017 have logically received a lot of attention in the literature, with studies investigating their origin, ecological impacts near the burnt area, and partly their effect on particulate matter surface concentrations measured by air quality networks in the region. However, their atmospheric impact in a broader sense, including meteorological feedback and atmospheric composition other than particulate matter had not been investigated. Using the online coupled version of WRF-CHIMERE, satellite data and local measurements, Lapere et al. [2021a] estimated the aerosol direct and indirect effects due to the excess emissions from the fires, as well as the 3D extent of the plume for different pollutants and their relation to surface concentrations and aerosol optical depth in Santiago. Despite the relatively short duration of the event (a few days), my work highlighted a **substantial aerosol direct feedback leading to decreased radiation (-100 $\mathbf{W/m^2}$), temperatures (-1 K) and boundary layer heights (-100 m)**. The aerosol indirect effect was found to be less important than hypothesized: a clear **thickening effect on cloud was obtained**, but condensation nuclei from the fires did not explain the whole cloud formation, as is discussed in the Perspectives section thereafter. The simulations also highlighted a dense widespread plume for several compounds, greatly affecting surface concentrations in central Chile, especially in Santiago (+150% in $PM_{2.5}$ and +50% in CO) and over the Pacific Ocean, along a 2,000 km trajectory. The computation of deposition fluxes of said pollutants suggest ecological impacts on remote locations too.

There is a climatic component to the exceptional magnitude of the 2017 mega-fires, in connection with the 2010-2018 mega drought. Such dry spells are forecast to become more common in the near future, thus pointing to more intense fire seasons as well, and a normalization of the 2017 event. In this context, it is paramount to better constrain the atmospheric feedback of biomass burning in central Chile. In particular, a substantial feedback related to direct and indirect aerosol effects was evidenced in connection with the presence of the Pacific ocean and the Andes, implying a perturbation of meteorology in the region that is likely to become more frequent in the coming years.

• **How much and how does black carbon deposit on elevated glaciers of the Chilean Andes?**

Before this thesis, the state of knowledge on black carbon and the central Chilean Andes could be summarized as follows: (i) black carbon loads in snow and ice in the Andes are too high to be of natural origin only, (ii) for glaciers in the vicinity of Santiago the capital city is *likely* the main black carbon provider but no estimate exists as to its actual contribution, (iii) atmospheric measurement campaigns diverge when trying to evidence the transport of urban pollutants from Santiago into Andean canyons. Regarding point (i), Lapere et al. [2021b] and Chapter 5.2 show that **anthropogenic black carbon emissions reach the highest elevations of the central Andes and are responsible for large deposition fluxes on glaciers in the region**, with a monthly average 158 $\mu g\,m^{-2}\,month^{-1}$ and 634 $\mu g\,m^{-2}\,month^{-1}$ in summer and winter, respectively. Such magnitudes are **comparable to what is found over the Tibetan Plateau**, that comparatively receives a much greater attention from the research community and exhibits radiative consequences more dramatic

than what is currently estimated for the Chilean Andes. My modeling experiments were the **first to quantify deposition rates with a spatially continuous regional picture**, and with an investigation of the underlying time dynamics, showing regular deposits in summertime and more variance in wintertime. These two studies also show that *'likely'* is the operative word when it comes to the previous literature mentioning Santiago emissions as the main source of black carbon deposition (point (ii)). Indeed, **my work suggests that even though Santiago emissions dominate summertime deposition on glaciers (50% in the central Andes), the same cannot be said in wintertime** when they are only a minor contributor (14%), even in the direct vicinity of the capital city (18%) where they affect only a small area, which is contrary to what was believed so far. As for point (iii), the wintertime pathway was investigated and the **key role of intrusions into canyons in connection with mountain-valley circulation was evidenced** in Lapere et al. [2021b] and Huneeus et al. [2021], and the **summertime circulation was shown to imply an increased export potential, combining exacerbated mountain-valley patterns and synoptic-scale forcing**.

Atmospheric pollution is often looked at from the perspective of public health issues. Clearly, there is also a feedback on climate and the environment, particularly when it comes to black carbon deposition on glaciers. The location of a mega-city like Santiago, struggling with its air quality, next to ice-covered mountains that are a major source of fresh water, thus raises concern of major impacts. The isolated and hard to access nature of the cryosphere in the central Andes does not allow for extensive measurements. My modeling approach led to a first ever map of black carbon deposition on glaciers. It revealed similar stakes as over the Tibetan Plateau thus suggesting to reconsider the radiative forcing possibly underestimated previously. It also contradicted some commonly accepted assumptions in the literature. In addition, I showed that summertime, which is a period of lesser concern for policy-making due to meteorologically-driven lower aerosols concentrations, is an even greater period of concern when it comes to the export of black carbon towards the Andes. Hopefully these results will provide guidance in addressing the questions surrounding black carbon in the Andes with a more in-depth and enlightened approach.

Perspectives

• Dry and wet deposition

Chemistry-transport models are getting more and more sophisticated when it comes to refining processes such as chemical parameterizations, atmospheric feedback, or aerosols representation. The constant evolution of high-performance computing and development of high-resolution emissions inventories also contribute to improving the accuracy of models. Nevertheless, the adequate representation of deposition processes is still largely overlooked. Today, the termination of the atmospheric life of compounds through deposition is essentially considered an adjustment variable for the closure of grid boxes mass balance, instead of a validated, faithful representation of the actual underlying processes, unlike most components of models. Although the approach to model deposition is physically relevant, more often than not the parameters of the scheme are tuned so that, all other things being equal, modeled atmospheric concentrations fit observations best. Some of the key results presented in this thesis rely on the assumption that deposition fluxes yielded by CHIMERE are somewhat accurate. Although they indeed compare well with one measurement and the literature on other regions, this assumption might seem a little presumptuous given the previous statements. Consequently, a natural follow-up research topic is the representation of deposition in chemistry-transport models. At the time of writing these lines, I am currently investigating this question, with research interests oriented towards (i) the sensitivity of simulated aerosol optical depth and surface concentrations to the choice of dry deposition scheme (including the development and testing of a new scheme in CHIMERE), (ii) a comparison with deposition fluxes measured in the region of Atacama by Chilean colleagues, (iii) a review of the state of the literature on wet deposition modeling with a view to improve this process in CHIMERE.

• Black carbon radiative forcing estimation

In the continuity of the previous point, once deposition fluxes are better constrained, a direct estimation of the albedo and radiative forcing effects of black carbon deposition on snow and ice would be a valuable asset. So far, the evolution of such surface properties is not coupled with CHIMERE since the modeling chain does not consider the fate of black carbon particles once they are deposited on a soil that cannot lead to re-suspension. The influence on albedo and by extension the radiative forcing of this contaminant are therefore not assessed

within the model. These effects can nevertheless be deduced using simplified models when post-processing CHIMERE outputs, thereby providing rough estimates. Possibilities exist however, to try and quantify this effect more properly. In particular, one could imagine coupling CHIMERE with a hydrological model such as WRF-Hydro [Gochis et al., 2015] and/or a snowpack model such as Crocus [Brun et al., 1989] for instance. Such a modeling setup could provide insightful data regarding albedo change and, on longer time scales, evidence and quantify the implications for river run-off and water resources of black carbon deposition on glaciers, in the Andes or in any part of the world. The response of the snowpack to its black carbon content is complex and depends on many parameters (snow grains radii and shape, snow depth and density, solar radiation...) [e.g. Flanner et al., 2021]. This justifies the idea of including a dedicated, sophisticated module into the modeling chain instead of performing simplified calculations in data post-processing. My PhD work demonstrates that such a tool would provide valuable information to better constrain the consequences of air pollution on water environments, which is why I am currently investigating its feasibility.

• Aerosol indirect effect

Among the main hypotheses and questions in Lapere et al. [2021a] was the connection between the cloud cover near the coast of Chile and the biomass burning plume originating from the 2017 mega-fires. Satellite images arguably lead to believe that the aerosols emitted by the fires acted as cloud condensation nuclei once they reached the Pacific Ocean: cloud cover is mostly nonexistent in the region, except along the trajectory of the fire plume where it starts forming near the coast. As a result, the assumption was made that those clouds only existed due to the massive input of aerosols from the fires into a water saturated but pristine air mass. Although the simulations revealed a significant thickening of the clouds in the area of interest when fire emissions are considered, said clouds existed beforehand, in the control simulation, only with a smaller optical depth. My work thus did not prove my hypothesis right. Nevertheless, it did not prove it wrong either, since possible biases in the input meteorological fields can lead to the wrongful formation of clouds in the control case. This non-conclusive outcome led to the following general consideration: are chemistry-transport simulations suited for the study of meteorological impacts of short-lived air pollution events?

Indeed, chemistry-transport models usually rely on analysis (e.g. GFS) or reanalysis (e.g. ERA5) data for the meteorological initial and boundary conditions. These fields incorporate observations, at least partially, so that they represent a state of the atmosphere that is not independent from the studied event. In our fire case for instance, if the clouds of interest were observed and are incorporated into the forcing fields, they will appear in the simulation regardless of emissions, even if they were actually nucleated solely from fire emissions. It is not possible, in this context, to represent a state of the atmosphere that is fully oblivious of the event. By extension, any sensitivity analysis such as the one I performed, even with a perfect representation of chemistry and transport, will underestimate the meteorological feedback of aerosols because it is already included in the atmospheric state in control case, at least partially.

One solution could be to use analog meteorological forcing, i.e. data from a different period, with similar conditions to that of the event, but without its occurrence. The identification of such analogs is feasible, although they would not match perfectly the atmospheric conditions we are looking for. Along the same idea, one could imagine using meteorological forecast not including observations instead of (re)analyses, with a several-days lead time to remain unaffected by the studied event. There is also a limitation to this approach, related to the accuracy of the forecast.

The question is complex, but of significant importance and usually ignored in publications investigating air pollution feedback during short events. Dedicating research towards it is however necessary to improve confidence in impact studies of aerosol feedback. The first preliminary step is to develop a method to quantify the error that is currently made due to the bias on meteorology, to assess its significance.

• Dust-pollution interaction

Throughout this thesis, when dealing with deposition of aerosols on glaciers, emphasis was put on black carbon. Dust is a light-absorbing species too, emitted in large quantities by the friction of strong winds on barren soils. It is also a critical type of pollutant in this respect. Even more so considering that dust plumes can travel long distances and interact with anthropogenic emissions from urban areas along the way. Indeed, the dust-pollution interaction can have three consequences: (i) the optical properties of dust aerosols are affected (e.g. coagulation with other aerosols) which in turn modifies its albedo impact upon deposition [Klingmüller et al., 2019], (ii) the uptake of reactive gases and secondary coating favors new particle formation and growth thereby also affecting the radiative balance directly and indirectly [Nie et al., 2020, Tian et al., 2020, Klingmüller

et al., 2020], (iii) the chemical aging of dust increases particle size and scavenging efficiency [Abdelkader et al., 2015] thereby likely implying a different deposition pattern compared with non-aged dust.

So far, the only modeling studies integrating the dust-pollution interaction were performed with the global CTM EMAC [Abdelkader et al., 2015, Klingmüller et al., 2019, 2020] at coarse resolution, and were not interested in the fate of dust beyond its atmospheric chemical interactions. The questions that follow are then: what is needed to implement the interactions between dust and anthropogenic pollutants (aerosols and gases) in CHIMERE to run the model at high resolution? How does it affect atmospheric composition, dust deposition and ground albedo? Does it improve model performance? Several geographical areas are of interest for such investigations.

Chile is one of them with large sources of dust and anthropogenic pollutants close to one another and in the direct vicinity of glaciers. In particular, light-absorption by impurities in snow is dominated by dust instead of BC in the northern Chilean Andes [Rowe et al., 2019] so that a better knowledge on dust composition and aging in that region is important.

Another possible case study is the influence of anthropogenic emissions in Western Africa on the aging and chemical composition of Saharan dust. Indeed, dust emitted in Africa and transported across the Atlantic Ocean is known to be a major source of nutrients for the Amazon [e.g. Bristow et al., 2010]. Along the transport, mixing with sea-salts and sulfates occur, changing its chemical composition [e.g. Adachi et al., 2020]. Between emission in the Sahara and deposition in the Amazon, the dust plume flies over several polluted African mega-cities which can possibly also affect its composition and thus modify the nutrient input in the Amazon. Implementing dust-pollution interactions into high resolution chemistry-transport simulations over Western Africa could help reveal and quantify this effect. Developing the modeling of this process requires sophistication and refinement in the modeling of aerosols first. In parallel, a collaboration with lab experimenters to better understand the chemical reactions at play to be implemented in the model would be an asset.

Appendix

The Southern Atlantic Anomaly: a limitation to satellite remote sensing over Chile?

Satellite-based measurements of optical depth and total columns of trace gases are valuable when it comes to studying large-scale phenomena associated with climate and atmospheric processes. In the context of this PhD work, satellite data proved useful to assess the model's ability to reproduce the density and extent of pollutants plumes. However, before actually conducting the analysis, it was not clear whether satellite data could be used over this region of the world. Here is why.

Van Allen radiation belts

High-energy ions and electrons emitted by the sun interact with the Earth's magnetosphere. When reaching our region of space, these particles follow the lines of the magnetic field generated by our planet, which leads to the creation of two radiation trapping belts (or Van Allen belts) in the atmosphere [Van Allen and Franck, 1959, Walt, 1994]. Figure A1a shows the first sketch ever of these two high energy belts, as described by Van Allen in 1959 [Van Allen and Franck, 1959]. The inner belt roughly extends between 1,600 km and 13,000 km above Earth's surface, while the outer belt is between 19,000 km to 40,000 km [NASA, 2013].

Satellites usually orbit either between the Earth and the inner belt (Low-Earth Orbiting satellites, such as NASA's Terra and Aqua carrying MODIS instruments extensively used for aerosols measurement), or between the two belts (GPS satellites), which are the safe areas - Figure A1b. Indeed, high-energy particles can damage several components of operating satellites such as the solar cells, electronic circuits or sensors, sometimes producing spurious signals [Walt, 1994]. That is why satellites' orbits are assigned in between these high energy belts, or otherwise usually turned off if crossing the belts, in order to avoid damage or false data records.

(a) (b)

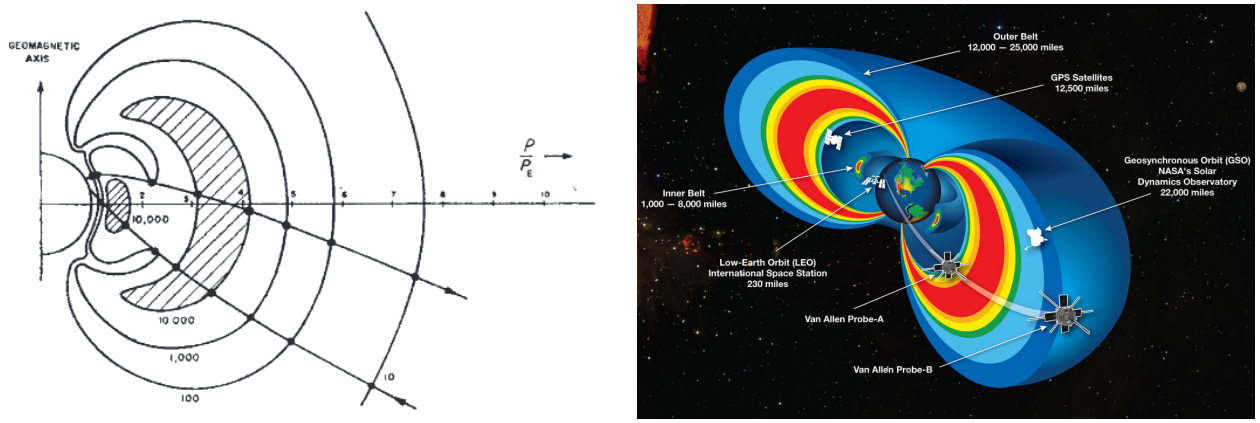

Figure A1: (a) Intensity structure of the radiation region around the Earth. Source Van Allen and Franck [1959]. (b) Van Allen radiation belts. Source NASA [2013].

South Atlantic Anomaly

However, the Earth's magnetic field, responsible for the formation of the Van Allen belts, is not constant throughout the planet. It shows a very weak minimum localized in the South Atlantic, referred to as the South Atlantic Anomaly (SAA) as depicted in Figure A2. Its center, although moving through geological times with a westward drift is currently over Brazil, and the low intensity field area encompasses most of Chile, except Patagonia [Pinto Jr et al., 1992, Kono, 2009]. This magnetic low arises from the misalignment between the Earth's magnetic and rotational axes and leads to a much closer inner Van Allen belt over this region, starting at 200 km altitude [Noel et al., 2014]. As a result, most satellites overpassing South America, including NASA's Terra and Aqua carrying MODIS instruments which orbits around 705 km, if not shut down for safety, record extremely noisy data [Noel et al., 2014] which is unfit for our purposes.

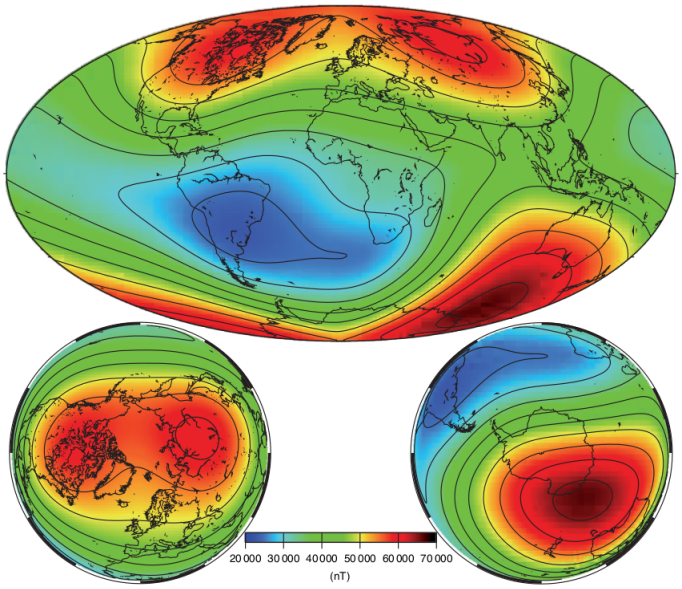

Figure A2: Scalar field intensity F at Earth's surface in 2005 as given by the CHAOS model - contour interval 5000 nT [Kono, 2009]

In practice however, this potential hurdle did not come out in our work as I was able to retrieve realistic data of trace gases columns and aerosol optical depth when needed. A more problematic limitation came from the steep topography of the region of Santiago, as mountainous terrains usually render satellite data unfit for analysis [e.g. Kar et al., 2010].

Our work in the media

Lapere et al. [2020]

Given its practical implications and somewhat unusual scope, Lapere et al. [2020] received media coverage from a national Chilean newspaper (*El Mercurio*) in June 2019 (before publication), and from AGU's *EOS* (`https://eos.org/articles/pollution-spikes-in-chile-tied-to-soccer-fans-barbecuing`) and *Nature Research Highlights* (`https://www.nature.com/articles/d41586-020-01406-5`) in May 2020 right after its publication.

El Mercurio 06/06/2019

EL MERCURIO
JUEVES 6 DE JUNIO DE 2019

NACIONAL C 7

Investigador francés Rémy Lapere advierte sobre posibles episodios críticos luego de los partidos de la Roja en Brasil

"Efecto asado" enciende antesala de la Copa América: alertan por impacto en la contaminación

AGU's Eos 05/11/2020

ATMOSPHERIC SCIENCES News

Pollution Spikes in Chile Tied to Soccer Fans' Barbecuing

In Santiago, mysterious pollution spikes—tenfold above normal levels—occur during televised soccer matches and are caused by tens of thousands of barbecues, new results reveal.

ATMOSPHERIC SCIENCES News

Niveles Altos de Contaminación en Chile se Relacionan Con Parrilladas de Hinchas del Fútbol

Nature Research Highlights 05/12/2020

ENVIRONMENTAL SCIENCES · 12 MAY 2020

The meaty link between a city's football matches and its foul air

Chilean fans' fervour for grilling leads to pollution spikes when the national team plays.

Lapere et al. [2021a]

Lapere et al. [2021a] was published in Volume 12, Issue 3 of MDPI Atmosphere, and served as cover story for this issue. The issue cover along with the associated short story are presented below.

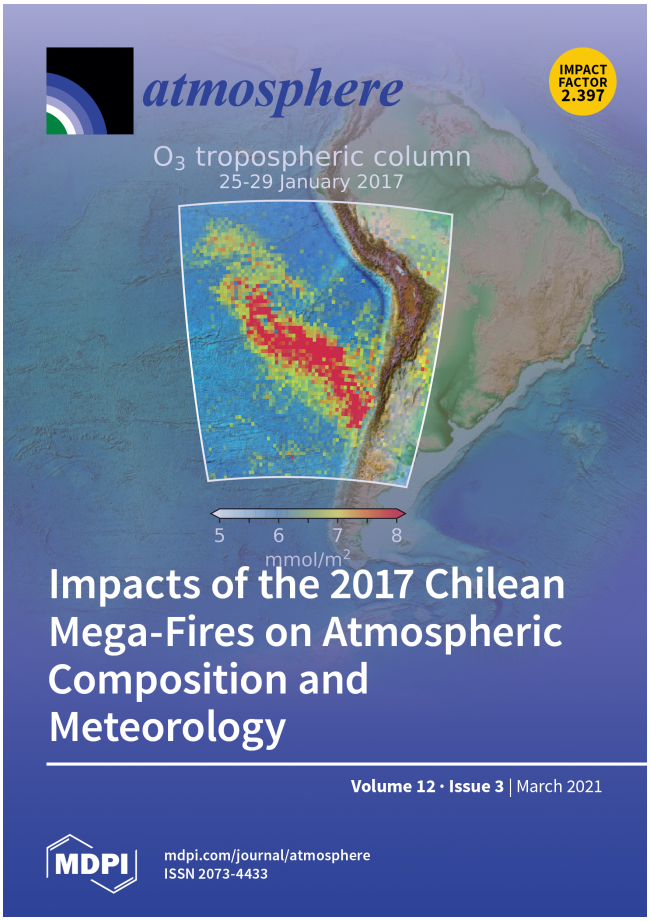

Historic wildfires were recorded in Central Chile in the summer of 2017. From these records, satellite data and modeling revealed a massive plume, which affected atmospheric composition, meteorology and cloud cover over 2000 km and as high as 7 km altitude. The air quality in Santiago dramatically worsened across several consecutive days. Large amounts of pollutants were deposited over land and the ocean, having a wide range of possible environmental consequences. Fire-generated aerosols significantly thickened the clouds over the Pacific Ocean and decreased surface radiation over land, which has led to cooler temperatures and a shallower mixing layer. These implications are paramount for the future regional climate as events of this magnitude might begin to occur more frequently.

Bibliography

M. Abdelkader, S. Metzger, R. E. Mamouri, M. Astitha, L. Barrie, Z. Levin, and J. Lelieveld. Dust–air pollution dynamics over the eastern Mediterranean. *Atmos. Chem. Phys.*, 15:9173–9189, 2015. doi: 10.5194/acp-15-9173-2015.

K. Adachi, N. Oshima, Z. Gong, S. de Sá, A. P. Batemana, S. T. Martin, J. F. de Brito, P. Artaxo, G. G. Cirino, A. J. S. III, and P. R. Buseck. Mixing states of Amazon basin aerosol particles transported over long distances using transmission electron microscopy. *Atmos. Chem. Phys.*, 20:11923–11939, 2020. doi: 10.5194/acp-20-11923-2020.

Aire Santiago. Balance 1997-2017, 2018. URL `http://airesantiago.gob.cl/balance-1997-2017/`.

H. Akimoto. Global Air Quality and Pollution. *Science*, 302:1716–1719, 2003. doi: 10.1126/science.1092666.

N. Álamos, N. Huneeus, M. Opazo, M. Osses, S. Puja, N. Pantoja, R. Calvo, H. D. van der Gon, A. Schueftan, and R. Reyes. High resolution inventory of atmospheric emissions from transport, industrial, energy, mining and residential sectors of Chile. *Earth Syst. Data Sci. Discuss.*, in review:[preprint], 2021. doi: 10.5194/essd-2021-216.

A. Alaniz, R. Barahona-Segovia, I. Nuñez-Hidalgo, C. González-Césped, J. A. S. Rojas Osorio, B. Hora, C. Marchant, C. Gutierréz-Gómez, R. Arias, P. Toro Mujica, P. Escobar-Bahamondes, J. Huerta, C. MARTINEZ, M. Vicuña, N. Guerrero, V. Orellana, J. Tapia, M. Rodríguez, P. Castillo, and G. Fuentes. *Chile: Environmental History, Perspectives and Challenges*. Environmental Research Advances. NOVA Science Publishers Inc., New York, 2019. ISBN 978-1-53615-666-9.

C. W. Allen. *Astrophysical quantities*. Athlone Press, 1976.

M. O. Amdur. Health effects of air pollutants: sulfuric acid, the old and the new. *Environ Health Perspect*, 81: 109–113, 1989. doi: 10.1289/ehp.8981109.

A. Amiri-Farahani, R. J. Allen, K.-F. Li, P. Nabat, and D. M. Westervelt. A La Niña-like climate response to south African biomass burning aerosol in CESM simulations. *J. Geophys. Res. Atmos.*, 125, 2020. doi: 10.1029/2019JD031832.

A. Anda and B. Illes. Impact of Simulated Airborne Soot on Maize Growth and Development. *J. Environ. Prot.*, 3:773–781, 2012. doi: 10.4236/jep.2012.38092.

N. Andela, J. W. Kaiser, G. R. van der Werf, and M. J. Wooster. New fire diurnal cycle characterizations to improve fire radiative energy assessments made from MODIS observations. *Atmos. Chem. Phys.*, 15:8831–8846, 2015. doi: 10.5194/acp-15-8831-2015.

M. Andrade-Flores, N. Rojas, M. L. Melamed, O. L. Mayol-Bracero, M. Grutter, L. Dawidowski, J. C. Antuña-Marrero, C. Rudamas, L. Gallardo, R. Mamani-Paco, M. de Fatima Andrade, and N. Huneeus. Fostering a collaborative atmospheric chemistry research community in the Latin America and Caribbean region. *Bull. Am. Meteorol. Soc.*, 97:1929–1939, 2016. doi: 10.1175/BAMS-D-14-00267.1.

M. O. Andreae. Emission of trace gases and aerosols from biomass burning - an updated assessment. *Atmos. Chem. Phys.*, 19:8523–8546, 2019. doi: 10.5194/acp-19-8523-2019.

A. Arakawa and V. R. Lamb. Computational Design of the Basic Dynamical Processes of the UCLA General Circulation Model. *Methods Comput. Phys. Adv. Res. Appl.*, 17:173–265, 1977. doi: 10.1016/B978-0-12-460817-7.50009-4.

D. J. Arent, R. S. J. Tol, E. Faust, J. P. Hella, S. Kumar, K. M. Strzepek, F. L. Tóth, and D. Yan. *Key economic sectors and services.* In: Climate Change 2014: Impacts, Adaptation, and Vulnerability. Part A: Global and Sectoral Aspects. Contribution of Working Group II to the Fifth Assessment Report of the Intergovernmental Panel on Climate Change [Field, C.B., V.R. Barros, D.J. Dokken, K.J. Mach, M.D. Mastrandrea, T.E. Bilir, M. Chatterjee, K.L. Ebi, Y.O. Estrada, R.C. Genova, B. Girma, E.S. Kissel, A.N. Levy, S. MacCracken, P.R. Mastrandrea, and L.L.White (eds.)]. Cambridge University Press, Cambridge, United Kingdom and New York, NY, USA, 1132 pp, 2014.

R. Bahadur, P. S. Praveen, Y. Xu, and V. Ramanathan. Solar absorption by elemental and brown carbon determined from spectral observations. *Proc. Natl. Acad. Sci.*, 109:17366–17371, 2012. doi: 10.1073/pnas.1205910109.

F. Barraza, F. Lambert, H. Jorquera, A. M. Villalobos, and L. Gallardo. Temporal evolution of main ambient $PM_{2.5}$ sources in Santiago, Chile, from 1998 to 2012. *Atmos. Chem. Phys.*, 17:10093–10107, 2017. doi: 10.5194/acp-17-10093-2017.

B. S. Barrett, J. F. Carrasco, and A. P. Testino. Madden–Julian Oscillation (MJO) Modulation of Atmospheric Circulation and Chilean Winter Precipitation. *J. Clim.*, 25:1678–1688, 2012a. doi: 10.1175/JCLI-D-11-00216.1.

B. S. Barrett, S. J. Fitzmaurice, and S. R. Pritchard. Intraseasonal variability of surface ozone in Santiago, Chile: Modulation by phase of the Madden–Julian Oscillation (MJO). *Atmos. Environ.*, 57:55–62, 2012b. doi: 10.1016/j.atmosenv.2012.04.040.

S. N. Beegum, A. Tuomiranta, I. Gherboudj, J. Flemming, and H. Ghedira. Simulation of aerosol deposition flux over the Arabian Peninsula with CHIMERE-2017: Sensitivity to different dry deposition schemes. *Atmos. Res.*, 241:104949, 2020. doi: 10.1016/j.atmosres.2020.104949.

M. L. Bell, D. L. Davis, N. Gouveia, V. H. Borja-Aburto, and L. A. Cifuentes. The avoidable health effects of air pollution in three Latin American cities: Santiago, São Paulo, and Mexico City. *Environ. Res.*, 100:431–440, 2006. doi: 10.1016/j.envres.2005.08.002.

J. A. Bernstein, N. Alexis, H. Bacchus, I. L. Bernstein, P. Fritz, E. Horner, N. Li, S. Mason, A. Nel, J. Oullette, K. Reijula, T. Reponen, J. Seltzer, A. Smith, and S. M. Tarlo. The health effects of nonindustrial indoor air pollution. *J. Allergy Clin. Immunol.*, 121:585–591, 2008. doi: 10.1016/j.jaci.2007.10.045.

B. Bessagnet, L. Menut, R. Lapere, F. Couvidat, J.-L. Jaffrezo, S. Mailler, O. Favez, R. Pennel, and G. Siour. High Resolution Chemistry Transport Modeling with the On-line CHIMERE-WRF Model over the French Alps - Analysis of a Feedback of Surface Particulate Matter Concentrations on Mountainous Meteorology. *Atmosphere*, 11:565, 2020. doi: 10.3390/atmos11060565.

I. Bey, D. J. Jacob, R. M. Yantosca, J. A. Logan, B. D. Field, A. M. Fiore, Q. Li, H. Y. Liu, L. J. Mickley, and M. G. Schultz. Global modeling of tropospheric chemistry with assimilated meteorology: Model description and evaluation. *J. Geophys. Res.*, 106:23073–23095, 2001. doi: 10.1029/2001JD000807.

J. P. Boisier, R. Rondanelli, R. D. Garreaud, and F. M. noz. Anthropogenic and natural contributions to the Southeast Pacific precipitation decline and recent megadrought in central Chile. *Geophys. Res. Lett.*, 43:413–421, 2016. doi: 10.1002/2015GL067265.

T. C. Bond, D. G. Streets, K. F. Yarber, S. M. Nelson, J.-H. Woo, and Z. Klimont. A technology-based global inventory of black and organic carbon emissions from combustion. *J. Geophys. Res.*, 109:D14203, 2004. doi: 10.1029/2003JD003697.

O. Boucher, D. Randall, P. Artaxo, C. Bretherton, G. Feingold, P. Forster, V.-M. Kerminen, Y. Kondo, H. Liao, U. Lohmann, P. Rasch, S. Satheesh, S. Sherwood, B. Stevens, and X. Zhang. *Clouds and Aerosols.* In: Climate Change 2013: The Physical Science Basis. Contribution of Working Group I to the Fifth Assessment Report of the Intergovernmental Panel on Climate Change [Stocker, T.F., D. Qin, G.-K. Plattner, M. Tignor, S.K. Allen, J. Boschung, A. Nauels, Y. Xia, V. Bex and P.M. Midgley (eds.)]. Cambridge University Press, Cambridge, United Kingdom and New York, NY, USA., 2013.

D. M. J. S. Bowman, A. Moreira-Muñoz, C. A. Kolden, R. O. Chávez, A. A. Muñoz, F. Salinas, Á. González-Reyes, R. Rocco, F. de la Barrera, G. J. Williamson, N. Borchers, L. A. Cifuentes, J. T. Abatzoglou, and F. H. Johnston. Human-environmental drivers and impacts of the globally extreme 2017 Chilean fires. *Ambio*, 48:350–362, 2019. doi: 10.1007/s13280-018-1084-1.

S. Brands, G. Fernández-García, M. T. Montecelo, N. G. Fernández, A. D. S. Estévez, P. E. C. García, A. N. V. andPedro Melo Da Costa, P. C. Tomé, C. Otero, M. L. Macho, and J. Taboada. Sensitivity of the CHIMERE model to changes in model resolution and chemistry over the northwestern Iberian Peninsula. *Atmos. Chem. Phys. Discussions*, 2019. doi: 10.5194/acp-2019-351.

M. Brauer, G. Freedman, J. Frostad, A. van Donkelaar, R. Martin, F. Dentener, R. V. Dingenen, K. Estep, H. Amini, J. Apte, K. Balakrishnan, L. Barregard, D. Broday, V. Feigin, S. Ghosh, P. Hopke, L. Knibbs, Y. Kokubo, Y. Liu, S. Ma, L. Morawska, J. Sangrador, G. Shaddick, H. Anderson, T. Vos, M. Forouzanfar, R. Burnett, and A. Cohen. Ambient air pollution exposure estimation for the Global Burden of Disease 2013. *Environ. Sci. Technol.*, 50:79–88, 2016. doi: 10.1021/acs.est.5b03709.

Breeze Technologies. How much did EU cities and states pay in air pollution fines in recent years?, 2021. URL `https://www.breeze-technologies.de/blog/how-much-did-eu-cities-states-pay-in-air-pollution-fines/`.

R. Briant, P. Tuccella, A. Deroubaix, D. Khvorostyanov, L. Menut, S. Mailler, and S. Turquety. Aerosol–radiation interaction modelling using online coupling between the WRF 3.7.1 meteorological model and the CHIMERE 2016 chemistry-transport model, through the OASIS3-MCT coupler. *Geosci. Model Dev.*, 10:927–944, 2017. doi: 10.5194/gmd-10-927-2017.

C. S. Bristow, K. A. Hudson-Edwards, and A. Chappell. Fertilizing the Amazon and equatorial Atlantic with West African dust. *Geophys. Res. Lett.*, 37:L14807, 2010. doi: 10.1029/2010GL043486.

E. Brun, E. Martin, V. Simon, C. Gendre, and C. Coléou. An energy and mass model of snow cover suitable for operational avalanche forecasting. *J. Glaciol.*, 35:333–342, 1989. doi: 10.3189/S0022143000009254.

D. Byun and K. L. Schere. Review of the Governing Equations, Computational Algorithms, and Other Components of the Models-3 Community Multiscale Air Quality (CMAQ) Modeling System. *Appl. Mech. Rev.*, 59:51–77, 2006. doi: 10.1115/1.2128636.

J. Cao, J. C. Chow, F. S. Lee, and J. G. Watson. Evolution of $PM_{2.5}$ Measurements and Standards in the U.S. and Future Perspectives for China. *Aerosol Air Qual. Res.*, 13:1197–1211, 2013. doi: 10.4209/aaqr.2012.11.0302.

J. N. Cape. Direct damage to vegetation caused by acid rain and polluted cloud: Definition of critical levels for forest trees. *Environ. Pollut.*, 82:167–180, 1993. doi: 10.1016/0269-7491(93)90114-4.

D. C. Carslaw, N. J. Farren, A. R. Vaughan, W. S. Drysdale, S. Young, and J. D. Lee. The diminishing importance of nitrogen dioxide emissions from road vehicle exhaust. *Atmos. Environ. X*, 1:100002, 2019. doi: 10.1016/j.aeaoa.2018.100002.

W. P. L. Carter. Development of the SAPRC-07 chemical mechanism. *Atmos. Environ.*, 44:5324–5335, 2010. doi: 10.1016/j.atmosenv.2010.01.026.

M. Castillo, A. Plaza, and R. Garfias. A recent review of fire behavior and fire effects on native vegetation in Central Chile. *Glob. Ecol. Conserv.*, 24:e01210, 2020. doi: 10.1016/j.gecco.2020.e01210.

Centro de Ciencias del Clima y la Resiliencia. Explorador Climático, 2019. URL `http://explorador.cr2.cl/`.

F. Cereceda-Balic, M. R. Palomo-Marín, E. Bernalte, V. Vidal, J. Christie, X. Fadic, J. L. Guevara, C. Miro, and E. P. Gil. Impact of Santiago de Chile urban atmospheric pollution on anthropogenic trace elements enrichment in snow precipitation at Cerro Colorado, Central Andes. *Atmos. Environ.*, 47:51–57, 2012. doi: 10.1016/j.atmosenv.2011.11.045.

Z. Chen, O. Torres, M. P. McCormick, W. Smith, and C. Ahn. Comparative study of aerosol and cloud detected by CALIPSO and OMI. *Atmos. Environ.*, 51:187–195, 2012. doi: 10.1016/j.atmosenv.2012.01.024.

Z. Chen, J.-N. Wang, G.-X. Ma, and Y.-S. Zhang. China tackles the health effects of air pollution. *The Lancet*, 382:1959–1960, 2013. doi: 10.1016/S0140-6736(13)62064-4.

S. H. Chung and J. H. Seinfeld. Climate response of direct radiative forcing of anthropogenic black carbon. *J. Geophys. Res.*, 110:D11102, 2005. doi: 10.1029/2004JD005441.

C. Clerbaux. Daily IASI/Metop-B ULB-LATMOS carbon monoxide (CO) L2 product (total column), 2018. AERIS data infrastructure.

C. Clerbaux, A. Boynard, L. Clarisse, M. George, J. Hadji-Lazaro, H. Herbin, D. Hurtmans, M. Pommier, A. Razavi, S. Turquety, C. Wespes, and P.-F. Coheur. Monitoring of atmospheric composition using the thermal infrared IASI/MetOp sounder. *Atmos. Chem. Phys.*, 9:6041–6054, 2009. doi: 10.5194/acp-9-6041-2009.

COESA. U.S. Committee on Extension to the Standard Atmosphere, U.S. Standard Atmosphere, 1976. URL `https://ccmc.gsfc.nasa.gov/modelweb/atmos/us_standard.html`.

P. Collela and P. R. Woodward. The piecewise parabolic method (PPM) for gas-dynamical simulations. *J. Comput. Phys.*, 54:174–201, 1984. doi: 10.1016/0021-9991(84)90143-8.

Copernicus. MACC Project - Documentation on Regional Systems, 2018. URL `http://www.gmes-atmosphere.eu/about/documentation/regional/`.

Copernicus Atmosphere Monitoring Service. Global Fire Assimilation System, 2016. `https://apps.ecmwf.int/datasets/data/cams-gfas/`, last accessed May 1^{st} 2020.

Copernicus Climate Change Service. ERA5: Fifth generation of ECMWF atmospheric reanalyses of the global climate, 2017.

A. M. Cordova, J. Arévalo, J. C. Marín, D. Baumgardner, G. B. Raga, D. Pozo, C. A. Ochoa, and R. Rondanelli. On the Transport of Urban Pollution in an Andean Mountain Valley. *Aerosol Air Qual. Res.*, 16:593–605, 2016. doi: 10.4209/aaqr.2015.05.0371.

Corporación Nacional Forestal. CONAF, 2020. `https://www.conaf.cl/incendios-forestales/incendios-forestales-en-chile/estadisticas-historicas/`, last access: 1 May 2020.

CR2. The 2010-2015 mega-drought: A lesson for the future. Technical report, Center for Climate and Resilience Research, Santiago, Chile, 2015. `http://www.cr2.cl/megasequia`, last access: 1 May 2020.

P. Cudlín, J. Seják, J. Pokorný, J. Albrechtová, O. Bastian, and M. Marek. Chapter 24 - Forest Ecosystem Services Under Climate Change and Air Pollution. *Dev. Environ. Sci.*, 13:521–546, 2013. doi: 10.1016/B978-0-08-098349-3.00024-4.

M. Cussac, V. Marécal, V. Thouret, B. Josse, and B. Sauvage. The impact of biomass burning on upper tropospheric carbon monoxide: a study using MOCAGE global model and IAGOS airborne data. *Atmos. Chem. Phys.*, 20:9393–9417, 2020. doi: 10.5194/acp-20-9393-2020.

S. De Craemer, J. Vercauteren, F. Fierens, W. Lefebvre, and F. J. R. Meysman. Using Large-Scale NO2 Data from Citizen Science for Air-Quality Compliance and Policy Support. *Environ. Sci. Technol.*, 54:11070–11078, 2020. doi: 10.1021/acs.est.0c02436.

F. de la Barrera, F. Barraza, P. Favier, V. Ruiz, and J. Quense. Megafires in Chile 2017: Monitoring multiscale environmental impacts of burned ecosystems. *Sci. Total Environ.*, 637-638:1526–1536, 2018. doi: 10.1016/j.scitotenv.2018.05.119.

B. Després and F. Lagoutière. Un schéma non linéaire anti-dissipatif pour l'équation d'advection linéaire. *CR l'Acad. Sci. I-Math.*, 328:939–943, 1999. doi: 10.1016/S0764-4442(99)80301-2.

H. S. M. A. Diederen, R. Guicherit, and J. C. T. HolLonder. Visibility reduction by air pollution in The Netherlands. *Atmos. Environ.*, 19:377–383, 1967. doi: 10.1016/0004-6981(85)90105-2.

H. Diémoz, F. Barnaba, T. Magri, G. Pession, D. Dionisi, S. Pittavino, I. K. F. Tombolato, M. Campanelli, L. S. D. Ceca, M. Hervo, L. D. Liberto, L. Ferrero, and G. P. Gobbi. Transport of Po Valley aerosol pollution to the northwestern Alps - Part 1: Phenomenology. *Atmos. Chem. Phys.*, 19:3065–3095, 2019a. doi: 10.5194/acp-19-3065-2019.

H. Diémoz, G. P. Gobbi, T. Magri, G. Pession, S. Pittavino, I. K. F. Tombolato, M. Campanelli, and F. Barnaba. Transport of Po Valley aerosol pollution to the northwestern Alps - Part 2: Long-term impact on air quality. *Atmos. Chem. Phys. Discuss*, submitted, 2019b. doi: 10.5194/acp-19-10129-2019.

T. D. Dillehay, C. Ocampo, J. Saavedra, A. O. Sawakuchi, R. M. Vega, M. Pino, M. B. Collins, L. S. Cummings, I. Arregui, X. S. Villagran, G. A. Hartmann, M. Mella, A. González, and G. Dix. New Archaeological Evidence for an Early Human Presence at Monte Verde, Chile. *PLOS One*, 10:e0145471, 2015. doi: 10.1371/journal.pone.0145471.

Dirección Meteorológica de Chile. Portal de Servicios Climáticos, 2019. URL `https://climatologia.meteochile.gob.cl/`. last accessed May 11^{st} 2021.

M. C. Dodge. Effect of selected parameters on predictions of a photochemical model. Technical report, US Environmental Protection Agency, EPA-600/3-77/048, 1977.

P. Dominutti, T. Nogueira, A. Fornaro, and A. Borbon. One decade of VOCs measurements in São Paulo megacity: Composition, variability, and emission evaluation in a biofuel usage context. *Sci. Total Environ.*, 738:139790, 2020. doi: 10.1016/j.scitotenv.2020.139790.

S. C. Doney, N. Mahowald, I. Lima, R. A. Feely, F. T. Mackenzie, J.-F. Lamarque, and P. J. Rasch. Impact of anthropogenic atmospheric nitrogen and sulfur deposition on ocean acidification and the inorganic carbon system. *Proc. Natl. Acad. Sci.*, 104:14580–14585, 2007. doi: 10.1073/pnas.0702218104.

P. Doubrawa and D. Muñoz-Esparza. Simulating Real Atmospheric Boundary Layers at Gray-Zone Resolutions: How Do Currently Available Turbulence Parameterizations Perform? *Atmosphere*, 11:345, 2020. doi: 10.3390/atmos11040345.

D. Ehhalt, M. Prather, F. Dentener, R. Derwent, E. Dlugokencky, E. Holland, I. Isaksen, J. Katima, V. Kirchhoff, P. Matson, P. Midgley, and M. Wang. *In: Climate Change 2001: The Physical Science Basis. Contribution of Working Group I to the Third Assessment Report of the Intergovernmental Panel on Climate Change*, chapter Atmospheric Chemistry and Greenhouse Gases. [Houghton, J.T., Y. Ding, D.J. Griggs, M. Noguer, P.J. van der Linden, X. Dai, K. Maskell, and C.A. Johnson (eds.)], Cambridge University Press, Cambridge, United Kingdom and New York, NY, USA, 2001.

E. W. Emerson, A. L. Hodshire, H. M. DeBolt, K. R. Bilsback, J. R. Pierce, G. R. McMeeking, and D. K. Farmer. Revisiting particle dry deposition and its role in radiative effect estimates. *PNAS*, 117:26076–26082, 2020. doi: 10.1073/pnas.2014761117.

Energy Policy Institute at the University of Chicago. Air Quality Life Index, 2017. URL `https://aqli.epic.uchicago.edu/`.

C. E. Enyoh, A. W. Verla, W. Qingyue, F. O. Ohiagu, A. H. Chowdhury, E. C. Enyoh, T. Chowdhury, E. N. Verla, and U. P. Chinwendu. An overview of emerging pollutants in air: Method of analysis and potential public health concern from human environmental exposure. *Trends Environ. Anal. Chem.*, 28:e00107, 2021. doi: 10.1016/j.teac.2020.e00107.

ESGF. The Earth System Grid Federation: An open infrastructure for access to distributed geospatial data. *Future Gener. Comput. Syst.*, 36:400–417, 2014. doi: 10.1016/j.future.2013.07.002.

European Union. Council Directive 1999/13/EC of 11 March 1999 on the limitation of emissions of volatile organic compounds due to the use of organic solvents in certain activities and installations. *Official Journal of the European Communities*, 1999. URL `http://data.europa.eu/eli/dir/1999/13/oj`.

R. J. Farber, P. R. Welsing, and C. Rozzi. PM_{10} and ozone control strategy to improve visibility in the los angeles basin. *Atmos. Environ.*, 28:3277–3283, 1994. doi: 10.1016/1352-2310(94)00160-M.

V. Fiedler, F. Arnold, S. Ludmann, A. Minikin, T. Hamburger, L. Pirjola, A. Dörnbrack, and H. Schlager. African biomass burning plumes over the Atlantic: aircraft based measurements and implications for H_2SO_4 and HNO_3 mediated smoke particle activation. *Atmos. Chem. Phys.*, 11:3211–3225, 2011. doi: 10.5194/acp-11-3211-2011.

M. G. Flanner, C. S. Zender, J. T. Randerson, and P. J. Rasch. Present-day climate forcing and response from black carbon in snow. *J. Geophys. Res.*, 112:D11202, 2007. doi: 10.1029/2006JD008003.

M. G. Flanner, J. Arnheim, J. M. Cook, C. Dang, C. He, X. Huang, D. Singh, S. M. Skiles, C. A. Whicker, and C. S. Zender. SNICAR-AD v3: A Community Tool for Modeling Spectral Snow Albedo. *Geosci. Model Dev. Discuss.*, in review:preprint, 2021. doi: 10.5194/gmd-2021-182.

G. A. Folberth, D. A. Hauglustaine, J. Lathière, and F. Brocheton. Interactive chemistry in the Laboratoire de Météorologie Dynamique general circulation model: model description and impact analysis of biogenic hydrocarbons on tropospheric chemistry. *Atmos. Chem. Phys.*, 6:2273–2319, 2006. doi: 10.5194/acp-6-2273-2006.

D. Fowler, P. Brimblecombe, J. Burrows, M. R. Heal, P. Grennfelt, D. S. Stevenson, A. Jowett, E. Nemitz, M. Coyle, X. Liu, Y. Chang, G. W. Fuller, M. A. Sutton, Z. Klimont, M. H. Unsworth, and M. Vieno. A chronology of global air quality. *Philos. Trans. R. Soc. A-Math. Phys. Eng. Sci.*, 378:20190314, 2020. doi: 10.1098/rsta.2019.0314.

M. A. Friedl, D. Sulla-Menashe, B. Tan, A. Schneider, N. Ramankutty, A. Sibley, and X. Huang. MODIS Collection 5 global land cover: Algorithm refinements and characterization of new datasets, 2001-2012, Collection 5.1 IGBP Land Cover, 2010. URL `http://lpdaac.usgs.gov`.

L. Gallardo, G. Olivares, J. Langner, and B. Aarhus. Coastal lows and sulfur air pollution in Central Chile. *Atmos. Environ.*, 36:3829–3841, 2002. doi: 10.1016/S1352-2310(02)00285-6.

L. Gallardo, F. Barraza, A. Ceballos, M. Galleguillos, N. Huneeus, F. Lambert, C. Ibarra, M. Munizaga, R. O'Ryan, M. Osses, S. Tolvett, A. Urquiza, and K. D. Véliz. Evolution of air quality in Santiago: The role of mobility and lessons from the science-policy interface. *Elem. Sci. Anth.*, 6:38, 2018. doi: 10.1525/elementa.293.

R. D. Garreaud. The Andes climate and weather. *Adv. Geosci.*, 22:3–11, 2009. doi: 10.5194/adgeo-22-3-2009.

R. D. Garreaud, J. A. Rutllant, and H. Fuenzalida. Coastal Lows along the Subtropical West Coast of South America: Mean Structure and Evolution. *Mon. Weather Rev.*, 130:75–88, 2002. doi: 10.1175/1520-0493(2002)130<0075:CLATSW>2.0.CO;2.

R. D. Garreaud, C. Alvarez-Garreton, J. Barichivich, J. P. Boisier, D. Christie, M. Galleguillos, C. LeQuesne, J. McPhee, and M. Zambrano-Bigiarini. The 2010-2015 megadrought in central Chile: impacts on regional hydroclimate and vegetation. *Hydrol. Earth Syst. Sci.*, 21:6307–6327, 2017. doi: 10.5194/hess-21-6307-2017.

R. D. Garreaud, J. P. Boisier, R. Rondanelli, A. Montecinos, H. H. Sepúlveda, and D. Veloso-Aguila. The Central Chile Mega Drought (2010-2018): A climate dynamics perspective. *Int. J. Climatol.*, 40:421–439, 2020. doi: 10.1002/joc.6219.

D. Gochis, W. Yu, and D. Yates. The NCAR WRF-Hydro Technical Description and User's Guide. Technical report, NCAR, Boulder, CO, US, 2015.

S. K. Godunov. A difference method for numerical calculation of discontinuous solutions of the equations of hydrodynamics. *Mat. Sb.*, 47:271–306, 1959.

M. E. González, S. Gómez-González, A. Lara, R. Garreaud, and I. Díaz-Hormazábal. The 2010-2015 Megadrought and its influence on the fire regime in central and south-central Chile. *Ecosphere*, 9:8, 2018. doi: 10.1002/ecs2.2300.

E. Gramsch, F. Cereceda-Balic, P. Oyola, and D. von Baer. Examination of pollution trends in Santiago de Chile with cluster analysis of PM10 and Ozone data. *Atmos. Environ.*, 40:5464–5475, 2006. doi: 10.1016/j.atmosenv.2006.03.062.

E. Gramsch, D. Cáceres, P. O. F. Reyes, Y. Vásquez, and M. A. R. G. Sánchez. Influence of surface and subsidence thermal inversion on $PM_{2.5}$ and black carbon concentration. *Atmos. Environ.*, 98:290–298, 2014. doi: 10.1016/j.atmosenv.2014.08.066.

E. Gramsch, A. Muñoz, J. Langner, L. Morales, C. Soto, P. Pérez, and M. A. Rubio. Black carbon transport between Santiago de Chile and glaciers in the Andes Mountains. *Atmos. Environ.*, 232:117546, 2020. doi: 10.1016/j.atmosenv.2020.117546.

C. Granier, B. Bessagnet, T. Bond, A. D'Angiola, H. Denier van der Gon, G. J. Frost, A. Heil, J. W. Kaiser, S. Kinne, Z. Klimont, S. Kloster, J.-F. Lamarque, C. Liousse, T. Masui, F. Meleux, A. Mieville, T. Ohara, J.-C. Raut, K. Riahi, M. G. Schultz, S. J. Smith, A. Thompson, J. van Aardenne, G. R. van der Werf, and D. P. van Vuuren. Evolution of anthropogenic and biomass burning emissions of air pollutants at global and regional scales during the 1980-2010 period. *Climatic Change*, 109:163, 2011. doi: 10.1007/s10584-011-0154-1.

C. Granier, S. Darras, H. D. van der Gon, J. Doubalova, N. Elguindi, B. Galle, M. Gauss, M. Guevara, J.-P. Jalkanen, J. Kuenen, C. Liousse, B. Quack, D. Simpson, and K. Sindelarova. The Copernicus Atmosphere Monitoring Service global and regional emissions. Technical report, Copernicus Atmosphere Monitoring Service, 2019.

G. A. Grell, S. E. Peckham, R. Schmitz, S. A. McKeen, G. Frost, W. C. Skamarock, and B. Eder. Fully coupled "online" chemistry within the WRF model. *Atmos. Environ.*, 39:6957–6975, 2005. doi: 10.1016/j.atmosenv.2005.04.027.

A. Guenther, T. Karl, P. Harley, C. Wiedinmyer, P. I. Palmer, and C. Geron. Estimates of global terrestrial isoprene emissions using MEGAN (Model of Emissions of Gases and Aerosols from Nature). *Atmos. Chem. Phys.*, 6:3181–3210, 2006. doi: 10.5194/acp-6-3181-2006.

W. J. Gutowski Jr., F. Giorgi, B. Timbal, A. Frigon, D. Jacob, H.-S. Kang, K. Raghavan, B. Lee, C. Lennard, G. Nikulin, E. O'Rourke, M. Rixen, S. Solman, T. Stephenson, and F. Tangang. Wcrp coordinated regional downscaling experiment (cordex): a diagnostic mip for cmip6. *Geosci. Model Dev.*, 9:4087–4095, 2016. doi: 10.5194/gmd-9-4087-2016.

H. Haas, H. J. Jakobs, and M. Memmesheimer. Analysis of a regional model (EURAD) near surface gas concentration predictions using observations from networks. *Met. Atmos. Phys*, 57:173–200, 1995. doi: 10.1007/BF01044160.

O. L. Hadley and T. W. Kirchstetter. Black-carbon reduction of snow albedo. *Nat. Clim. Change*, 2:437–440, 2012. doi: 10.1038/NCLIMATE1433.

M. Han, F. Yang, and H. Sun. A bibliometric and visualized analysis of research progress and frontiers on health effects caused by $PM_{2.5}$. *Environ. Sci. Pollut. Res.*, 28:30595–30612, 2021. doi: 10.1007/s11356-021-14086-z.

R. Hanna and P. Oliva. The effect of pollution on labor supply: Evidence from a natural experiment in Mexico City. *J. Public Econ.*, 122:68–79, 2015. doi: 10.1016/j.jpubeco.2014.10.004.

S. L. Haslett, J. W. Taylor, M. Evans, E. Morris, B. Vogel, A. Dajuma, J. Brito, A. M. Batenburg, S. Borrmann, J. Schneider, C. Schulz, C. Denjean, T. Bourrianne, P. Knippertz, R. Dupuy, A. Schwarzenböck, D. Sauer, C. Flamant, J. Dorsey, I. Crawford, and H. Coe. Remote biomass burning dominates southern West African air pollution during the monsoon. *Atmos. Chem. Phys.*, 19:15217–15234, 2019. doi: 10.5194/acp-19-15217-2019.

E. Hedberg, L. Gidhagen, and C. Johansson. Source contributions to PM10 andarsenic concentrations in Central Chile using positive matrix factorization. *Atmos. Environ.*, 39:549–561, 2005. doi: 10.1016/j.atmosenv.2004.11.001.

S. Henne, M. Furger, S. Nyeki, M. Steinbacher, B. Neininger, S. F. J. de Wekker, J. Dommen, N. Spichtinger, A. Stohl, and A. S. H. Prévôt. Quantification of topographic venting of boundary layer air to the free troposphere. *Atmos. Chem. Phys.*, 4:497–509, 2004. doi: 10.5194/acp-4-497-2004.

S. Henne, J. Dommen, B. Neininger, S. Reimann, J. Staehelin, and A. S. H. Prévôt. Influence of mountain venting in the Alps on the ozone chemistry of the lower free troposphere and the European pollution export. *J. Geophys. Res.*, 110:D22307, 2005. doi: 10.1029/2005JD005936.

A. C. Hill and N. Littlefield. Ozone. Effect on Apparent Photosynthesis, Rate of Transpiration, and Stomatal Closure in Plants. *Environ. Sci. Technol.*, 3:52–56, 1969. doi: 10.1021/es60024a002.

R. Hock, G. Rasul, C. Adler, B. Cáceres, S. Gruber, Y. Hirabayashi, M. Jackson, A. Kääb, S. Kang, S. Kutuzov, A. Milner, U. Molau, S. Morin, B. Orlove, and H. Steltzer. *High Mountain Areas.* In: IPCC Special Report on the Ocean and Cryosphere in a Changing Climate [H.-O. Pörtner, D. C. Roberts, V. Masson-Delmotte, P. Zhai, M. Tignor, E. Poloczanska, K. Mintenbeck, A. Alegría, M. Nicolai, A. Okem, J. Petzold, B. Rama, N. M. Weyer (eds.)]. In press., 2019.

A. J. Hodson. Understanding the dynamics of black carbon and associated contaminants in glacial systems. *WIREs Water*, 1:141–149, 2014. doi: 10.1002/wat2.1016.

A. Hodzic, S. Madronich, B. Bohn, S. Massie, L. Menut, and C. Wiedinmyer. Wildfire particulate matter in Europe during summer 2003: meso-scale modeling of smoke emissions, transport and radiative effects. *Atmos. Chem. Phys.*, 7:4043–4064, 2007. doi: 10.5194/acp-7-4043-2007.

B. Holben, D. Tanre, A. Smirnov, T. F. Eck, I. Slutsker, N. Abuhassan, W. W. Newcomb, J. Schafer, B. Chatenet, F. Lavenu, Y. J. Kaufman, J. Vande Castle, A. Setzer, B. Markham, D. Clark, R. Frouin, R. Halthore, A. Karnieli, N. T. O'Neill, C. Pietras, R. T. Pinker, K. Voss, and G. Zibordi. An emerging ground-based aerosol climatology: Aerosol optical depth from AERONET. *J. Geophys. Res.*, 106:12067–12097, 2001. doi: 10.1029/2001JD900014.

T. Holloway, H. L. II, and P. Kasibhatla. Global distribution of carbon monoxide. *J. Geophys. Res.*, 105: 12123–12147, 2000. doi: 10.1029/1999JD901173.

H. A. Holmes, J. K. Sriramasamudram, E. R. Pardyjak, and C. D. Whiteman. Turbulent Fluxes and Pollutant Mixing during Wintertime Air Pollution Episodes in Complex Terrain. *Environ. Sci. Technol.*, 49:13206–13214, 2015. doi: 10.1021/acs.est.5b02616.

A. Holz, J. Paritsis, I. A. Mundo, T. T. Veblen, T. Kitzberger, G. J. Williamson, E. Aráoz, C. Bustos-Schindler, M. E. González, H. R. Grau, and J. M. Quezadak. Southern Annular Mode drives multicentury wildfire activity in southern South America. *Proc. Natl. Acad. Sci. U.S.A.*, 114:9552–9557, 2017. doi: 10.1073/pnas.1705168114.

J. Houston and A. J. Hartley. The central Andean west-slope rainshadow and its potential contribution to the origin of hyper-aridity in the Atacama Desert. *Int. J. of Climatol.*, 23:1453–1464, 2003. doi: 10.1002/joc.938.

N. Huneeus, H. D. van der Gon, P. Castesana, C. Menares, C. Granier, L. Granier, M. Alonso, M. F. Andrade, L. Dawidowski, L. Gallardo, D. Gomez, Z. Klimont, G. Janssens-Maenhout, M. Osses, S. E. Puliafito, N. Rojas, O. Sánchez-Ccoyllo, S. Tolvett, and R. Y. Ynoue. Evaluation of anthropogenic air pollutant emission inventories for South America at national and city scale. *Atmos. Environ.*, 235:117606, 2020. doi: 10.1016/j.atmosenv.2020.117606.

N. Huneeus, R. Lapere, A. Mazzeo, C. Ordoñez, N. Donoso, R. Muñoz, and J. A. Rutllant. Deep winter intrusions of urban black carbon into a canyon near Santiago, Chile: A pathway towards Andean glaciers. *Environ. Pollut.*, 291:118124, 2021. doi: 10.1016/j.envpol.2021.118124.

M. Ilabaca, I. Olaeta, E. Campos, J. Villaire, M. M. Tellez-Rojo, and I. Romieu. Association between Levels of Fine Particulate and Emergency Visits for Pneumonia and other Respiratory Illnesses among Children in Santiago, Chile. *J Air Waste Manag Assoc*, 49:154–163, 1999. doi: 10.1080/10473289.1999.10463879.

INE. Censo 2017: Síntesis de resultados. Technical report, Instituto Nacional de Estadísticas, 2018. URL `http://www.censo2017.cl/descargas/home/sintesis-de-resultados-censo2017.pdf`.

Instituto Nacional de Estadísticas. Anuarios Parque de Vehiculos en Circulacion, 2016. URL `http://historico.ine.cl/canales/chile_estadistico/estadisticas_economicas/transporte_y_comunicaciones/parquevehiculos.php`.

International Cryosphere Climate Initiative. Andes and black carbon, 2018. URL `http://iccinet.org/andes-and-black-carbon`.

IPCC. Contribution of Working Group I to the Fourth Assessment Report of the Intergovernmental Panel on Climate Change. Technical report, Intergovernmental Panel on Climate Change, 2007.

IPCC. RCP Database, 2009. URL `http://www.iiasa.ac.at/web-apps/tnt/RcpDb`.

IPCC. Climate Change 2013: The Physical Science Basis. Contribution of Working Group I to the Fifth Assessment Report of the Intergovernmental Panel on Climate Change. Technical report, Intergovernmental Panel on Climate Change, 2013.

A. Ito and J. E. Penner. Historical emissions of carbonaceous aerosols from biomass and fossil fuel burning for the period 1870-2000. *Global Biogeochem. Cycles*, 19:GB2028, 2005. doi: 10.1029/2004GB002374.

D. J. Jacob. *Introduction to Atmospheric Chemistry*. Princeton University Press, 1999.

M. Z. Jacobson. Effects of biomass burning on climate, accounting for heat and moisture fluxes, black and brown carbon, and cloud absorption effects. *J. Geophys. Res. Atmos.*, 119:8980–9002, 2014. doi: 10.1002/2014JD021861.

G. Janssens-Maenhout, M. Crippa, D. Guizzardi, F. Dentener, M. Muntean, G. Pouliot, T. Keating, Q. Zhang, J. Kurokawa, R. Wankmüller, H. Denier van der Gon, J. J. P. Kuenen, Z. Klimont, G. Frost, S. Darras, B. Koffi, and M. Li. HTAPv2.2: a mosaic of regional and global emission grid maps for 2008 and 2010 to study hemispheric transport of air pollution. *Atmos. Chem. Phys.*, 15:11411–11432, 2015. doi: 10.5194/acp-15-11411-2015.

Z.-M. Ji. Modeling black carbon and its potential radiative effects over the Tibetan Plateau. *Adv. Clim. Change Res.*, 7:139–144, 2016. doi: 10.1016/j.accre.2016.10.002.

H. Jorquera and F. Barraza. Source apportionment of ambient $PM_{2.5}$ in Santiago, Chile: 1999 and 2004 results. *Sci. Total Environ.*, 435-436:418–429, 2012. doi: 10.1016/j.scitotenv.2012.07.049.

C. O. Justice, J. R. G. Townshend, E. F. Vermote, E. Masuoka, R. E. Wolfe, N. Saleous, D. P. Roy, and J. T. Morisette. An overview of MODIS Land data processing and product status. *Remote Sens. Environ.*, 83:3–15, 2002. doi: 10.1016/S0034-4257(02)00084-6.

M. Kampa and E. Castanas. Human health effects of air pollution. *Environ. Pollut.*, 151:362–367, 2007. doi: 10.1016/j.envpol.2007.06.012.

S. Kang, Y. Zhang, Y. Qian, and H. Wang. A review of black carbon in snow and ice and its impact on the cryosphere. *Earth-Sci. Rev.*, 210:103346, 2020. doi: 10.1016/j.earscirev.2020.103346.

J. Kar, J. Fishman, J. K. Creilson, A. Richter, J. Ziemke, and S. Chandra. Are there urban signatures in the tropospheric ozone column products derived from satellite measurements? *Atmos. Chem. Phys.*, 10:5213–5222, 2010. doi: 10.5194/acp-10-5213-2010.

I. G. Kavouras, P. Koutrakis, F. Cereceda-Balic, and P. Oyola. Source Apportionment of PM_{10} and $PM_{2.5}$ in Five Chilean Cities Using Factor Analysis. *J Air Waste Manag Assoc*, 51:451–464, 2001. doi: 10.1080/10473289.2001.10464273.

A. Khan, O. Plana-Ripoll, S. Antonsen, J. Brandt, C. Geels, H. Landecker, P. F. Sullivan, C. B. Pedersen, and A. Rzhetsky. Environmental pollution is associated with increased risk of psychiatric disorders in the US and Denmark. *PLOS Biol.*, 17:e3000513, 2019. doi: 10.1371/journal.pbio.3000353.

Z. Klimont, K. Kupiainen, C. Heyes, P. Purohit, J. Cofala, P. Rafaj, J. Borken-Kleefeld, and W. Schöpp. Global anthropogenic emissions of particulate matter including black carbon. *Atmos. Chem. Phys.*, 17:8681–8723, 2017. doi: 10.5194/acp-17-8681-2017.

K. Klingmüller, J. Lelieveld, V. A. Karydis, and G. L. Stenchikov. Direct radiative effect of dust–pollution interactions. *Atmos. Chem. Phys.*, 19:7397–7408, 2019. doi: 10.5194/acp-19-7397-2019.

K. Klingmüller, V. A. Karydis, S. Bacer, G. L. Stenchikov, and J. Lelieveld. Weaker cooling by aerosols due to dust–pollution interactions. *Atmos. Chem. Phys.*, 20:15285–15295, 2020. doi: 10.5194/acp-20-15285-2020.

M. Klose, O. Jorba, M. G. Ageitos, J. Escribano, M. L. Dawson, V. Obiso, E. D. Tomaso, S. Basart, G. M. Pinto, F. Macchia, P. Ginoux, J. Guerschman, C. Prigent, Y. Huang, J. F. Kok, R. L. Miller, and C. P. García-Pando. Mineral dust cycle in the Multiscale Online Nonhydrostatic AtmospheRe CHemistry model (MONARCH) Version 2.0. *Geosci. Model Dev. Discuss.*, in review, 2021. doi: 10.5194/gmd-2021-32.

D. Koch and A. D. D. Genio. Black carbon semi-direct effects on cloud cover: review and synthesis. *Atmos. Chem. Phys.*, 10:7685–7696, 2010. doi: 10.5194/acp-10-7685-2010.

M. Kono. *Geomagnetism: Treatise on Geophysics*. Elsevier, 2009.

I. B. Konovalov, M. Beekmann, I. N. Kuznetsova, A. Yurova, and A. M. Zvyagintsev. Atmospheric impacts of the 2010 Russian wildfires: integrating modelling and measurements of an extreme air pollution episode in the Moscow region. *Atmos. Chem. Phys.*, 11:10031–10056, 2011. doi: 10.5194/acp-11-10031-2011.

I. B. Konovalov, M. Beekmann, E. V. Berezin, H. Petetin, T. Mielonen, I. N. Kuznetsova, , and M. O. Andreae. The role of semi-volatile organic compounds in the mesoscale evolution of biomass burning aerosol: a modeling case study of the 2010 mega-fire event in Russia. *Atmos. Chem. Phys.*, 15:13269–13297, 2015. doi: 10.5194/acp-15-13269-2015.

R. Koppmann. *Volatile Organic Compounds in the Atmosphere*. Blackwell Publishing Ltd, 2007.

M. Kossmann, U. Corsmeier, S. F. J. D. Wekker, F. Fiedler, R. Vögtlin, N. Kalthoff, H. Güsten, and B. Neininger. Observations of handover processes between the atmospheric boundary layer and the free troposphere over mountainous terrain. *Contributions to Atmospheric Physics*, 72:329–350, 1999.

B. Languille, V. Gros, N. Bonnaire, C. Pommier, C. Honoré, C. Debert, L. Gauvin, S. Srairi, I. Annesi-Maesano, B. Chaix, and K. Zeitouni. A methodology for the characterization of portable sensors for air quality measure with the goal of deployment in citizen science. *Sci. Total Environ.*, 708:134698, 2020. doi: 10.1016/j.scitotenv.2019.134698.

R. Lapere, L. Menut, S. Mailler, and N. Huneeus. Soccer games and record breaking PM2.5 pollution events in Santiago, Chile. *Atmos. Chem. Phys.*, 20:4681–4694, 2020. doi: 10.5194/acp-20-4681-2020.

R. Lapere, S. Mailler, and L. Menut. The 2017 mega-fires in central chile: Impacts on regional atmospheric composition and meteorology assessed from satellite data and chemistry-transport modeling. *Atmosphere*, 12: 344, 2021a. doi: 10.3390/atmos12030344.

R. Lapere, S. Mailler, L. Menut, and N. Huneeus. Pathways for wintertime deposition of anthropogenic light-absorbing particles on the Central Andes cryosphere. *Environ. Pollut.*, 272:115901, 2021b. doi: 10.1016/j.envpol.2020.115901.

R. Lapere, L. Menut, S. Mailler, and N. Huneeus. Seasonal variation in atmospheric pollutants transport in central Chile: dynamics and consequences. *Atmos. Chem. Phys.*, 21:6431–6454, 2021c. doi: 10.5194/acp-21-6431-2021.

M. Lattuati. *Contribution à l'étude du bilan de l'ozone troposphérique à l'interface de l'Europe et de l'Atlantique Nord: modélisation lagrangienne et mesures en altitude*. PhD thesis, Université Paris, France, 1997.

J. L. Laughner and R. C. Cohen. Direct observation of changing NOx lifetime in North American cities. *Science*, 366:723–727, 2019. doi: 10.1126/science.aax6832.

C. Lee, R. V. Martin, A. van Donkelaar, H. Lee, R. R. Dickerson, J. C. Hains, N. Krotkov, A. Richter, K. Vinnikov, and J. J. Schwab. SO_2 emissions and lifetimes: Estimates from inverse modeling using in situ and global, space-based (SCIAMACHY and OMI) observations. *J. Geophys. Res.*, 116:D06304, 2011. doi: 10.1029/2010JD014758.

S. Y. Lee. Emissions from street vendor cooking devices (charcoal grilling). Technical report, United States Environmental Protection Agency, 1999.

P. A. Leighton. *Photochemistry of Air Pollution*. Academic Press. New York und London, 1961.

J. Li, F. Wang, G. Michalski, and B. Wilkins. Atmospheric deposition across the Atacama Desert, Chile: Compositions, source distributions, and interannual comparisons. *Chem. Geol.*, 525:435–446, 2019. doi: 10.1016/j.chemgeo.2019.07.037.

A. Liberti. Modern methods for air pollution monitoring. *Pure Appl. Chem.*, 44:519–534, 1975. doi: 10.1351/pac197544030519.

M. Lippmann. Health effects of tropospheric ozone. *Environ. Sci. Technol.*, 25:1954–1962, 1991. doi: 10.1021/es00024a001.

R. Lu and R. P. Turco. Ozone distributions over the Los Angeles basin: three-dimensional simulations with the smog model. *Atmos. Environ.*, 30:4155–4176, 1996. doi: 10.1016/1352-2310(96)00153-7.

Z. Lu and I. N. Sokolik. The Impacts of Smoke Emitted from Boreal Forest Wildfires on the High Latitude Radiative Energy Budget – A Case Study of the 2002 Yakutsk Wildfires. *Atmosphere*, 9:410, 2018. doi: 10.3390/atmos9100410.

M. T. Lund, B. H. Samset, R. Skeie, D. Watson-Parris, J. M. Katich, J. P. Schwarz, and B. Weinzierl. Short Black Carbon lifetime inferred from a global set of aircraft observations. *npj Clim Atmos Sci*, 1:31, 2018. doi: 10.1038/s41612-018-0040-x.

R. A. Madden and P. R. Julian. Description of Global-Scale Circulation Cells in the Tropics with a 40–50 Day Period. *J. Atmos. Sci.*, 29:1109–1123, 1972. doi: 10.1175/1520-0469(1972)029<1109:DOGSCC>2.0.CO;2.

S. Mailler, D. Khvorostyanov, and L. Menut. Impact of the vertical emission profiles on background gas-phase pollution simulated from the EMEP emissions over Europe. *Atmos. Chem. Phys.*, 13:5981–5998, 2013. doi: 10.5194/acp-13-5987-2013.

S. Mailler, L. Menut, D. Khvorostyanov, M. Valari, F. Couvidat, G. Siour, S. Turquety, R. Briant, P. Tuccella, B. Bessagnet, A. Colette, L. Létinois, K. Markakis, and F. Meleux. CHIMERE-2017: from urban to hemispheric chemistry-transport modeling. *Geosci. Model Dev.*, 10:2397–2423, 2017. doi: 10.5194/gmd-10-2397-2017.

S. Mailler, R. Pennel, L. Menut, and M. Lachâtre. Using the Després and Lagoutiére (1999) antidiffusive transport scheme: a promising and novel method against excessive vertical diffusion in chemistry-transport models. *Geosci. Model Dev.*, 14:2221–2233, 2021. doi: 10.5194/gmd-14-2221-2021.

M. Majdi, S. Turquety, K. Sartelet, C. Legorgeu, L. Menut, and Y. Kim. Impact of wildfires on particulate matter in the Euro-Mediterranean in 2007: sensitivity to some parameterizations of emissions in air quality models. *Atmos. Chem. Phys.*, 19:785–812, 2019. doi: 10.5194/acp-19-785-2019.

M. Majdi, Y. Kim, S. Turquety, and K. Sartelet. Impact of mixing state on aerosol optical properties during severe wildfires over the Euro-Mediterranean region. *Atmos. Environ.*, 220:117042, 2020. doi: 10.1016/j.atmosenv.2019.117042.

F. F. Malavelle, J. M. Haywood, L. M. Mercado, G. A. Folberth, N. Bellouin, S. Sitch, and P. Artaxo. Studying the impact of biomass burning aerosol radiative and climate effects on the Amazon rainforest productivity with an Earth system model. *Atmos. Chem. Phys.*, 19:1301–1326, 2019. doi: 10.5194/acp-19-1301-2019.

M. Mallet, F. Solmon, P. Nabat, N. Elguindi, F. Waquet, D. Bouniol, A. M. Sayer, K. Meyer, R. Roehrig, M. Michou, P. Zuidema, C. Flamant, J. Redemann, and P. Formenti. Direct and semi-direct radiative forcing of biomass-burning aerosols over the southeast Atlantic (SEA) and its sensitivity to absorbing properties: a regional climate modeling study. *Atmos. Chem. Phys.*, 20:13191–13216, 2020. doi: 10.5194/acp-20-13191-2020.

J. C. Marín, G. B. Raga, J. Arévalo, D. Baumgardner, A. M. Córdova, D. Pozo, A. Calvo, A. Castro, R. Fraile, and M. Sorribas. Properties of particulate pollution in the port city of Valparaiso, Chile. *Atmos. Environ.*, 171:301–316, 2017. doi: 10.1016/j.atmosenv.2017.09.044.

A. Mazzeo, N. Huneeus, C. Ordoñez, A. Orfanoz-Cheuquelaf, L. Menut, S. Mailler, M. Valari, H. D. van der Gon, L. Gallardo, R. Muñoz, R. Donoso, M. Galleguillos, M. Osses, and S. Tolvett. Impact of residential combustion and transport emissions on air pollution in Santiago during winter. *Atmos. Environ.*, 190:195–208, 2018. doi: 10.1016/j.atmosenv.2018.06.043.

R. O. McClellan. Setting ambient air quality standards for particulate matter. *Toxicology*, 181-182:239–347, 2002. doi: 10.1016/S0300-483X(02)00459-6.

I. McKendry and J. Lundgren. Tropospheric layering of ozone in regions of urbanized complex and/or coastal terrain: a review. *Prog. Phys. Geogr.*, 24:329–354, 2000. doi: 10.1177/030913330002400302.

D. S. McKenna, P. Konopka, J.-U. Grooß, G. Günther, R. Müller, R. Spang, D. Offermann, and Y. Orsolini. A new Chemical Lagrangian Model of the Stratosphere (CLaMS) 1. Formulation of advection and mixing. *J. Geophys. Res.*, 107, 2002. doi: 10.1029/2000JD000114.

D. B. McWethy, A. Pauchard, R. A. García, A. Holz, M. E. González, T. T. Veblen, J. Stahl, and B. Currey. Landscape drivers of recent fire activity (2001-2017) in south-central Chile. *PLoS ONE*, 13:e0201195, 2018. doi: 10.1371/journal.pone.0201195.

C. Menares, L. Gallardo, M. Kanakidou, R. Seguel, and N. Huneeus. Increasing trends (2001-2018) in photochemical activity and secondary aerosols in Santiago, Chile. *Tellus B Chem Phys Meteorol*, 72:1–18, 2020. doi: 10.1080/16000889.2020.1821512.

M. Ménégoz, G. Krinner, Y. Balkanski, A. Cozic, O. Boucher, and P. Ciais. Boreal and temperate snow cover variations induced by black carbon emissions in the middle of the 21st century. *The Cryosphere*, 7:537–554, 2013. doi: 10.5194/tc-7-537-2013.

M. Ménégoz, G. Krinner, Y. Balkanski, O. Boucher, A. Cozic, S. Lim, P. Ginot, P. Laj, H. Gallée, P. Wagnon, A. Marinoni, and H. W. Jacobi. Snow cover sensitivity to black carbon deposition in the Himalayas: from atmospheric and ice core measurements to regional climate simulations. *Atmos. Chem. Phys.*, 14:4237–4249, 2014. doi: 10.5194/acp-14-4237-2014.

L. Menut, R. Vautard, C. Flamant, C. Abonnel, M. Beekmann, P. Chazette, P. H. Flamant, D. Gombert, D. Guédalia, D. Kley, M. P. Lefebvre, B. Lossec, D. Martin, G. Mégie, P. Perros, M. Sicard, and G. Toupance. Measurements and modelling of atmospheric pollution over the Paris area: an overview of the ESQUIF Project. *Ann. Geophys.*, 18:1467–1481, 2000. doi: 10.1007/s00585-000-1467-y.

L. Menut, B. Bessagnet, D. Khvorostyanov, M. Beekmann, N. Blond, A. Colette, I. Coll, G. Curci, G. Foret, A. Hodzic, S. Mailler, F. Meleux, J.-L. Monge, I. Pison, G. Siour, S. Turquety, M. Valari, R. Vautard, and M. G. Vivanco. CHIMERE 2013: a model for regional atmospheric composition modelling. *Geosci. Model Dev.*, 6:981–1028, 2013. doi: 10.5194/gmd-6-981-2013.

L. Menut, S. Mailler, B. Bessagnet, G. Siour, A. Colette, F. Couvidat, and F. Meleux. An alternative way to evaluate chemistry-transport model variability. *Geosci. Model Dev.*, 10:1199–208, 2017. doi: 10.5194/gmd-10-1199-2017.

L. Menut, C. Flamant, S. Turquety, A. Deroubaix, P. Chazette, and R. Meynadier. Impact of biomass burning on pollutant surface concentrations in megacities of the Gulf of Guinea. *Atmos. Chem. Phys.*, 18:2687–2707, 2018. doi: 10.5194/acp-18-2687-2018.

L. Menut, B. Bessagnet, R. Briant, A. Cholakian, F. Couvidat, S. Mailler, R. Pennel, G. Siour, P. Tuccella, S. Turquety, and M. Valari. The CHIMERE v2020r1 online chemistry-transport model. *Geosci. Model Dev. Discuss.*, In review, 2021. doi: 10.5194/gmd-2021-96.

J. Ming, C. Xiao, Z. Du, and X. Yang. An overview of black carbon deposition in High Asia glaciers and its impacts on radiation balance. *Advances in Water Resources*, 55:80–87, 2012. doi: 10.1016/j.advwatres.2012.05.015.

Ministerio del Medio Ambiente. Establece Plan de Prevención y Descontaminación Atmosférica para la Región Metropolitana de Santiago, 2017. URL `https://www.leychile.cl/N?i=1111283&f=2017-11-24&p=`.

Ministerio del Medio Ambiente. Sistema de Información Nacional de Calidad del Aire, 2018. URL `https://sinca.mma.gob.cl/index.php/`.

MMA. Análisis General para el Impacto Económico y Social (AGIES) de la Norma de Calidad Primaria de Material Particulado 2.5. Technical report, Ministerio del Medio Ambiente, 2012. URL `http://planesynormas.mma.gob.cl/archivos/2014/proyectos/235_6__Folio_N_881_al_1008.pdf`.

V. A. Mohnen, W. Goldstein, and W.-C. Wang. Tropospheric Ozone and Climate Change. *Air & Waste*, 43:1332–1344, 1993. doi: 10.1080/1073161X.1993.10467207.

L. T. Molina, S. Madronich, J. S. Gaffney, E. Apel, B. de Foy, J. Fast, R. Ferrare, S. Herndon, J. L. Jimenez, B. Lamb, A. R. Osornio-Vargas, P. Russell, J. J. Schauer, P. S. Stevens, R. Volkamer, , and M. Zavala. An overview of the MILAGRO 2006 Campaign: Mexico City emissions and their transport and transformation. *Atmos. Chem. Phys.*, 10:8697–8760, 2010. doi: 10.5194/acp-10-8697-2010.

L. T. Molina, L. Gallardo, M. Andrade, D. Baumgardner, M. Borbor-Córdova, R. Bórquez, G. Casassa, F. Cereceda-Balic, L. Dawidowski, R. Garreaud, N. Huneeus, F. Lambert, J. L. McCarty, J. M. Phee, M. Mena-Carrasco, G. B. Raga, C. Schmitt, and J. P. Schwarz. Pollution and its impacts on the South American Cryosphere (PISAC). *Earth's Future*, 3:345–369, 2015. doi: 10.1002/2015EF000311.

A. Monod, B. C. Sive, P. Avino, T. Chen, D. R. Blake, and F. S. Rowland. Monoaromatic compounds in ambient air of various cities: a focus on correlations between the xylenes and ethylbenzene. *Atmos. Environ.*, 35: 135–149, 2001. doi: 10.1016/S1352-2310(00)00274-0.

A. Montecinos and P. Aceituno. Seasonality of the ENSO-Related Rainfall Variability in Central Chile and Associated Circulation Anomalies. *J. Clim.*, 16:281–296, 2003. doi: 10.1175/1520-0442(2003)016<0281:SOTERR>2.0.CO;2.

F. Moreno, E. Gramsch, P. Oyola, and M. A. Rubio. Modification in the Soil and Traffic-Related Sources of Particle Matter between 1998 and 2007 in Santiago de Chile. *J Air Waste Manag Assoc*, 60:1410–1421, 2010. doi: 10.3155/1047-3289.60.12.1410.

S. Munir, H. Chen, and K. Ropkins. Modelling the impact of road traffic on ground level ozone concentration using a quantile regression approach. *Atmos. Environ.*, 60:283–291, 2012. doi: 10.1016/j.atmosenv.2012.06.043.

R. C. Muñoz and R. I. Alcafuz. Variability of Urban Aerosols over Santiago, Chile: Comparison of Surface PM_{10} Concentrations and Remote Sensing with Ceilometer and Lidar. *Aerosol Air Qual. Res.*, 12:8–19, 2012. doi: 10.4209/aaqr.2011.08.0133.

R. C. Muñoz and A. A. Undurraga. Daytime Mixed Layer over the Santiago Basin: Description of Two Years of Observations with a Lidar Ceilometer. *J. Appl. Meteorol. Clim.*, 49:1728–1741, 2010. doi: 10.1175/2010JAMC2347.1.

R. C. Muñoz, L. Armi, J. A. Rutllant, M. Falvey, C. D. Whiteman, R. D. Garreaud, A. Arriagada, F. Flores, and N. Donoso. Raco Wind at the Exit of the Maipo Canyon in Central Chile: Climatology, Special Observations, and Possible Mechanisms. *J. Appl. Meteor. Climatol.*, 59:725–749, 2020. doi: 10.1175/JAMC-D-19-0188.1.

G. Myhre, D. Shindell, F.-M. Bréon, W. Collins, J. Fuglestvedt, J. Huang, D. Koch, J.-F. Lamarque, D. Lee, B. Mendoza, T. Nakajima, A. Robock, G. Stephens, T. Takemura, and H. Zhang. *In: Climate Change 2013: The Physical Science Basis. Contribution of Working Group I to the Fifth Assessment Report of the Intergovernmental Panel on Climate Change*, chapter Anthropogenic and Natural Radiative Forcing. [Stocker, T.F. and Qin, D. and Plattner, G.-K. and Tignor, M. and Allen, S.K. and Boschung, J. and Nauels, A. and Xia, Y. and Bex, V. and Midgley, P.M.], Cambridge University Press, Cambridge, United Kingdom and New York, NY, USA, 2013.

NARSTO. *Particulate matter science for policy makers: a NARSTO assessment.* Cambridge University Press, 2004.

NASA. Radiation Belts with Satellites, 2013. URL `https://www.nasa.gov/mission_pages/sunearth/news/gallery/20130228-radiationbelts.html`.

National Research Council. *Rethinking the Ozone Problem in Urban and Regional Air Pollution.* The National Academies Press, Washington, DC, 1991. doi: 10.17226/1889.

NCEP. NCEP FNL Operational Model Global Tropospheric Analyses, continuing from July 1999, 2000. URL `https://doi.org/10.5065/D6M043C6`.

W. Nie, A. Ding, T. Wang, V.-M. Kerminen, C. George, L. Xue, W. Wang, Q. Zhang, T. Petäjä, X. Qi, X. Gao, X. Wang, X. Yang, C. Fu, and M. Kulmala. Polluted dust promotes new particle formation and growth. *Sci. Rep.*, 4:6634, 2020. doi: 10.1038/srep06634.

E. Nielsen, M. Dybdahl, and P. B. Larsen. Health Effects Assessment of Exposure to Particles from Wood Smoke. Technical report, Danish Environmental Protection Agency, 2008. URL https://orbit.dtu.dk/files/137906875/Health_effects_assessment_of_exposure_to_particles_from_wood_smoke_2008.pdf.

V. Noel, H. Chepfer, C. Hoareau, M. Reverdy, and G. Cesana. Effects of solar activity on noise in CALIOP profiles above the South Atlantic Anomaly. *Atmos. Meas. Tech.*, 2014. doi: 10.5194/amt-7-1597-2014.

OECD. The Economic Consequences of Outdoor Air Pollution. Technical report, Organisation for Economic Co-operation and Development, 2016.

OECD. Domestic product - GDP long-term forecast - OECD data, 2019. URL https://data.oecd.org/gdp/gdp-long-term-forecast.htm.

OECD. Income inequality indicator, 2021. Accessed on 17 February 2021.

A. Omar, D. M. Winker, M. A. Vaughan, Y. Hu, C. R. Trepte, R. A. Ferrare, K.-P. Lee, C. A. Hostetler, C. Kittaka, R. R. Rogers, R. E. Kuehn, and Z. Liu. The CALIPSO Automated Aerosol Classification and Lidar Ratio Selection Algorithm. *J. Atmos. Ocean. Tech.*, 26:1994–2014, 2009. doi: 10.1175/2009JTECHA1231.1.

M. Osses, N. Rojas, C. Ibarra, V. Valdebenito, I. Laengle, N. Pantoja, D. Osses, K. Basoa, S. Tolvett, N. Huneeus, L. Gallardo, and B. Gómez. High-definition spatial distribution maps of on-road transport exhaust emissions in Chile, 1990–2020. *Earth Syst. Sci. Data Discuss.*, in review:[preprint], 2021. doi: 10.5194/essd-2021-218.

Our World in Data. Air Pollution, 2017. URL https://ourworldindata.org/air-pollution.

Panel Ciudadano de la Universidad del Desarrollo. Santiaguinos esperan con altas expectativas el partido de hoy... y un 29% hará asado. *El Mercurio*, June 26^{th} 2016. URL https://gobierno.udd.cl/cpp/noticias/2017/01/17/santiaguinos-esperan-con-altas-expectativas-el-partido-de-hoy-y-un-29-hara-asado/.

M. C. Peel, B. L. Finlayson, and T. A. Mcmahon. Updated world map of the Köppen-Geiger climate classification. *Hydrol. Earth Syst. Sci.*, 11:1633–1644, 2007. doi: 10.5194/hess-11-1633-2007.

F. Pellicciotti, S. Ragettli, M. Carenzo, and J. McPhee. Changes of glaciers in the Andes of Chile and priorities for future work. *Sci. Tot. Environ.*, 493:1197–1210, 2013. doi: 10.1016/j.scitotenv.2013.10.055.

J. E. Penner, M. Andreae, H. Annegarn, L. Barrie, J. Feichter, D. Hegg, A. Jayaraman, R. Leaitch, D. Murphy, J. Nganga, and G. Pitari. *Aerosols, their direct and indirect effects.* In: Climate Change 2001: The Scientific Basis Contribution of Working Group I to the Third Assessment Report of the Intergovernmental Panel on Climate Change [Houghton, J.T., Y. Ding, D.J. Griggs, M. Noguer, P.J. van der Linden, X. Dai, K. Maskell, and C.A. Johnson (eds.)]. Cambridge University Press, Cambridge, United Kingdom and New York, NY, USA, 881pp, 2001.

J. C. Péré, B. Bessagnet, M. Mallet, F. Waquet, I. Chiapello, F. Minvielle, V. Pont, and L. Menut. Direct radiative effect of the Russian wildfires and its impact on air temperature and atmospheric dynamics during August 2010. *Atmos. Chem. Phys.*, 14:1999–2013, 2014. doi: 10.5194/acp-14-1999-2014.

J.-E. Petit, T. Amodeo, F. Meleux, B. Bessagnet, L. Menut, D. Grenier, Y. Pellan, A. Ockler, B. Rocq, V. Gros, J. Sciare, and O. Favez. Characterising an intense PM pollution episode in March 2015 in France from multi-site approach and near real time data: Climatology, variabilities, geographical origins and model evaluation. *Atmos. Environ.*, 155:68–84, 2017. doi: 10.1016/j.atmosenv.2017.02.012.

G. Pfister, D. Baumgartner, R. Maderbacher, and E. Putz. Aircraft measurements of photolysis rate coefficients for ozone and nitrogen dioxide under cloudy conditions. *Atmos. Environ.*, 34:4019–4029, 2000. doi: 10.1016/S1352-2310(00)00149-7.

S. D. Piccot, J. J. Watson, and J. W. Jones. A global inventory of volatile organic compound emissions from anthropogenic sources. *J. Geophys. Res.*, 97:D9, 1992. doi: 10.1029/92JD00682.

O. Pinto Jr, W. Gonzalez, I. Pinto, A. Gonzalez, and O. M. Jr. The South Atlantic Magnetic Anomaly: three decades of research. *Journal of Atmospheric and Terrestrial Physics*, 1992. doi: 10.1016/0021-9169(92)90137-A.

C. A. Pope and D. W. Dockery. Health Effects of Fine Particulate Air Pollution: Lines that Connect. *J. Air Waste Manag. Assoc.*, 56:709–742, 2006. doi: 10.1080/10473289.2006.10464485.

S. E. Puliafito, D. G. Allende, P. S. Castesana, and M. F. Ruggeri. High-resolution atmospheric emission inventory of the argentine energy sector. Comparison with edgar global emission database. *Heliyon*, 3:e00489, 2017. doi: 10.1016/j.heliyon.2017.e00489.

G. Qin and M. Huang. A Study on Rain Acidification Processes in Ten Cities of China. *Water, Air & Soil Pollut.*, 130:163–174, 2001. doi: 10.1023/A:1012267922923.

K. M. Ragsdale, B. S. Barrett, and A. P. Testino. Variability of particulate matter (PM10) in Santiago, Chile by phase of the Madden–Julian Oscillation (MJO). *Atmos. Environ.*, 81:304–310, 2013. doi: 10.1016/j.atmosenv.2013.09.011.

D. A. Rahn and R. D. Garreaud. A synoptic climatology of the near-surface wind along the west coast of south america. *Int. J. Climatol.*, 34:780–792, 2014. doi: 10.1002/joc.3724.

Ramboll. Camx user's guide comprehensive air quality model with extentions, 2021. URL `http://www.camx.com/`.

M. D. Resquin, D. Santágata, L. Gallardo, D. Gómez, C. Rössler, and L. Dawidowski. Local and remote black carbon sources in the Metropolitan Area of Buenos Aires. *Atmos. Environ.*, 182:105–114, 2018. doi: 10.1016/j.atmosenv.2018.03.018.

M. Reyers, M. Hamidi, and Y. Shao. Synoptic analysis and simulation of an unusual dust event over the Atacama Desert. *Atmos Sci Lett.*, 20:e899, 2019. doi: 10.1002/asl.899.

K. Riahi, A. Grübler, and N. Nakicenovic. Scenarios of long-term socio-economic and environmental development under climate stabilization. *Technol. Forecast. Soc. Change*, 74:887–935, 2007. doi: 10.1016/j.techfore.2006.05.026.

K. Riahi, S. Rao, V. Krey, C. Cho, V. Chirkov, G. Fischer, G. Kindermann, N. Nakicenovic, and P. Rafaj. RCP 8.5-A scenario of comparatively high greenhouse gas emissions. *Clim. Change*, 109:33, 2011. doi: 10.1007/s10584-011-0149-y.

S. Roberts, L. Arseneault, B. Barratt, S. Beevers, A. Danese, C. L. Odgers, T. E. Moffitt, A. Reuben, F. J. Kelly, and H. L. Fisher. Exploration of NO2 and PM2.5 air pollution and mental health problems using high-resolution data in London-based children from a UK longitudinal cohort study. *Psychiatry Res.*, 272:8–17, 2019. doi: 10.1016/j.psychres.2018.12.050.

S. Robertson and M. R. Miller. Ambient air pollution and thrombosis. *Part. Fibre Toxicol.*, 15:1, 2018. doi: 10.1186/s12989-017-0237-x.

I. Romieu, H. Weitzenfeld, and J. Finkelman. Urban Air Pollution in Latin America and the Caribbean. *Journal of the Air & Waste Management Association*, 41:1166–1171, 1991. doi: 10.1080/10473289.1991.10466910.

P. M. Rowe, R. R. Cordero, S. G. Warren, E. Stewart, S. J. Doherty, A. Pankow, M. Schrempf, G. Casassa, J. Carrasco, J. Pizarro, S. MacDonell, A. Damiani, F. Lambert, R. Rondanelli, N. Huneeus, F. Fernandoy, and S. Neshyba. Black carbon and other light-absorbing impurities in snow in the Chilean Andes. *Sci. Rep.*, 9:4008, 2019. doi: 10.1038/s41598-019-39312-0.

M. A. Rubio, E. Lissi, E. Gramsch, and R. D. Garreaud. Effect of Nearby Forest Fires on Ground Level Ozone Concentrations in Santiago, Chile. *Atmosphere*, 6:1926–1938, 2015. doi: 10.3390/atmos6121838.

J. Rutllant and R. Garreaud. Meteorological Air Pollution Potential for Santiago, Chile: Towards an Objective Episode Forecasting. *Environ. Monit. Assess.*, 34:223–244, 1995. doi: 10.1007/BF00554796.

P. E. Saide, M. Mena-Carrasco, S. Tolvett, P. Hernandez, and G. R. Carmichael. Air quality forecasting for winter-time $PM_{2.5}$ episodes occurring in multiple cities in central and southern Chile. *J. Geophys. Res. Atmos.*, 121:558–575, 2016. doi: 10.1002/2015JD023949.

P. A. Sanhueza, M. A. Torreblanca, L. A. Diaz-Robles, L. N. Schiappacasse, M. P. Silva, and T. D. Astete. Particulate Air Pollution and Health Effects for Cardiovascular and Respiratory Causes in Temuco, Chile: A Wood-Smoke-Polluted Urban Area. *J Air Waste Manag Assoc*, 59:1481–1488, 2012. doi: 10.3155/1047-3289.59.12.1481.

P. Sarricolea, R. Serrano-Notivoli, M. Fuentealba, M. Hernández-Mora, F. de la Barrera, P. Smith, and O. Meseguer-Ruiz. Recent wildfires in Central Chile: Detecting links between burned areas and population exposure in the wildland urban interface. *Sci. Total Environ.*, 706:135894, 2020. doi: 10.1016/j.scitotenv.2019.135894.

R. S. Schemenauer, H. Fuenzalida, and P. Cereceda. A Neglected Water Resource: The Camanchaca of South America. *Bull. Am. Meteorol. Soc.*, 69:138–147, 1988. doi: 10.1175/1520-0477(1988)069<0138:ANWRTC>2.0.CO;2.

R. Schmitz. Modelling of air pollution dispersion in Santiago de Chile. *Atmos. Environ.*, 39:2035–2047, 2005. doi: 10.1016/j.atmosenv.2004.12.033.

R. J. Seguel, C. A. Mancilla, R. Rondanelli, M. A. Leiva, and R. G. Morales. Ozone distribution in the lower troposphere over complex terrain in Central Chile. *J. Geophys. Res. Atmos.*, 118:2966–2980, 2013. doi: 10.1002/jgrd.50293.

R. J. Seguel, L. Gallardo, Z. L. Fleming, and S. Landeros. Two decades of ozone standard exceedances in Santiago de Chile. *Air Qual Atmos Health*, 13:593–605, 2020. doi: 10.1007/s11869-020-00822-w.

J. H. Seinfeld and S. N. Pandis. *Atmospheric Chemistry and Physics: From Air Pollution to Climate Change. Second Edition.* John Wiley & Sons, Inc., Hoboken, New Jersey, 2006.

R. Shaiganfar, S. Beirle, H. Denier van der Gon, S. Jonkers, J. Kuenen, H. Petetin, Q. Zhang, M. Beekmann, and T. Wagner. Estimation of the Paris NO_x emissions from mobile MAX-DOAS observations and CHIMERE model simulations during the MEGAPOLI campaign using the closed integral method. *Atmos. Chem. Phys.*, 17:7853–7890, 2017. doi: 10.5194/acp-17-7853-2017.

H. H. Shin and S.-Y. Hong. Representation of the Subgrid-Scale Turbulent Transport in Convective Boundary Layers at Gray-Zone Resolutions. *Mon. Weather Rev.*, 143:250–271, 2015. doi: 10.1175/MWR-D-14-00116.1.

M. Shiraiwa, Y. Li, A. P. Tsimpidi, V. A. Karydis, T. Berkemeier, S. N. Pandis, J. Lelieveld, T. Koop, and U. Pöschl. Global distribution of particle phase state in atmospheric secondary organic aerosols. *Nat. Commun.*, 8:15002, 2017. doi: 10.1038/ncomms15002.

G. Shrestha, S. J. Traina, and C. W. Swanston. Black Carbon's Properties and Role in the Environment: A Comprehensive Review. *Sustainability*, 2:294–320, 2010. doi: 10.3390/su2010294.

S. Sillman. The relation between ozone, NOx and hydrocarbons in urban and polluted rural environments. *Atmos. Environ.*, 33:1821–1845, 1999. doi: 10.1016/S1352-2310(98)00345-8.

A. Singh and M. Agrawal. Acid rain and its ecological consequences. *J. Environ. Biol.*, 29:15–24, 2008. doi: PMID:18831326.

W. C. Skamarock, J. B. Klemp, J. Dudhia, D. O. Gill, D. M. Barker, M. G. Duda, X.-Y. Huang, W. Wang, and J. G. Powers. A Description of the Advanced Research WRF Version 3. *NCAR Technical Note*, 27, 2008.

M. Sofiev, T. Ermakova, and R. Vankevich. Evaluation of the smoke-injection height from wild-land fires using remote-sensing data. *Atmos. Chem. Phys.*, 12:1995–2006, 2012. doi: 10.5194/acp-12-1995-2012.

L. N. Soza, P. Jordanova, O. Nicolis, L. Střelec, and M. Stehlík. Small sample robust approach to outliers and correlation of atmospheric pollution and health effects in Santiago de Chile. *Chemom. Intell. Lab. Syst.*, 185:73–84, 2019. doi: 10.1016/j.chemolab.2018.12.010.

A. Stohl, C. Forster, A. Prank, P. Seibert, and G. Wotawa. Technical note: The Lagrangian particle dispersion model FLEXPART version 6.2. *Atmos. Chem. Phys.*, 5:2461–2474, 2005. doi: 10.5194/acp-5-2461-2005.

R. B. Stull. *An Introduction to Boundary Layer Meteorology*. Atmospheric and Oceanographic Sciences Library. Springer Netherlands, 1988. ISBN 9789027727695. doi: 10.1007/978-94-009-3027-8.

S. Szopa, D. A. Hauglustaine, and P. Ciais. Relative contributions of biomass burning emissions and atmospheric transport to carbon monoxide interannual variability. *Geophys. Res. Lett.*, 34:L18810, 2007. doi: 10.1029/2007GL030231.

X. Tao, Z. Tong, Z. Yixuan, and Z. Qiang. Declines in mental health associated with air pollution and temperature variability in China. *Nat. Commun.*, 10:2165, 2019. doi: 10.1038/s41467-019-10196-y.

H. Teyssèdre, M. Michou, H. L. Clark, B. Josse, F. Karcher, D. Olivié, V.-H. Peuch, D. Saint-Martin, D. Cariolle, J.-L. Attié, P. Nédélec, P. Ricaud, V. Thouret, R. J. van der A, A. Volz-Thomas, and F. Chéroux. A new tropospheric and stratospheric Chemistry and Transport Model MOCAGE-Climat for multi-year studies: evaluation of the present-day climatology and sensitivity to surface processes. *Atmos. Chem. Phys.*, 7:5815–5860, 2007. doi: 10.5194/acp-7-5815-2007.

The World Bank and Institute for Health Metrics and Evaluation. The Cost of Air Pollution: Strengthening the Economic Case for Action. Technical report, University of Washington, Seattle, 2016. URL `https://openknowledge.worldbank.org/bitstream/handle/10986/25013/108141.pdf`.

Y. Tian, X. Pan, T. Nishizawa, H. Kobayashi, I. Uno, X. Wang, A. Shimizu, and Z. Wang. Variability of depolarization of aerosol particles in the megacity of Beijing: implications for the interaction between anthropogenic pollutants and mineral dust particles. *Atmos. Chem. Phys.*, 18:18203–18217, 2020. doi: 10.5194/acp-18-18203-2018.

TNO. Lotos-euros air quality modelling and emissions, 2021. URL `https://lotos-euros.tno.nl/`.

F. Toledo, C. Garrido, M. Díaz, R. Rondanelli, S. Jorquera, and P. Valdivieso. AOT Retrieval Procedure for Distributed Measurements With Low-Cost Sun Photometers. *J. Geophys. Res. Atmos.*, 123:1113–1131, 2018. doi: 10.1002/2017JD027309.

R. A. Toro, C. S. Donoso, R. A. Seguel, R. G. E. Morales, and M. A. Leiva G. Photochemical ozone pollution in the Valparaiso Region, Chile. *Air Qual Atmos Health*, 7:1–11, 2014. doi: 10.1007/s11869-013-0218-7.

R. A. Toro, M. Kvakić, Z. B. Klaić, D. Koračin, R. G. E. Morales, and M. A. Leiva G. Exploring atmospheric stagnation during a severe particulate matter air pollution episode over complex terrain in Santiago, Chile. *Environ. Pollut.*, 244:705–714, 2019. doi: 10.1016/j.envpol.2018.10.067.

K. Tørseth, W. Aas, K. Breivik, A. M. Fjæraa, M. Fiebig, A. G. Hjellbrekke, C. L. Myhre, S. Solberg, and K. E. Yttri. Introduction to the European Monitoring and Evaluation Programme (EMEP) and observed atmospheric composition change during 1972–2009. *Atmos. Chem. Phys.*, 12:5447–5481, 2012. doi: 10.5194/acp-12-5447-2012.

P. Tuccella, L. Menut, R. Briant, A. Deroubaix, D. Khvorostyanov, S. Mailler, G. Siour, and S. Turquety. Implementation of Aerosol-Cloud Interaction within WRF-CHIMERE Online Coupled Model: Evaluation and Investigation of the Indirect Radiative Effect from Anthropogenic Emission Reduction on the Benelux Union. *Atmosphere*, 10:20, 2019. doi: 10.3390/atmos10010020.

S. Turquety, L. Menut, B. Bessagnet, A. Anav, N. Viovy, F. Maignan, and M. Wooster. Apiflame v1.0: high-resolution fire emission model and application to the euro-mediterranean region. *Geosci. Model Dev.*, 7:587–612, 2014. doi: 10.5194/gmd-7-587-2014.

United Nations. World Population Prospects 2017, 2017. URL `https://esa.un.org/unpd/wpp/`.

United Nations Development Programme. Human Development Reports, 2018. URL `http://hdr.undp.org/en/composite/trends`.

United Nations Development Programme. Human Development Report 2020, 2020. URL `http://hdr.undp.org/sites/default/files/hdr2020.pdf`.

University of Maryland. GLCF: MODIS Land Cover, 2010. URL `http://glcf.umd.edu/data/lc/`.

R. Urrutia-Jalabert, M. González, A. Gonzalez Reyes, A. Lara, and R. Garreaud. Climate variability and forest fires in central and south-central chile. *Ecosphere*, 9:e02171, 2018. doi: 10.1002/ecs2.2171.

J. A. Van Allen and L. A. Franck. Radiation around the Earth to a radial distance of 107,400 km. *Nature*, 1959. doi: 10.1038/183430a0.

B. Van Leer. Towards the ultimate conservative difference scheme. IV. A new approach to Numerical convection. *J. Comput. Phys.*, 23:276–299, 1977. doi: 10.1016/0021-9991(77)90095-X.

D. P. van Vuuren, M. G. J. den Elzen, P. L. Lucas, B. Eickhout, B. J. Strengers, B. van Ruijven, S. Wonink, and R. van Houdt. Stabilizing greenhouse gas concentrations at low levels: an assessment of reduction strategies and costs. *Clim. Change*, 81:119–159, 2007. doi: 10.1007/s10584-006-9172-9.

D. P. van Vuuren, J. Edmonds, M. Kainuma, K. Riahi, A. Thomson, K. Hibbard, G. C. Hurtt, T. Kram, V. Krey, J.-F. Lamarque, T. Masui, M. Meinshausen, N. Nakicenovic, S. J. Smith, and S. K. Rose. The representative concentration pathways: an overview. *Clim. Change*, 109:5, 2011. doi: 10.1007/s10584-011-0148-z.

D. P. van Vuuren, E. Stehfest, M. G. J. den Elzen, T. Kram, J. van Vliet, S. Deetman, M. Isaac, K. K. Goldewijk, A. Hof, A. M. Beltran, R. Oostenrijk, and B. van Ruijven. RCP2.6: exploring the possibility to keep global mean temperature increase below 2°C. *Clim. Change*, 109:95, 2011. doi: 10.1007/s10584-011-0152-3.

A. Vara-Vela, M. de Fátima Andrade, Y. Zhang, P. Kumar, R. Y. Ynoue, C. E. Souto-Oliveira, F. J. da Silva Lopes, and E. Landulfo. Modeling of atmospheric aerosol properties in the São Paulo Metropolitan Area: Impact of biomass burning. *J. Geophys. Res. Atmos.*, 123:9935–9956, 2018. doi: 10.1029/2018JD028768.

S. Vardoulakis and P. Kassomenos. Sources and factors affecting PM10 levels in two European cities: Implications for local air quality management. *Atmos. Environ.*, 42:3949–3963, 2008. doi: 10.1016/j.atmosenv.2006.12.021.

A. Veira, S. Kloster, S. Wilkenskjeld, and S. Remy. Fire emission heights in the climate system - Part 1: Global plume height patterns simulated by ECHAM6-HAM2. *Atmos. Chem. Phys.*, 15:7155–7171, 2015. doi: 10.5194/acp-15-7155-2015.

J. G. Verwer. Gauss-Seidel iteration for stiff odes from chemical kinetics. *J. Sci. Comput.*, 15:1243–1250, 1994. doi: 10.1137/0915076.

E. Vicente, A. Vicente, M. Evtyugina, R. Carvalho, L. Tarelho, F. Oduber, and C. Alves. Particulate and gaseous emissions from charcoal combustion in barbecue grills. *Fuel Process. Technol.*, 176:296–306, 2018. doi: 10.1016/j.fuproc.2018.03.004.

H. von Storch, H. Langenberg, and F. Feser. A spectral nudging technique for dynamical downscaling purposes. *Mon. Weather Rev.*, 128:3664–3673, 2000. doi: 10.1175/1520-0493(2000)128<3664:ASNTFD>2.0.CO;2.

C. J. Walcek and H.-H. Yuan. Calculated Influence of Temperature-Related Factors on Ozone Formation Rates in the Lower Troposphere. *J. Appl. Meteor.*, 34:1056–1069, 1995. doi: 10.1175/1520-0450(1995)034<1056:CIOTRF>2.0.CO;2.

M. Walt. *Introduction to Geomagnetically Trapped Radiation*. Cambridge University Press, 1994.

Q. Wang, Z. Zhao, J. Tian, C. Zhu, H. Ni, Y. Zhang, N. Zhang, Z. Shan, Y. Han, and J. Cao. Seasonal Transport and Dry Deposition of Black Carbon Aerosol in the Southeastern Tibetan Plateau. *Aerosol Sci. Eng.*, 1:160–168, 2017. doi: 10.1007/s41810-017-0016-y.

M. G. Weinbauer, B. Guinot, C. Migon, F. Malfatti, and X. Mari. Skyfall-neglected roles of volcano ash and black carbon rich aerosols for microbial plankton in the ocean. *J. Plankton Res.*, 39:187–198, 2017. doi: 10.1093/plankt/fbw100.

H. Weng, J. Lin, R. Martin, D. B. Millet, L. Jaeglé, D. Ridley, C. Keller, C. Li, M. Du, and J. Meng. Global high-resolution emissions of soil NOx, sea salt aerosols, and biogenic volatile organic compounds. *Sci. Data*, 7:148, 2020. doi: 10.1038/s41597-020-0488-5.

M. Wesely. Parameterization of Surface Resistances to Gaseous Dry Deposition in Regional-Scale Numerical Models. *Atmos. Environ.*, 23:1293–1304, 1989. doi: 10.1016/0004-6981(89)90153-4.

S. E. West, P. Büker, M. Ashmore, G. Njoroge, N. Welden, C. Muhoza, P. Osano, J. Makau, P. Njoroge, and W. Apondo. Particulate matter pollution in an informal settlement in Nairobi: Using citizen science to make the invisible visible. *Appl. Geogr.*, 114:102133, 2020. doi: 10.1016/j.apgeog.2019.102133.

WGMS and National Snow and Ice Data Center (comps.). World Glacier Inventory, Version 1. Boulder, Colorado USA. NSIDC: National Snow and Ice Data Center, 1999, updated 2012. Last access 1^{st} October 2020.

D. C. Whiteman. *Mountain Meteorology: Fundamentals and Applications*. Oxford University Press, 2000.

WHO. Environmental Health Criteria 213 - Carbon Monoxide. Technical report, World Health Organization, 1999. URL `https://www.who.int/ipcs/publications/ehc/ehc_213_part_1.pdf`.

WHO. Health Aspects of Air Pollution with Particulate Matter, Ozone and Nitrogen Dioxide. Technical report, World Health Organization, 2003.

WHO. WHO Air quality guidelines for particulate matter, ozone, nitrogen dioxide and sulfur dioxide : global update 2005 : summary of risk assessment. Technical report, World Health Organization, 2006.

WHO. Global health risk - Mortality and burden of disease attributable to selected major risks. Technical report, World Health Organization, 2009.

WHO. World health statistics 2018: monitoring health for the SDGs, sustainable development goals. Technical report, World Health Organization, 2018. URL `https://apps.who.int/iris/bitstream/handle/10665/272596/9789241565585-eng.pdf`.

WHO and OECD. Economic cost of the health impact of air pollution in Europe: Clean air, health and wealth. Technical report, World Health Organization Regional Office for Europe and Organisation for Economic Co-operation and Development, 2015. URL `https://www.euro.who.int/__data/assets/pdf_file/0004/276772/Economic-cost-health-impact-air-pollution-en.pdf`.

E. Wilkins. Air pollution aspects of the London fog of December 1952. *Q. J. R. Meteorol. Soc.*, 80:267–271, 1954. doi: 10.1002/qj.49708034420.

D. M. Winker, M. A. Vaughan, A. Omar, Y. Hu, K. A. Powell, Z. Liu, W. H. Hunt, and S. A. Young. Overview of the CALIPSO Mission and CALIOP Data Processing Algorithms. *J. Atmos. Ocean. Technol.*, 26:2310–2323, 2009. doi: 10.1175/2009JTECHA1281.1.

D. M. Winker, J. Pelon, J. A. Coakley, Jr., S. A. Ackerman, R. J. Charlson, P. R. Colarco, P. Flamant, Q. Fu, R. M. Hoff, C. Kittaka, T. L. Kubar, H. Le Treut, M. P. Mccormick, G. Mégie, L. Poole, K. Powell, C. Trepte, M. A. Vaughan, and B. A. Wielicki. The CALIPSO mission: A global 3D view of aerosols and clouds. *Bull. Am. Meteorol. Soc.*, 91:1211–1230, 2010. doi: 10.1175/2010BAMS3009.1.

D. M. Winker, J. L. Tackett, B. J. Getzewich, Z. Liu, M. A. Vaughan, , and R. R. Rogers. The global 3-D distribution of tropospheric aerosols as characterized by CALIOP. *Atmos. Chem. Phys.*, 13:3345–3361, 2013. doi: 10.5194/acp-13-3345-2013.

J. C. Wyngaard. Toward Numerical Modeling in the 'Terra Incognita'. *J. Atmos. Sci.*, 61:1816–1826, 2004. doi: 10.1175/1520-0469(2004)061<1816:TNMITT>2.0.CO;2.

F. Yan, C. He, S. Kang, P. Chen, Z. Hu, X. Han, S. Gautam, C. Yan, M. Zhang, M. Sillanpää, P. A. Raymond, and C. Li. Deposition of Organic and Black Carbon: Direct Measurements at Three Remote Stations in the Himalayas and Tibetan Plateau. *J. Geophys. Res.*, 124:9702–9715, 2019. doi: 10.1029/2019JD031018.

J. Yang and B. Zhang. Air pollution and healthcare expenditure: Implication for the benefit of air pollution control in China. *Environ. Int.*, 120:443–455, 2018. doi: 10.1016/j.envint.2018.08.011.

G. Zängl. The impact of weak synoptic forcing on the valley-wind circulation in the Alpine Inn Valley. *Meteorol. Atmos. Phys.*, 105:37–53, 2009. doi: 10.1007/s00703-009-0030-y.

L. Zhang, S. Gong, J. Padro, and L. Barrie. A size-segregated particle dry deposition scheme for an atmospheric aerosol module. *Atmos. Environ.*, 35:549–560, 2001. doi: 10.1016/S1352-2310(00)00326-5.

Y. Zhang, S. Kang, Z. Cong, J. Schmale, M. Sprenger, C. Li, W. Yang, T. Gao, M. Sillanpää, X. Li, Y. Liu, P. Chen, and X. Zhang. Light-absorbing impurities enhance glacier albedo reduction in the southeastern Tibetan plateau. *J. Geophys. Res. Atmos.*, 122:6915–6933, 2017. doi: 10.1002/2016JD026397.

ECOLE DOCTORALE

Titre: Observation et modélisation des événements de pollution au Chili

Mots clés: Modélisation de chimie-transport • Pollution atmosphérique • Chili • Carbone suie

Résumé: Le Chili est fréquemment confronté à d'importants pics de pollution atmosphérique, notamment dans sa région centrale qui comprend la capitale, Santiago, et ses 7 millions d'habitants. Cette pollution est principalement d'origine anthropique (trafic, industrie, chauffage résidentiel) mais possède également une composante naturelle (poussières désertiques, sels marins, feux de forêt). Les concentrations atmosphériques élevées de polluants relevées dans cette région du monde, induisent à la fois à des problématiques de santé publique mais également environnementales et climatiques, en lien notamment avec la présence de glaciers de la cordillère des Andes à proximité des zones urbaines. Malgré la criticité de la pollution de l'air au Chili, la région reste peu étudiée, en particulier du point de vue de la modélisation atmosphérique, du fait d'une complexité géographique atypique.
Dans ce cadre, les travaux conduits dans cette thèse combinent l'analyse de données observées (localement et par satellite) et la modélisation de chimie-transport avec le modèle WRF-CHIMERE, dans le but d'étendre les connaissances relatives aux sources et impacts de la pollution de l'air au Chili. Plus spécifiquement, les questions scientifiques originales suivantes sont étudiées : quelles sont les trajectoires de transport de polluants à l'échelle régionale en été et en hiver ? Quelle est la contribution du transport longue distance à la qualité de l'air de Santiago ? Peut-on quantifier les impacts sur l'atmosphère des incendies records de l'été 2017 ? Quelle source de pollution explique les pics extrêmes de particules fines observés lors d'hivers récents ? Comment les émissions de carbone suie de Santiago s'exportent-elles vers les glaciers des Andes, et dans quelles proportions s'y déposent-elles ? La magnitude de ce dépôt et le processus de transport sous-jacent évoluent-il avec les saisons ?

Title: Observation and modeling of pollution events in Chile

Keywords: Chemistry-Transport Modeling • Air Pollution • Chile • Black Carbon

Abstract: Chile regularly faces high levels of atmospheric pollution, particularly in its central region which comprises the capital city, Santiago, and its 7 million inhabitants. This pollution originates mostly from anthropogenic sources (traffic, industry, residential heating) but also involves natural sources (mineral dust, sea salts, forest fires). The elevated concentrations of atmospheric pollutants observed in this region of the world are associated with public health issues as well as environmental and climatic impacts, in connection with the presence of glaciers of the Andes Cordillera near large urban basins. Despite the criticality of air pollution in Chile, the region is still under-investigated, especially from the atmospheric modeling perspective, due to a complex, atypical geographical configuration.
In this context, this thesis work combines the analysis of observations (from local and satellite data) and chemistry-transport modeling with WRF-CHIMERE, with a view to extending the current literature related to the sources and impacts of air contamination in Chile. More specifically, the following original scientific questions are investigated: What are the seasonal mean transport patterns of pollutants in summertime and wintertime at the scale of central Chile? To what extent does long-range transport contribute to air quality in Santiago? What were the atmospheric impacts of the historic 2017 forest fires? What pollution source led to the record-breaking extreme fine particles events observed in recent winters? Through which pathways do black carbon emissions from Santiago transport higher up to the Andes Cordillera and how much of it deposits on glaciers? Is there a seasonality in this deposition an the underlying pathway?

Institut Polytechnique de Paris
91120 Palaiseau, France